To the Graduate Council:

I am submitting herewith a dissertation written by Arvind Agarwal entitled "Laser Surface Engineering of Composite Titanium Diboride Coating on Steel: Synthesis and Characterization". I have examined the final copy of this dissertation for form and content and recommend that it be accepted in partial fulfillment of the requirements for the degree of Doctor of Philosophy, with a major in Metallurgical Engineering.

Narendra B. Dahotre, Major Professor

We have read this dissertation
and recommend its acceptance:

Accepted for the Council:

Associate Vice Chancellor and
Dean of the Graduate School

LASER SURFACE ENGINEERING OF COMPOSITE TITANIUM DIBORIDE COATING ON STEEL: SYNTHESIS AND CHARACTERIZATION

A Dissertation
Presented for the
Doctorate of Philosophy
Degree
The University of Tennessee, Knoxville

Arvind Agarwal
December 1999

To

My Parents
And
Best Friend Sulakshana Bhabhi

ACKNOWLEDGEMENT

I take this opportunity to express my heartfelt gratitude to my major advisor Dr. Narendra B. Dahotre whose able guidance and support was always the source of inspiration during my Ph.D work. I would like to express my sincere thanks to Drs. Mary Helen McCay, Peter Liaw and Thomas Meek who served as members on my Ph.D committee. Their valuable suggestions during my Ph.D proposal defense and on other occasions provided me a smooth path towards my goal.

I express my sincere thank to Dr. Lawrence F. Allard for his help and guidance with the TEM work and Ms. Laura Riester for the nanoindenetation work, at Oak Ridge National Laboratory (ORNL) that was sponsored by the Assistant Secretary for Energy Efficiency and Renewable Energy, Office of Transportation Technologies, as part of the High Temperature Materials Laboratory User Program (HTML), managed by Lockheed Martin Energy Research Corp. for the U.S. Department of Energy under contract number DE-AC05-96OR22464.

I would also like to thank Dr. T. S. Sudarshan at Materials Modification Inc., Fairfax, VA, who provided me samples for the PES work, which has well supplemented the LSE study of titanium diboride coatings. The financial assistance from the US Air Force (Contract No. F 40600-96-C-0004) is highly acknowledged.

Many people, which include UTSI staff members and fellow students, have helped me throughout the period of my Ph.D and it would have been impossible to complete the task without their help. First and foremost I would like to thank Ms. Lalitha R. Katipelli for her expert assistance in image processing. I sincerely thank Mr. Fred

Schwartz for laser processing of the samples. I would also like to thank Ms. Anuradha Godavarty for her help with TGA experimentation and neural network approach. My sincere thanks are due to Mr. Jim Hornkohl and Mr. Brent Blaha whom I always bugged with the computer related problems but they were very patient and helpful in overcoming those hurdles. I would also like to thank Mr. Newt Wright, Mr. Mike Hodges, Mr. Scott Scarborough, Mr. Doug Warnberg, Mr. Gary Payne and Mr. Jacob Cashion who helped me at the various stages of my experiments. A special word of thanks is due for Mr. Marvis White who familiarized me with the finer techniques of x-ray diffraction. Also, a special thank is owed to Ms. Linda Engels for her excellent graphic skills with preparation of illustrations. I am extremely thankful to Ms. Mary Lo for her continuous help for the literature search. I am very thankful to administrative staff of the Center for Laser Applications (CLA), viz. Ms. Carole Thomas, Ms. Lisa Turner and Ms. Diane Chellstorp for their assistance with the supplies and other administrative works.

Last but not the least, I would like to thank my M.S. advisor. Dr. R. Balsubramaniam at Department of Materials and Metallurgical Engineering at Indian Institute of Technology, Kanpur who taught me "*never say die*" approach in an exemplary manner.

ABSTRACT

The aim of the present study was to *identify* and *develop* an unique combination of coating technique and material, which could target its properties similar to that of an "ideal coating". In the present study, Nd:YAG laser was used as a tool to deposit ultrahard TiB_2 ceramic on AISI 1010 steel within a *fixed envelope* of processing parameters such as laser power and traverse speed. The thrust of the present study is on the material properties and behavior of the TiB_2 coating within the fixed envelope of these processing parameters. A uniform, continuous and crack free coating with a metallurgically sound interface is obtained. Coating is "composite" in nature comprising TiB_2 particles and the Fe from steel trapped in the laser melt zone. Such coating has been evaluated for various properties such as mechanical (hardness, elastic modulus, interfacial energy, fracture toughness and fracture morphology), chemical and structural (x-ray diffraction, SEM, TEM and HRTEM) and high temperature oxidation and corrosion properties. Coating is hard and tough in nature. A semi-quantitative model has been developed to estimate the elastic modulus of TiB_2 coating using nanoindentation technique. It also has been concluded that TiB_2 coating has a high interfacial energy suggesting a stronger and adherent interface. Composite TiB_2 coating has a significant oxidation resistance upto 800^0C. Also, it has shown improved high temperature corrosion resistance against liquid aluminum. Such features contribute significantly towards the goal of achieving an *ideal* coating.

TABLE OF CONTENTS

PART			PAGE
1.	INTRODUCTION		1
2.	LITERATURE REVIEW		4
	2.1	Background of laser and materials processing	5
	2.2	Surface modification techniques	6
	2.3	Ceramic coating deposited on metallic substrates using lasers	11
	2.4	Metal/Ceramic interface	12
	2.5	Ultrahard ceramic coating materials	16
	2.6	Boride based ceramics	17
	2.7	Properties of Titatnium Diboride	22
3.	EXPERIMENTAL PROCEDURES		26
	3.1	Materials and coating procedure	27
	3.2	Microstructural characterization	31
		3.2.1 TEM sample preparation	32
		3.2.2 Structural characterization	34
	3.3	Mechanical characterization	34
		3.3.1 Microhardness measurements	35
		3.3.2 Modulus of elasticity measurement using nanoindenter	35
		A. Background	35
		B. Nanoindentation measurements on composite TiB_2 coating	38
		3.3.3 Four-point bend test	42
		A. Background	42
		B. Four-point bend test on composite TiB_2 coating	44
		3.3.4 Uniaxial tensile test	47
	3.4	Tribological characterization	48
		3.4.1 Mass loss analysis	48
		3.4.2 Coefficient of friction	49
		3.4.3 Surface roughness measurement	49
	3.5	High Temperature Oxidation Experiments	51
		3.5.1 Thermogravimetric analysis	51
		3.5.2 Long duration exposure at elevated temperature	53
		3.5.3 Characterization of the oxide scale	54
	3.6	Dip test for evaluation of high temperature corrosion resistance against liquid aluminum	56
4.0	RESULTS AND DISCUSSIONS		60
	4.1	Thermodynamic predictions	61
	4.2	Microstructural characterization	63
		4.2.1 Scanning electron microscopy	65

4.2.2 Structural characterization 76
4.2.3 Transmission electron microscopy 79
A. Ceramic-Metal interface 89
4.3 Mechanical characterization 116
4.3.1 Microhardness measurements 117
4.3.2 Elastic modulus measurements using nanoindentation 119
A. Elastic modulus computation for composite coating 127
4.3.3 Interfacial strength evaluation by four-point bend test 131
4.3.4 Deformation behavior of composite coating under uniaxial tensile test 140
4.4 Tribological Characterization 147
4.4.1 Mass loss analysis 147
4.4.2 Coefficient of friction measurement 152
4.5 High temperature oxidation of TiB_2 coating in air 160
4.5.1 Oxidation kinetics 160
4.5.2 Oxide scale characterization 164
A. Cross-sectional morphology 164
B. Top surface oxide morphology 173
C. Structural characterization of oxide scale 173
4.5.3 Neural network application to high temperature oxidation 190
A. Background 190
B. Application of professional II/Plus software 191
4.6 High temperature corrosion resistance against liquid aluminum 202

5.0 CONCLUSIONS 219

6.0 RECOMMENDATIONS 225

LIST OF REFERENECS 227

APPENDICES 243
Appendix I - Introduction to pulse electrode surfacing technique to deposit ceramic coatings on metals 244
Appendix II - Pulse electrode deposition of superhard boride coating on ferrous alloy 247
Appendix III- Evolution of interface in pulsed electrode deposited titanium diboride on copper and steel 257
Appendix IV - Synthesis of boride coating on steel using high energy density processes: comparative study of evolution of microstructure 264
Appendix V - Pulsed electrode surfacing of steel with TiC coating: microstructure and wear properties 279
Appendix VI - Comparative wear in titanium diboride coatings on steel using high energy density processes 288
Appendix VII - In-situ synthesis of intermetallic and ceramic coating 319

using pulse electrode surfacing
Appendix VIII - List of publication from the present work 326

VITA 329

LIST OF TABLES

TABLE		PAGE
2.1	List of Wetting Parameters for Various Metal-Ceramic System	16
2.2	Superhard Coating Materials, Deposition Techniques and Applications	18
2.3	Crystal Structures of Borides of Various Metals	21
2.4	Salient Physical Properties of Titanium Diboride (TiB_2)	24
2.5	Potential Application of TiB_2 based Materials as a Function of its Basic Properties	25
3.1	Matrix of Processing Parameters, Precursor Composition and Corresponding Sample Nomenclature	31
3.2	Test Methods to Determine Adhesion in Coating-Substrate Systems	43
3.3	Experimental Matrix for Long Duration Exposure and Corresponding Sample Nomenclature	54
4.1	Thermodynamic Properties of Borides of Titanium and Iron	62
4.2	Microstructural Features of Laser Deposited TiB_2 Coating on AISI 1010 steel	68
4.3	Elemental Composition in Various Microstructural Zones	75
4.4	Crystal Structures of the Relevant Phase(s)	76
4.5	Microhardness Values at Various Locations in Coating and Substrate	117
4.6	Experimental Elastic Modulus (E) and Hardness (H) Values as Obtained from the Load-Displacement Curves of Nanoindenter	120

4.7	Experimental and Theoretical Values of Mechanical Properties of TiB_2, Fe Matrix and 1010 Steel Substrate	126
4.8	Theoretical and Experimental Elastic Modulus Values of Composite Boride Coating for Various Laser Processing Speed	129
4.9	List of Theoretical and Computed Material Properties for TiB_2 Coating/Steel Substrate System (LSE 3 sample)	133
4.10	Work of Adhesion (W_{ad}) and Fracture Energy (G_c) of Metal/Ceramic Interfaces	139
4.11	Failure Stress for Various Ceramic Coating/Metal Substrate Under Uniaxial Tensile Stresses	143
4.12	Summary of TiB_2 Coating and its Tribological Characteristics	159
4.13	Oxidation Kinetic Constants for Composite TiB_2 Coating for Various Constant Temperatures of Exposure	162
4.14	Comprehensive List of Major Phases Present in the Oxide Scale	180
4.15	List of Layers and Corresponding Elements used for Neural Computations	192
4.16	Oxidation Kinetic Constants for Composite-TiB_2 Coating using TGA Experiments and Interpolated Data using Neural Networks	198
4.17	Crystal Structure of the Relevant Phases Present in Different Samples	213
4.18	Microhardness Values at Various Locations for D4 and D 24 Samples	215

LIST OF FIGURES

FIGURE		PAGE
2.1	The wavelength of different lasers in the electromagnetic spectrum	7
2.2	Wetting angle θ of a liquid drop resting on a solid substrate	13
2.3	Structure of various borides	20
2.4	Ti-B phase diagram	23
3.1	SEM micrograph showing TiB_2 powder morphology	28
3.2	A schematic illustration of the laser surface engineering (LSE) Process	29
3.3	A schematic illustration of the sample preparation technique for TEM and Uniaxial tensile test	33
3.4	Typical load-indentation curves from a continuous indentation test	39
3.5	Geometry and loading parameters used in a fracture mechanics analysis	40
3.6	A schematic illustration of the four-point bend test experimental setup	45
3.7	A schematic illustration of the block-on-disk type tribometer setup	50
3.8	A schematic illustration of the sample preparation technique for thermo-gravimetric analysis (TGA)	52
3.9	A schematic illustration of the methodology adopted to perform the x-ray on C2 and C3 samples	55

3.10	A schematic illustration of the dip test experimental set-up	58
3.11	A summary of experimental procedures and analysis	59
4.1	Free energy of formation of borides of Fe and Ti as a function of temperature	64
4.2	A schematic drawing illustrating the microstructural evolution in the cross-section of the laser-modified surface of AISI 1010 steel	66
4.3	SEM micrographs of the cross-section of the laser engineered samples LSE 1, (b) LSE 2 and (c) LSE 3.	67
4.4	High magnification SEM micrographs showing cellular dendritic interface in samples: (a) LSE 1, (b) LSE 2 and (c) LSE 3	70
4.5	SEM micrographs of the laser melted zone illustrating boride particles in samples: (a) LSE 1, (b) LSE 2 and (c) LSE 3	72
4.6	Laser melted zone for the sample LSE 3 (a) SEM micrograph showing acicular boride particles, (b) corresponding X-ray elemental map for Ti and (c) X-ray elemental map for Fe.	73
4.7	X-ray diffraction spectrum of LSE 3 sample	77
4.8	Bright field TEM images showing "composite" nature of the coating with faceted TiB_2 particles of various shapes and sizes embedded in Fe-rich matrix	80
4.9	Bright field TEM images showing "composite" nature of the coating with faceted TiB_2 particles of various shapes and sizes embedded in Fe-rich matrix	81
4.10	Bright field TEM image showing a very small TiB_2 particle (appx.	83

size ~200nm) suggesting fragmentation during laser surface engineering process

4.11 Bright field TEM image showing ultra-fine dendritic network of Fe within the coating region 84

4.12 Dark field TEM image of the ultra-fine Fe dendrites with dissolved TiB_2 within the dendritic spacing. EDS spectra corresponding to spot A and B suggests dissolution of TiB_2 particles within the dendritic spacing 85

4.13 SAD patterns from the area shown in Figure 4.12 corresponding to a combination of HCP structure of TiB_2 along [0001] direction and BCC structure of Fe along [111] direction: (a) low magnification and (b) high magnification 86

4.14 HR-TEM image showing presence of twins within a TiB_2 particle 88

4.15 Bright field TEM image of TiB_2/Fe interface within the coating region 90

4.16 HR-TEM images showing a nanosized reaction zone between the TiB_2 particle and Fe 94

4.17 TEM image showing a reaction zone between the TiB_2 particle and the corresponding EDS spectrums 95

4.18 Bright field TEM image of a nano-size TiB_2 particle surrounded by a binder and Fe-rich matrix zone 96

4.19 EDS spectrum from spots A (binder), B (Fe-rich matrix) and C (TiB_2) particle of Figure 4.18 97

4.20	HR-TEM image of two dimensional lattice fringes on TiB_2 side and one dimensional lattice fringes on Fe side. Semi-coherent interface and nano-crystalline product are marked with arrow	99
4.21	HR-TEM image of TiB_2/Fe interface viewed along [0001] TiB_2 direction	101
4.22	SAD patterns obtained from the region shown in Figure 4.21 (a) from Fe side and (b) from TiB_2 side	102
4.23	(a) Bright field TEM image of a TiB_2 particle containing several faults and dislocations	103
4.23	(b) SAD pattern corresponding to Figure 4.23 (a)	105
4.24	(a) HR-TEM image of the TiB_2/Fe interface showing the presence of several domains of stacking faults on TiB_2 side	106
4.24	(b) Digitally sharpened version of Figure 4.24 (a)	107
4.25	Bright field TEM image of fine black color precipitates within a TiB_2 particle	108
4.26	Bright field TEM images of (a) columnar and (b) dendritic features within the TiB_2 particles	109
4.27	High magnification view of a region within the TiB_2 particle and EDS spectra from spot A (TiB_2 particle) and spot B (black precipitate within the TiB_2 particle)	110
4.28	HR-TEM image of the nano-size precipitate as Moire fringes within a TiB_2 particle. EDS spectrum from these precipitate (spot B) suggests high Fe concentration	112

4.29 High magnification view of the nano-size precipitates (Moire fringes) 113
Arrows indicate a periodicity between two sets of planes that cause formation of such fringes

4.30 SAD pattern from the TiB_2 particle containing Moire fringes. The 114
periodicity/short range order is revealed by the fine spots between the two successive larger reflections

4.31 SEM micrographs of the cross-section showing microhardness 118
indentations on: (a) cluster of TiB_2 particles, melt zone/substrate interface and the heat affected zone in the substrate and (b) mixture of Fe and TiB_2

4.32 Load-displacement curve from the nanoindentation of (a) TiB_2 particle, 122
(b) Fe-rich matrix region in the "composite" coating zone and 123
(c) unaffected AISI 1010 steel substrate 124

4.33 Nanoindentation marks on a cluster of TiB_2 particle: (a) low 125
magnification view and (b) high magnification view

4.34 Theoretical and experimental elastic modulus of the "composite" boride 128
coating for various laser traverse speeds

4.35 SEM micrographs of the cross section of the four-point bend test samples: 134
(a) blunted precrack/notch suggesting plastic deformation and (b) vertical cracks throughout the coating thickness

4.36 SEM micrographs of the cross-section of four-point bend samples 136
showing (a) crack propagation through brittle TiB_2 particles and
(b) crack blunting at the coating/substrate interface due to localized
(c) plastic deformation of the substrate

4.37	Stress-Strain curve showing deformation behavior of "composite" TiB_2 coating under uniaxial tensile stress	142
4.38	Low magnification view of the SEM micrograph showing overall fracture morphology of the composite TiB_2 coating under uniaxial tensile stresses	144
4.39	High magnification views of the fracture morphology showing mixed mode of fracture occurring in "composite" TiB_2 coating	146
4.40	(a) SEM micrograph showing smooth surface topography of the laser engineered surface obtained in LSE 3 sample and	148
	(b) surface roughness profile	149
4.41	Cumulative weight losses over a 20-minute period during dry sliding wear block-on- disk test. Inset shows wear rates corresponding to various surfaces	150
4.42	(a) SEM micrograph of the worn surface of TiB_2 coated sample and corresponding X-ray elemental maps for (b) Ti and (c) Fe	153
4.43	Low magnification SEM micrograph of the wear scar showing the absence of cracks at the worn/unworn interface	154
4.44	Surface roughness profile of the wear surface of LSE 3 sample	155
4.45	X-ray diffraction spectra of the TiB_2 coated surface : before and after wear	156
4.46	Variation in coefficient of friction with time during dry sliding test	158
4.47	Oxidation kinetics for "composite" TiB_2 coating showing parabolic rate of reaction for 600, 700, 800 and 1000^0C	161

4.48	Arrhenius plot for the parabolic rate of oxidation of "composite" TiB_2 Coating	163
4.49	Low magnification SEM micrographs showing cross sectional view of (a) A1 sample (b) A2 sample and (c) A3 sample after long term exposure at 600^0C	166
4.50	Low magnification SEM micrographs showing cross sectional view of (a) B1 sample (b) B2 sample and (c) B3 sample after long term exposure at 800^0C	167
4.51	Low magnification SEM micrographs showing cross sectional view of (a) C1 sample (b) C2 sample and (c) C3 sample after long term exposure at 1000^0C	168
4.52	X-ray maps showing elemental distribution of Ti and Fe corresponding to Figure 4.51(a)	169
4.53	High magnification SEM micrographs showing cross sectional view of (a) B1 sample (b) B2 sample and (c) B3 sample after long term exposure at 800^0C	171
4.54	(a) SEM micrograph of the cross section of layer oxide formed on C1 sample and corresponding x-ray maps for (b) Ti and (c) Fe distribution	172
4.55	Top surface morphology indicating oxide growth in (a) A3, (b) B3 and (c) C1 samples	174
4.56	Roughness contours of the surface morphology of the oxide growth in (a) A3, (b) B3 and (c) C1 samples corresponding to Figure 4.55	175
4.57	X-ray diffraction spectra for A series samples	178

4.58	X-ray diffraction spectra for B series samples	179
4.59	X-ray diffraction spectra for (a) C1 sample, (b) C2 top and bottom and (c) C3 top and bottom	182
4.60	A schematic suggesting the possible oxidation routes and products occurring in "composite" TiB_2 coating	185
4.61	Oxidation kinetics for "composite" TiB_2 coating for trained and experimental data between 600-700^{0}C	195
4.62	Oxidation kinetics for "composite" TiB_2 coating for trained and experimental data between 700-800^{0}C	196
4.63	Oxidation kinetics for "composite" TiB_2 coating for trained and experimental data between 800-1000^{0}C	197
4.64	Arrhenius plot for parabolic rate of oxidation using the neural network data	200
4.65	Overall view of D4 and D24 samples after dip test (a) coated side and (b) uncoated side	203
4.66	Low magnification SEM micrograph of the cross section of TiB_2 coated AISI 1010 steel (a) dipped in liquid A356 Al for 4 hours and (c) dipped in liquid A356 Al for 24 hours	205
4.67	(a) High magnification SEM micrograph of the crack in the coating and corresponding X-ray elemental maps for (b) Al, (c) Ti and (d) Fe	206
4.68	(a) High magnification SEM micrograph of the cross section of D4 sample and corresponding x-ray elemental maps for (b) Al, (c) Ti and (d) Fe	208

4.69	(a) High magnification SEM micrograph of the cross section of D 24 sample and corresponding x-ray elemental maps for (b) Al, (c) Ti and (d) Fe	209
4.70	High magnification view of the dissolved TiB_2 particles in the laser melt zone in sample D 24	210
4.71	X-ray diffraction spectra from the top surface of TiB_2 coated AISI 1010 steel sample in (a) undipped condition, (b) after dipping in liquid A356 Al for 4 hours and (c) after dipping in liquid A356 Al for 24 hours	212
4.72	(a) SEM micrograph showing the attack of liquid A356 Al on uncoated side of D 4 sample and corresponding x-ray elemental maps for (b) Al and (c) Fe	214
4.73	(a) SEM micrograph showing the attack of liquid A356 Al on uncoated side of D 24 sample and corresponding x-ray elemental maps for (b) Al and (c) Fe	216
4.74	High magnification SEM micrograph showing the microhardness indentations and massive attack of liquid A356 Al on uncoated side of D 24 sample	218

LIST OF ABBREVIATIONS

LSE	Laser Surface Engineering
SEM	Scanning Electron Microscope
TEM	Transmission Electron Microscope
HRTEM	High-Resolution Transmission Electron Microscopy
EDS	Energy Dispersive Spectroscopy
XRD	X-Ray Diffractometry
SAD	Selected Area Diffraction
TGA	Thermogravimetric Analysis
PES	Pulse Electrode Surfacing
HTML	High Temperature Materials Laboratory
ORNL	Oak Ridge National Laboratory
ROM	Rule of Mixtures
HCP	Hexagonal Close Packing
BCC	Body Centered Cubic
MOVCD	Metal-Organic Chemical Vapor Deposition
EBV	Electron Beam Vaporization
PLD	Pulsed Laser Deposition
CVD	Chemical Vapor Deposition
LSM	Laser Surface Modification
LEFM	Linear Elastic Fracture Mechanics

LIST OF SYMBOLS

W_a	Work of adhesion
θ	Wetting angle
σ_{sv}	Surface energy for solid vapor interface
σ_{lv}	Surface energy for liquid vapor interface
σ_{sl}	Surface energy for solid liquid interface
H	Hardness
P	Load
A	Projected area of contact
h	depth of penetration
ψ	Semi apical angle for conical indenter
K	Stress intensity factor
P_r	Crack opening force
c	Crack length
α	Empirical constant for indenter geometry
M	Bending moment
F	Critical force for causing delamination
w	Width of the four-point bend test sample
l	Length of the four-point bend test sample
G_{ss}	Critical energy release rate
h_1	Coating thickness

h	Total sample thickness (coating + substrate)
ν_1	Poisson's ratio of the coating
ν_2	Poisson's ratio of the substrate
E_1	Elastic modulus of the coating
E_2	Elastic modulus of the substrate
μ_1	Shear modulus of the coating
μ_2	Shear modulus of the substrate
ε	Bimaterial constant
β	Measure of in-plane mismatch
σ_{yy}	Stress at crack tip (at crack plane y = 0)
G_c	Critical energy release rate
K_c	Critical stress intensity factor
$\overline{K}$	Complex conjugate of stress intensity factor
W_f	Frictional energy
ΔV	Change in voltage
ΔI	Change in current
μ	Coefficient of friction
N	Normal load
v	Linear speed of the disk
R_a	Average surface roughness
ΔG	Gibb's free energy of formation
ΔH	Enthalpy of formation

V_p	Volume fraction of TiB_2 particles
V_m	Volume fraction of Fe matrix
E_p	Elastic modulus of TiB_2
E_m	Elastic modulus of Fe matrix
$E_{coating}$	Effective elastic modulus of composite coating (based on ROM)
$E^C_{coating}$	Computed elastic modulus of coating
$E^T_{coating}$	Theoretical elastic modulus of coating
E^C_{matrix}	Computed elastic modulus of matrix
$\frac{\Delta m}{a}$	Change in mass per unit area
k	Oxidation rate constant
T	Temperature
Q	Activation energy

Part 1

INTRODUCTION

I. INTRODUCTION

The ability to change the surface characteristics of a component/structure without changing the bulk material properties by use of surface coatings has opened up many new and diversified applications in a various technological areas. Surface engineering or modification has also lead to the development of various coating techniques and materials. Such coatings will enable the use of the structure/component even in the aggressive environments. Ceramic-based coatings have enormous commercial potential for applications such as high temperature coatings for turbine blades, conductive and erosion resistant coatings for arc heaters, protective and wear resistant coatings for machine and tools. Moreover, they are also used in electronic industry (high temperature sensors), modern sports industry (golf club heads, snow ski, shoe spikes etc) and medical equipment. An "ideal coating" could possibly be identified by its properties such as high hardness, high temperature strength, wear and erosion resistance, oxidation and corrosion resistance and strong adherence to the substrate. Conventionally, surface modification processes like chemical vapor deposition (CVD), physical vapor deposition (PVD) and thermal spray are being used to deposit various ceramic coatings. However, the use of these techniques has been limited by several factors such as the need for high input energy, cost of a vacuum chamber, size of the work piece, poor bond strength and environmental hazards. Several new coating methods such as pulse electrode surfacing, ion beam assisted deposition techniques and laser assisted techniques are being investigated by the researchers all over the world.

The aim of the present study was to *identify* and *develop* a unique combination of coating technique and material, which could target its properties similar to that of an "ideal coating". ***Laser Surface Engineering*** (LSE) process was employed to deposit refractory titanium diboride (TiB_2) ceramic coating on AISI 1010 steel substrate. Laser Surface Engineering (LSE) is one such versatile process that offers several advantages over other surface modification techniques. The surface properties can be tailored to the requirement of the application by varying process variables such as laser traverse speed, power, beam size and composition of precursor. Also, coatings produced by LSE are metallurgically bonded providing a sound and adherent interface between the coating and substrate. In the present study, laser was used as a tool to deposit TiB_2 within a *fixed envelope* of processing parameters such as laser power and traverse speed. Such processing parameters were fixed after extracting experience from the several trials and the available literature. The thrust of the present study is on the material properties and behavior of the TiB_2 coating within the fixed envelope of these processing parameters. The present study is being compiled based on such facts. Part 2 deals with the review of the literature related to ceramic coatings and laser processing. Experimental procedures adopted to carry out such investigations are described in Part 3. Part 4 presents the results and discussion of this study while Part 5 incorporates conclusions and suggestions for the further investigations are made in Part 6.

Part 2

LITERATURE REVIEW

2. LITERATURE REVIEW

2.1 Background of Laser and Materials Processing

Since the first successful operation of laser in 1960, laser technology has advanced a great deal and its implications in materials processing have been clearly recognized. The extremely high flux of electromagnetic energy applied by laser to a very thin surface layer of workpiece produces a highly localized heat source which can be used to engineer the microstructure and properties of a wide range of materials. In general, laser applications to materials processing can be grouped into two major classes: (a) application requiring the delivery of limited and well controlled amount of energy to the workpiece such as semiconductors annealing and etching, integrated circuits substrates scribing, marking in electronics; (b) applications requiring substantial amounts of energy to induce the required phase transformations in the workpiece such as cutting, welding, heat treatments and cladding. Many surface-related failures by mechanism involving wear, corrosion, erosion or high temperature oxidation can be minimized by laser surface modification process (1-4). Hence, last decade has seen the increased use of lasers in industry for surface modification applications. Surface modifications using a laser can take place in a variety of forms, depending upon laser type and the materials that it is interacting with.

The three main types of laser used in surface modifications are the carbon dioxide (CO_2) laser (continuous/pulsed), the neodinium-doped yttrium aluminum garnet (Nd: YAG) laser (continuous/pulsed) and the excimer laser (pulsed). Other lasers such as the

copper vapor, ruby or argon ion lasers can also be used to promote surface modification, but their use in the industry at present has been limited. Figure 2.1 shows the location of some of these lasers in the electromagnetic spectrum (5). With the two commonly industrially used IR lasers, namely the CO_2 laser (wavelength, 10.6 μm) and the Nd: YAG laser (wavelength, 1.06 μm), the substrate is usually modified by a heat related process. Photochemical processes usually occur using the industrial UV laser, namely the excimer laser. Surface modification can, therefore, occur using both these types of interactions and the surface can be modified according to the end application required.

2.2 Surface Modification Techniques

Typical surface alteration processes using lasers traditionally include (i) transformation hardening, (ii) surface melting, (iii) surface cladding, (iv) surface alloying and (v) other techniques (surface smoothening, texturing, coating removal and micromachining). In surface modification techniques, the interaction time between the laser and the substrate is of fundamental importance in determining which of the above mentioned processes will occur. Due to such overlapping of the various laser surface modification processes (e.g. cladding, alloying and melting), a new term "Laser Surface Engineering" (LSE) has been coined by the author in the present study. The present study is oriented towards depositing a high temperature oxidation, corrosion and wear resistant coating using lasers. Hence, a literature review of only similar laser processes is included. Processes like transformation hardening, texturing, coating removal and micromachining are not being discussed here.

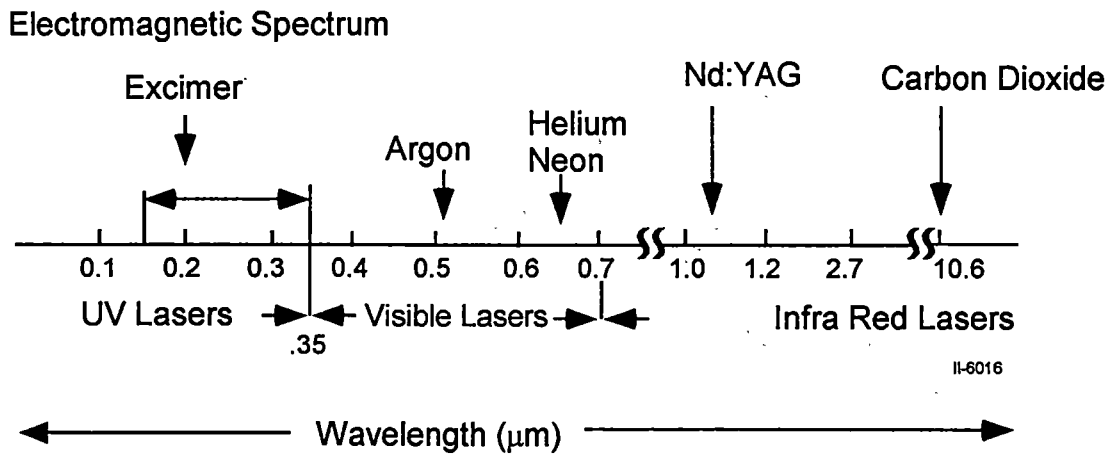


Figure 2.1.The wavelengths of different lasers in the electromagentic spectrum.

Laser surface engineering is a process where a thin layer at the surface and/or subsurface region of a metal is melted by a laser beam with the simultaneous addition or infiltration of preplaced powder of mixture of desired element(s). This changes the surface chemical composition of the metallic substrate. The substrate B coated with a powder layer of A is irradiated with the laser beam. A large fraction of the laser energy is lost by specular and diffuse reflection in most metals and for the most laser wavelengths used for laser materials processing. However, a part of the laser energy is absorbed by the surface and it raises the surface temperature above the melting point instantaneously. The liquid-solid interface moves through the alloy element layer towards the substrate. Within a short time, the liquid-solid interface reaches the substrate and interdiffusion begins between the elements A and the substrate B. By the time the maximum melt depth is achieved, the laser beam has swept across the spot and solidification starts. Solidification completes very quickly and forms a surface alloy/composite. Composition of the phase(s) formed in the surface modification such as this depends upon alloy depends upon several processing variables and material properties. Solidification is very rapid in laser surface modification ($> 10^5$ K/s). Thus, solid state diffusion can be neglected. Rapid solidification often leads to novel metastable phase(s) and sometimes even metallic glasses. High cooling rates (10^5 to 10^{11} K/s) attained in laser surface modification are responsible for the novel metastable phase(s) (1-2,6-7). The modified surface thus processed can have superior chemical, physical and mechanical properties. The depth of the laser modified zone can be controlled by the processing parameters such as laser power and traverse speed and material parameters such as type and composition of the powder.

The major independent process variables for laser surface modification are as follows: (i) laser power, (ii) traverse speed, (iii) thickness of the precoated powder layer, (iv) beam shape and size, (v) thermophysical properties (e.g. thermal conductivity, reflectivity, viscosity etc.) of the substrate and the mixing element and (vi) degree of overlapping of each laser track. By controlling these process parameters, depth, width, solute content and microstructure of the laser modified zone can be altered according to the requirements. However, the most important factors among these are power, traverse speed and diameter of the laser beam. An increase in power increases the depth irrespective of the level of the beam diameter and speed (7-9). An increase in total power will supply more energy at the surface that will enhance heat flow into the substrate, increasing the depth of laser modified zone. An increase in speed with other variables being held constant, restricts the laser- material interaction time and leads to a decrease in the depth of laser modified zone. If the beam diameter is increased with the power and speed being constant, power density decreases at the surface leading to a decrease in depth of laser alloyed zone. Decreasing beam diameter would increase the power density, which in turn will increase the melt depth. However, beam diameter should not be decreased too much as it may cross the keyhole threshold for that material system. If keyhole threshold were crossed then total internal reflection would occur leading to a dramatically increased depth leading to conditions suitable for cutting and welding. Width of laser modified zone can be independently controlled by beam power and speed. An increase in total beam power for a given speed, will dump more energy on the surface which will increase the temperature gradients. This increases fluid flow driven by surface tension and convective heat transfer (8). On the contrary, an increase in traverse

speed for a given laser power will decrease the duration of laser material interaction. Thus, substrate will absorb less energy leading to a decrease in width of laser modified zone.

Apart from the power, traverse speed and beam diameter, concentration of the laser modified zone depends on the thickness of predeposited powder layer. An increase in beam power increases the depth and width of the melt zone. Thus, there is a larger melt volume in which powder is dispersed resulting in lower solute concentration. On the contrary, by increasing traverse speed, width and depth of the melt zone decrease leading to an effective increase in solute concentration (9).

Laser surface modification offers several advantages over other surface modification techniques. The most important advantage stems from the fact that laser surface modification is a non-equilibrium synthesis. Composition of the modified surface layer produced by laser aided synthesis often exceed the solid solubility limit beyond equilibrium phase diagram. Due to such processing conditions, kinetics of the process affect the transport of the constituent elements during phase transformation. This results in a wide variety of microstructures with different crystallographic phase(s) and chemical compositions, thereby promoting the possibility of new materials with novel properties. The surface structure can be tailored to the surface requirement of the application. The bonding between the coating and the substrate is metallurgical in nature providing a strong and adherent interface (1). Moreover, laser beam has an excellent spatial resolution, which makes it ideal for depositing coating on miniature size components such as electronic sensors to be used at high temperature. Another advantage of laser surface modification comes from the fact that Nd: YAG laser beam can be transported to

any remote corner through fiber optics. This allows deposition of coatings on components or parts, which are remotely located.

2.3 Ceramic Coatings Deposited on Metallic Substrates using Lasers

The technique of coating metals with ultrahard ceramic particles using laser processing is being developed to meet the extreme requirements of wear, oxidation and corrosion resistance (10-19). Because of its high energy density, the laser beam is able to melt the metallic substrate and may even partly melt the ceramic powder. As a result, solid bonding can be formed between the ceramic and the metal. However, as the physical properties between the ceramic and the metallic materials are much different, e.g. the crystallographic structures and the thermal expansions, cracks usually develop at the ceramic/metal interface as well as within the coating during the rapid solidification and cooling processes. A good adhesion may prevent the formation of cracks. In addition, chemical reactions between ceramic and metals may lead to a good wetting promoting adhesion. Dehosson et. al have done extensive work about the deposition of ceramics such as Cr_2O_3, SiC, Al_2O_3, SiO_2 on steel and aluminum substrates (11,13,20-23). Several critical issues such as wetting of metal by ceramics, metastable phase formation, interfacial strength are discussed to elucidate the intricacies involved in the science of metal/ceramic interfaces.

2.4 Metal/Ceramic Interface

Substantial research is being done on the science involved in the formation of a metal ceramic interface (23-28). However, there are several complexities leading to a lack of clear understanding of the science. Bonding of dissimilar materials, such as ceramics to metals, require the formation of an interface (24). To achieve a proper bonding between the substrate and the coating, the substrate should wet the coating material or vice-versa. The wettability of a solid material by liquid is usually characterized by the contact angle, θ, of the liquid drop formed on the solid substrate. Figure 2.2 shows the classic model of wetting angle measurements by sessile drop technique. The main relations describing the wetting are given by equations 2.1 (Young's Equation) and 2.2 (Dupre's relation) for wetting angle (θ) and the work of adhesion W_a, respectively (25).

$$\cos\theta = \frac{\sigma_{sv} - \sigma_{ls}}{\sigma_{lv}} \qquad (2.1)$$

$$W_a = \sigma_{lv}(1+\cos\theta) \qquad (2.2)$$

σ_{sv}, σ_{ls} and σ_{lv} are the interphase tensions at the interfaces between solid-vapor, liquid-solid and liquid-vapor, respectively. Also, the interfacial adhesion strength between ceramic particle and metallic melt is often represented by the work of adhesion, W_a, which is defined as work per unit area of interface, necessary to separate reversibly a solid/liquid interface to create a solid/vapor interface (25). Work of adhesion, W_a, reflects directly the importance of energetical interactions between the solid and liquid phases. A higher value W_a suggests the stronger interactions (29-30).

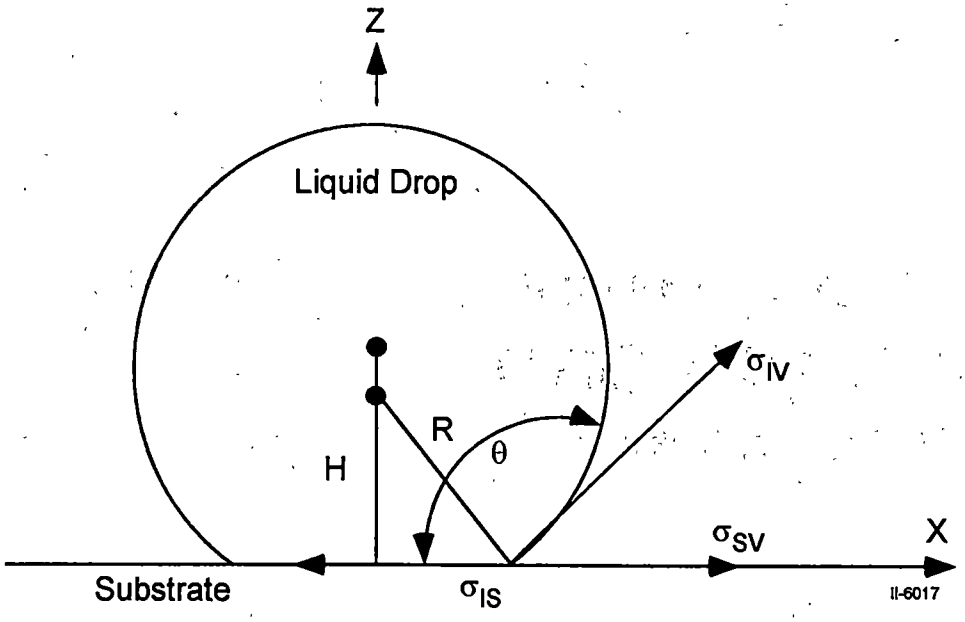


Figure 2.2. Wetting angle θ of a liquid drop resting on a solid substrate. The wetting angle is established by the equilibrium of forces at the three-phase boundary.

Equation 2.1 can be obtained by the mechanical equilibrium of forces at the three-phase boundary (Figure 2.2). The same equilibrium of forces can be applied to a system of liquids resulting in a similar but somewhat more complex relation for wetting angle. Although wetting occurs for $\theta < 90^0$, spreading occurs only for $\theta = 0^0$, the formation of a coating that completely covers the substrate can not be predicted from wetting considerations alone. In practice, the equilibrium state of wetting is always not reached, and consequently the Young's equation would not be valid and requires modifications. There are many circumstances where a non-equilibrium contact angle plays a role: wetting kinetics, rough and heterogeneous surface, chemical reactions as well as the wetting irreversibility of liquid metals on ceramic substrates. In itself, wetting kinetics is an important in study in surface engineering. For instance in laser coating technology of a ceramic layer on a metallic substrate, a fast wetting process is required, e.g. on the order of 0.1 second, since laser processing itself is a very fast process (13). If the wetting process is too slow, the metal-ceramic interface would not have adhered completely before the solidification of materials took place, and consequently the ceramic coating would fail after cooling (21). The spreading of a liquid drop on a solid surface represents a spontaneous wetting process. Yet, investigations of wetting kinetics of liquid metals on ceramics are scarcely available (30). With increasing temperature, the wetting time decreases rapidly. However, no accurate measurements have been reported at higher temperatures. In the study of a thin liquid polymer film spreading on a solid surface, a hydrodynamic model of wetting kinetics has been well established, where the difference of interfacial tension between the non-equilibrium state and the equilibrium state is

treated as the driving force and viscosity drag of the liquid film is the resistance to the wetting (25). On the contrary, the wetting kinetics of a liquid drop on a solid surface has not been modeled with a hydrodynamic approach in detail for ceramic-metal system.

For the fundamental understanding of the metal-ceramic interface, one has to distinguish between two different class of systems, depending on the reactivity and stability of the solid substrate in contact with the liquid metal. On non-reactive systems, which are characterized by extremely rapid kinetics of wetting and by very weak temperature dependent variations of the wetting angle θ, the nature of the solid surface is not significantly modified by its contact with a metallic phase. The degree of wetting is only the result of the establishment of chemical equilibrium bonds achieved by the mutual saturation of the free valances of the contacting surfaces. The establishment of such bonds is not accompanied by the rupture of the interatomic bonds in each of the contacting phases (29). In reactive systems, however, wetting of the liquid metal on the solid substrate frequently occurs with extensive chemical reaction and the formation of a new solid compound at the solid metal/ceramic interface. These types of systems are characterized by the pronounced kinetics of wetting and by strong temperature dependent variations of θ (29). It has been reported that some of the reaction products promote wetting and hence forms a strong ceramic-metal interface (20-21,31-32). Table 2.1 lists the important variables to assess a metal-ceramic interface for some of the selected material systems (33).

Work of adhesion for TiC/Si and TiC/Mg is significantly higher than TiC/Al (Table 2.1). Thus, presence of Si and Mg in the precursor and 6061 Al is expected to increase the wettability and hence interfacial strength between TiC and Al melt thereby

resulting in an adherent coating. Such hypothesis has been further experimentally verified in a recent study by Katipelli et al (17). It should be observed that Fe-based alloys have good wettability for Ti based refractory alloys. Such effects have been reported in earlier experimental studies as well (21, 34-37).

Table 2.1. List of Wetting Parameters for Various Metal-Ceramic System

Ceramic	Metallic Melt	Surface Energy, σ_{lv} of Liquid-Vapor Interface (mJ/m^2)	Wetting Time (minute)	Contact Angle in Degrees	Work of Adhesion, W_a (mJ/m^2)
TiC	Al	914	15	118	485
	Si	860	15	32	1720
	Mg	583	15	50	960
	Fe	1900	1	39	3578
TiB_2	Al	915	15	160	55
	Si	860	15	34	1575
	Fe	1785	< 1	49	2955

2.5 Ultrahard Ceramic Coating Materials

Conventionally, ceramic materials are processed using powder metallurgy route e.g. dry pressing, hot isostatic pressing (HIP), slip casting, tape casting and sintering. Such processes are very expensive, as they require high temperature processing (38). Moreover, near net shape forming is also impossible. However, surface engineering seems to be an alternate way to modify the surface properties similar to that of hard ceramic without altering the bulk properties of the engineering component or structure.

The science of hard coatings is a challenging problem with immediate technological applications. Hard and wear resistant coatings are an important segment in the world economy, for instance machine tools, a $15 billion per year industry, and the magnetic recording industry expects annual revenue close to $100 billion worldwide. Hard coatings systems designed for use in the next generation of materials applications must achieve a combination of physical properties; including excellent thermal and chemical stability, wear resistance, high hardness, toughness and good adhesion. Several material systems and coating technologies are emerging to develop hard coatings for a variety of applications. A list of superhard coating materials, possible ways of deposition of these coating and their applications are listed in Table 2.2. Though lot of research work has been done and ongoing about ceramic coatings, literature about boride-based coatings is not as abundant as carbide and nitrides based ceramic coatings.

2.6 Boride based Ceramics

Binary metal borides range from compounds with low boron content such as Be_5B to those with primarily B-B bonds such as LnB_{100}, where Ln represents the lanthanide elements (56). Because of the larger atomic size of B (≈ 0.91 Å), compared to C (≈ 0.77 Å) or N (≈ 0.71 Å), interstitial substitution of boron in the undistorted octahedral site is rare, resulting primarily in B-B bonding for borides. Important factors that control the compositions of the borides are the ratio of atomic sizes of the boron to metal atoms; the electrochemical factor linked with electronic transitions; and electron concentration, determined by the degree of localization and delocalization of electrons.

Table 2.2. Superhard Coating Materials, Deposition Techniques and Applications

Coating Material	Deposition Techniques	Applications	References
TiC	• MOCVD • EBV • PES • LSE	Microelectronics, Tools, wear and erosion resistant coatings	(39) (39) (37) (17)
VC	• Toyota Diffusion • PLD	Protective coating for steel dies in Al die casting	(40) (41)
SiC	• LSM • CVD	Wear and erosion resistant coating	(22) (42)
WC	• Plasma Spray	Coating for cutting tools	(43)
TiB_2	• Plasma Spray • Magnetron Sputtering • PES • EBV	Microelectronics, Protective coating for machine tools and dies	(44) (45) (35) (45)
AlN	• PES • Magnetron Sputtering • PLD	Microelectronics, Optoelectronics	(46) (47) (48)
BN	• PVD • Ion Implantation • Magnetron Sputtering	Superhard coating	(49) (50) (51)
C_xN_y	• Magnetron Sputtering • CVD • Ion Beam Deposition	Superhard coating	(52) (53) (54)
TiN	• Magnetron Sputtering • PLD	Hard and wear resistant coating, Microelectronics	(47) (55)
Al_2O_3	• LSM • Plasma Spray	Hardfacing coating	(21) (43)
ZrO_2	• Plasma Spray	Thermal Barrier Coating	(43)

MOCVD: Metal-Organic Chemical Vapor Deposition, EBV: Electron Beam Vaporization, PES: Pulse Electrode Surfacing, LSE: Laser Surface Engineering, PLD: Pulsed Laser Deposition, LSM: Laser Surface Modification.

Borides may be classified into two groups based on crystallochemical considerations: boride structures of lower boron content (such as M_4B, M_3B, M_2B, M_3B_2, MB and M_3B_4, where M is a metal) or boron-rich compositions (MB_2, MB_4, MB_6, MB_{12}, MB_{49}, $MB_{66\text{-}100}$). The structures of lower boron content borides are determined by their metallic lattices, whereas the structure of the boron-rich borides are determined by their boron atoms, which form covalent B-B bonds. Figure 2.3 and Table 2.3 shows how the B atoms change from isolated atoms to chains to three-dimensional networks (56). Metal-rich borides with compositions between M_3B and MB_2 are composed of distorted trigonal prisms, whereas boron-rich borides are composed of rigid covalent boron lattices. As the degree of covalent bonding increases, melting point, modulus of elasticity and hardness of these borides also increases. Most boride compounds exist over a compositional range i.e. they are non-stoichiometric in nature. In monoborides and diborides, nonstoichiometry arises from either boron chain or lattice vacancies, not from metal vacancies (56).

In the present study, titanium diboride (TiB_2) has been deposited as coating material over AISI 1010 steel using laser surface engineering technique. Hence, a brief review about the properties and general nature of TiB_2 is presented in the following section.

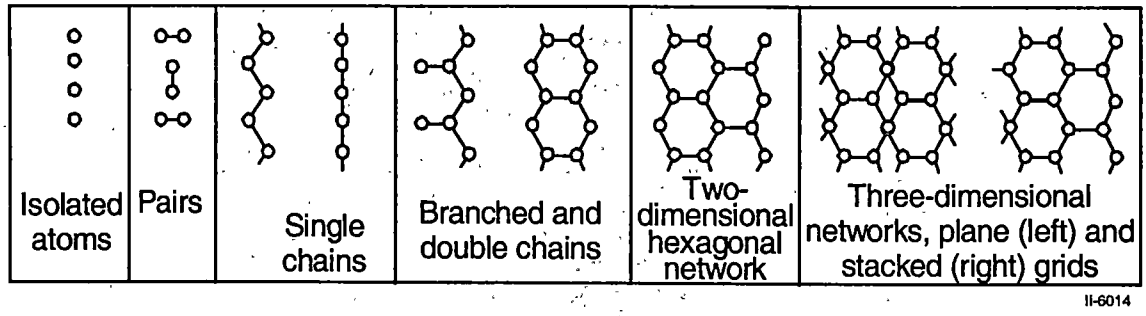


Figure 2.3. Structure of various borides

Table 2.3. Crystal Structures of Borides of Various Metals

Formula	Metal	Crystal System and Structure Type	Arrangement of Boron Atom
M_4B	Pd, Pt	Cubic, Pt_4B type	Isolated atoms
M_2B	Ta, Cr, Mo, W, Fe, Ni, Cr	Tetragonal, $CuAl_2$ type	Isolated atoms
M_3B_2	V, Nb, Ta, Mo	Tetragonal, U_3Si_2 type	Isolated pairs
MB	V, Nb, Ta, Mo, Cr, W, Ni	Rhombic, CrB type	Single chains
MB	Ti, Hf, Fe, Co	Rhombic, FeB type	Unknown
M_3B_4	V, Nb, Ta, Cr	Rhombic, Ta_3B_4 type	Double chains
MB_2	Ti, Zr, Hf, V, Nb, Cr, Mo, W, U, Al	Hexagonal, AlB_2 type	Two-dimensional hexagonal network
MB_4	Y, Lanthanides, Actinides	Tetragonal, UB_4 type	Three dimensional network
MB_6	Y, Lanthanides, Actinides	Cubic, CaB_6 type	Connected B_6 octahedrons
MB_{12}	Sc, Y, Zr,Mo, W	Cubic, UB_{12} type	24 cross-linked boron atoms surround a central metal atom
MB_{66}	Y, Pu, Lanthanides	YB_{66} type	Three-dimensional network of B_{12} clusters

2.7 Properties of Titanium Diboride (TiB_2)

TiB_2 is a boron-rich transition metal based ceramic, existing over a narrow range of stoichiometry as shown in the Ti-B phase diagram (Figure 2.4). It has partly covalent and partly metallic bonding (57-59). Metallic nature of the bonding is also revealed by the electrical conductivity of TiB_2, which is high and similar to the metals (35). It is theoretically postulated that if the ratio of the size of nonmetal atom to metallic atom is less than 0.59 then bonding is partly covalent and partly metallic (59). A *d* band substructure similar to transition metals also exists in transition metal-based ceramics, which leads to metallic bonding in such ceramics (57). A value has been assigned to the number of *d* electrons present in these transition metals and their compounds. Electrons in the *d* band substructure participate in the formation of a metallic bond and accordingly TiB_2 has 5.5*d* electrons available for bonding (57).

Titanium diboride (TiB_2) is a low density, hard ceramic material with excellent wear, abrasion and oxidation resistance (56). Also, it is chemically inert in corrosive environment, which makes it excellent coating material for variety of applications that are listed in Table 2.5 (60). Salient features (physical, chemical and mechanical properties) of TiB_2 are listed below in Table 2.4 (56).

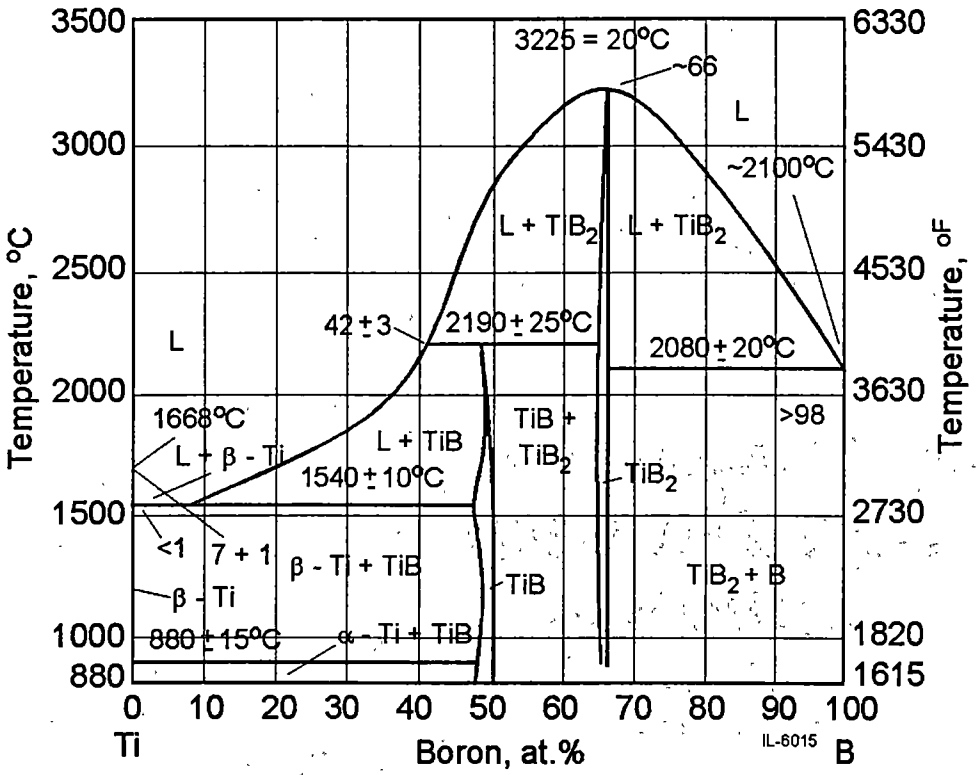


Figure 2.4. Ti-B phase diagram.

Table 2.4. Salient Physical Properties of Titanium Diboride (TiB_2)

Property	TiB_2
Crystal Structure	Hexagonal
Lattice Parameter	a = 3.03 Å, c = 3.23 Å
Melting Point	3225^0 C
Density	4.52 g/cc
Hardness	33 GPa
Modulus of Elasticity	551 GPa
Coefficient of Thermal Expansion	$\alpha_a = 6.63 \times 10^{-6}$ /K, $\alpha_c = 8.65 \times 10^{-6}$ /K
Thermal Conductivity	64.4 W/mK
Electrical Resistivity	9×10^{-6} Ω.cm
Fracture Toughness	5 $MPa.m^{1/2}$

Table 2.5. Potential Application of TiB_2 based materials as a Function of its Basic Properties

Basic Property	Applications
Superhard and Wear Resistance	• Wear resistant coatings • Grinding bodies • Wear resistant lining • Bearings • Sandblasting nozzles • Cermet hard alloys for cutting metals and drilling rocks
Infusibility, Resistance to high temperature oxidation and corrosion, Linear relationship between electrical resistance and temperature	• Protective coatings for molds and dies in aluminum casting industry • Electrolyzer lining for Al production components (Hall-Heroult Cell) • Casting funnels and gutterings in zinc and other nonferrous metals industry • Pipes for pumping molten metals • High temperature thermocouples for temperature measurements in molten metals and alloys • Heaters for high temperature resistance furnaces used in neutral, vacuum or reducing environment
Satisfactory resistance to neutron radiation	• TiB_2-Ti cermets for nuclear engineering

Part 3

EXPERIMENTAL PROCEDURES

3. EXPERIMENTAL PROCEDURES

3.1 Materials and Coating Procedure

In the present study, TiB_2 has been deposited on AISI 1010 steel substrate using laser. Commercially available TiB_2 and Ti powders were used for this study. These powders were supplied by CERAC, Milwaukee, WI. Both powders had a purity of 99.5 %. The average particle size range was 5.5 ± 1 μm. Figure 3.1 shows the TiB_2 powder morphology. TiB_2 particles are faceted with several shapes such as polygonal, hexagonal, disk-shaped and flakes. Hydroxypropyl Methyl Cellulose was used as water based organic solvent for making powder precursor. 49 gm of TiB_2 powder, 1 gm of Ti powder, 15 ml of water and 10 ml of organic solvent were mixed and sprayed using a manual spray gun at the room temperature. The average precursor coating thickness was 150 ± 15 μm. Sprayed coupons were dried at 70^0C for 1 hour prior to laser processing. Addition of 2 wt. % elemental Ti to TiB_2 was made on the assumption that Ti increases the wettability in the melt zone (61). Moreover, it was envisaged that additional Ti would recombine with any boron, which may disassociate during laser processing. Thin plates of AISI 1010 steel of size 7.5 cm x 15 cm x 0.3 cm were cleaned using sand blasting prior to precursor deposition.

A 2.5 kW Hobart HLP 3000 continuous wave Nd:YAG laser (1.06 μm wavelength) equipped with a fiber optic beam delivery system was employed for synthesis of laser assisted TiB_2 coatings. Figure 3.2 is a schematic illustration of the laser surface engineering (LSE) process. The fiber optic beam-delivery system consisted of

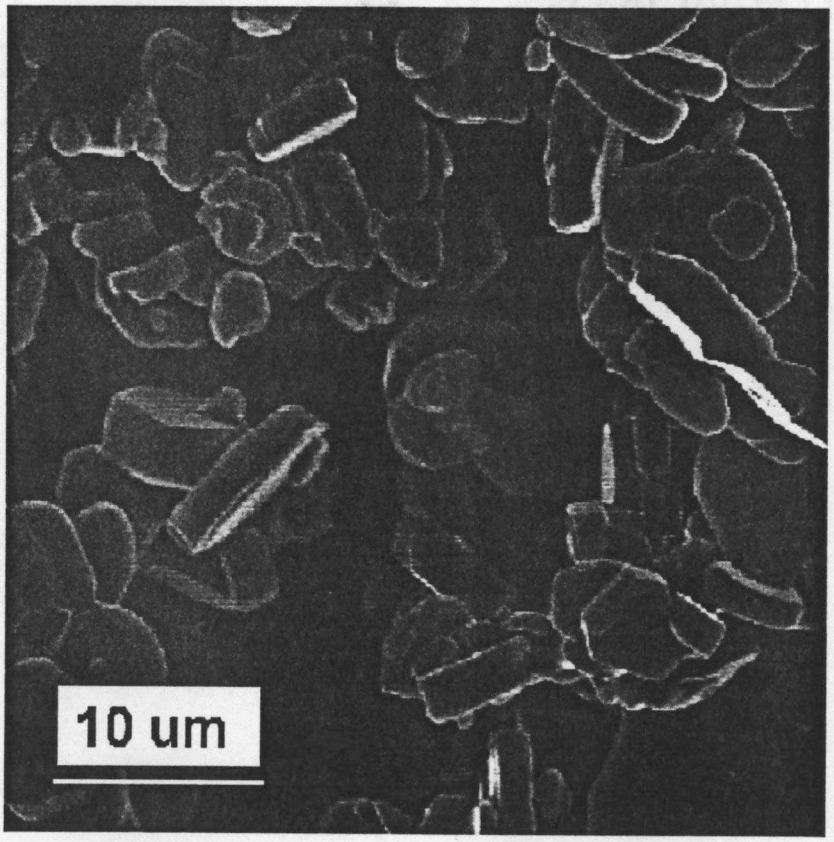


Figure 3.1. SEM micrograph showing morphology of TiB_2 powder.

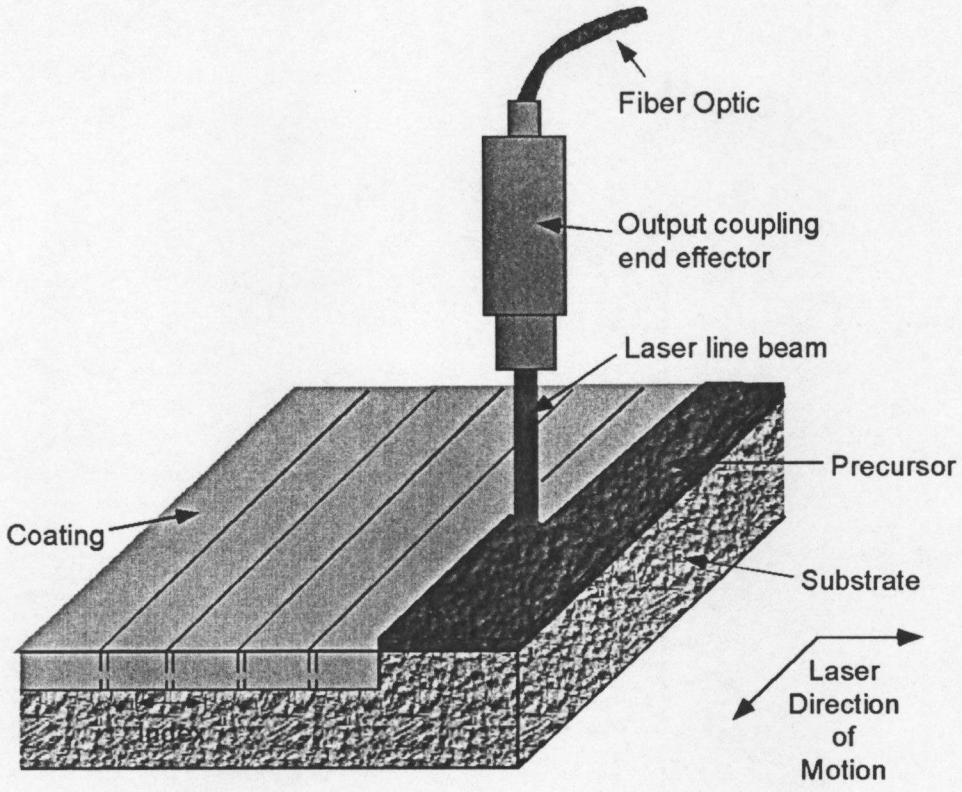


Figure 3.2. A schematic illustration of the laser surface engineering (LSE) process.

the input coupling module, the fiber optic and the output-coupling model. The input-coupling model focuses the laser output onto the end of the fiber. The optical fiber in the present system is 17 meters long and about 600 μm in diameter. The output-coupling module is a telescopic tube (6.35 cm diameter) that can be housed with various configurations of cylindrical and concave lenses firstly to collimate and then either to focus or defocus into various shapes of the beam onto the workpiece. In the present study, in order to provide a large sweeping coverage (i.e. rapid processing speed) and to reduce and/or to eliminate overlap between the successive laser passes, lenses within the output-coupling module were configured to provide a line beam of 3.5 mm length in TEM_{01} spatial distribution onto the sample surface. Such compact and rugged design of the output-coupling module on the optical fiber provided a higher degree of flexibility and access during laser surface processing. The processing parameters were chosen in accordance with the earlier reported literature (62-65). It has been found that for effective laser surface cladding / alloying / infiltration, beam power should be greater than 1 kW (62). In the present study, laser beam power was kept constant at 1.5 kW but laser traverse speed was varied. Table 3.1 lists all the processing parameters, precursor compositions and the nomenclature designated to resultant samples.

Table 3.1. Matrix of Processing Parameters, Precursor Composition and Corresponding Sample Nomenclature

Sample Designation	Laser Power (kW)	Laser Traverse Speed (cm/min)	Powder Precursor Composition (wt. %)
LSE 1	1.5	150	2 Ti + 98 TiB_2
LSE 2	1.5	175	2 Ti + 98 TiB_2
LSE 3	1.5	200	2 Ti + 98 TiB_2

3.2 Microstructural Characterization

Microstructural characterization of the coating and interface of the laser-engineered surface was accomplished using both scanning electron microscope (SEM) and transmission electron microscope (TEM). Samples for metallography were prepared by polishing on Buehler TEXMET 2000 cloth. This minimized the damage to dissimilar interface (ceramic/metal) during polishing. Nital was used as the etchant for TiB_2 coated steel samples. Metallographic specimens were heavily etched (20-30 seconds) in order to reveal the fine microstructure obtained during laser processing. Moreover, heavy etching was required to differentiate between TiB_2 particles and Fe matrix. Microstructural investigations within the laser melt zone and interface was conducted using ISI Super III-A scanning electron microscope along with energy dispersive spectroscopy (EDS) and x-ray mapping to characterize the elemental distribution in a

semi-quantitative manner. Quantitative microscopy was performed using Iridium software from IXRF System attached to the SEM.

3.2.1 Transmission Electron Microscope (TEM) Sample Preparation

Laser surface engineering is a non-equilibrium synthesis that results in formation of novel microstructure and metastable phase(s). It is often difficult to characterize such novel phase(s) using conventional techniques like SEM and XRD. Transmission electron microscopy is one such characterization technique, which allows observation of structure and phase(s) even at the atomic level. Hence, it was essential to investigate the "composite" coating under transmission electron microscope for a better understanding of TiB_2 particle/Fe interface and structural and chemical transformations. TiB_2 particle/Fe matrix interface within the coating and the coating morphology in laser engineered sample was investigated at High Temperature Materials Laboratory (HTML) of Oak Ridge National Laboratory (ORNL) Oak Ridge, TN using a Hitachi HF-2000 Field Emission Transmission Electron Microscope operated at 200 kV. The steel samples coated with TiB_2 were sectioned in a plane parallel to the coating/substrate interface using a slow-speed Buehler Isomet diamond saw (Figure 3.3). These samples were further mechanically ground to approximately 300 μm thickness. A 2 mm square section of this sample was mounted on an epoxy stub and was further ground and polished to approximately 150 μm thickness using an Buehler Isomet Minimet Polisher. A Gatan 656 dimple grinder was used for further thinning the sample to 20 μm. The sample was very fragile at this stage. For final polishing, it was mounted on a carbon ring for support and then ion milled for 6 hours at setting of 6.5 kV on a twin gun Gatan 691 Precision Ion

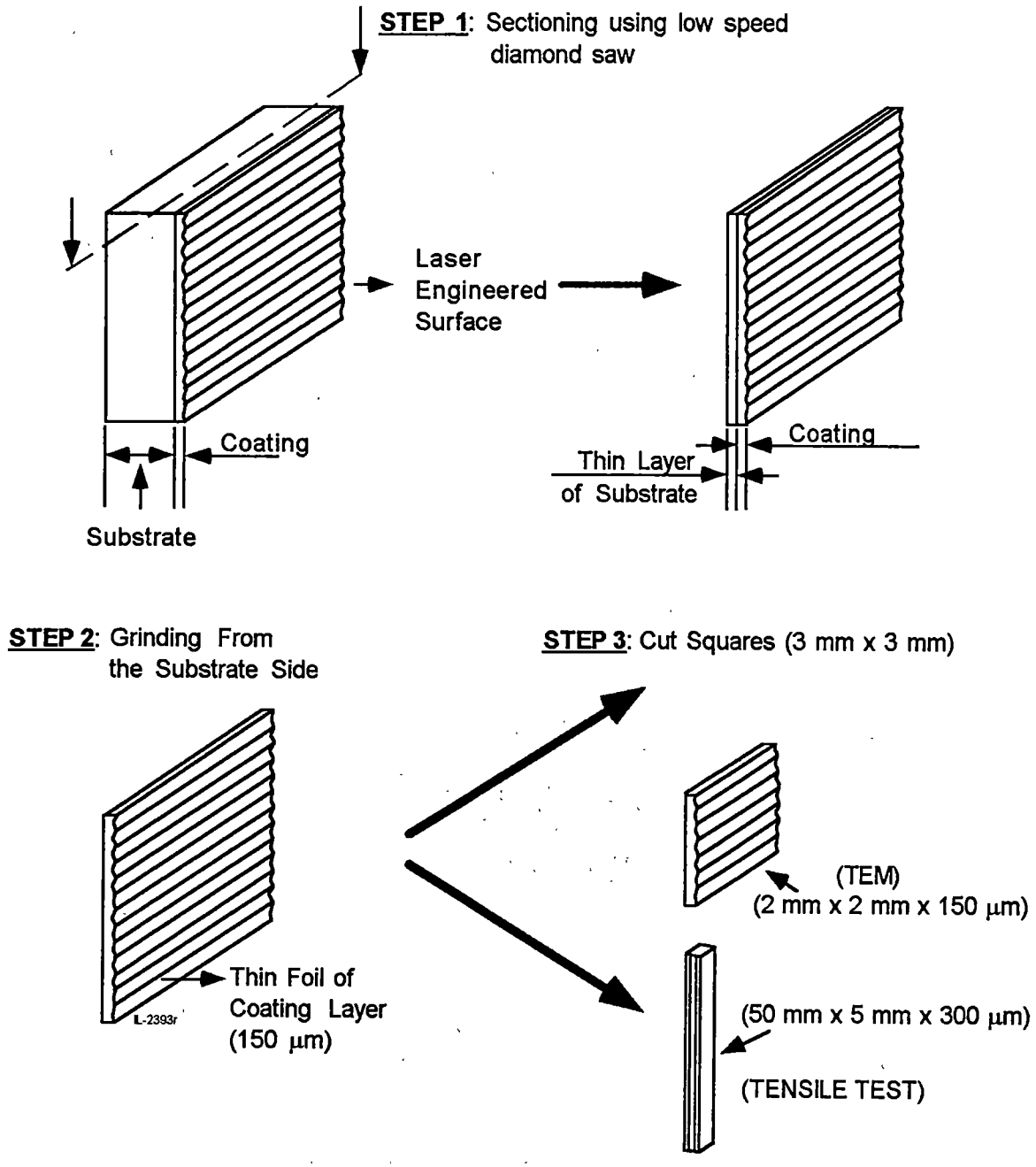


Figure 3.3. A schematic illustration of the sample preparation technique for TEM and Uniaxial Tensile Test.

polishing System. Due to the "composite" nature of laser assisted coating where hard TiB_2 particles were embedded in plain carbon steel matrix, ion milling was very critical, as it required differential level of milling.

3.2.2 Structural Characterization

The properties of a material are evaluated by the phase(s) and their crystal structure. Identification of the phase(s) and their crystal structure is very essential to study the phase transformations after laser surface engineering process, high temperature oxidation and corrosion and dry sliding wear. Such information provides the insight into the possible reaction mechanisms occurring during the above-mentioned operations. Structural characterization for phase identification was carried out on a Philips Norelco x-ray diffractometer with CuK_α radiation (1.54 Å) operating at 40 kV and 30 mV. The diffractometer is interfaced with the personal computer that allowed automatic operation of the x-ray unit as well as the data acquisition and analysis.

3.3 Mechanical Characterization

In most applications, the minimum criterion for acceptable performance is that adhesion of the coating to the substrate should be sufficient for the entire lifetime of the component in its operating environment. Thus, it is necessary to measure the *interfacial strength or fracture toughness* of the coating/substrate interface. This measurement is also useful when used in conjunction with microstructural studies of specific interfaces in order to obtain a better understanding of the adhesion mechanisms involved. Although

many tests have been suggested in literature for such analysis, none of these tests gives a complete quantitative measure of adhesion. Thus, several supplementary mechanical tests (e.g. microhardness testing, nanoindentation, four-point bend test and uniaxial tensile test) have been planned for laser deposited TiB_2 coating in this study in order to evaluate the mechanical properties viz. hardness, young's modulus, interfacial strength/energy and fracture toughness. These quantitative tests would provide a comprehensive knowledge about the mechanical behavior of the coatings and interface.

3.3.1 Microhardness Measurements

Hardness of the coating is often a measure of wear resistance of the coating. Hence, microhardness measurements were performed on a Buehler Micromet II microhardness tester using a Knoop indenter with a normal load of 300 gm applied for 15 seconds. Microhardness measurements were made within the coating, heat affected zone and unaffected steel substrate. Several indentations were made in each region to achieve reasonable average value for microhardness.

3.3.2 Modulus of Elasticity Measurement using Nanoindenter

A. Background

Nanoindentation is widely accepted as an important tool for measuring the mechanical properties of thin films and small volume of materials. By this technique mechanical properties such as hardness, H and elastic modulus E of thin films and coatings can be measured by the continuous measurement of force and displacement as an indentation, is made (66-71). The greatest advantage of this technique is to probe a

surface and map its properties on spatially resolved basis with a resolution of up to 1 μm (69). This allows measurement of mechanical properties form the various microstructural features and phase(s) that are present in the "composite" material system. This technique is used to characterize elastic property such as E (Young's modulus) and plastic property such as hardness, H.

An indenter (Berkovich or Vickers) is pressed into the specimen at the desired location in a continuous or stepwise mode. The indenter load and displacement during loading and unloading are recorded. Loads used in this technique are in range of 1mN to several newtons. The depth varies between several tens of nanometer and several micrometer. Some typical load-depth curves for loading and unloading are shown in Figure 3.4 (72). The principal mechanical property determined in indentation tests is hardness H, which is defined as the load P divided by the projected area of the contact surface A (equation 3.1) (67).

$$H = \frac{P}{A} \qquad (3.1)$$

Area of the contact surface is determined from equation 3.2, where ψ is the semiapical angle for conical indenter as shown in Figure 3.5 (67). Depth of penetration h, is determined from load displacement curve as shown in Figure 3.4.

$$A = \pi h^2 \tan^2 \psi \qquad (3.2)$$

Depth sensing indentation also provides a measure of the elastic modulus, which is determined from the slope of the unloading curve. It is computed as shown in equation 3.3 (67).

$$E = \frac{\pi^{0.5}}{2}\frac{1}{A^{0.5}}\frac{dP}{dh} \qquad (3.3)$$

In an interesting work, Pharr et. al. have shown the possibility of measuring fracture toughness by the use of nanoindenter (69). Several models have been developed to study fracture toughness as a function of crack-length but all of them are based on an early work by Lawn, Evans and Marshall (73). The basis of that analysis is evinced in Figure 3.5. For most brittle materials like ceramics, the indentation crack is assumed to be of half-penny shape as shown in Figure 3.5. Under such conditions, system behaves like a center-loaded, half-penny crack for which stress intensity factor is given by equation 3.4.(73).

$$K \sim \frac{P_r}{c^{1.5}} \qquad (3.4)$$

Based on another model of Hill's expanding cavity (74), crack opening force P_r, produced by residual stress field is related to the peak indentation load and the included angle of the indenter, ψ, through equation 3.5.

$$P_r = P\frac{E^{0.5}}{H^{0.5}}\cot\psi^{0.67} \qquad (3.5)$$

where H and E are the hardness and modulus of the material. Combining equation 3.4 and 3.5 and assuming that the crack arrests when it grows to a length at which the stress intensity factor is just equal to the fracture toughness, one can obtain equation 3.6 (73).

$$K_c = \alpha\frac{E^{0.5}}{H^{0.5}}\frac{P}{c^{1.5}} \qquad (3.6)$$

The empirical constant α depends on the geometry of the indenter. The value of α has been determined by several researchers for various types of indenter including Berkovich and Vickers indenters (75).

Based on above mentioned models and equations, hypothesis can be extended to ceramic coating/metal substrate system to investigate the various mechanical properties such as elastic modulus (E), hardness (H) and fracture toughness. The indentations at various locations such as coating and the interface will provide the variation in properties. Nanoindentation will prove to be an important tool to measure the properties of specific microstructural features and phases. It should be noted that a microhardness tester could not be used for such analysis because microhardness indenter is bigger in size than such segregated zones. Thus, it is expected that nanoindenter will determine the hardness H and modulus E of these ceramic coatings

B. Nanoindentation Measurements on Composite TiB_2 Coating

As stated earlier nanoindentation technique measures the local properties of the phase. This characteristic of localized measurement has been used to measure the elastic modulus (E) for the individual phases viz. TiB_2 particle and Fe-rich matrix. Elastic modulus of the composite coating has been computed using rule of mixture (ROM). It is important to stress here that main constituent of "composite" boride coating are TiB_2 particles and Fe-rich matrix (see section 4.1). Hence, it is a perfect assumption to compute the elastic modulus of "composite" coating using ROM. Moreover, TiB_2 particles were uniformly distributed within the Fe-rich matrix, which further justifies the

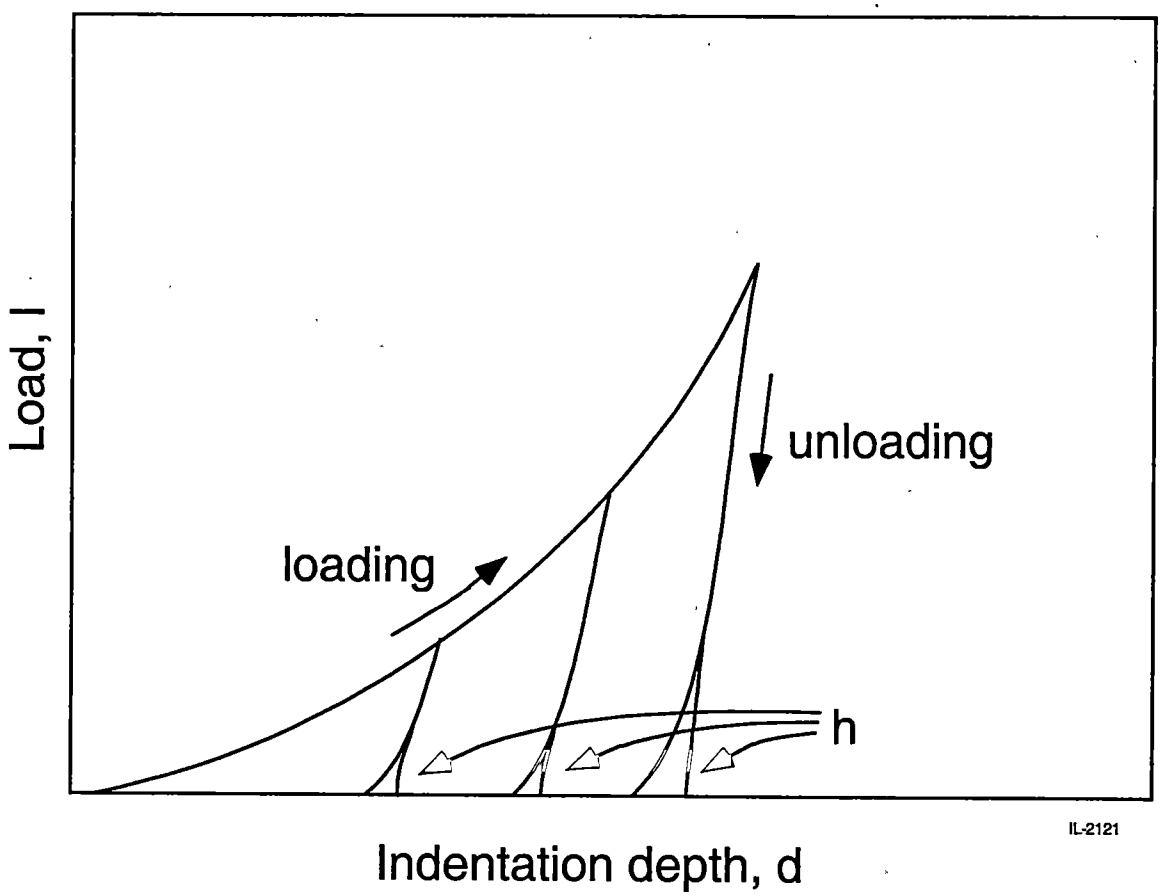


Figure 3.4. Typical load-indentation curve curves from a continuous indentation test.

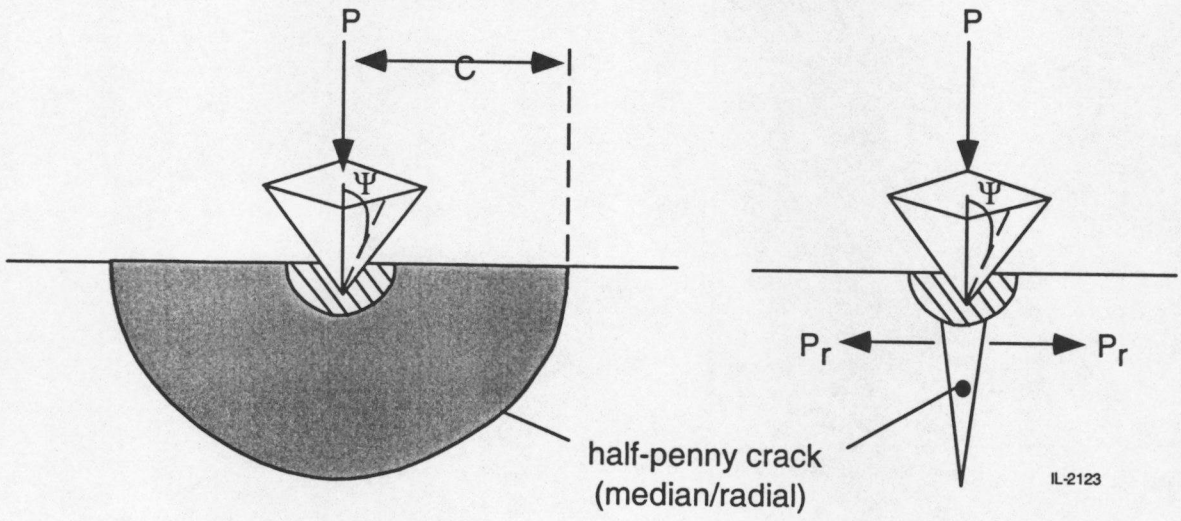


Figure 3.5. Geometry and loading parameters used in a fracture mechanics analysis.

use of ROM for E computations. The computed value of elastic modulus of composite coating will further be used to evaluate the interfacial energy/strength of the coating/substrate interface using four-point bend test.

Mechanical properties of the "composite" TiB_2 measurements were performed on the NANO INDENTER® II at High Temperature Materials Laboratory (HTML) of Oak Ridge National Laboratory (ORNL), Oak Ridge, TN. Samples were metallographically polished to a perfect flatness and mirror finish. Smoothness of the sample was the most important criterion for valid indentation data. Nanoindentaion was recorded with indentations made on large TiB_2 particles (> 5 μm) and the matrix region. Such experimentation was carried out to assure that data was recorded form the individual phase. Each relevant microstructural feature of the coating was indented 15-25 times with the Berkovich indenter tip for hardness (H) and elastic modulus (E) measurements. Indentations were made at various locations in the samples to provide a good statistical sampling. Results were highly reproducible with an error range of 2 %. Each indentation constituted of six segments. During segment 1, indenter approached the sample surface. Sample was loaded to a constant depth of 300 nm during segment 2 and held at that stage. Holding period was referred as segment 3. Segment 4 was an unloading segment to 80 % of the load. Indenter was still in contact with the sample surface when a hold period (segment 5) of 60 seconds was introduced to sense thermal drift which was used to correct load-displacement curve during E and H computations. Segment 6 was the final unloading segment. E and H computations were carried out based on the technique developed by Oliver and Pharr (66). Images of the indentations marked by the nanoindenter were recorded by a Pixera digital camera attached to the microscope.

These images of the nanoindentation mark will provide the information about the cracking of ceramic particles, if any.

3.3.3 Four-point Bend Test

A. Background

The adhesion of the coating is the most critical theme of the coating-substrate system. In most applications the minimum criterion for acceptable performance is that the adhesion of the coating to the substrate should be sufficient so that the coating remains in place for the lifetime of the component in its operating environment. Thus, it is essential to measure the level of adhesion between substrate and coating in order to guarantee that coating is fit for the purpose. Even though there is a wide range of adhesion tests that exist to determine the adhesion, unfortunately standardized and specific experiments to test such combinations of system properties are not well developed. Moreover, none of these tests is sufficient enough to provide information about adhesion properties in various types of coatings. Table 3.2 lists all the available test methods that can be used to determine interfacial strength of the coating (76). The mechanical methods are of more practical interest. In these methods, adhesion is determined by applying a force to the coating-substrate system. The force is either applied normal or parallel to the coating -substrate interface similar to pull or shearing stress tests.

As an alternative to determining the adhesive strength of the interfacial region formed in ceramic-metal joints, a number of tests based on fracture mechanics have been developed (76). These provide data such as fracture energy, which is closely interrelated

with the bond or adhesive strength of the interfacial region (77). For thicker coatings (coating thickness > 50 μm), Clyne and coworkers developed a four-point bend test to measure the interfacial strength (78). Dehosson et. al. has also used such analysis to evaluate the ceramic-metal interface produced by laser processing (28). Figure 3.6 shows a schematic of a typical four-point bend test set up to evaluate the interfacial properties. The critical energy release rate is calculated by comparing the total strain energy before and after a propagation event and then dividing the difference by the area of contact. The details about the fracture mechanics and equations involved in such analysis will be discussed later in part 4 (results and discussion).

Table 3.2. Test Methods to Determine Adhesion in Coating-Substrate Systems

Qualitative	Quantitative
Mechanical Methods	**Mechanical Methods**
• Scotch Tape Test	• Direct Pull-off Test
• Abrasion Test	• Indentation Test
• Bend and Scratch Test	• Bend Test
	• Laser Spallation Test
	• Scratch Test
Non-Mechanical Methods	**Non-Mechanical Methods**
X-ray Diffraction	• Thermal Method
	• Nucleation Test

B. Four-Point Bend Test on Composite TiB_2 Coating

Four-point bend test is an appropriate method to evaluate the interfacial properties (critical energy release rate and fracture toughness) of a bimaterial (28). The specimen used in the flexure experiments consists of a bimaterial beam (Figure 3.6) with overall dimensions 50 x 5 x 1.5 mm. Coating thickness was 200 μm. The sides of the specimen were polished to facilitate microscopic (optical and SEM) observations during and after the testing. However, the top surface of the coating was in as received conditions to prevent the formation of surface cracks due to grinding and/or polishing.

The flexure test consists of two steps, the first of which is making a precrack through the thickness of the coating. Such crack was introduced in the coating using a slow speed diamond saw (Figure 3.6). The specimen is then loaded in four-point flexure on an Instron TT-B Universal Testing machine until delamination along the interface occur or the new crack propagate through entire coating thickness to reach the coating/substrate interface (Figure 3.6). The cross-head speed was maintained at a low speed of 0.02 mm/s. In systems where the coating makes up a substantial part of the total system, the load of delamination is determined by the load at which a sharp load drop occurs. However, as the coating is only a small part (nearly one-eighth thickness of the total beam thickness) of the total system in the present case, delamination is not accompanied by a significant load drop. Hence, point of delamination or crack propagation was identified by a two-prong technique. Apart from a "small" drop in load, specimens were unloaded at pre-selected intermediate stages to observe the crack initiation and propagation under the optical microscope. At the point of delamination and/or after the new cracks have propagated through the entire thickness of the coating

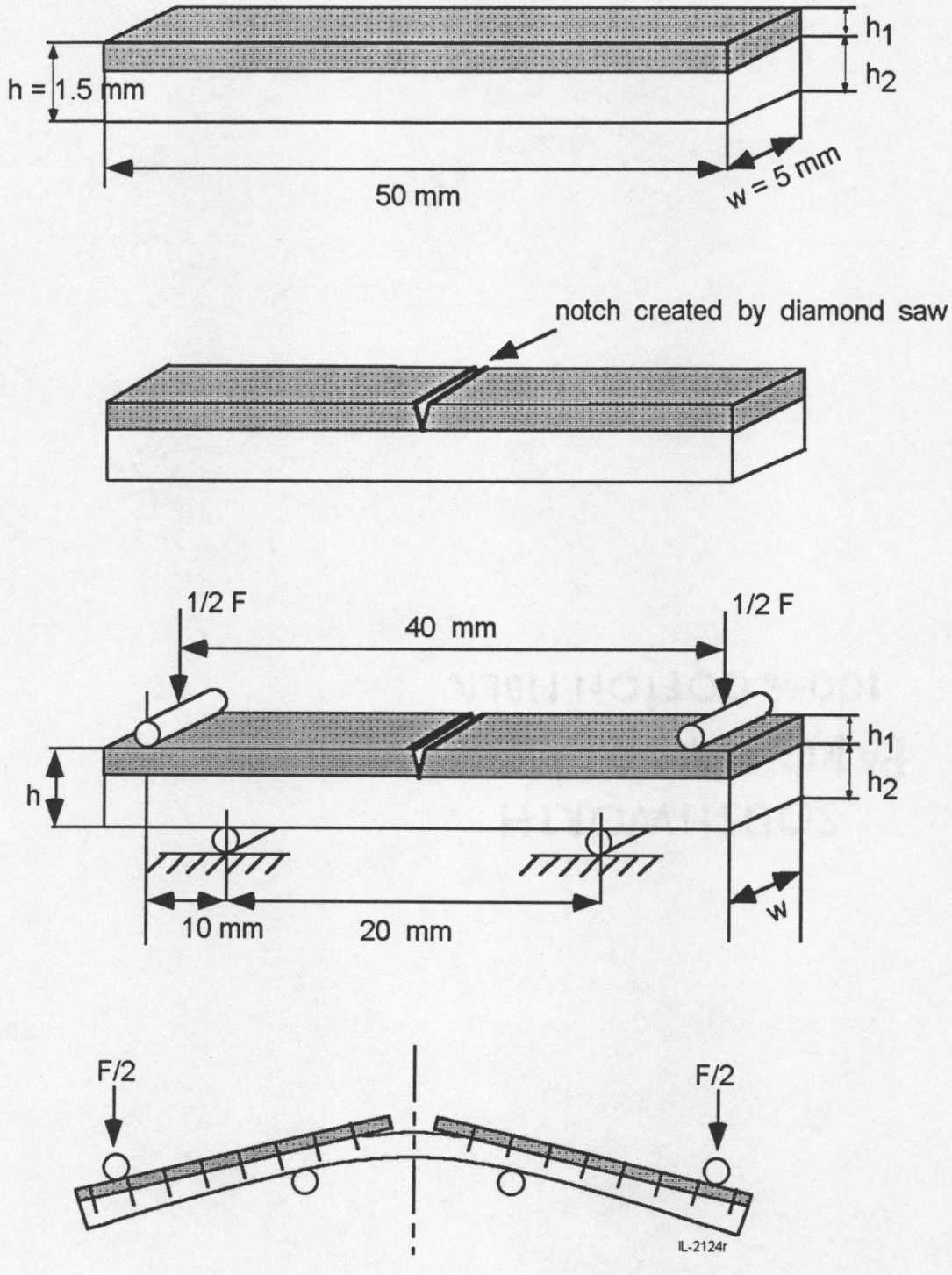


Figure 3.6. A schematic illustration of the four-point bend experimental setup.

Figure 3.6

and reaches interface, load tends to get constant suggesting the beginning of load bearing via plastic deformation of the substrate material. Hence, this point is recorded as the maximum load being sustained by the coating. All further computations have been done with this value of load. Several samples were tested and analyzed using such four-point flexure method to provide a good statistical sampling of the interfacial properties.

The four-point flexure test is based on the storage of a well-known amount of elastic energy on bending and a release of this elastic energy on fracture. The specimen rests on two rollers with other two rollers exerting a force on the specimen (Figure 3.3c) resulting in a constant bending moment M in the region between the inner rollers. Bending moment M, is expressed as in equation 3.7 (28):

$$M = \frac{Fl}{2w} \qquad (3.7)$$

where F is the critical load corresponding to delamination, w is the width of the sample and 1 is the distance between outer and inner roller as shown in Figure 3.6. Such configuration results in the same stress state condition throughout the region in between the inner rollers, making the experiment insensitive to the exact location of fracture. Consequently, the strain energy release upon delamination of the coating should exhibit steady state characteristics. The steady state energy release rate G_{ss} can be deduced from the difference in the strain energy in the cracked and uncracked beam. Since there is negligible strain energy in the beam above the crack, i.e. in the delaminated coating, the energy release rate is simply the difference in strain energy of the uncracked section and the section of the lower beam beneath the crack, i.e. of the substrate plus coating and the

substrate respectively. Based on the description for coatings, i.e. $h_1 << h_2 \approx h$, the strain energy release rate is approximated by equation 3.8 (28,79).

$$G_{ss} = \frac{18M^2(1-\upsilon_2^2)^2 E_1}{(1-\upsilon_1^2)E_2^2}\frac{h_1}{h^4} \qquad (3.8)$$

As can be seen from equation 3.8, the strain energy release rate depends critically on the measured value of $h_2 \approx h$. Interfacial crack propagation occurs when the strain energy release rate G_{ss} equals the critical energy release rate G_c of the interfacial failure. It should be emphasized that this test method does not depend upon the interfacial crack length (84). Thus, four-point bend test allows the determination of interfacial fracture energy using easily measurable parameters. As stated earlier, the detailed equations dealing with fracture mechanics fundamentals are explained in later section of results and discussion (Section 4.2.3). The stress intensity factor K characterizing the bimaterial interface can also be computed.

3.3.4 Uniaxial Tensile Test

In the real world, coatings are exposed to various external stresses that might cause coating damage. In particular, cracks are developed by tensile stress, and this significantly deteriorates the coating properties. In the previous section, interfacial energy (coating/substrate) has been determined by four-point flexure test, which also produces tensile stresses on the coating. However, in the present case, effect of uniaxial tensile stresses on the laser deposited TiB_2 coating has been evaluated. The need of such study was generated by the curiosity to study the fracture morphology of the laser deposited "composite" TiB_2 coating.

Sample preparation for tensile test of "coating" was similar to the TEM sample preparation (Figure 3.3). The steel samples coated with TiB_2 were sectioned from the substrate side parallel to the coating/substrate interface using a slow- speed Buehler Isomet diamond saw. These samples were further mechanically ground from the substrate side to approximately 300 μm thickness. First, it was thought to carry out the tensile test of the coating material itself (200 μm thick), however, such samples were very fragile for uniaxial tensile testing. Hence, total thickness of the tensile sample was maintained at 300 μm, which constituted of 200 μm thick coating and 100 μm thick substrate. It is important to mention at this point that laser surface engineering produced 200 μm thick coating which was "composite" in nature with TiB_2 particles embedded in Fe matrix (64,81). Flat strips of dimensions 50 x 5 x 0.3 mm were used as tensile test samples. Gauge length of the samples was fixed at 20 mm. Tensile tests were conducted on an Instron TT-B Universal Testing machine under a fixed loading rate of 0.02 mm/s. Load-displacement curves were recorded for the several samples to evaluate the tensile strength of the coating. Further, fracture surfaces were subjected to cross section SEM examination to understand the fracture morphology of the coating.

3.4 Tribological Characterization

3.4.1 Mass Loss Analysis

Generally, refractory ceramics are superhard and possess possess excellent wear resistance. Hence, it was essential to evaluate the tribological properties (e.g. wear and friction) of "composite" TiB_2 coating. Tribological properties of the TiB_2 coating were

measured using a block-on-disk tribometer. A schematic of the block-on disk tribometer setup is shown in Figure 3.7. Coated coupons of dimension 25 mm x 25 mm x 3 mm were tested for dry sliding wear against a hardened steel ring rotating at a linear speed of 4.4 m/s. The dry sliding wear test was conducted for a total of 20 minutes duration with an applied normal load of 2 kg. Weight loss measurements were made after successive 2 minutes.

3.4.2 Coefficient of Friction

Coefficient of friction (μ) was also recorded for a 20-minute period by an interfaced computer, which acquired data in the form of electrical output power of the motor. Even though data was recorded at a frequency of 1Hz for a total test time of 20 minutes, only an average of 10 successive points was taken for computing the coefficient of friction, μ.

3.4.3 Surface Roughness Measurements

Surface roughness of the coated surface was examined using a WYKO VISION RST 500 optical profilometer. No sample preparation is needed for surface roughness measurements. Each surface measurement is carried out on an area of 1.8 mm x 2.4 mm. The resolution of roughness measurement is very high at 5-10 nm. Surface roughness measurements were performed on as-coated samples, wear surface and oxidized samples. Such measurements provide excellent information about the possible wear mechanism occurring in the "composite" coating (18). Surface roughness measurements on oxidized samples provided the details of oxide growth and morphology (16).

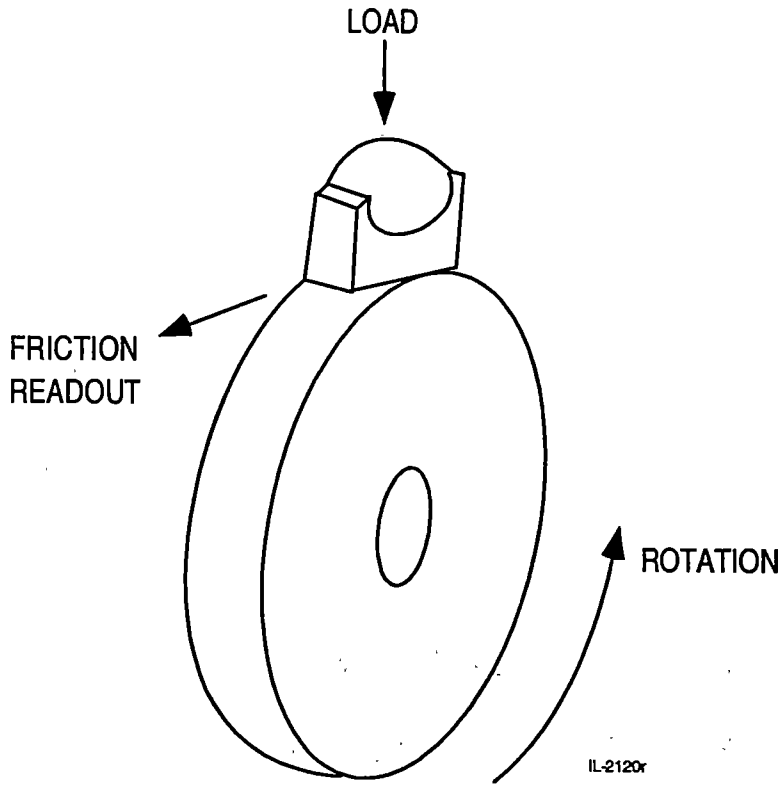


Figure 3.7. A schematic illustration of the block-on-disk type tribometer setup.

3.5 High Temperature Oxidation Experiments

Elevated temperature oxidation behavior of TiB_2 coating in air was evaluated by two procedures: (a) thermogravimetric analysis (TGA) to study oxidation kinetics and (b) long-term exposure to study oxide scale growth and morphology.

3.5.1 Thermogravimetric Analysis (TGA)

Oxidation kinetics of "only" TiB_2 coating was studied using a Perkin Elmer TGA 7 Thermogravimetric Analyzer. Sample preparation was critical for such analysis, as it should account for the oxidation of only "coating" and not substrate. Figure 3.8 shows the various steps involved in preparation of the sample for TGA. Sample preparation is similar to TEM sample preparation (Figure 3.3). TiB_2 coated steel sample (LSE 3) was sectioned using a low speed Buehler Isomet diamond saw. It was further ground mechanically from the substrate side to a thickness of 150 μm. It is important to mention again at this point that laser surface engineering produced 200 μm thick coating which was "composite" in nature with TiB_2 particles embedded in Fe matrix. This ensured that the left over foil (150 μm thick) constitutes of only the coating layer and does not have substrate part, which could have contributed towards weight gain during TGA. Square test specimens of size 3 mm x 3 mm were cut from this thin foil for oxidation kinetic studies. The specimens were cleaned in acetone, followed by drying and weighing. Total surface area for each specimen was also recorded. Oxidation tests were carried out in commercial grade bottled air at 600^0C, 700^0C, 800^0C and 1000^0C. Furnace with a test

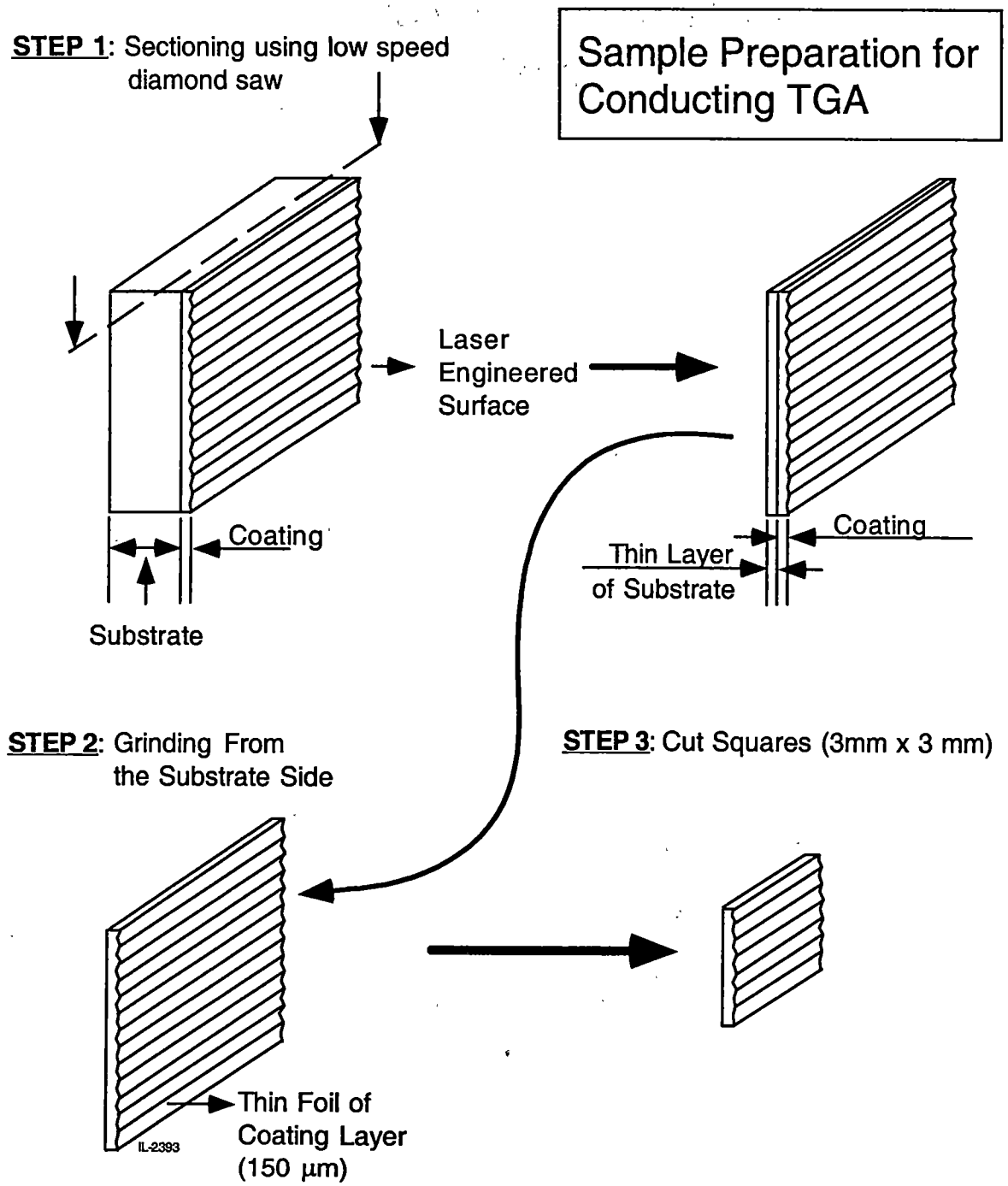


Figure 3.8. A schematic illustration of the sample preparation technique for thermogravimetric analysis (TGA).

sample in it was operated at an incremental rate of 5^0C per minute with an initial temperature of 50^0 C until the test temperature was attained. It was held at the test temperature for 3 hours after the temperature was attained. A continuous plot of change in weight vs. time was recorded for each of the test temperatures. These curves were used for predicting oxidation kinetics of laser deposited TiB_2 coating on AISI 1010 steel substrate.

3.5.2 Long Duration Exposure at Elevated Temperature

Long term exposure of the TiB_2 coated surface was carried out to observe the integrity of the coating, coating/substrate interface, phase transformations and morphological features of the oxide scale formed on the surface. TiB_2 coated steel coupons (LSE 3) of size 20 mm x 20 mm x 5 mm were exposed in a muffle furnace in air to temperature of 600^0C, 800^0C and 1000^0C for various time intervals. Table 3.3 shows the experimental matrix with sample nomenclature. Hereafter, samples will be referred with this nomenclature in the study. It should also be noted that such samples were not used for oxidation kinetic study, as there was a substantial weight gain due to the oxidation of steel substrate, which was not possible to be separated from weight gain due to only oxidation of coating.

Table 3.3. Experimental matrix for long duration exposure and corresponding sample nomenclature

Exposure Time (hours)	600^0C	800^0C	1000^0C
10	A1	B1	C1
30	A2	B2	C2
50	A3	B3	C3

3.5.3 Characterization of the Oxide Scale

Oxide scale formed on the coated surface after long duration exposure was characterized for surface morphology and topography using a ISI Super III-A scanning electron microscope. EDS and x-ray mapping were coupled with SEM to characterize the elemental distribution in a semi-quantitative manner. Cross sectional examination of coated samples after oxidation was also performed. Metallographic samples were prepared by polishing on Buehler TEXMET 2000 cloth to reveal the microstructure. Nital was used as etchant for the oxidized samples. Structural characterization for phase(s) identification in oxide scale was carried out on a Philips Norelco x-ray diffractometer with CuK_α radiation operated at 40kV and 20mA. Coating layer separated in C2 and C3 samples after oxidation. Hence, x-ray diffractomtery was performed on both top and bottom part of the separated layer (Figure 3.9). Such experimentation provided valuable information about oxidation mechanism and phase(s)

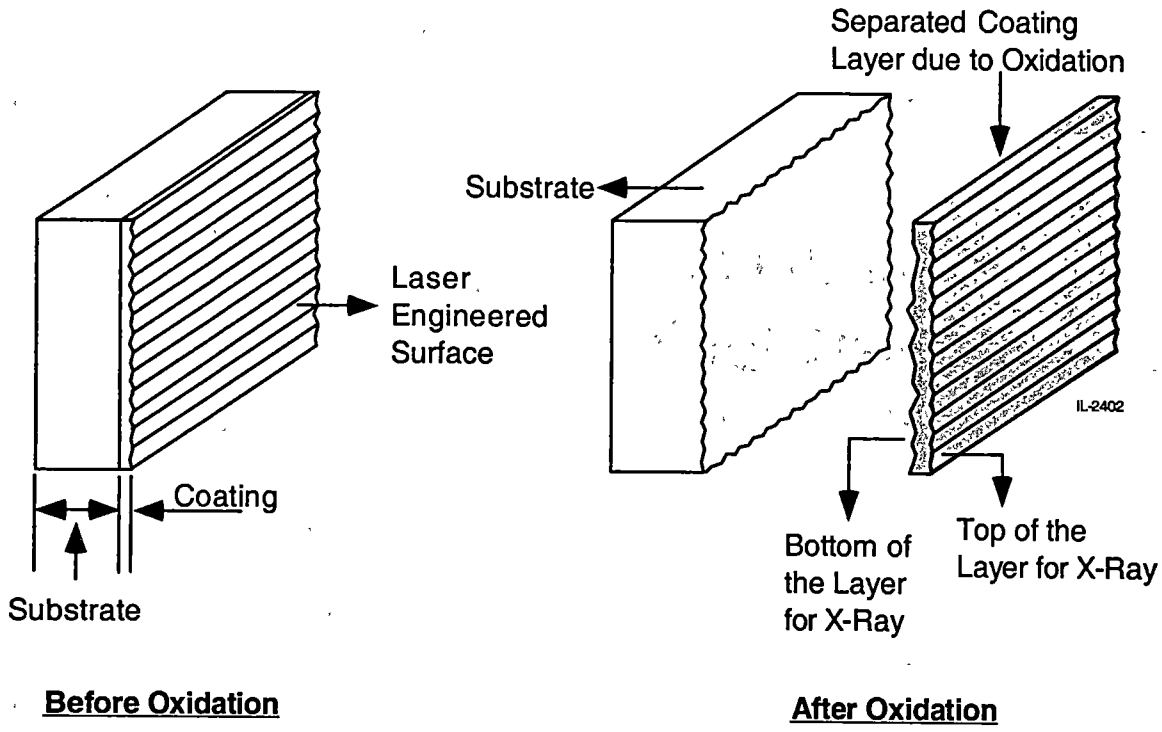


Figure 3.9. A schematic illustration of the methodology adopted to perform x-ray analysis on C2 and C3 samples.

formed in the top layer as well as the coating/substrate interface. Surface roughness of the oxidized surface was examined using a WYKO VISION optical profilometer.

3.6 Dip Test for Evaluation of Corrosion Resistance

The current operation in aluminum melting and casting facilities involves the application of ceramic slurry coatings on molten aluminum delivery systems for protection against corrosion by liquid aluminum (82). The ceramic slurry coatings on molds and tools have a short life and need frequent touch-up, resulting in high casting operation on cost and frequent casting quality problems. Moreover, these slurry coatings are deposited using plasma spray technique, which does not promote metallurgical bond formation with the substrate. Hence, these coatings spall off and have a poor service life. Titanium diboride (TiB_2) has excellent corrosion resistance against metallic aluminum and cryolite, which makes it suitable candidate as a coating material for inert cathode used in Hall-Heroult cell for aluminum electrolysis (44,83). Hence, laser deposited "composite" TiB_2 coating was evaluated for its high temperature corrosion properties against liquid aluminum.

TiB_2 coated steel coupons (LSE 3 sample) of size 15 mm x 50 mm were sectioned for dip test in A356 Al (7 wt % Si, 0.3 wt % Mg, 0.6 wt % Fe, 0.35 wt % Zn, balance Al) melt. A 356 Al is a commonly used casting alloy. The test was carried out in air in a muffle furnace at a temperature of 780 ^{0}C and one atmosphere pressure for 4 hr and 24 hr. This is a typical processing temperature providing sufficient superheat to the molten Al. Two samples were preheated to 150 ^{0}C for 1 hour and then immersed in molten A

356 Al for 4 hr and 24 hr respectively. Hereafter, these samples will be referred as D4 (immersed for 4 hr) and D24 (immersed for 24 hr) in this study. These samples were immersed in such a way that top 25 mm portion of the coated sample was exposed to the atmosphere above the melt. Figure 3.10 is the schematic illustration of the dip test experimental set-up. Test samples were taken out of the furnace after 4 hr and 24 hr respectively. These sample were air cooled on a ceramic block to avoid rapid quenching. The overall examination of the immersed samples was performed visually and with a low magnification magnascope. Cross sectional examination of the coating and interface was performed using scanning electron microscope (SEM) and EDS. Structural characterization for phase(s) identification was also carried out on a Philips Norelco x-ray diffractometer with CuK_α radiation operating at 40 kV and 20 mA.

Figure 3.11 summarizes all the experimental procedures adopted in the present study. It also provides an idea about the methodologies adopted to synthesize and characterize an "ideal" coating for various requirements.

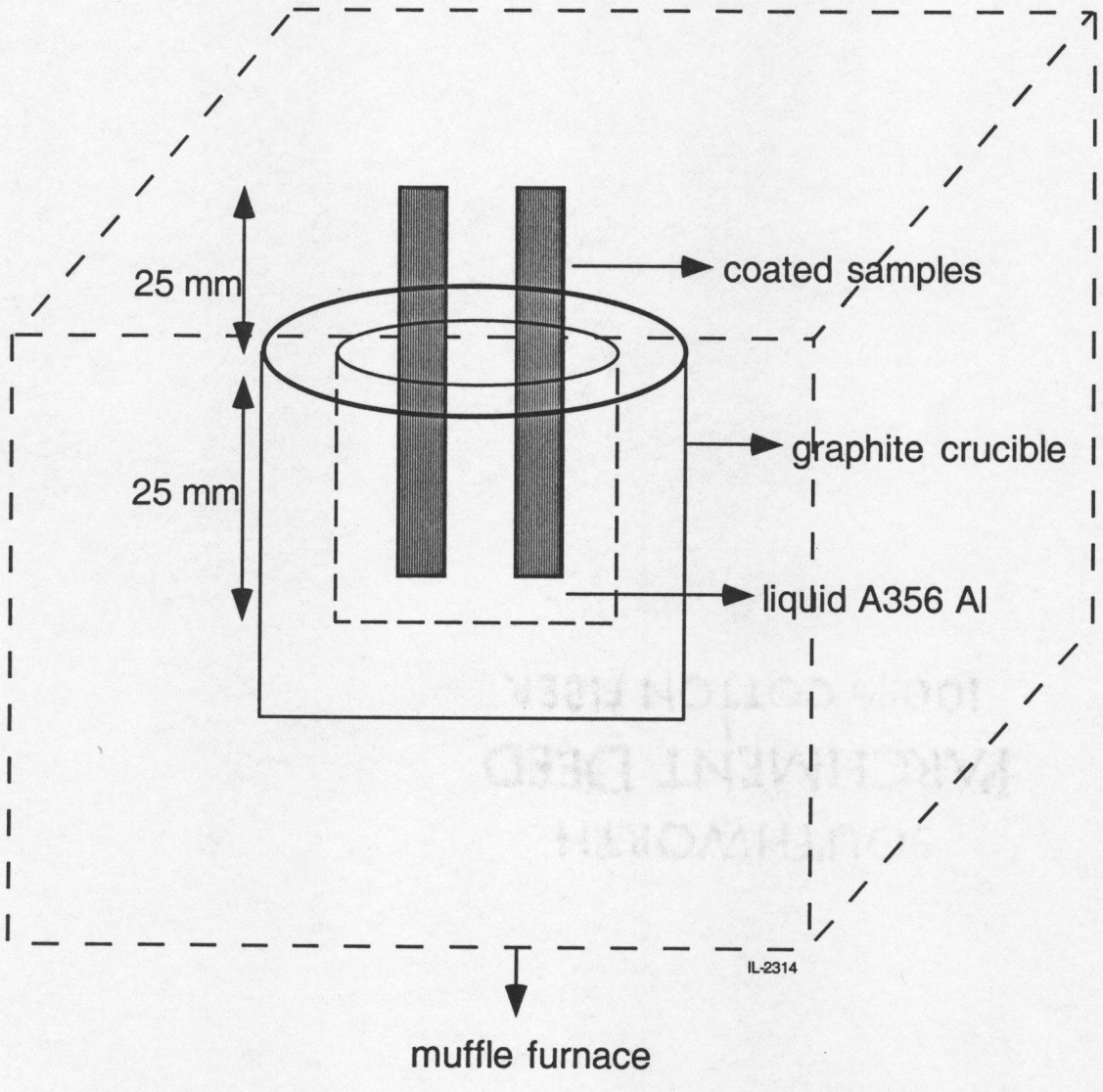


Figure 3.10. Schematic illustration of the dip test experimental set-up.

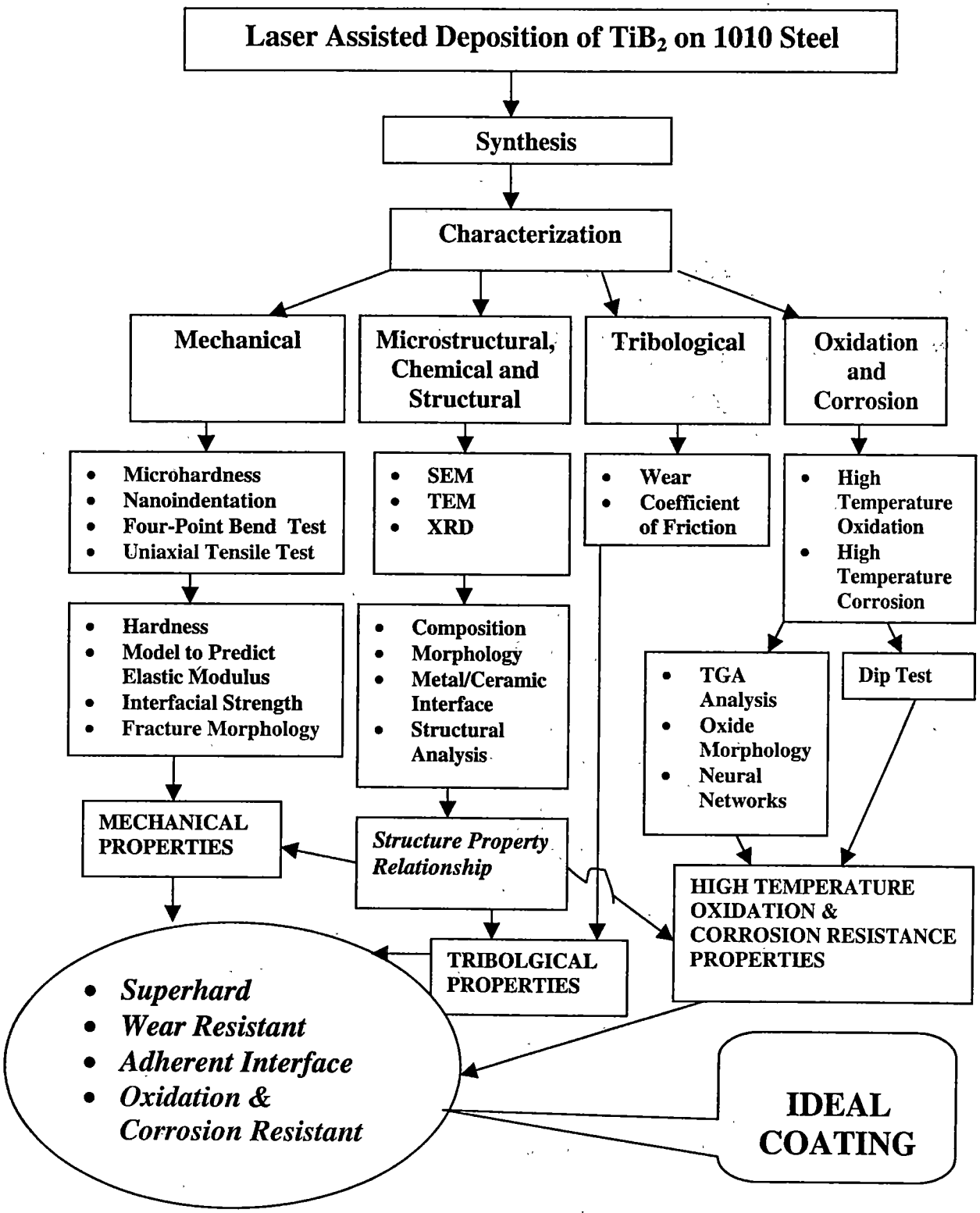


Figure 3.11. A summary of experimental procedures and analysis

Part 4

RESULTS AND DISCUSSION

4. RESULTS AND DISCUSSION

4.1 Thermodynamic Predictions

It is essential to study the thermodynamics of the system to understand the nature of chemical reactions taking place during the coating process. In the present study, therefore, attempts are made firstly to thermodynamically predict the possible reactions and secondly verify the existence of these reaction products using analytical techniques such as EDS, XRD and TEM. Such combined thermodynamic and analytical approach provides an insight into the mechanical, chemical and thermophysical properties of the coated sample. It is, however, pointed out that ***often*** the thermodynamic conditions prevailing during laser processing deviate from the equilibrium conditions thereby making equilibrium phase diagram consideration less applicable and more difficult to predict the process products. In view of the fact that laser processing being very complex non-equilibrium process, and in lack of data in the open literature on various reaction products during such non-equilibrium processes, a first approximation that generation of products based on equilibrium phase diagrams can be considered. These equilibrium products can be considered as sources for further generation of stoichiometric and/or non-stoichiometric derivations. In the Fe-Ti-B system under investigation, primarily, the following reactions are possible. The free energy of formation of borides of Fe and Ti and their temperature ranges are obtained from various sources (84).

Ti-B system:

$$Ti + B = TiB \qquad (4.1)$$

$$Ti + 2B = TiB_2 \qquad (4.2)$$

$$3Ti + 4B = Ti_3B_4 \qquad (4.3)$$

Thermodynamic data for this metastable phase Ti_3B_4 are unknown. Henceforth, only TiB and TiB_2 will be considered for the further analysis and discussion.

Fe- B system:

$$Fe + B = FeB \qquad (4.4)$$

$$2Fe + B = Fe_2B \qquad (4.5)$$

Fe - Ti system:

$$Fe + Ti = FeTi \qquad (4.6)$$

$$2Fe + Ti = Fe_2Ti \qquad (4.7)$$

Gibbs free energies and enthalpies of formation of the borides of Ti and Fe for various temperatures are presented in Table 4.1 (84). These data are based upon the borothermic reduction of oxides as done by Samsonov and Vinitski (84). However, lack of thermodynamic data for the formation of Ti_3B_4, FeTi and Fe_2Ti and other compounds makes stability predictions difficult for many systems.

Table 4.1. Thermodynamic Properties of Borides of Titanium and Iron

	Free Energy of Formation, ΔG (kJ/mol)			Enthalpy of Formation, ΔH (kJ/mol)		
Phase	**298 K**	**1000K**	**2000K**	**298K**	**1000K**	**2000K**
TiB	-159.7	-157.4	-160.3	-160.3	-165.3	-186.0
TiB_2	-319.7	-308.3	-347.9	-323.8	-326.6	-347.9
FeB	-69.5	---	---	-71.1	-72.9	---
Fe_2B	-71.8	---	---	-71.1	-77.9	---

Figure 4.1 shows the free energy of formation of borides of Ti as a function of temperature. It is evident from the graph that free energy of formation is almost independent of temperature up to 2000 K. This implies that entropy (obtained from the slope of the curve) for the formation of above borides is almost negligible. Thus, it is reasonable to assume that free energy of formation of above borides vary in the similar manner even at the temperature attained during laser surface engineering. It is evident from Table 4.1 and Figure 4.1 that TiB_2 is the most stable phase in the Fe-Ti-B system. Although theoretical stability of TiB_2 is confirmed by the thermodynamic considerations, it is important to experimentally validate the existence of laser deposited TiB_2 coating by carrying out various characterization techniques such as microstructural characterization, chemical characterization, structural characterization and mechanical characterization. It is a well-known fact that a strong correlation exists between material processing, microstructure and its properties.

4.2 Microstructural Characterization

The detailed discussion about the microstructural characterization is based on the SEM observations, x-ray diffraction analysis, EDS and high-resolution transmission electron microscopy (HR-TEM) studies of the samples listed in experimental matrix shown in Table 3.1.

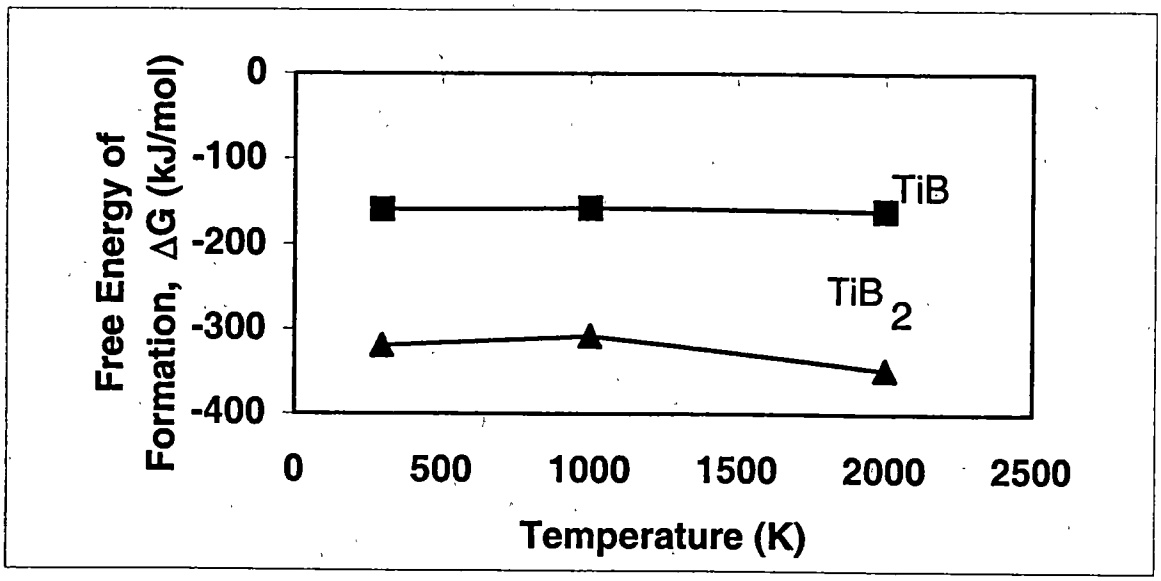


Figure 4.1. Gibb's free energy of formation of borides of Ti as a function of temperature.

4.2.1 Scanning Electron Microscopy

Figure 4.2 illustrates a schematic of the typical microstructure in the cross section of the sample produced within a range of combination of material-process parameters employed in the present investigation. Such schematic representation is provided for understanding the relative locations of various microstructures with respect to each other during the following discussion. The discussion is often based on high magnification views of these regions in isolated manner. Figures 4.3a, 4.3b and 4.3c are the low magnification SEM micrographs of the cross sections of sample LSE 1, LSE 2 and LSE 3 respectively. These micrographs show a continuous, adherent and crack free laser engineered "composite" TiB_2 coating on AISI 1010 steel substrate. The laser melt zone constitutes a mixture of TiB_2 ceramic particles in Fe-rich matrix. A thin layer of steel substrate melts and mixes with TiB_2 due to convection currents within the melt zone resulting in a composite coating. The distribution of TiB_2 particles in laser melt zone is more uniform for the samples LSE 2 (Figure 4.3b) and LSE 3 (Figure 4.3c) which are processed at higher speeds of 175 cm/min and 200 cm/min respectively. Table 4.2 provides a comprehensive quantitative analysis of the microstructural features corresponding to all the processing conditions listed in Table 3.1.

Table 4.2 suggests a decrease in the coating thickness with an increase in processing speed. This is attributed to the reduced interaction time at high processing speeds. At higher speed, there is lesser time for the sweeping laser beam to interact with the substrate and precursor. This results in a melt pool of low depth but with a higher concentration of TiB_2 particles.

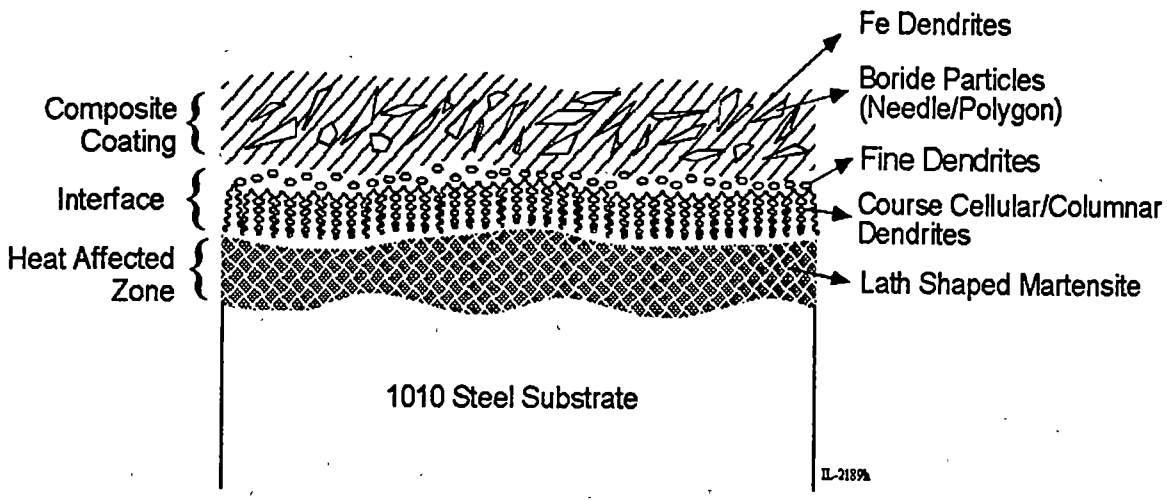


Figure 4.2. A schematic drawing illustrating the microstructural evolution in the cross-section of the laser-modified surface of AISI 1010 steel.

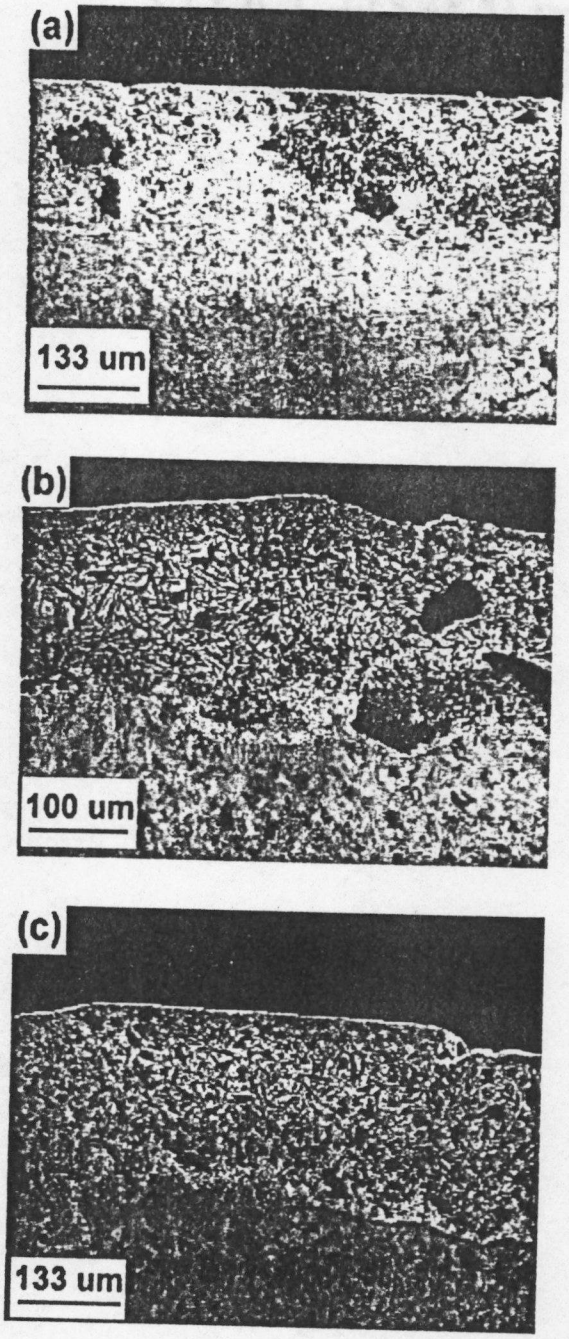


Figure 4.3. SEM micrographs of the cross-section of the laser engineered samples (a) LSE 1, (b) LSE 2 and (c) LSE 3.

Table 4.2. Microstructural Features* of Laser Deposited TiB_2 Coating on AISI 1010 steel

Microstructural Features	LSE 1	LSE 2	LSE 3
Coating Thickness (μm)	215 ± 10	210 ± 10	185 ± 15
Dendrite Zone Size (μm)	25-30	10-15	10-15
Primary Dendrite/Cell Spacing, δp (μm)	3.5 ± 0.3	3.0 ± 0.2	3.0 ± 0.1
Secondary Dendrite Spacing, δ_s (μm)	1.1 ± 0.1	1.0 ± 0.1	0.9 ± 0.2
TiB_2 Particle Distribution	Slightly Uniform	Uniform	Uniform
TiB_2 Particle Morphology	Polygon + Acicular	Acicular	Acicular
TiB_2 Particle Size # (μm)	5-8 for polygon, Aspect ratio is 6.0 for acicular	Aspect ratio 8-12	Aspect ratio 8-12
Volume Fraction of TiB_2 in Coating	0.52	0.66	0.69

* Observations and measurements based on SEM analysis. Measurements were recorded as an average of four readings.

Based on the diameter for a polygon shaped particle whereas the ratio of longer to shorter dimension for acicular particle.

Figure 4.4 includes high magnification SEM micrographs that reveal a continuous, adherent and metallurgically sound interface between laser engineered "composite" TiB_2 coating samples and AISI 1010 steel substrate in LSE 1, LSE 2 and LSE 3 samples. There is no crack initiation or delamination at the interface and a dendritic/cellular interface is produced in each case. Also, the lath shaped martensite is seen in the interfacial region of the heat-affected zone within the substrate. This can be explained on the basis of rapid heating and cooling rates attained during laser surface treatment. The temperature at the interfacial region of the AISI 1010 steel substrate reaches high enough to cause complete austenitization which further transforms to martensite due to high quenching rates.

The solidification structure of the coating/substrate interface and laser melt zone depends upon the degree of constitutional supercooling. The rapid kinetics within the laser melt zone leads to variation in the temperature at various locations due to the existence of different phases such as TiB_2, Fe and other metastable phases. Consequently, such variations in temperature results in variation in the degree of constitutional supercooling leading to a complex solidification structure in both the interfacial region and laser melted zone. This phenomenon is evident from Figure 4.4 with the presence of the different size and morphology of dendritic/cellular zone at the interface. Figure 4.4a show large cellular/dendritic zone at the interface where as a finer zone of dendrites is seen in Figure 4.4c. Figure 4.4a shows the micrograph of the sample, which was processed at the lowest processing speed of 150 cm/min. Thus, there was a larger interaction time for the melt zone which implies lower cooling rates as compared

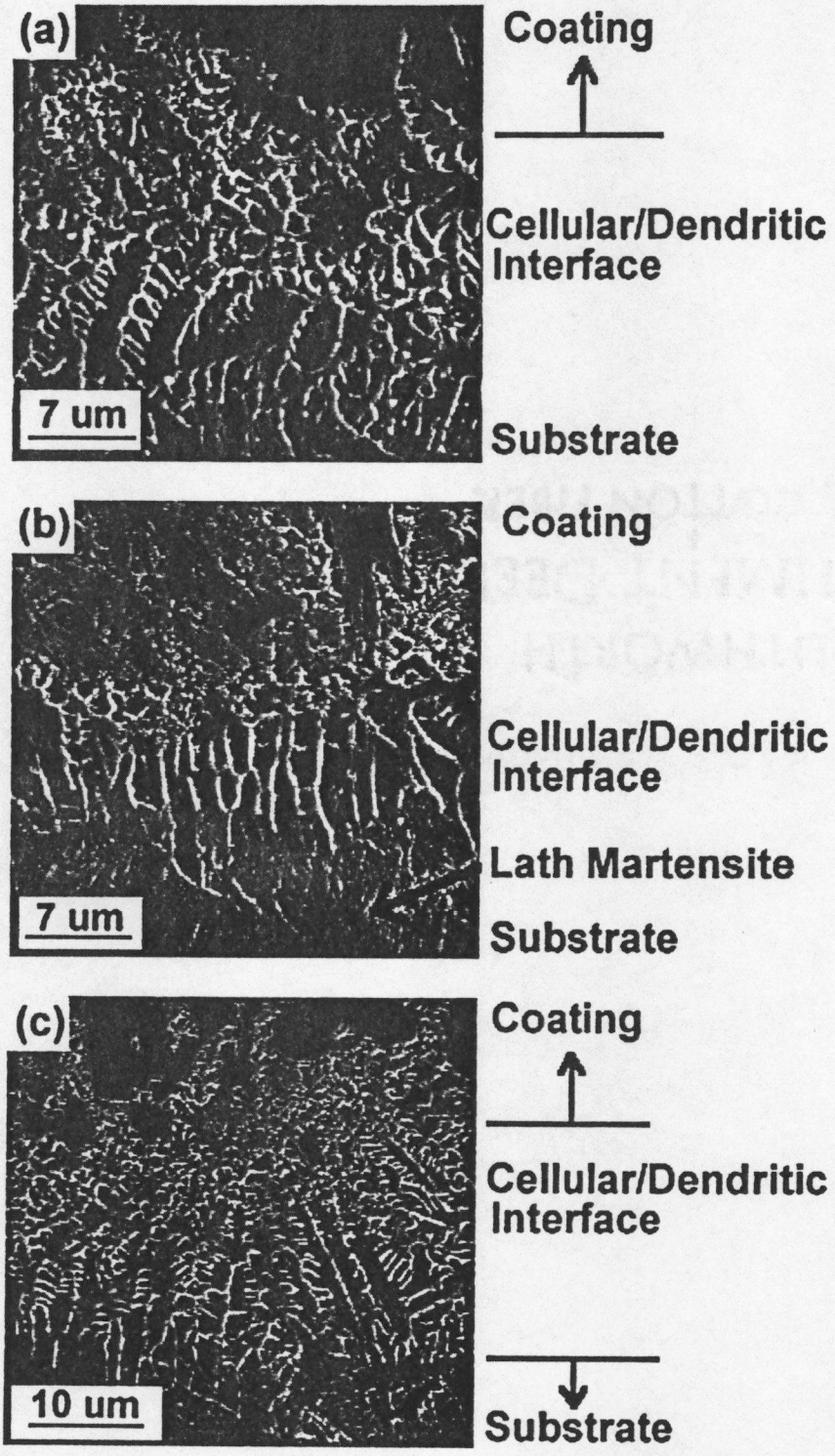


Figure 4.4. High magnification SEM micrographs showing cellular dendritic interface in samples: (a) LSE 1, (b) LSE 2 and (c) LSE 3.

to the LSE 3 sample which was processed at highest speed of 200 cm/min. A higher degree of cooling rate is achieved for LSE3 sample resulting in the finer dendrites as shown in Figure 4.4c and Table 4.2. It should also be observed that in all cases, the initial growth at the interface is towards the coating with a coarse cellular morphology. These coarse cellular dendrites transform into finer dendrites on going further into the melt zone. This feature is prominent in Figure 4.4c. This could again be attributed to the increasing cooling rates on going away from the interface into laser the melt zone. A higher cooling rate suggests refinement of microstructure such as cellular to coarse dendrites which could be further refined into equiaxed dendrites (62,85). Table 4.2 lists the secondary dendrite arm spacing in the range of 0.8 -1.3 μm. Such fine arm spacing suggests a very high cooling rate estimated in the range 10^3 to 10^6 K/s (86).

The high magnification micrographs of the structure within the laser melted zone of LSE series samples are presented in Figures 4.5 and 4.6a. The laser melt zone suggests a composite structure of TiB_2 particles within fine equiaxed dendritic matrix of Fe. These fine equiaxed dendrites within the melt zone are revealed after heavy etching of the samples. This has been more clearly illustrated in Figures 4.5c and 4.6a which show fine dendrites whereas Figure 4.5a does not show the equiaxed dendrites as it was not heavily etched. Such fine microstructure of equiaxed dendrites in the melt zone is corroborative of very high cooling rates involved in laser surface modification. It is essential that melt must be undercooled in order to establish the necessary temperature gradient for equiaxed dendrite formation (85). In the laser melt zone, TiB_2 particles are surrounded by liquid melt, which has to be undercooled to form equiaxed dendrites. TiB_2 particles have a higher thermal conductivity (65 $Wm^{-1} K^{-1}$) than melt which is essentially liquid Fe

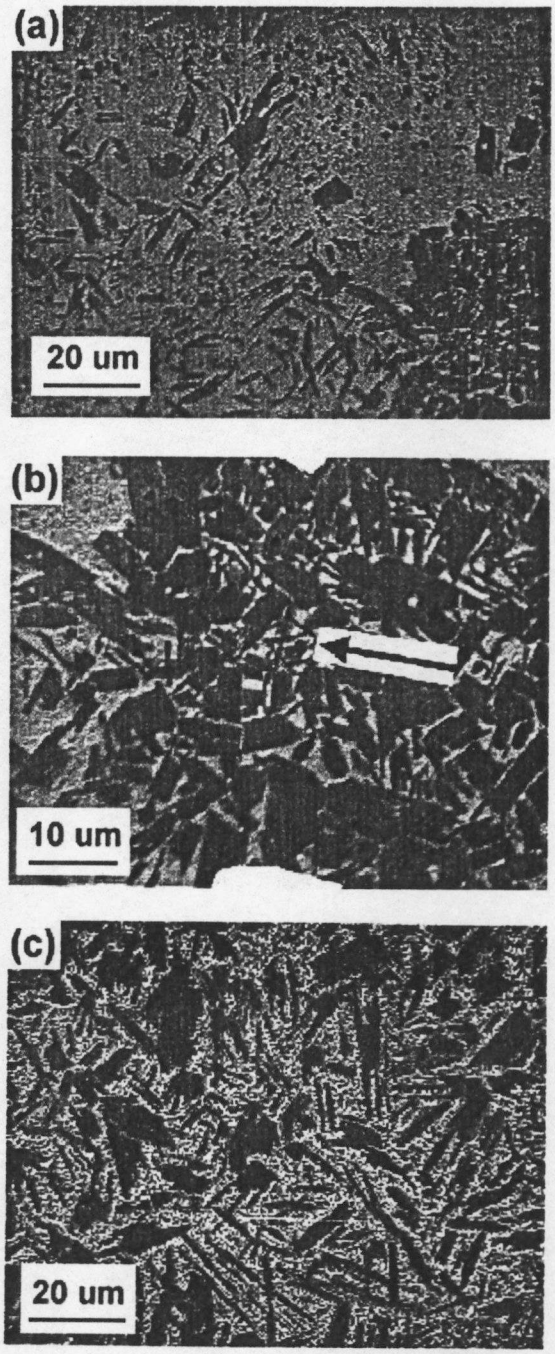


Figure 4.5. SEM micrographs of the laser melted zone illustrating boride particles in samples (a) LSE 1, (b) LSE 1 and (c) LSE 2.

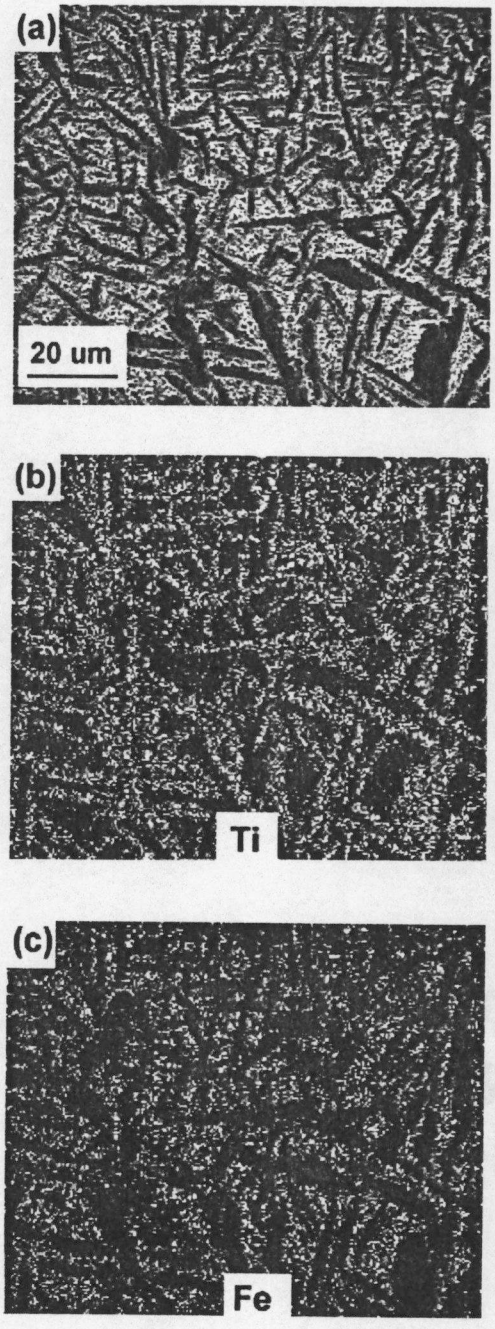


Figure 4.6. Laser melted zone for the sample LSE 3 (a) SEM micrograph showing acicular boride particles, (b) corresponding X-ray elemental map for Ti and (c) X-ray elemental map for Fe.

having thermal conductivity of 50 Wm^{-1} K^{-1} (64). Thus, TiB_2 particles extract more heat from the liquid melt, further assisting in formation of fine and equiaxed dendrites.

It has been mentioned earlier that LSE 2 and LSE 3 samples result in the uniform distribution of TiB_2 particles in the melt zone whereas sample LSE1 has non-uniform distribution (Figure 4.3). Figure 4.5a shows the melt zone in LSE 1 sample, which was processed at a speed of 150 cm/min. It consists of a mixture of polygon shaped and few acicular/needle shaped TiB_2 particles. Figure 4.5c and 4.6a are the microstructures of the laser melt zone in LSE 2 and LSE 3 samples which were processed at higher speeds of 175 cm/min and 200 cm/min, respectively. TiB_2 particles are uniformly distributed in the melt zone and the shape of particles is highly acicular in these samples with an aspect ratio between 8 and 12. The volume fraction of TiB_2 particles is high for the LSE 2 and LSE 3 samples (Table 4.2). This suggests that transformation into needle shaped particles is pronounced with an increasing laser speed. The beginning of the change in TiB_2 particle morphology is clearly indicated in Figure 4.5. It shows existence of the needle shaped particles within a cluster of polygon shaped particles (shown by arrow). This indicates that some of the polygon shaped TiB_2 particles break down/reform into needle shaped particles.

Table 4.3 lists the elemental composition in the various microstructural zones of the coating, interface and the substrate. Table 4.3 along with Figure 4.6b suggest that although needle shaped boride particles are rich in Ti, there is some additional Fe which has reacted to form some new phase. It can be observed that equiaxed dendrites in melt zone have 9 to 15 wt.% Ti. Such high content of Ti in the matrix could possibly be attributed to the fragmentation of some of the TiB_2 particles into very fine particles,

which have mixed with liquid Fe. Some of these fragmented TiB_2 particles are observed in the region just above the interfacial cellular dendrites in Figure 4.4c. This produces a zone of mixture of Fe and TiB_2, which has 35 to 45 wt. % Fe content. It is, therefore, essential to understand the chemical reactions, if any, occurring in the melt zone. In the earlier section (4.1), it was observed that thermodynamically TiB_2 is the most stable phase in Fe-Ti-B system. It is inferred that Fe does not react chemically with TiB_2 but acts as a binder for TiB_2 ceramic producing a tough coating (35-36). However, it is also possible that laser surface engineering, which is a high energy density and non-equilibrium synthesis process may cause some chemical reactions between Fe and TiB_2 leading to the formation of novel and metastable phase(s) (81). These metastable phase(s) may be of various stoichiometry and composition such as Fe_xB_y , Ti_mB_n or $(Fe,Ti)_aB_b$ as observed in the following analysis.

Table 4.3. Elemental Composition in Various Microstructural Zones

Location	Wt. % Ti	Wt. % Fe
Polygon shaped TiB_2 particles	94.0 - 96.0	4.0-6.0
Needle/Acicular shaped Boride particles	82.5 - 92.2	7.8 - 17.5
Equiaxed dendrites in melt zone	9.0 - 15.0	85.0- 91.0
Mixture of TiB_2 and Fe just above the interfacial cellular dendrites	55.0 - 65.0	35.0 - 45.0
Cellular dendrites at the interface	2.2 - 5.5	94.5 - 97.8
Martensitic zone in the substrate	1.0 - 1.5	98.5 - 99.0

4.2.2 Structural Characterization

X-ray diffraction spectrum of the coated surface for LSE 3 sample is shown in Figure 4.7. LSE 1 and LSE 2 also revealed similar x-ray diffraction spectra. It is observed that TiB_2 is the most prominent phase in coating. However, there are several other peaks, which confirm formation of metastable phases during laser processing. In an earlier study based on Pulsed Electrode Surfacing (PES) of TiB_2 coating-Fe substrate system, metastable peaks were not observed for TiB_2 deposited on steel using PES method (35,81). The energy density input during LSE process (15 MW/m^2) is several order of magnitudes higher than PES process (0.1MW/m^2) (81). Hence, it supports the hypothesis that some Fe has chemically reacted with TiB_2 due to high incident energy input by laser. These various metastable phases and their crystal structures detected by x-ray diffraction are listed in Table 4.4.

Table 4.4. Crystal Structures of the Relevant Phase(s)

Phase	Crystal Structure	Space Group	Lattice Parameter (Å)
TiB_2	Hexagonal	P6/mmm	a = 3.03 c = 3.23
TiB	Orthorhombic	Pnma	a = 6.12 b = 3.06 c = 4.56
Fe_3B	Tetragonal	P42/n	a = 8.69 c = 4.31
FeB_{49}	Rhombohedral	R-3m	a = 10.95 c = 23.860
$Fe_{2.12}B_{103.36}$	Rhombohedral	R-3m	a = 10.95 c = 23.861

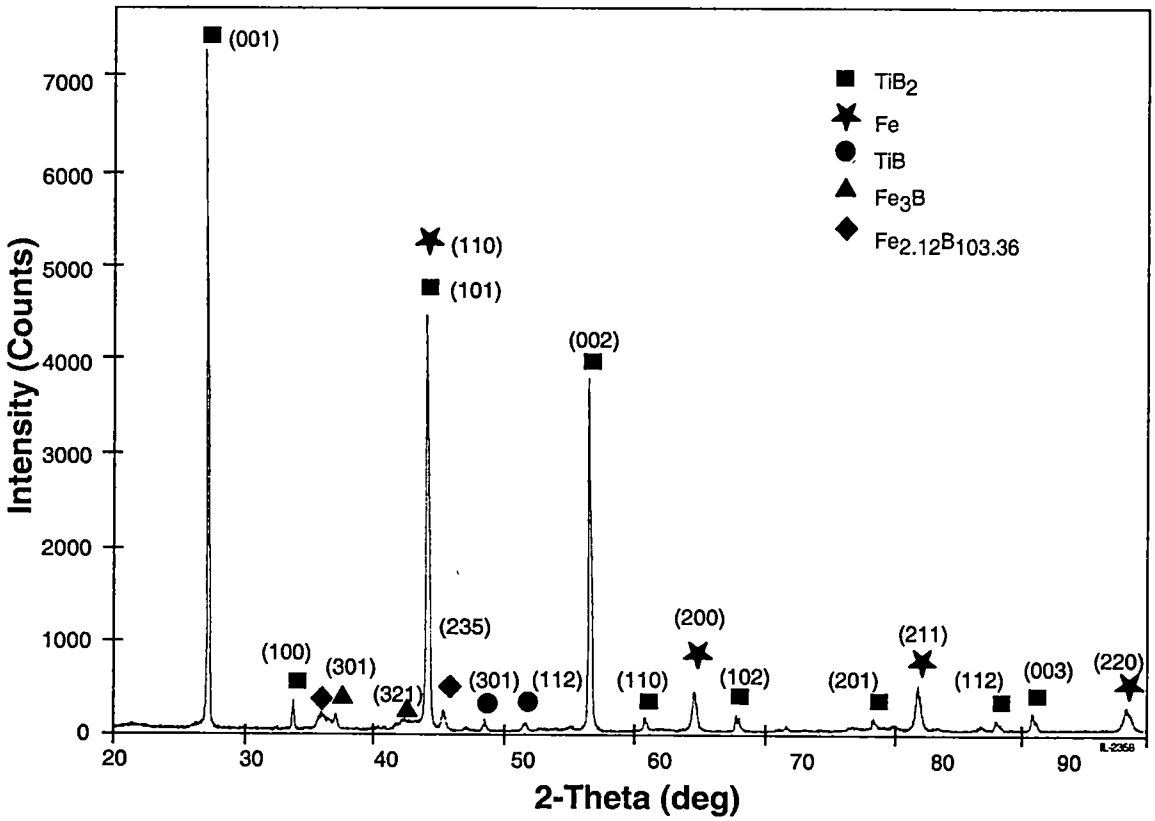


Figure 4.7. X-ray diffraction spectrum of LSE 3 sample.

The formation of TiB has been reported elsewhere, as in the following equation (87,88).

$$TiB_2 + Ti = 2TiB \qquad (4.8)$$

This indicates, in some instances, that TiB_2 has dissociated and then recombined to form TiB. Excess boron could combine with Fe to form metastable phase(s) such as Fe_xB_y as shown in Figures 4.7 and Table 4.4. Some peaks were unidentified with the existing powder diffraction data files. It is also possible that some of the Ti atoms may substitute with Fe atoms to form compounds of type as $(Fe, Ti)_mB_n$. Such possibility stems from the fact that very small difference between atomic radii of Ti and Fe can form a substitutonal compound with TiB_2 (89). Ti has atomic radius of 1.45 Å whereas Fe has a radius of 1.24 Å. Furthermore, EDS analysis presented earlier in Table 4.3 shows additional Fe in the needle shaped boride particles.

It is yet not clear whether all TiB_2 powder melted and reprecipitated during the laser processing. The acicular shaped morphology suggests some sort of reforming occurring within the TiB_2 particles. However, x-ray diffraction spectrum of the acicular particles suggests that TiB_2 is the only major phase in the coating. This suggested that shape change is dominated by some structural phenomenon instead of chemical phenomenon. The detailed study of phase transformations of TiB_2 was not the aim of the present study. However, the issue of metastable phase formation in Fe-TiB_2 system has been discussed in great detail using transmission electron microscopy in the following section. It was envisaged that TEM image of the melt zone, corresponding selected area diffraction (SAD) pattern and microanalysis will give a better understanding of the novel phase(s) formed, as a consequence of non-equilibrium synthesis. It is important to state at this point of time that only LSE 3 samples were used for all further investigations in

this study. LSE 3 sample was processed at highest laser traverse speed and consists of highest volume fraction of TiB_2 particles.

4.2.3 Transmission Electron Microscopy

TEM observations and analysis were made within the "composite" coating region. Figures 4.8 and 4.9 show bright field TEM images of the "composite" coating morphology. The common morphology suggests that TiB_2 particles are faceted and randomly distributed in the Fe matrix. This implies that there is no preferred crystallographic orientation relationship between TiB_2 particle and Fe matrix. Another feature is revealed in Figures 4.8a, 4.8b and 4.8c that illustrate images of hexagonal shaped TiB_2 particles distributed in the Fe matrix. These hexagonal shaped TiB_2 particles are faceted with facets on the $\{1\,\bar{1}\,00\}$ prism planes, which are high packing density planes of TiB_2 phase (90). Slip line features are observed within the TiB_2 particles (Figure 4.8d). These could possibly be artifacts created during TEM sample preparation. However, all TiB_2 particles and TiB_2/Fe interface are free from cracks. Furthermore, both Figures 4.9b and 4.9c show partial sintering of TiB_2 particles at the edges. TiB_2 particles that exist in close proximity of each other experience high temperature due to laser energy input tend to fuse/agglomerate at the edges. However, such behavior is not very prominent due to random distribution of TiB_2 particles (Figures 4.8 and 4.9) and rapid heating and cooling rates experienced during laser processing. Figure 4.9b shows a crack within the TiB_2 particle. Such crack could possibly be attributed to mechanical damage while grinding, polishing and ion milling during TEM sample preparation. It

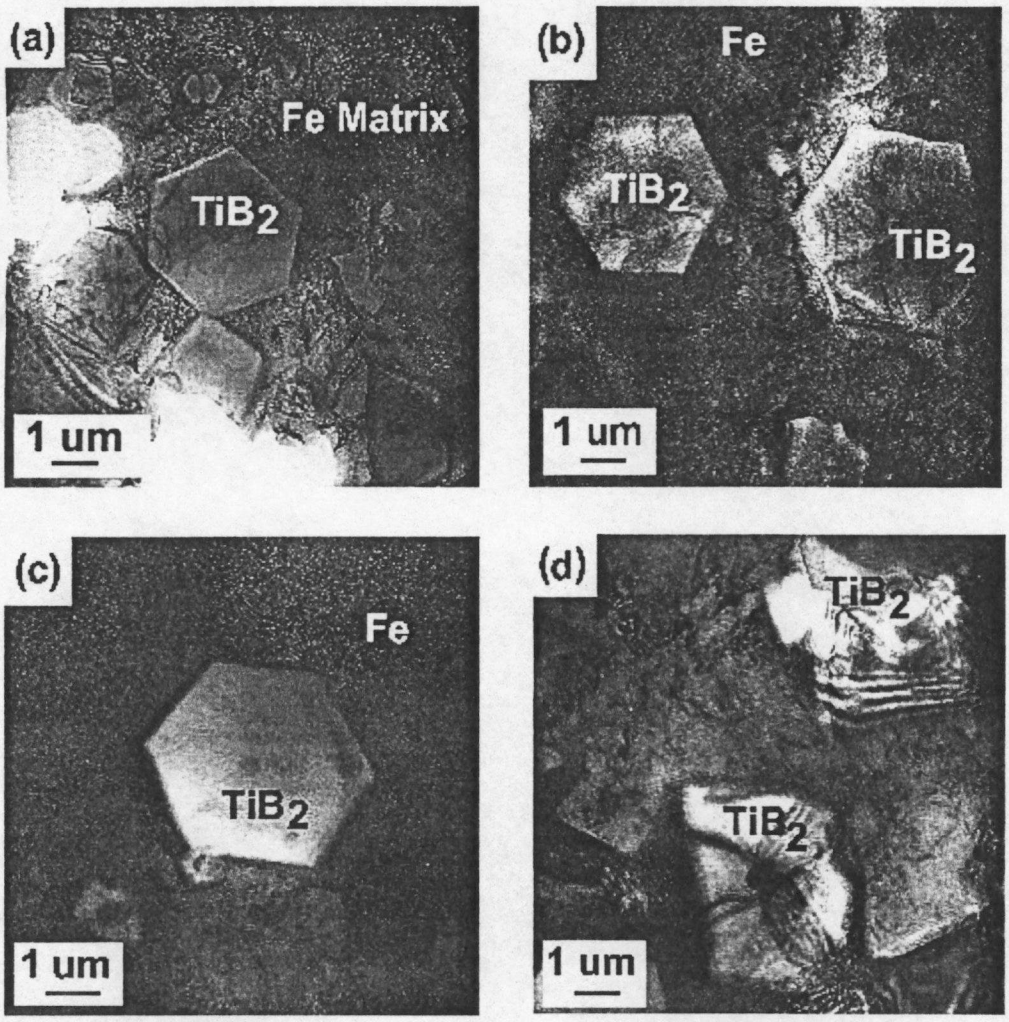


Figure 4.8. Bright field TEM images showing "composite" nature of the coating with faceted TiB_2 particles of various shapes and sizes embedded in Fe-rich matrix.

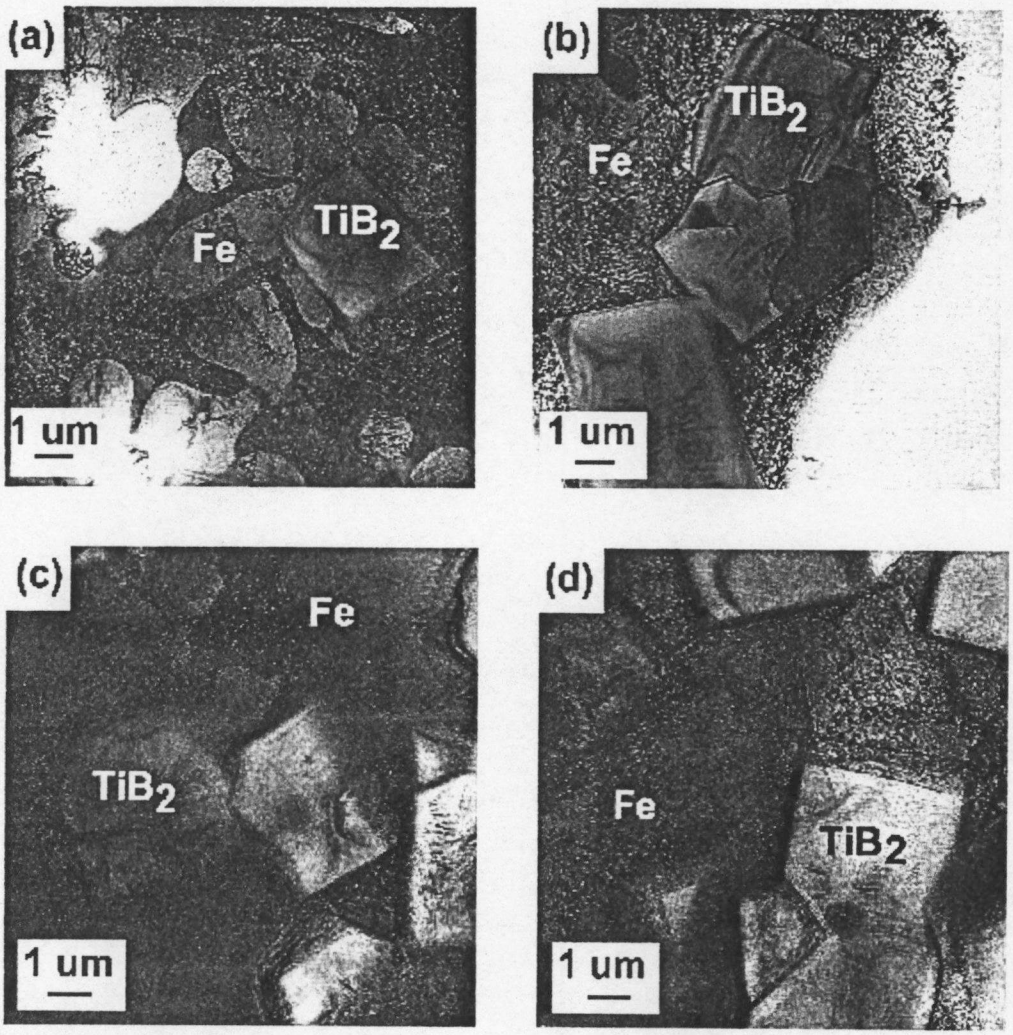


Figure 4.9. Bright field TEM images showing "composite" nature of the coating with faceted TiB_2 particles of various shapes and sizes embedded in Fe-rich matrix.

should be noted that there is no other visible crack within any other TiB_2 particle or at the particle/matrix interface.

In earlier discussion (Section 4.2) it was showed that "composite" coating region contains TiB_2 particles of various shapes and size embedded in Fe-rich matrix. It was also argued that some of the TiB_2 particles break into ultra-fine particles and get dissolved within the Fe-rich matrix. Figure 4.10 shows a very small TiB_2 particle (size ≈200 nm) embedded in Fe-rich matrix. The presence of such fine particles in the matrix confirms that some of the TiB_2 particles disintegrate into very fine particles due to high energy density of laser beam. Figure 4.11 is a bright field TEM image showing ultra-fine dendritic network of Fe within the coating region. Ultra-fine dendrites within the coating region are indicative of extremely high cooling rates experienced during laser surface engineering (6-9).

Figure 4.12 is a dark field image showing network of ultra-fine Fe dendrites with dissolved TiB_2 within dendritic spacing. EDS spectrum corresponding to spot A on dendrites show Fe peaks whereas spot B between dendrites reveals Fe and Ti peaks. Ti peaks are indicative of dissolved boride particles within Fe dendrites. This fact is further corroborated by the selected area diffraction (SAD) pattern of the same area as shown in Figure 4.13. SAD pattern shown in Figure 4.13b is a combination of hexagonal structure of TiB_2 along [0001] direction and BCC structure of Fe along $[\bar{1}\,11]$ direction. Four letter index has been used in this particular case to distinguish between the reflections from hexagonal TiB_2 and BCC Fe (Figure 4.13b). In the later sections, only three letter index has been used to characterize hexagonal TiB_2. This further proves presence of dissolved boride particles within Fe rich matrix (91). Also, diffraction pattern shown in Figures

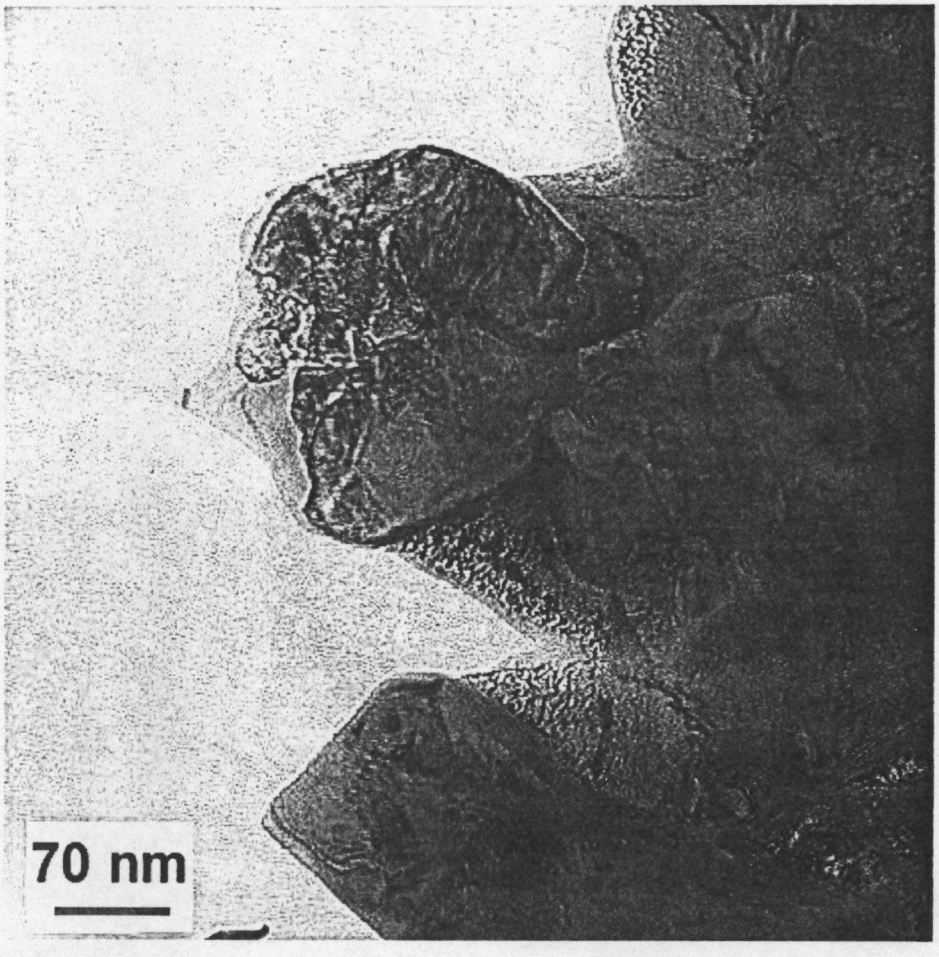


Figure 4.10. Bright field TEM image showing a very small TiB_2 particle (appx. size ~200nm) suggesting fragmentation during laser surface engineering process.

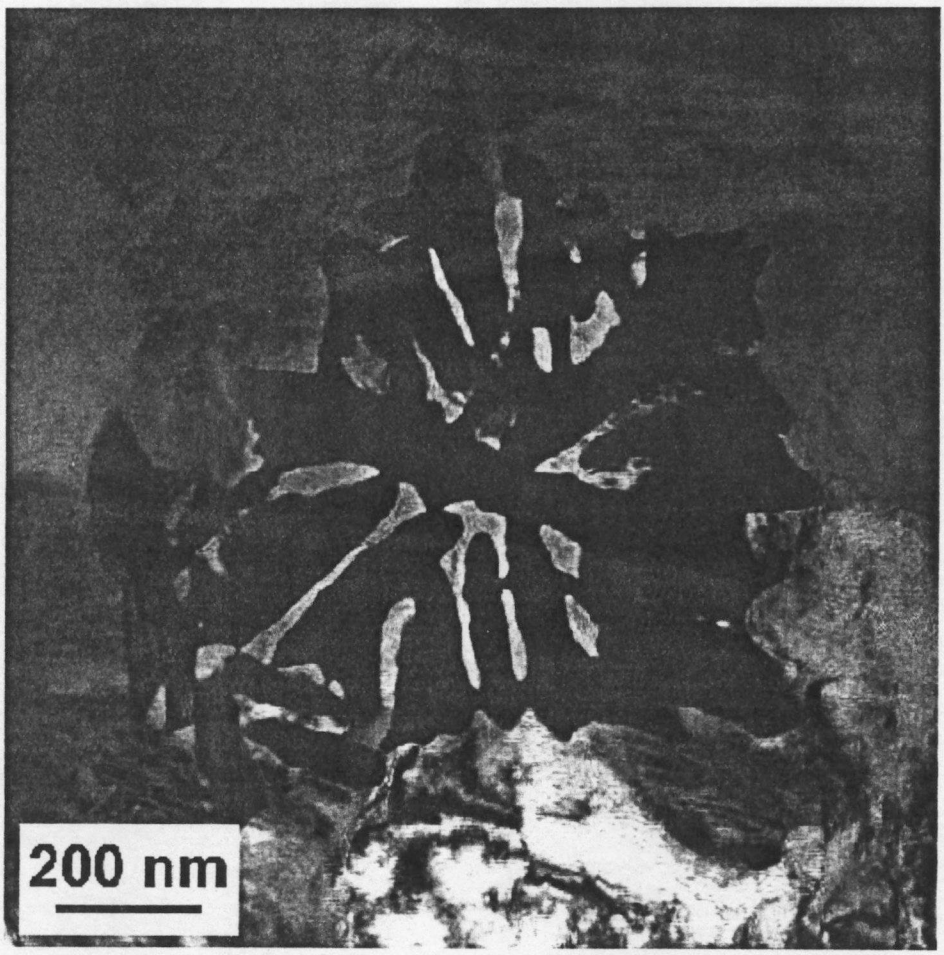


Figure 4.11. Bright field TEM image showing ultra-fine dendritic network of Fe within the coating region.

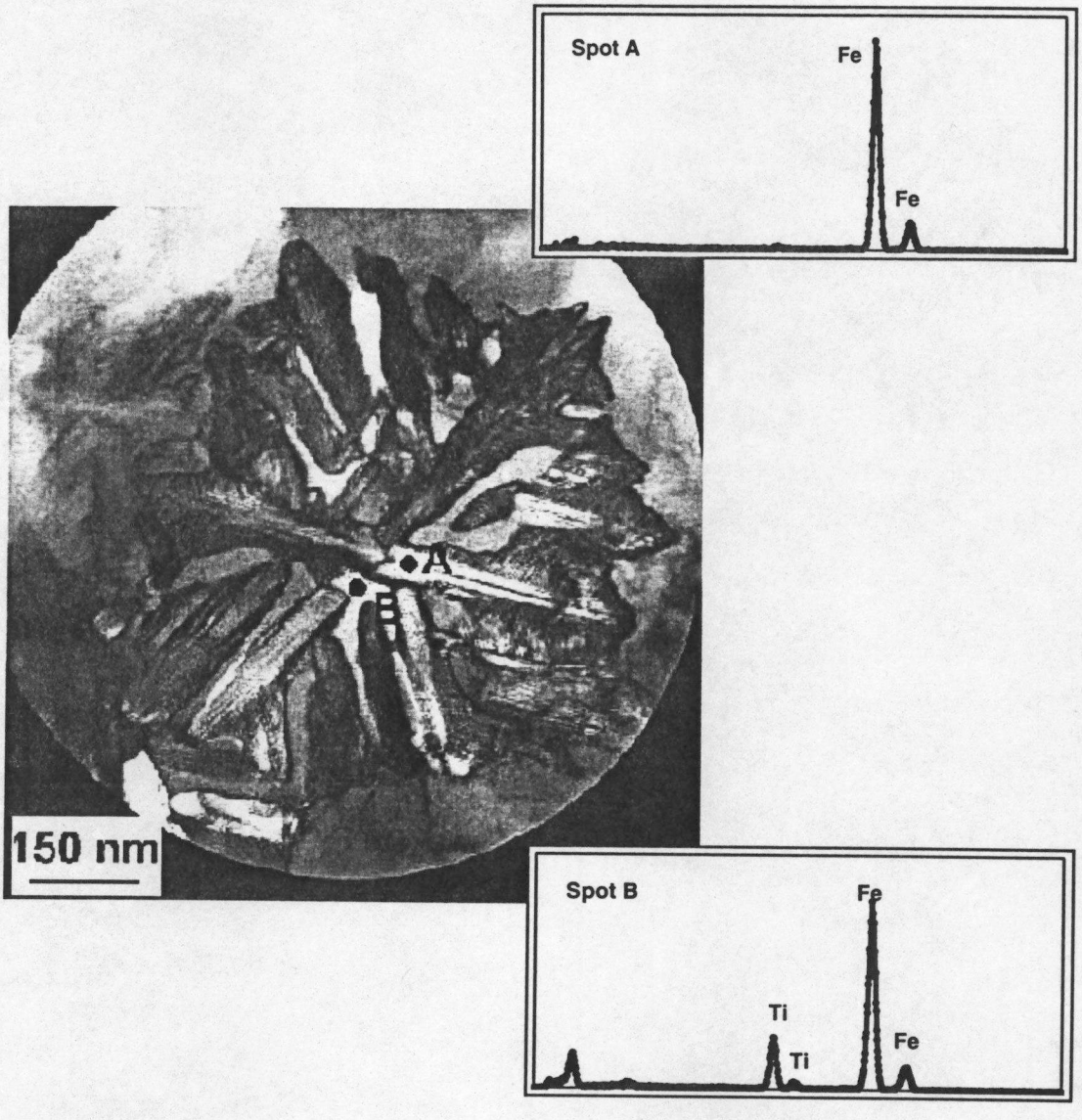


Figure 4.12. Dark field TEM image of the ultra-fine Fe dendrites with dissolved TiB_2 within the dendritic spacing. EDS spectra corresponding to spot A and B suggests dissolution of TiB_2 particles within the dendritic spacing.

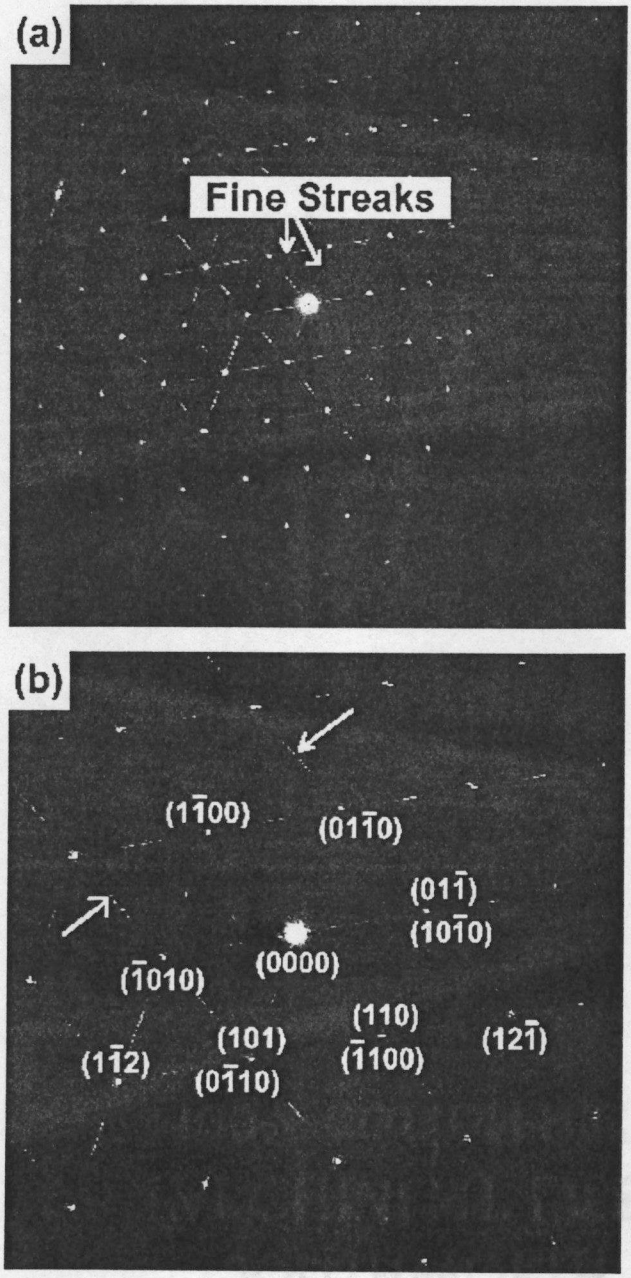


Figure 4.13. SAD patterns from the area shown in Figure 4.12 corresponding to a combination of HCP structure of TiB_2 along [0001] direction and BCC structure of Fe along [111] direction: (a) low magnification and (b) high magnification.

4.13a and 4.13b show some addition reflections in form of regular and continuous streaks (marked with arrows) which are neither from TiB_2 nor Fe. Such diffraction pattern is generally obtained by the presence of very fine precipitates and twinning (92-94). A high-resolution image in Figure 4.14 confirms presence of micro-twins within a TiB_2 particle. These twins are formed in a highly localized region of size varying between 10 nm -20 nm. The mechanism of formation of twins in the TiB_2 particle could be explained by the formation of metastable phase of type Fe_xB_y , Ti_mB_n or $(Fe,Ti)_aB_b$. TiB_2 is hexagonal in nature with a stacking sequence on close packed plane being ABABABAB..... Some of the Fe reacts with TiB_2 to form phases such as Fe_xB_y and Ti_mB_n that has been shown in the x-ray spectrum (Figure 4.7). These metastable phases have unconventional crystal structure such as orthorhombic and rhombohedral (Table 4.4). Twinning may be induced in TiB_2 particles during the shearing occurred for the phase transformation from hexagonal to orthorhombic structure. Similar case of twinning also has been observed in an earlier laser based study where Cr_2O_3 reacts with Fe to form a spinel (20). Also, it has been postulated that heat input can result in precipitation of different phases accompanied with highly localized twinning (93). It should be recalled that laser processing is a high energy density process, which can cause some unconventional structural transformations along with nucleation of metastable phase(s). Such fact is also evident from the x-ray spectrum of the coated surface which shows traces of metastable phase(s) of type Fe_aB_b and Ti_mB_n with unconventional crystal structure such as orthorhombic and tetragonal (Figure 4.7). TEM investigations were carried out to locate the presence of metastable phase(s). Ceramic/metal interface is one of the potential site for such phase formation. Ceramic/metal interface also plays an

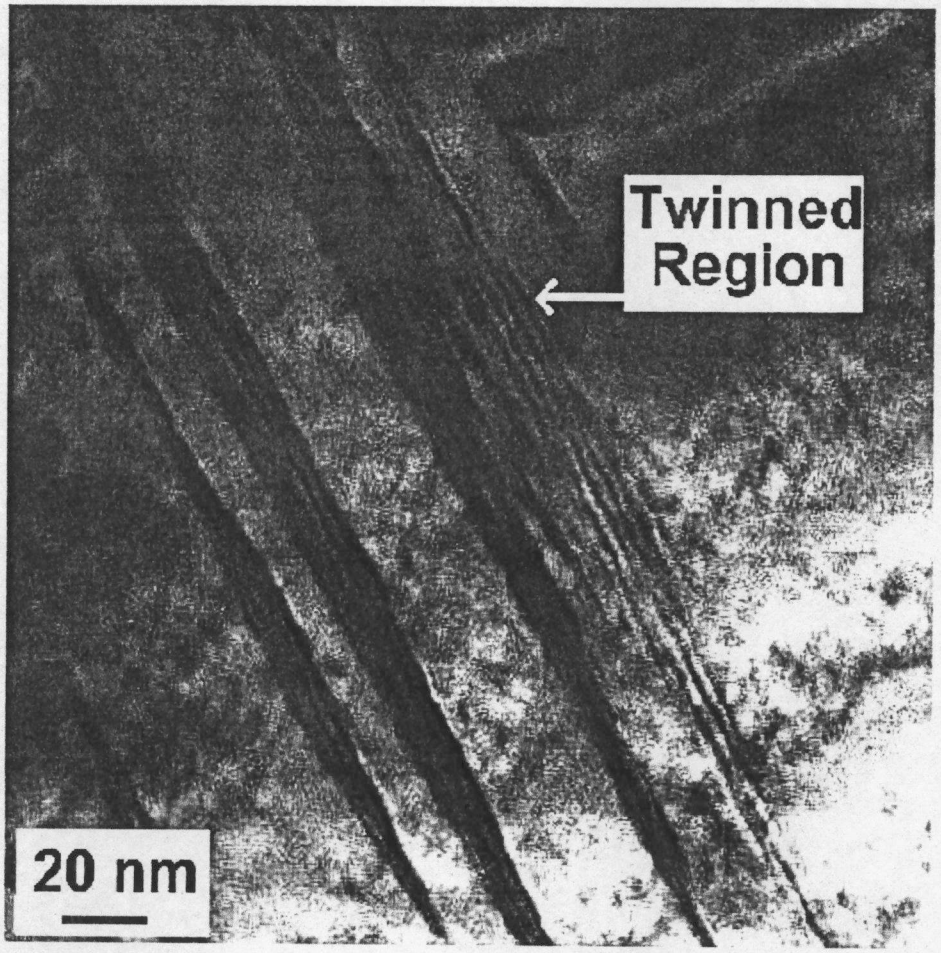


Figure 4.14. HR-TEM image showing presence of twins within a TiB_2 particle.

important role in evaluating the mechanical properties of the coating. The importance of ceramic/metal interface has been addressed in detail in section 2.4. TEM investigations of TiB_2 particle/Fe interface within the "composite" coating is presented in the following section.

A. Ceramic-Metal Interface

Figure 4.15 shows the interface between TiB_2 particles and Fe matrix, which is smooth and does not indicate any crack or delamination. This is an indication of strong bond between the ceramic particle (TiB_2) and metal (Fe) matrix at the microstructural level. The strength of a ceramic-metal interface depends upon the wetting between the two materials (25-26). The wetting phenomenon of the ceramics by the metal has been addressed by several researchers (24, 27, 95-97). It has been experimentally proven that refractory ceramics are in general wetted by transition elements (35-37, 98). It is shown that Ti based ceramic easily wets Fe at high temperatures and wetting progresses further with time (98). This has also been experimentally proved during the in-situ synthesis of Fe-TiC composite (36,96). Such difference in the wetting nature is explained by the electronic structure of the metals, which will be discussed in the following section (96). Table 2.1 lists the wetting angles of certain refractory ceramics by certain molten metals. The wetting angle between TiB_2 and Fe is 49 degrees suggesting a good wetting. Moreover, wetting time is less than 1 minute, which is further accelerated during laser surface engineering (16). Work of adhesion between TiB_2 and Fe is 2955 mJ/m^2, which further suggests a strong metal-ceramic interface (Table 2.1).

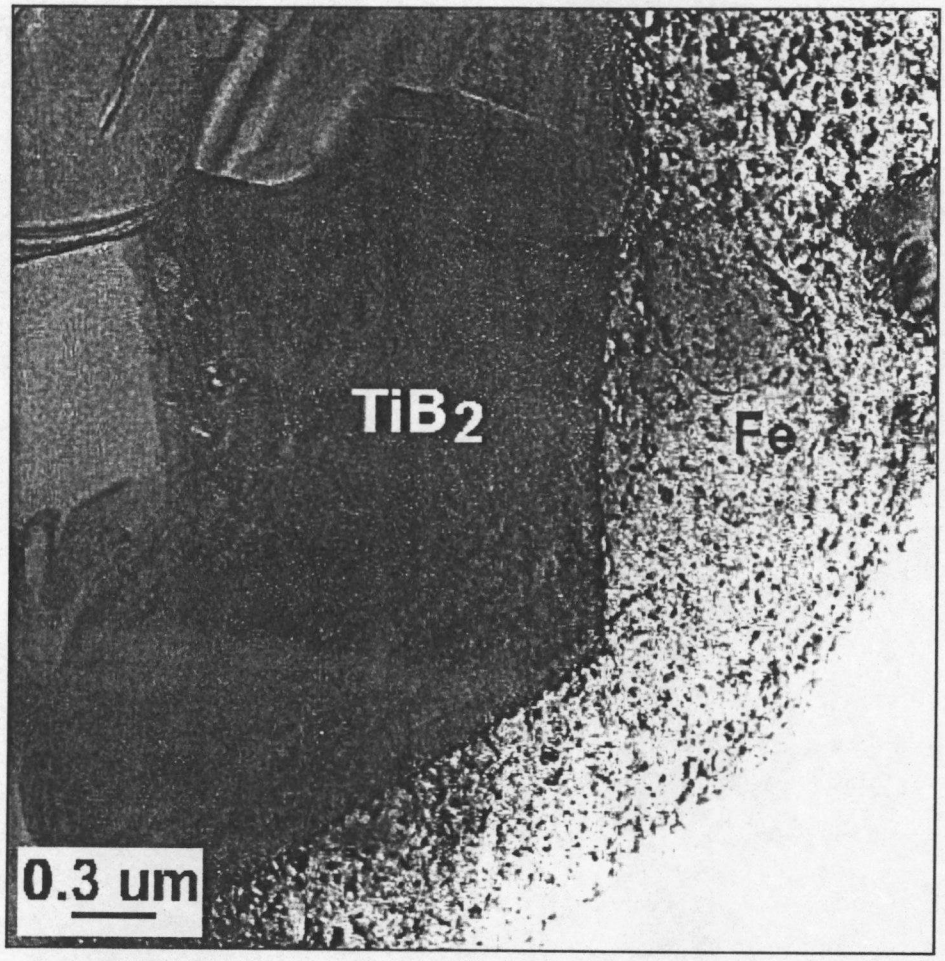


Figure 4.15. Bright field TEM image of TiB_2/Fe interface within the coating region.

A detailed analysis of role of metals as binder for ceramics and their wetting characteristics based on the electronic structure has been addressed (96). The wetting phenomenon has been attributed to the unfilled ***d***-orbitals in transition metals and their compounds such as borides and carbides (57,96)

TiB_2 is a transition metal based ceramic and it has partly covalent and partly metallic bonding (57-59). Metallic nature of the bonding is also revealed by the electrical conductivity of TiB_2, which is high and similar to the metals (35). It is theoretically postulated that if the ratio of the size of nonmetal atom to metallic atom is less than 0.59 then bonding is partly covalent and partly metallic (59). Further, it is also confirmed and postulated for the transition metal based ceramics that the covalent bonding in such compounds is not as important as metallic bonding (57). A ***d*** band substructure similar to transition metals also exists in transition metal based ceramics, which leads to metallic bonding in such ceramics (57). A value has been assigned to number of ***d*** electrons present in these transition metals and their compounds. Electrons in the ***d*** band substructure participate in the formation of a metallic bond and accordingly, TiB_2 has 5.5 ***d*** electrons available for bonding (57).

Based on the theoretical and experimental results, an empirical rule for the suitable choice of binder used in sintering of transition metal based ceramics has been proposed (96). For a transition metal or compound having an unfilled inner ***d*** shell in the state d^x , a transition metal in the state d^y would be the most suitable binder (x and y represent the number of electrons in the unfilled ***d*** shells) if the following condition is satisfied.

$$x + y = 11 \qquad (4.9)$$

It is also suggested that a selection of material system which gives x + y = 10 or x + y = 12 would also provide good bonding but it would be inferior to the system satisfying x + y = 11 condition.

In the material system TiB_2-Fe of the present study, Fe has unfilled ***d*** subshell with 6 electrons ($\mathbf{d^6s^2}$ configuration) and TiB_2 has 5.5 ***d*** electrons as assigned earlier (57). This satisfies above hypothesis (96) of equation (4.9)

$$(x = 5.5) + (y = 6) = 11.5 \qquad (4.10)$$

According to this hypothesis, Fe wets TiB_2 nicely and does not react with TiB_2 layer but remains as a binder similar to Co in WC-Co system. This fact has been earlier corroborated in the analysis based on electronic configuration which says that bonding in such material systems does not promote compound formation (57). Further this hypothesis has been verified and confirmed in another experimental study based on Cu-TiB_2 system where Cu acts as a poor binder for TiB_2 due to its completely filled ***d*** subshell (36). It should be recalled that such hypothesis is true for an equilibrium process. Therefore, on the contrary, it is reasonable to assume that some Fe may have chemically reacted with TiB_2 due to non-equilibrium synthesis experienced in high energy input by laser. Such phenomenon was earlier observed in x-ray diffraction spectrum (Figure 4.7) of LSE sample, which shows formation of some metastable phase(s) of type suggesting some chemical reaction between TiB_2 and Fe.

After extensive searching efforts, such a reaction zone between TiB_2 particle and Fe was revealed (Figure 4.16). The interface between TiB_2 particle and Fe matrix shows a reaction zone of approximately 50 nm. The size of the reaction zone is consistent at

several interfacial locations (Figure 4.16 and 4.17). The reaction products appeared as a dark black band on the Fe side and sharp needles growing towards TiB_2 particle (Figure 4.16a). Figure 4.17 is another such reaction zone between a large TiB_2 particle and Fe-rich matrix. EDS spectra from the various spots (A, B and C) are also shown in Figure 4.17. EDS spectrum from the reaction zone (spot B) shows high intensity peaks of both Ti and Fe whereas EDS spectra from Fe matrix (spot A) and TiB_2 particle (spot C) shows peaks for only Fe and Ti, respectively. This corroborates our hypothesis of non-equilibrium synthesis during laser processing. A similar approach has been adopted to show the existing reaction zone between an ultra-fine TiB_2 particle and Fe-rich matrix. Figure 4.18 shows an ultra-fine TiB_2 particle (size $\approx$ 400 nm) surrounded by a gray colored binder (spot A) and Fe matrix (spot B). EDS spectra from these various zones are shown in Figure 4.19. EDS spectra from the grayish zone (spot A) shows high intensity peak of both Ti and Fe (Figure 4.19a). It further proves the presence of a reaction zone between the TiB_2 particle and Fe matrix. It should be noted that reaction zone is significantly large for this particle. This is attributed to the smaller size of the particle. Reaction product tends to form a bridge between TiB_2 and Fe and acts like a binder. Several researchers have suggested that formation of interfacial reaction products promote wetting between ceramic/metal interface leading to a stronger and adherent interface (20,25,87,99-100). Moreover, nano-crystalline reaction product and phase(s) formed at ceramic/metal interface act as stress absorber, further, reducing the chances of crack propagation (20).

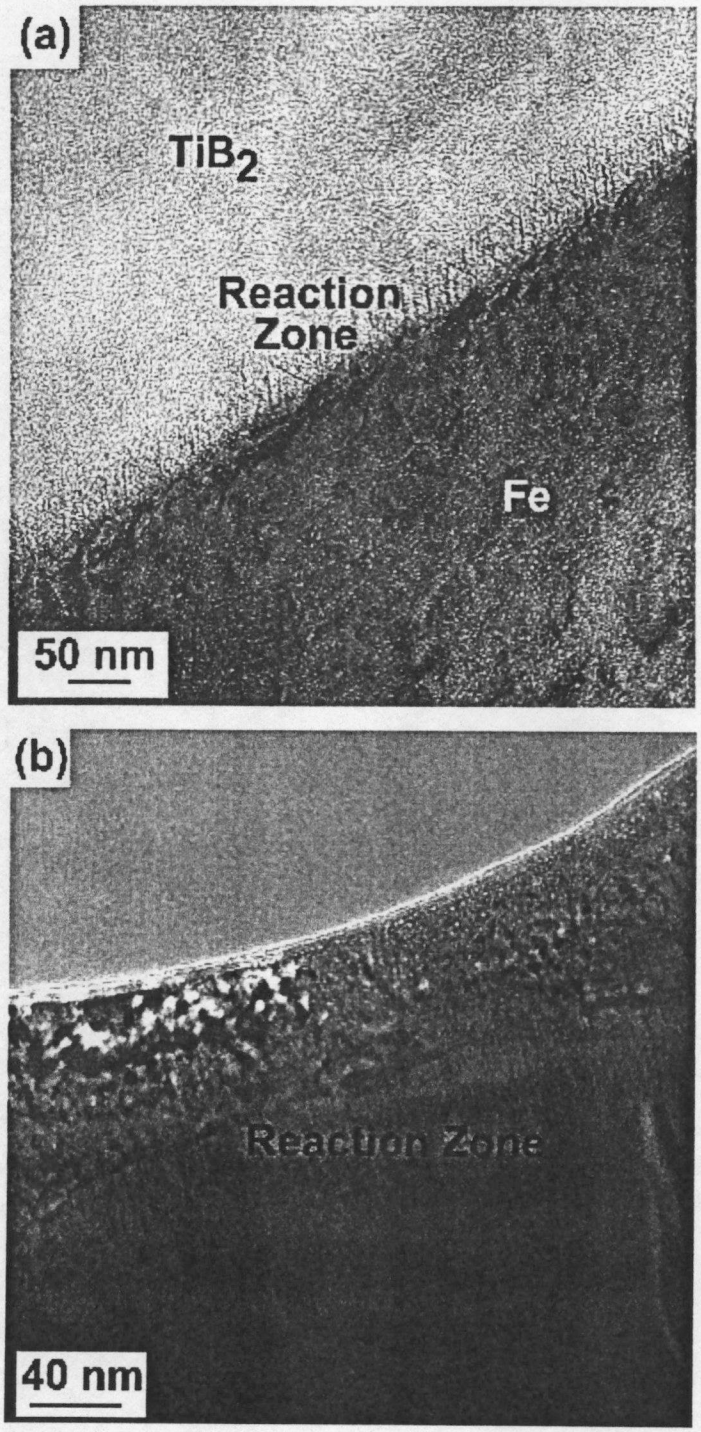


Figure 4.16. HR-TEM images showing a nanosized reaction zone between the TiB_2 particle and Fe.

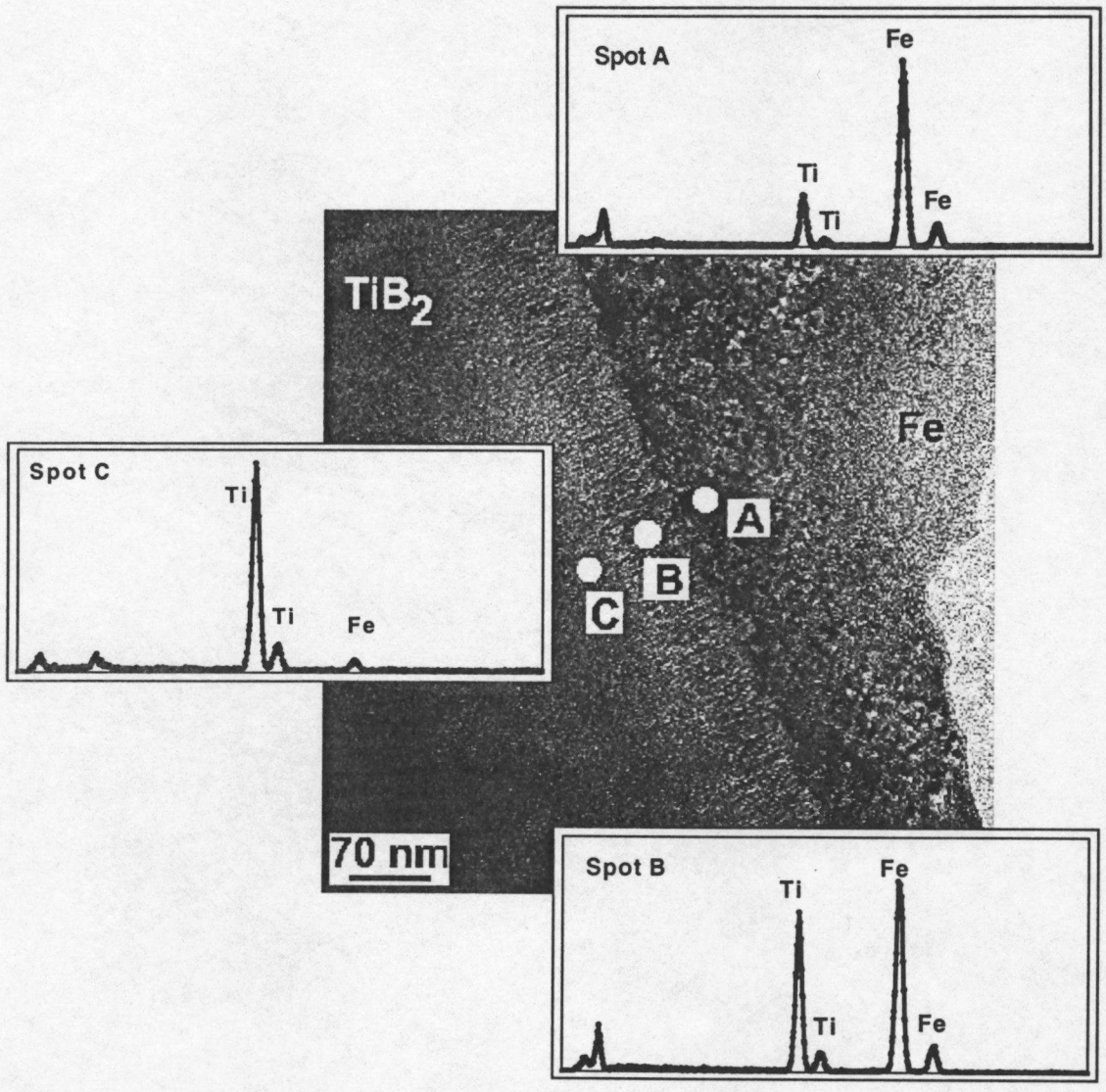


Figure 4.17. TEM image showing a reaction zone between the TiB_2 particle and the corresponding EDS spectrums.

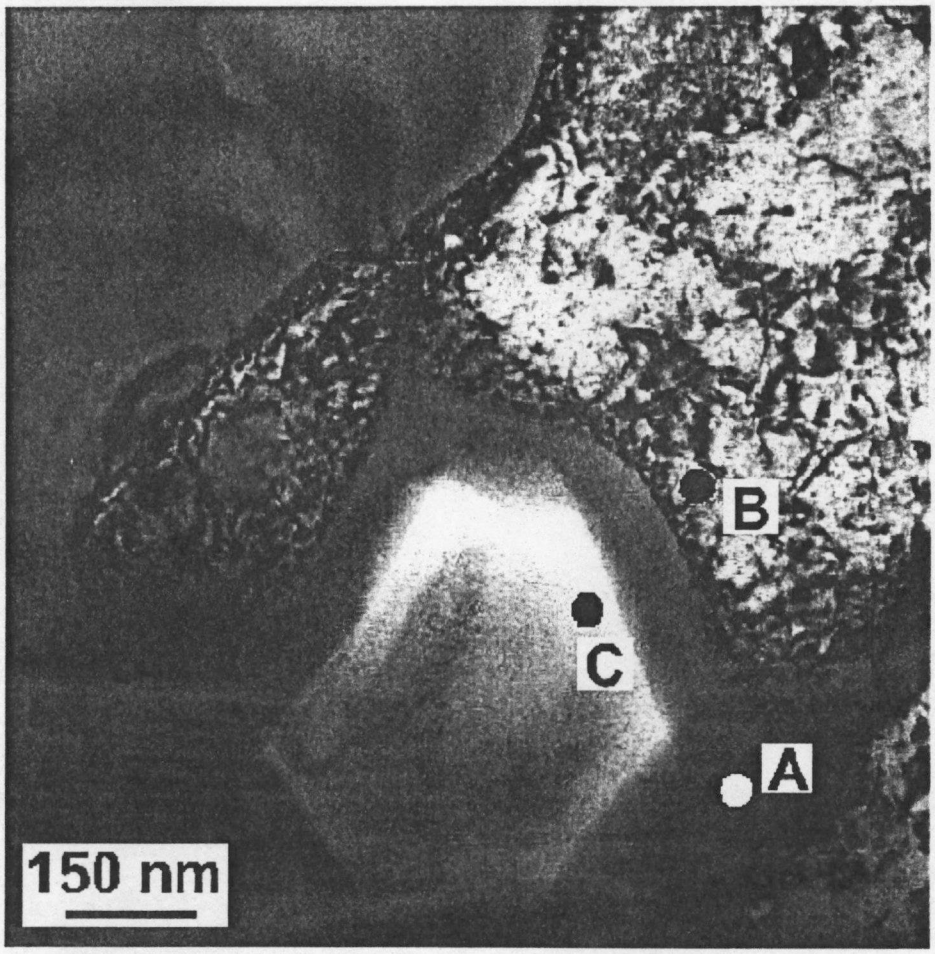


Figure 4.18. Bright field TEM image of a nano-size TiB_2 particle surrounded by a binder and Fe-rich matrix zone. EDS spectrum from three various spots are shown in Figure 4.19.

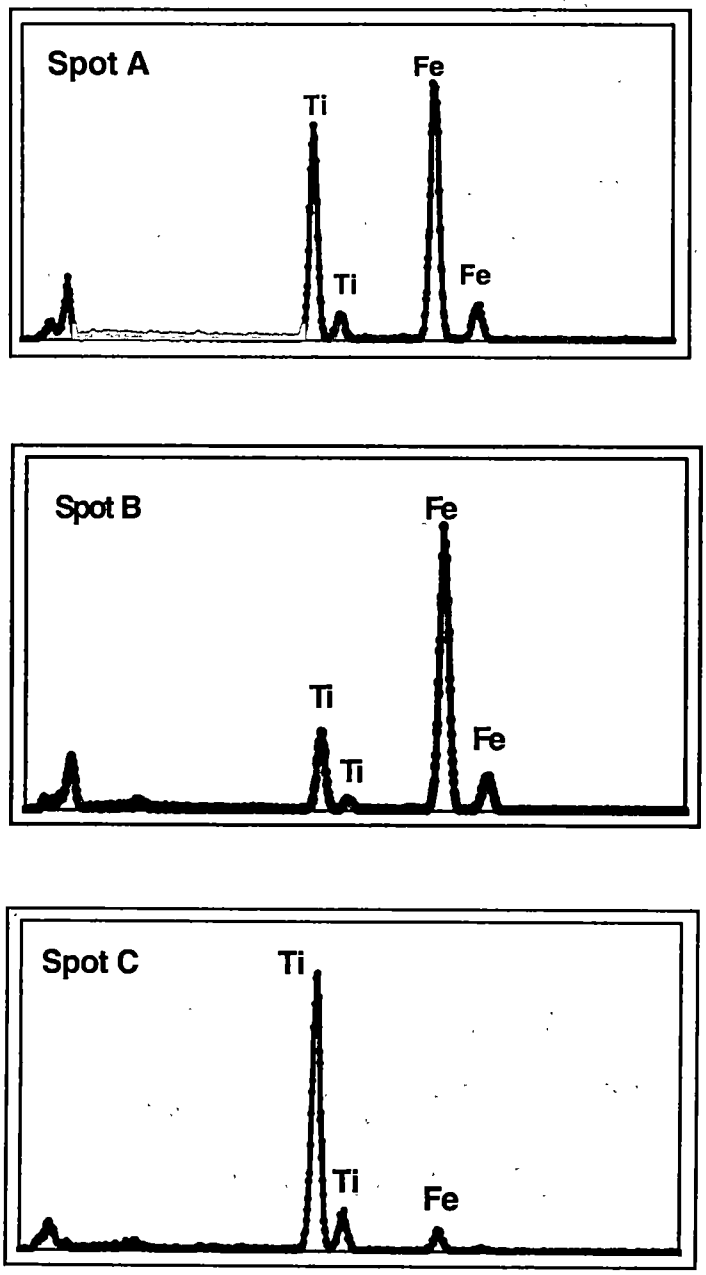


Figure 4.19. EDS spectrum from spots A (binder), B (Fe-rich matrix) and C (TiB_2) particle.

High Resolution Transmission Electron Microscopy (HR-TEM) provides a very precise information about the interface at the atomic level. These images can reveal many kinds of defects, which can be chemical or structural (26). Chemical defects occur if any deviation from the exact composition of two phases at the interface exists. Such deviation is often caused by the reaction product or interphase formation at the ceramic/metal interface. The type of defect that develops at the interface depends on the specific material system. For systems, that form interphase(s) or reaction products, it is important to characterize them. However, even if all the thermodynamic data and tielines are known, product may not be unambiguously identified due to kinetic considerations (26). Such fact is true for laser surface engineering process, which involves very rapid kinetics. Structural defect such as steps or facets at the interface, misfit dislocations and stacking faults can also be identified from high resolution microscopy. HR-TEM is possible if the interface is very thin (less than 20 nm) and is parallel to the incident electron beam (90). Figure 4.20 is a high-resolution transmission electron microscope image of two-dimensional lattice fringes on TiB_2 side and one-dimensional lattice fringes on Fe side. Dark islands observed on the Fe side are merely artifacts caused by the differential thinning of the sample. The dark band at the interface is atomically smooth and sharp (2-3 nm thick) in nature. Also, there is no atomic level amorphous phase or layer at the TiB_2/Fe interface. It suggests good ceramic/metal bond at the interface. However, two-dimensional lattice fringes extend up to 10-15 nm into one-dimensional Fe lattice and bonds directly with Fe with a minimal mismatch. This lattice mismatch leads to semi-coherent interface at few locations (shown by arrow in Figure 4.20). Such behavior has earlier been observed in 6061Al/Si_3N_4 composites where nanocrystalline

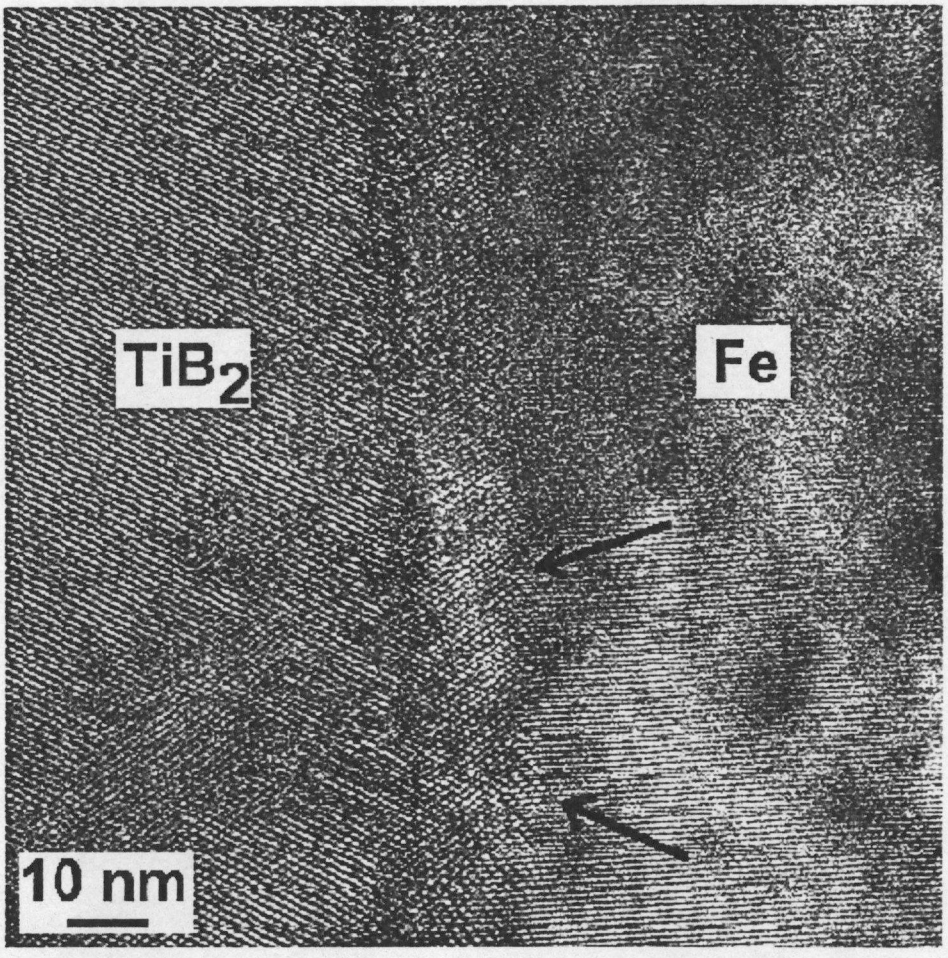


Figure 4.20. HR-TEM image of two dimensional lattice fringes on TiB_2 side and one dimensional lattice fringes on Fe side. Semi-coherent interface and nano-crystalline product are marked with arrow.

MgO and $MgAl_2O_4$ particles grew at the interface and bonded with Si_3N_4 whiskers (101). Thus, it is very likely that some nanocrystalline phase or reaction product forms at the interface and grows into Fe matrix. Again, such observation is in accordance with earlier hypothesis of formation of metastable phase(s) during laser processing. Figure 4.21 is another high-resolution TEM image showing lattice fringes of TiB_2 and Fe with the corresponding SAD pattern from two zones shown in Figure 4.22. Figure 4.22a shows diffraction pattern obtained from the Fe-rich side of the interface. It shows SAD pattern corresponding to BCC Fe along [001] direction of zone axis. However, there are additional diffraction spots, which do not correspond to Fe. Such spots (marked by arrow) further correspond to the presence of a reaction product or precipitate at the ceramic-metal interface. The SAD pattern obtained from TiB_2 side of the interface is shown in Figure 4.22b. It corresponds to diffraction spots obtained from TiB_2 along [0001] zone axis. However, some of these diffraction spots have diffused intensity along with the presence of double diffraction spots (see arrow). Such diffraction patterns are obtained in either of the two cases: a) when a reflection is not common to two grains, then for that reflection the diffracting crystal behaves like a wedge specimen with one surface parallel to the planar defect and b) the presence of dislocations and stacking faults can lead to distortion of volume which may lead into double diffraction spots (94). The presence of the reaction product has created a faulted region with an atomic mismatch at the interface (marked by arrow in Figures 4.20 and 4.21) which could give rise to the additional diffraction spots as seen in Figure 4.22b. Also, a distorted hexagonal shaped TiB_2 particle with heavily faulted structure, containing twins and array of dislocations is shown in Figure 4.23a. Due to the presence of dislocation, faults and possible

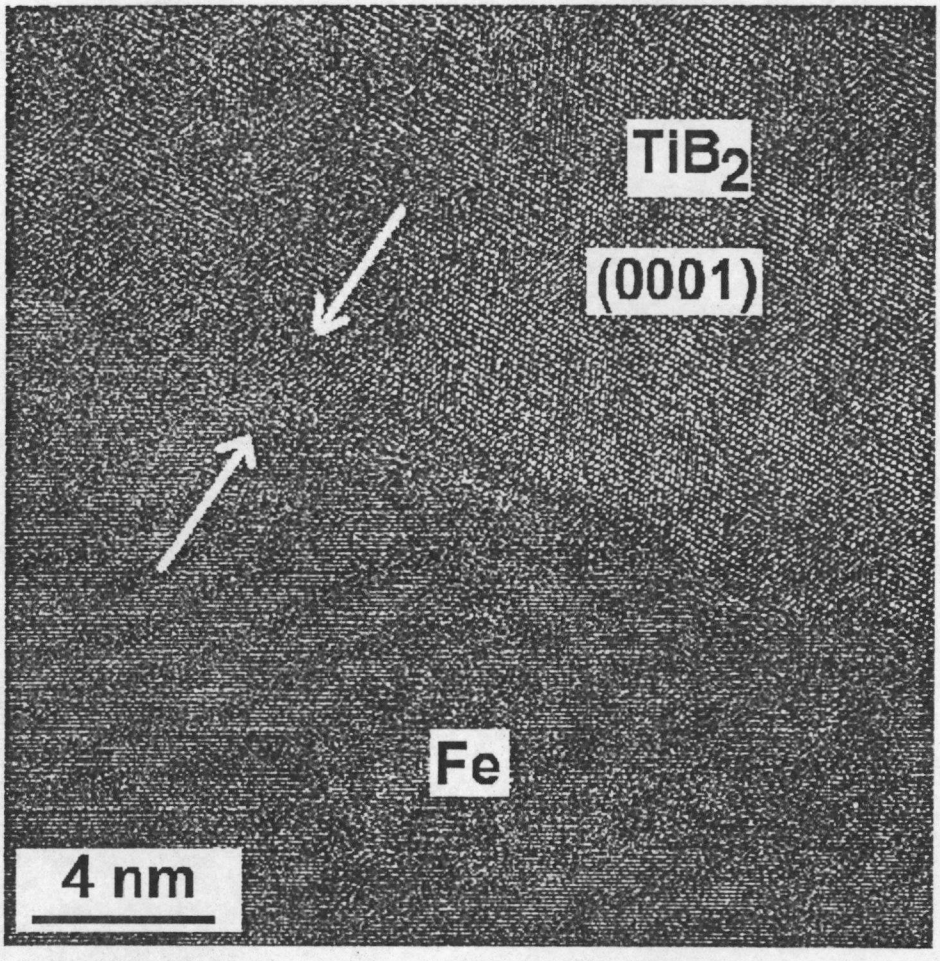


Figure 4.21. HR-TEM image of TiB_2/Fe interface viewed along [0001] TiB_2 direction.

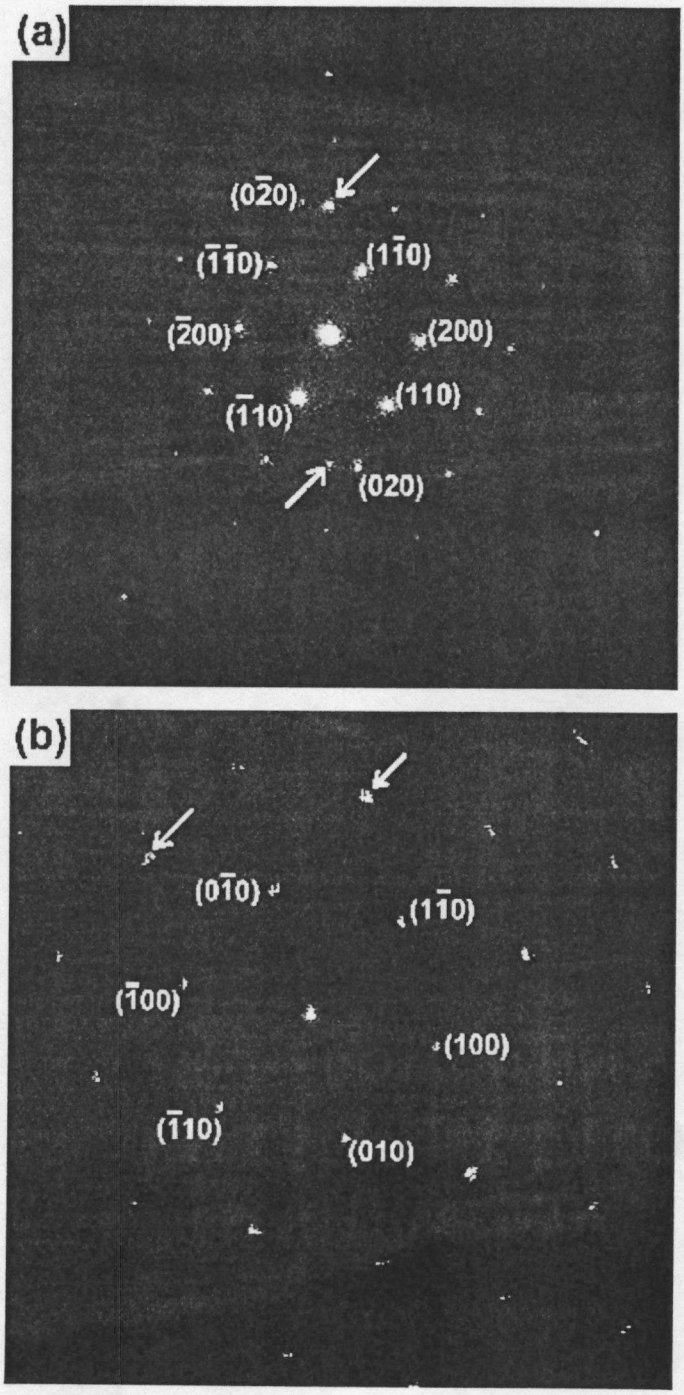


Figure 4.22. SAD patterns obtained from the region shown in Figure 4.21 (a) from Fe (BCC) side and (b) from TiB_2 (HCP) side.

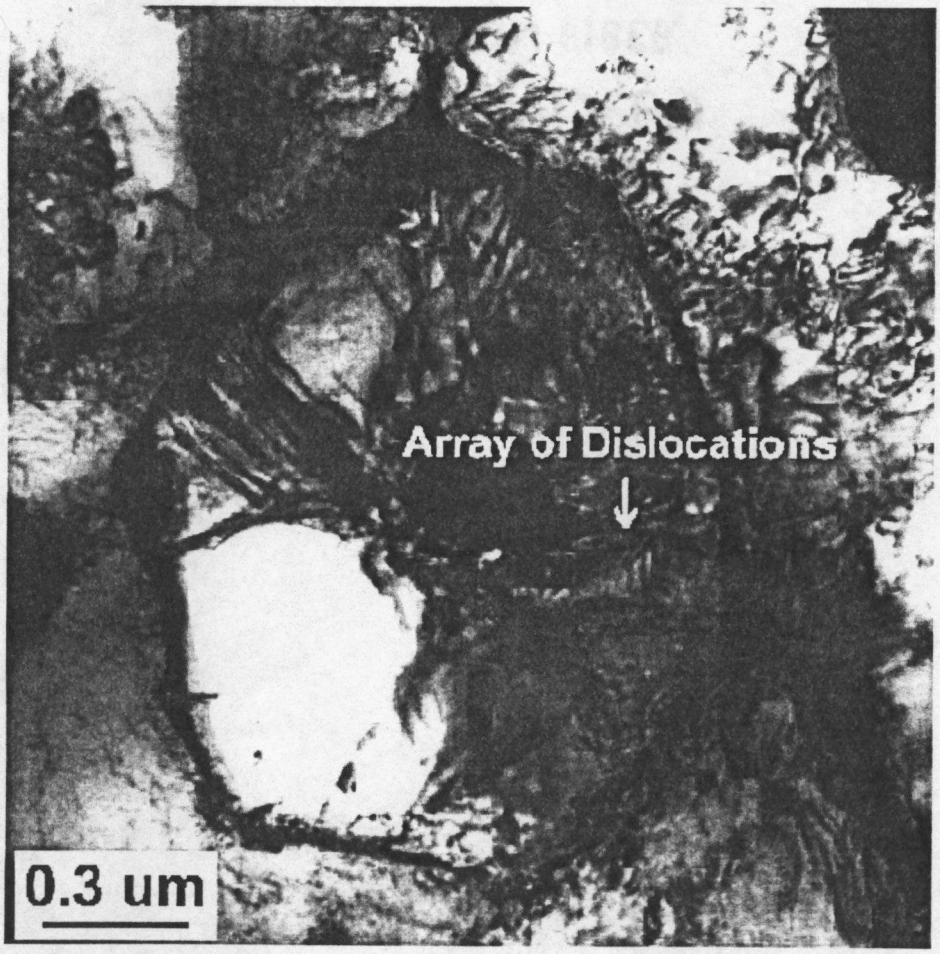


Figure 4.23(a). Bright field TEM image of a TiB_2 particle containing several faults and dislocations.

metastable phase(s), SAD pattern (Figure 4.23b) shows additional satellite reflections (marked by arrows). The presence of twins within the TiB_2 grain is further confirmed by the presence of streaks in the diffraction pattern. The presence of stacking faults at atomic scale is corroborated by the HR-TEM image shown in Figure 4.24a. Several domains of nano-sized stacking faults and atomically faceted grain boundaries are marked. Such features elucidate the presence of additional diffraction spots as seen earlier. Figure 4.24b is the digitally enhanced version of image shown in Figure 4.24a that reveals the nano-sized stacking faults domain more distinctly. It has been postulated that formation of reaction product produces a surface roughness at the ceramic/metal interface. Such roughness promotes bonding at the interface and increases the fracture resistance of the interface (26). Formation of reaction product at the TiB_2/Fe interface has been confirmed by HR-TEM and suggests a strong bond between the ceramic and metal.

TEM samples within the coating region were further subjected to search for the physical observation of metastable phase(s) or precipitates and defect structure. Figure 4.25 shows some black color precipitates within a TiB_2 particle. Columnar and dendrite shaped features were also observed in some other particles as shown in Figure 4.26. These regions were further investigated at high magnification for chemical and structural characterization. Figure 4.27 is a high magnification view of such precipitate along with corresponding EDS spectra at spots A and B. EDS spectrum from the blackish precipitate region (spot B) shows a small Fe peak apart from Ti peak. It suggests that there is a small amount of Fe, which has reacted with TiB_2 particle. This change,

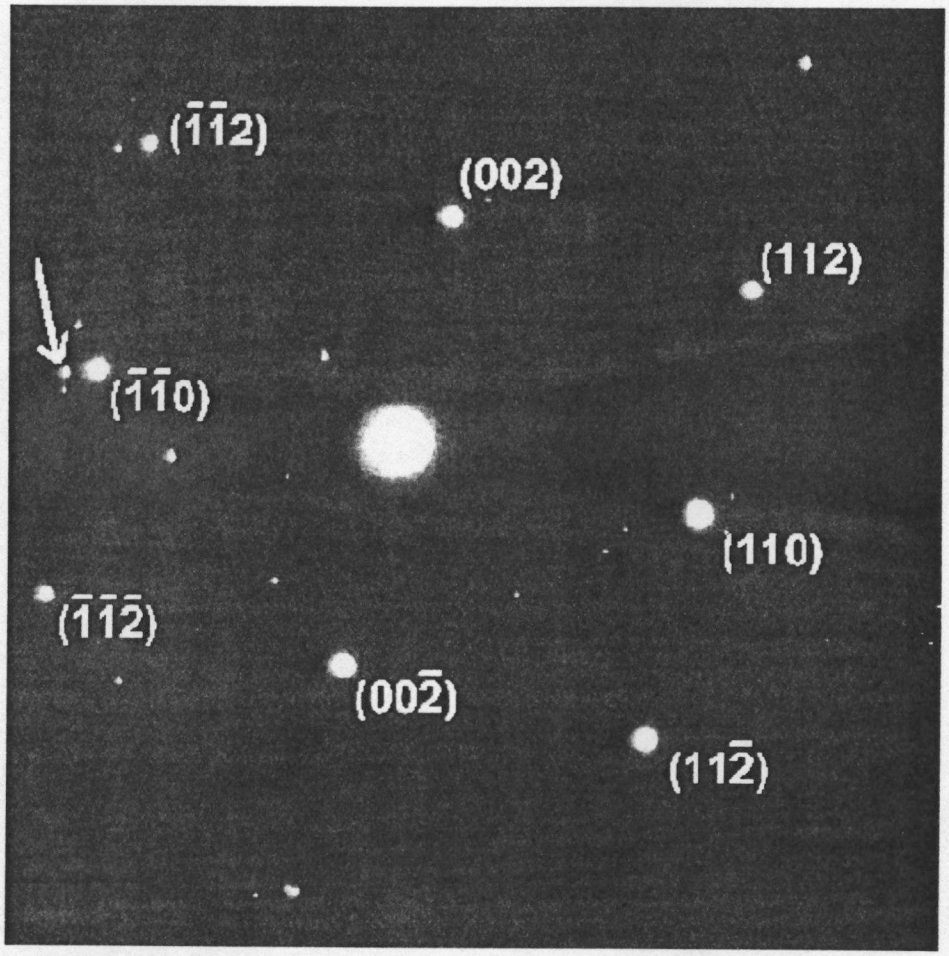


Figure 4.23(b). SAD pattern corresponding to Figure 4.23(a).

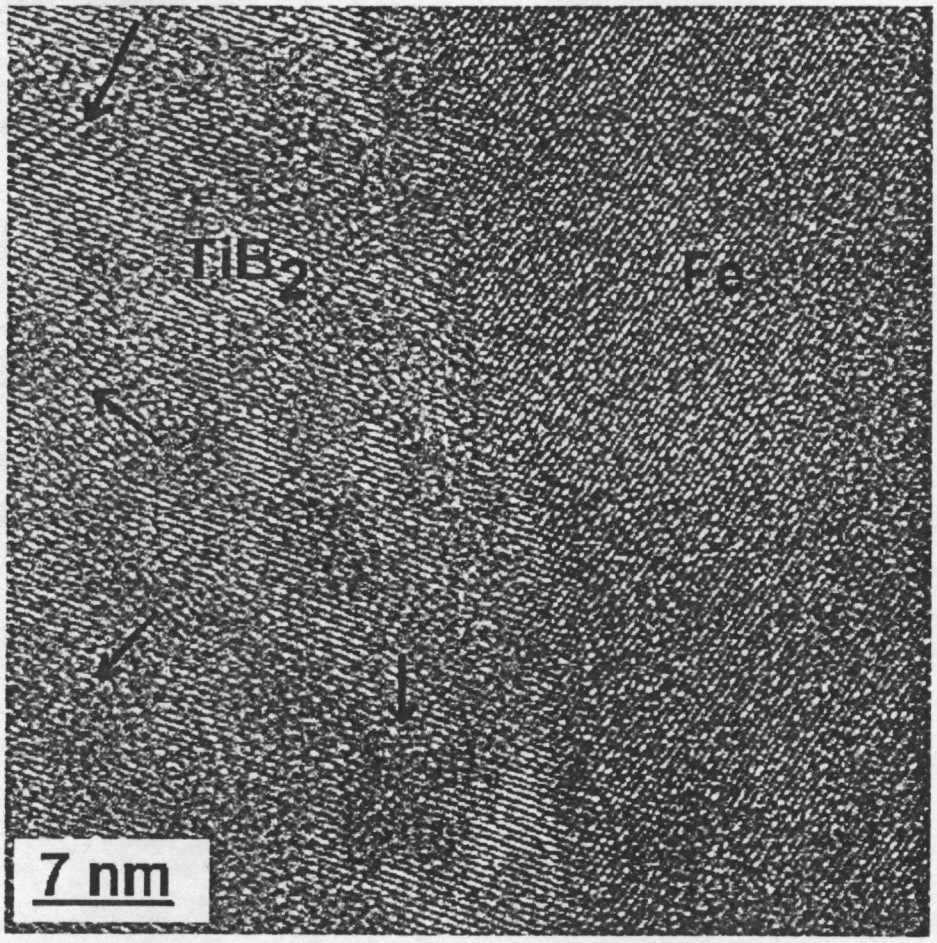


Figure 4.24(a). HR-TEM image of the TiB_2/Fe interface showing the presence of several domains of stacking faults on TiB_2 side.

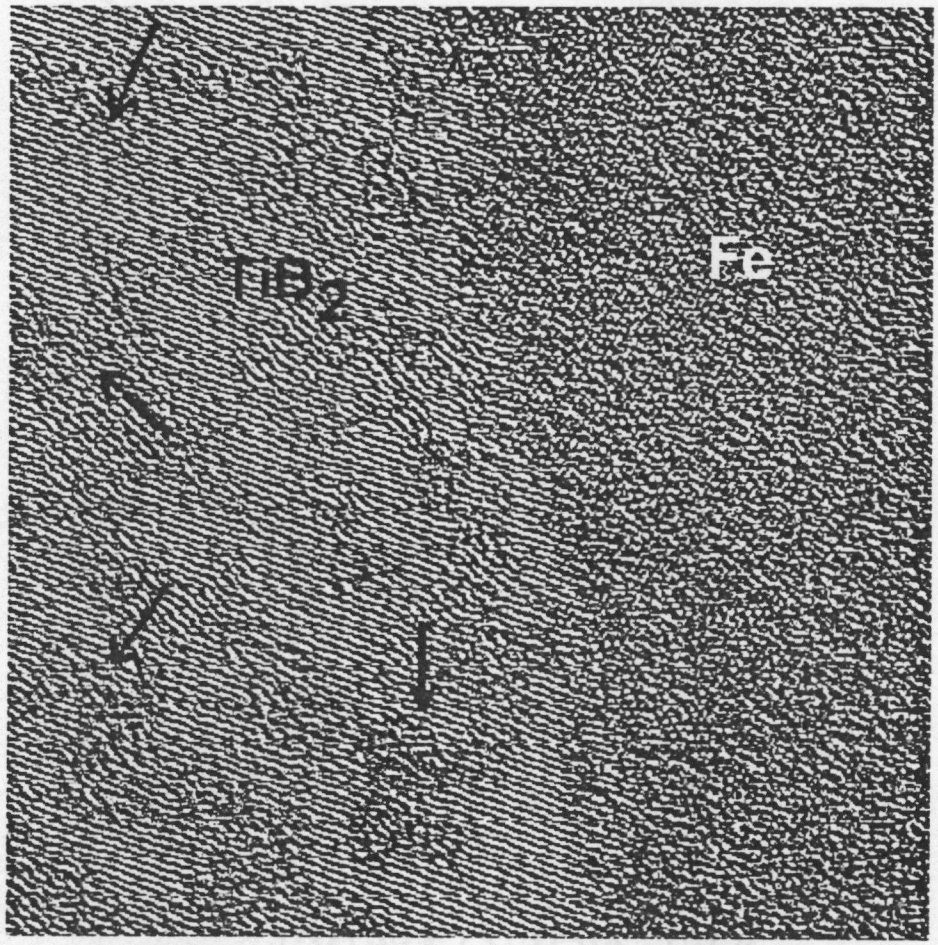


Figure 4.24(b). Digitally sharpened version of Figure 4.24(a) revealing nano-size domains of stacking faults and dislocations more distinctly.

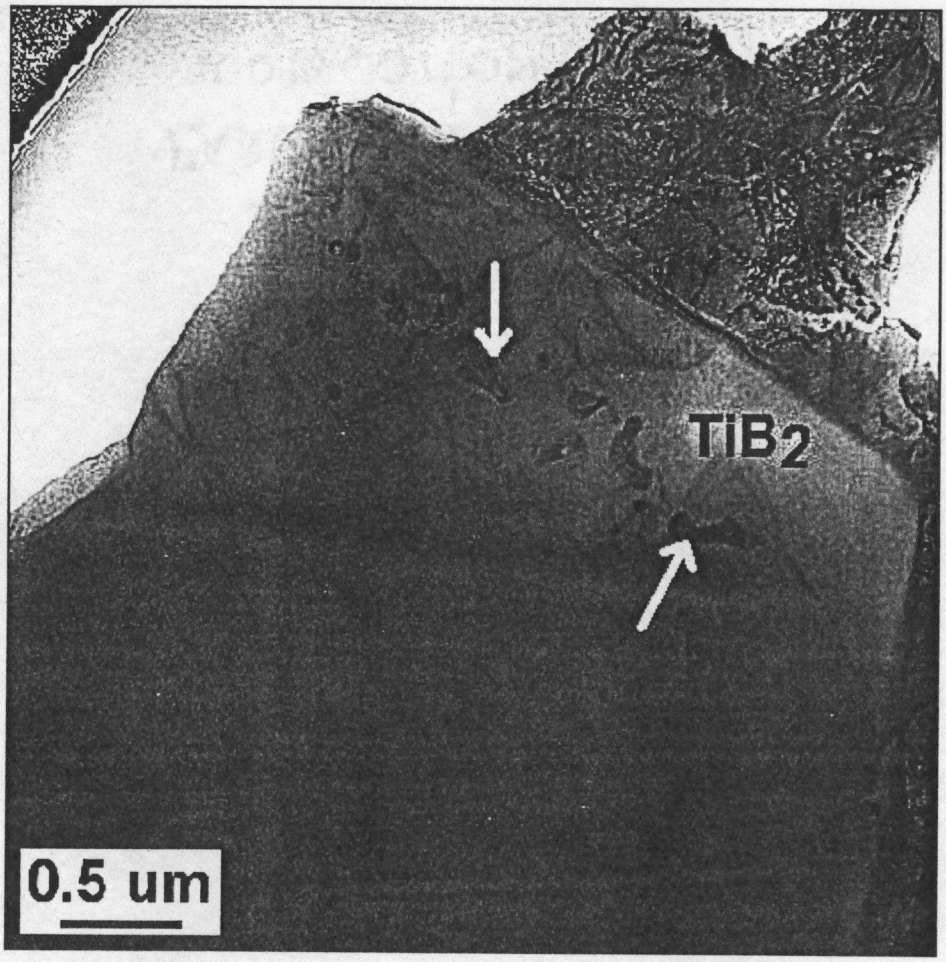


Figure 4.25. Bright field TEM image of fine black color precipitates within a TiB_2 particle.

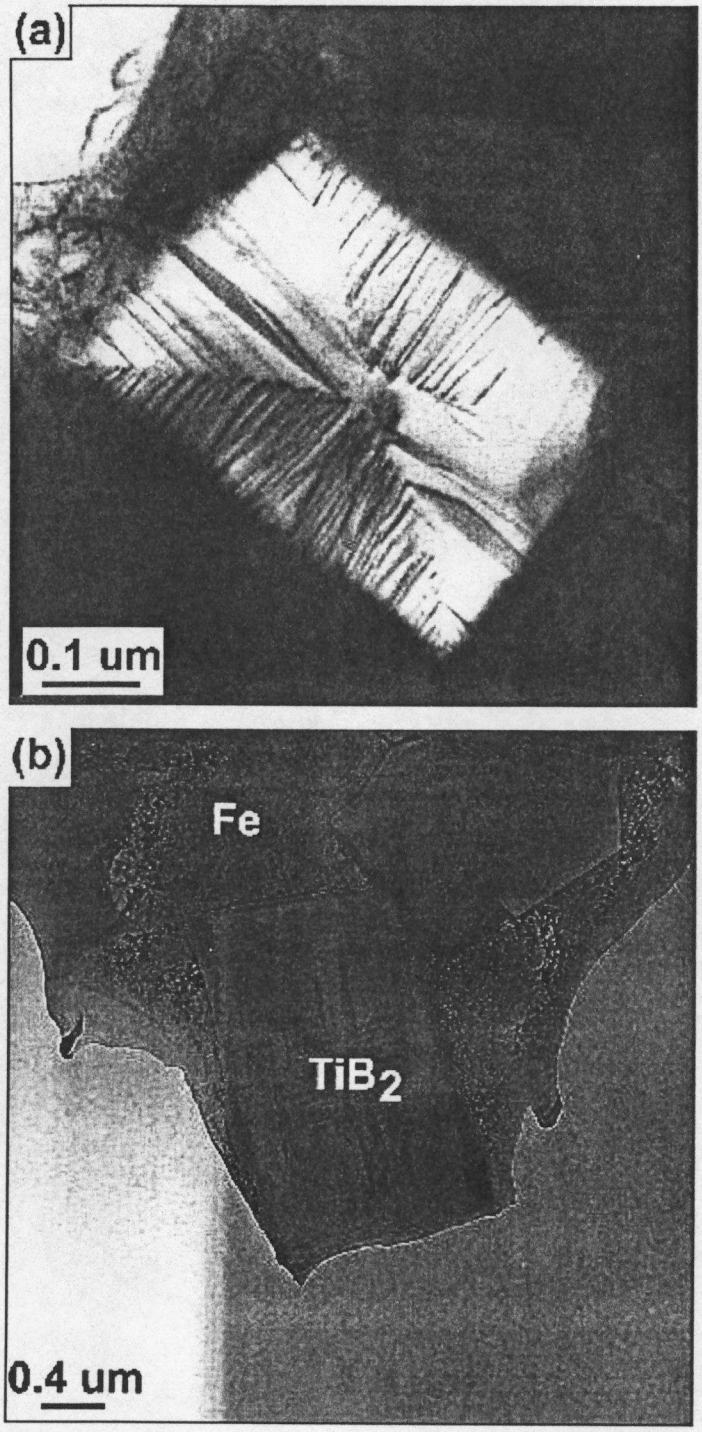


Figure 4.26. Bright field TEM images of (a) columnar and (b) dendritic features within the TiB_2 particles.

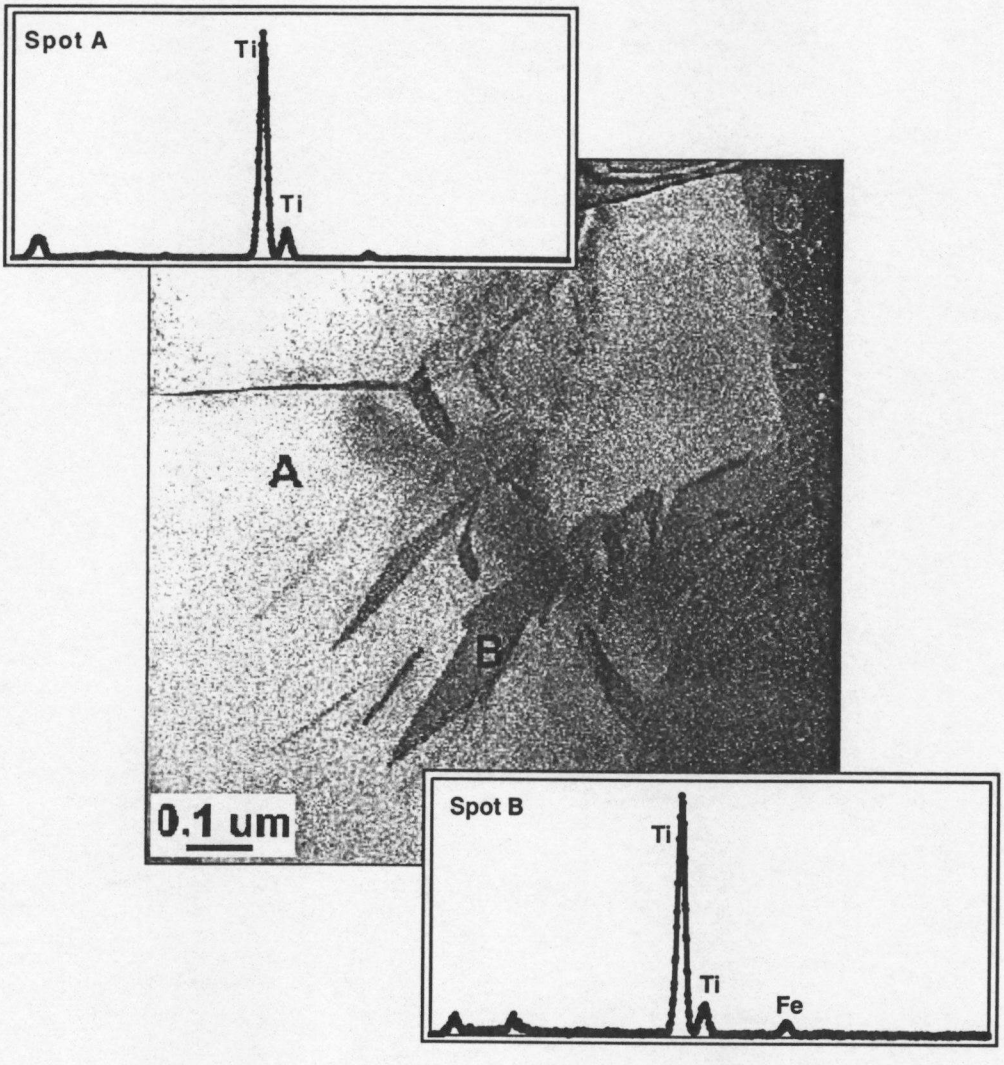


Figure 4.27. High magnification view of a region within the TiB_2 particle and EDS spectra from spot A (TiB_2 particle) and spot B (black precipitate within the TiB_2 particle).

however, was not very significant suggesting the formation of the columnar and dendritic features within TiB_2 particle is dominated by structural changes rather than chemical changes. After extensive search efforts, regions containing these metastable phase(s) and/or precipitates were found. Fine precipitates (size ≈ 50 -100 nm) within a TiB_2 particle are shown in Figure 4.28 along with the corresponding EDS spectra from the precipitate and TiB_2 particle. EDS spectrum from the nano-sized precipitate within TiB_2 grain suggests higher Fe concentration. This observation is in accordance with EDS analysis carried out using SEM (Table 4.3) where 8.5 to 17 wt.% Fe is present in the acicular shaped TiB_2 particles.

A HR-TEM image of the nano-sized precipitate can be seen as Moire fringe pattern in Figure 4.29. Moire patterns are formed by the interfering two sets of lines/planes which have nearly common periodicities (103). Their appearance looks same even if the two crystals are not in contact. SAD pattern from the TiB_2 particle containing these Moire patterns is shown in Figure 4.30. Most of the reflections are from hexagonal TiB_2 along $[1\,\bar{1}\,0]$ direction. However, a series of fine reflection spots between two diffraction spots of TiB_2 are also observed. Such series of fine reflection spots are indicative of existing periodicity or a short-range order within the precipitate. Moire fringes along with SAD pattern confirm about the existence of metastable precipitate with high Fe concentration and a short-range order. It is most likely that Fe diffuses into TiB_2 particle replacing some of the Ti atoms to form a substitutional solid solution of type $(Ti, Fe)_a\ B_b$ with a short range order. This phase has possibly precipitated as nano-sized particles, which are shown as Moire fringes.

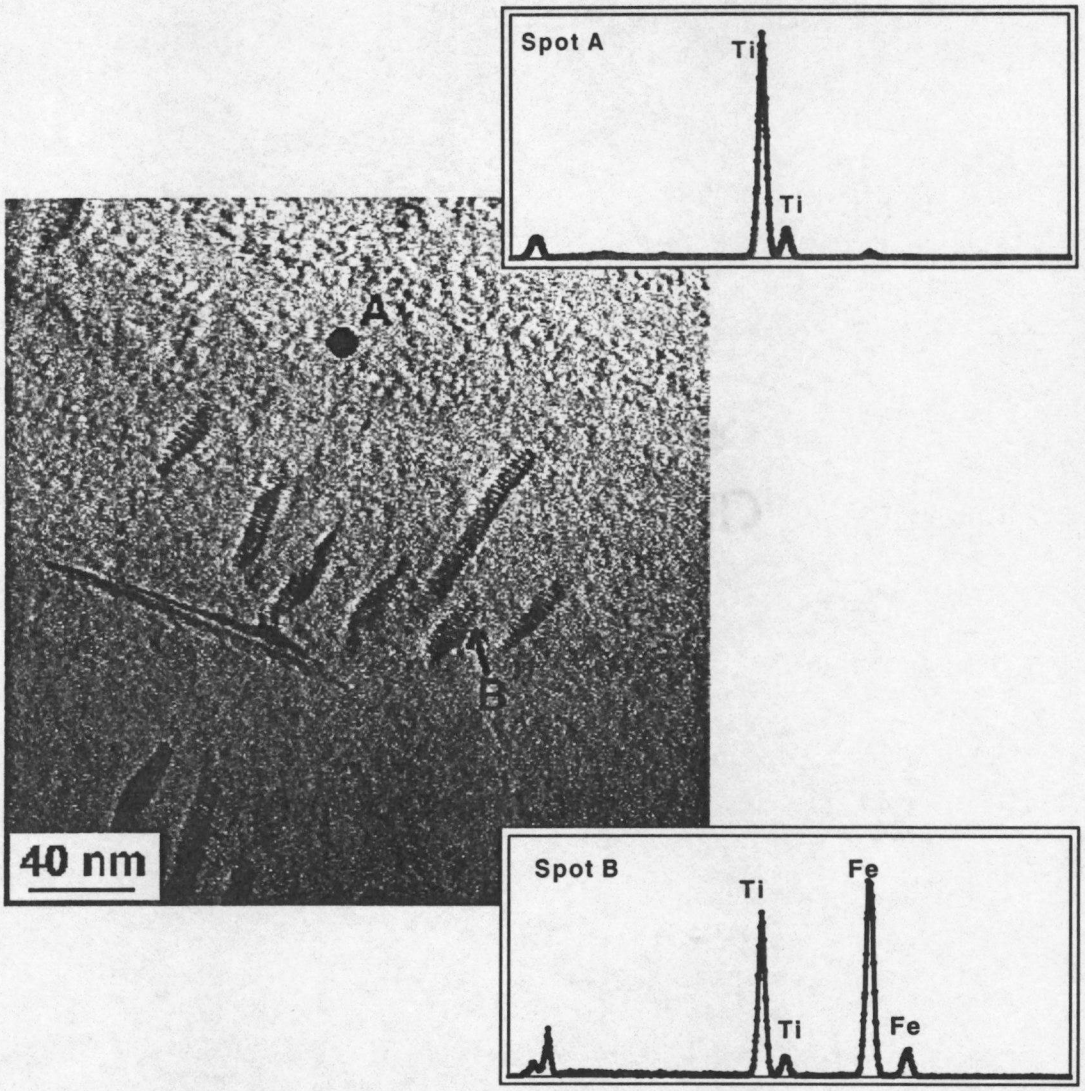


Figure 4.28. HR-TEM image of the nano-size precipitate as Moire fringes within a TiB_2 particle. EDS spectrum from these precipitate suggests high Fe concentration (spot B).

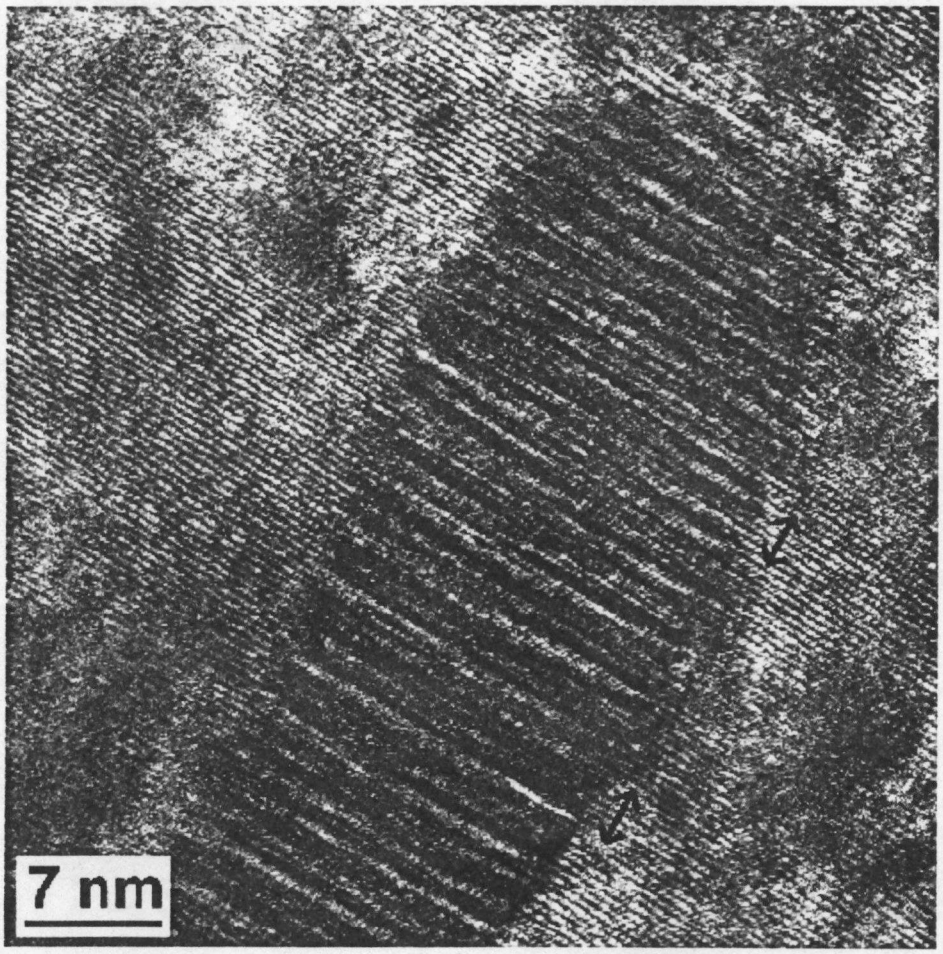


Figure 4.29. High magnification view of the nano-size precipitates (Moire fringes). Arrows indicate a periodicity between two sets of planes that cause formation of such fringes.

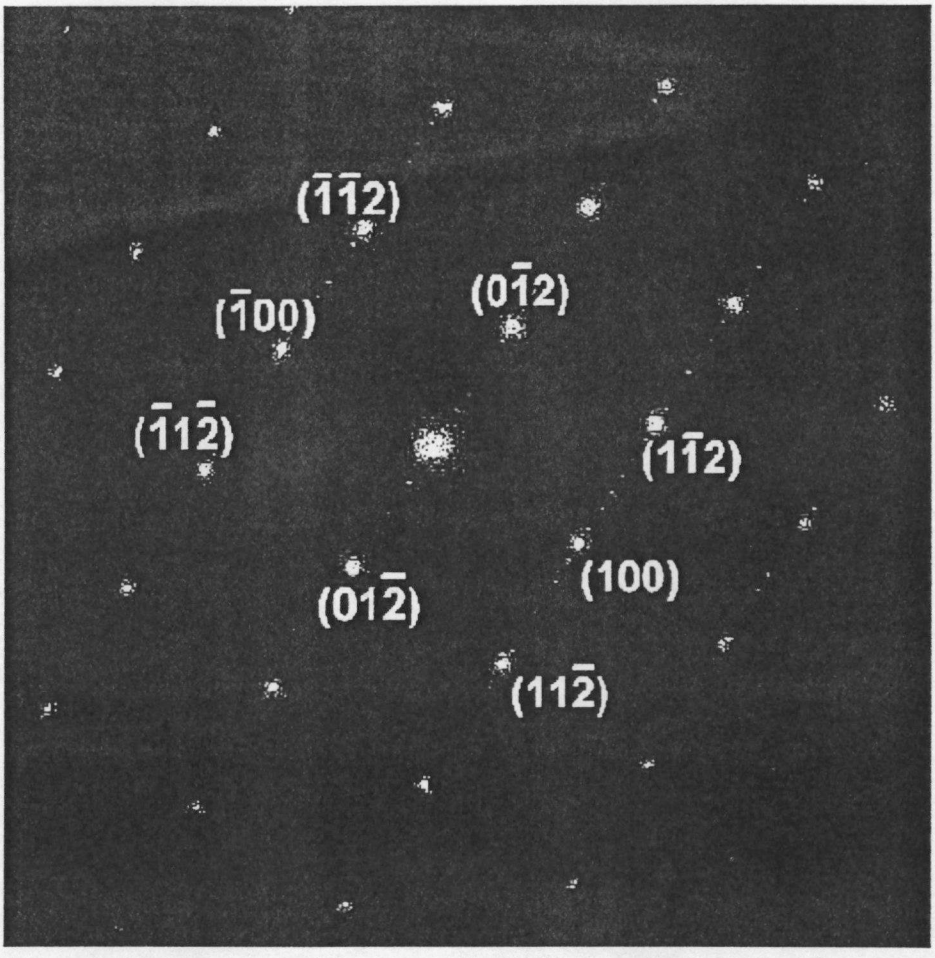


Figure 4.30. SAD pattern from the TiB_2 particle containing Moire fringes. The periodicity/short range order is revealed by the fine spots between the two successive larger reflections.

The reaction mechanism of the metastable phase formation can be understood in the following manner. It is assumed that some of the TiB_2 particle will melt due to high energy input during laser surface engineering process. However, molten TiB_2 will solidify first before the substrate material is completely resolidified. Therefore, the physical picture that emerges is that a solid state diffusion and compound formation processes may take place either from the liquid or from the resolidified Fe at the interface with TiB_2. It must be emphasized that at the melting temperature the vacancy concentration of a metal is expected to be at least one order of magnitude larger than that of a ceramic material (20). The Kirkendall effect requires a net flux of vacancies across the interface and this will alter local equilibrium concentrations and may influence the diffusion mechanism considerably. By these effects Ti and B could even diffuse into Fe and upon cooling become supersaturated solution which crystallizes as non-stoichiometric phases (20). Such effect is confirmed by the formation of non-stoichiometric phases such as $Fe_{2.12}B_{103.36}$ (Figure 4.7). The most striking difference in metal/ceramic interface formation compared to the classical diffusional bonding is the possibility of morphological instability and interface reactions leading to compound formation (20). Moreover, a sweeping uniform laser beam along the surface creates thermal cycles along the surface and the subsurface layers, and the process conducted under these conditions is no more isothermal (20). The classical diffusion equation becomes more complex with inclusion of time dependence of temperature. In laser melted structures the prediction of temperature cycle is, however, too complicated due to several parameters such as thermophysical properties (thermal conductivity, absorption coefficient, viscosity) of the material system, laser power and traverse speed, latent heat

due to melting, convection motion and the associated heat and mass flow. Hence, it is extremely difficult to predict the existing diffusion mechanism and all the possible reactions occurring in the materials processed using lasers.

From the detailed discussion about characterization of TiB_2 coated AISI 1010 steel surface, it can been concluded that TiB_2/Fe interface is sound and free from cracks at microscopic, chemical and atomic level. Such fact is supported by SEM observations, EDS analysis, TEM images and also validated by the high-resolution image of the TiB_2/Fe interface. Such atomic configuration minimizes the stresses at the interface and hence prevents crack initiation and propagation. Hence, TiB_2/Fe interface in the laser melt zone is sound and free from defects. However, it is essential further to characterize and verify such a sound TiB_2/Fe interface through its mechanical properties such as hardness, elastic modulus, interfacial strength and fracture toughness. Combination of structural and mechanical characterization of TiB_2/Fe interface is expected to demonstrate the effectiveness of the laser surface engineering (LSE) for ceramic coating on metal.

4.3 Mechanical Characterization

An exhaustive mechanical characterization of the "composite" TiB_2 coating has been done using a microhardness tester, nanoindenter, four-point flexure test and tensile test. There is no single technique, which could provide the mechanical properties of these coatings. These various techniques have been adopted to complement each other to provide a reasonable idea about the mechanical strength of the coating. A semi-

quantitative model has also been developed to predict the elastic modulus of the "composite" TiB_2 coating within a selected envelope of the laser processing parameters.

4.3.1 Microhardness Measurements

Table 4.5 lists the microhardness values (Knoop hardness) at different locations in the coating and substrate. Figure 4.31 include the SEM micrographs of the cross section with microhardness indentations within the laser melt zone, interface and the substrate.

Table 4.5. Microhardness Values at Various Locations in Coating and Substrate

Location of Microhardness Indentation	Microhardness Value (Knoop) at 300 gm Normal Load and 15 seconds loading time
Cluster of TiB_2 particles (Spot A in Figure 4.31a)	1742 ± 306
Mixture of (Fe +TiB_2) and TiB_2 particles (Spot D in Figure 4.31b)	622 ± 37
Interface of laser melt zone and steel substrate (Spot B in Figure 4.31a)	407 ± 21
Steel substrate (Spot C in Figure 4.31a)	140 ± 25

The smallest indentation (spot A) in Figure 4.31a suggests extremely high hardness values within the clustered zone of TiB_2 particles. This is evident from the fact that most of the indentation mark lies on TiB_2 particles, which have a very high hardness (56). In comparison, spot D in Figure 4.31b shows a lower hardness value (622 Knoop)

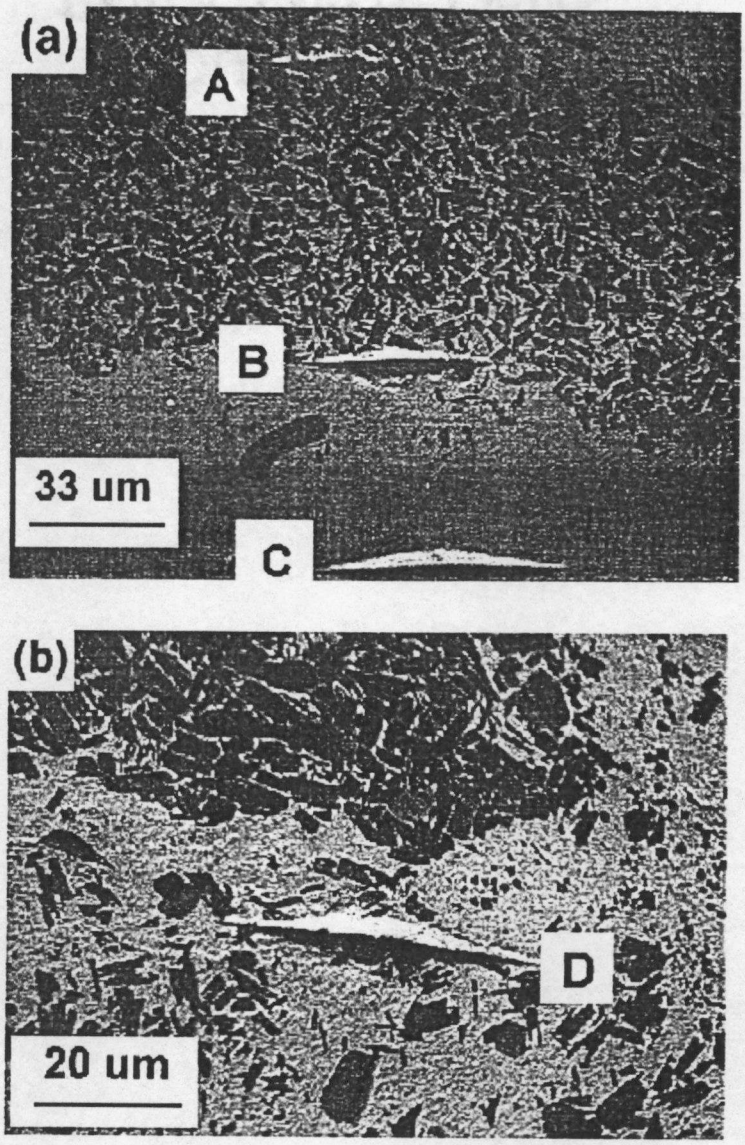


Fig 4. 31. SEM micrographs of the cross-section showing microhardness indentations on (a) cluster of TiB_2 particles, melt zone/substrate interface and the heat affected zone in the substrate and (b) mixture of Fe and TiB_2.

as indentation is placed on a mixture of Fe and TiB_2. This further, insinuates that some other phase(s) have formed that have hardness properties intermediate to that of pure TiB_2 and 1010 steel. It has been reported Fe_2B, FeB and TiB have hardness values lower than TiB_2 but higher than AISI 1010 steel (56,103). Thus, it is a reasonable assumption that phases like Fe_xB_y, Ti_mB_n or $(Fe,Ti)_aB_b$ may have hardness higher than steel but lower than TiB_2. Hence, an indentation mark of such a large size provides a combined average hardness value of the mixture of these phase(s). Nanoindentation studies have been conducted to determine the more precise hardness value of various microstructural features and phase(s). Results from such study are discussed in the following section 4.3.2.

Spot C illustrates the indentation on the AISI 1010 steel substrate away from the heat affected zone. The relative difference in the size of indentation provides an idea about the "soft" nature of AISI 1010 steel substrate. Spot B in Figure 4.31a shows the indentation at the interface. There is no delamination at the interface. Microhardness value at the laser melt zone/steel substrate interface provide a three fold higher hardness as compared to substrate. This is attributed to the lath shaped martensite at the interface.

4.3.2 Elastic Modulus Measurements using Nanoindentation

Nanoindentation is one such technique, which determines mechanical properties such as hardness, H and elastic modulus E of thin films and coatings by continuous measurement of force and displacement as an indentation is made (67-71). It offers several advantages over other hardness measurement tools. The greatest advantage of this technique stems from its ability to probe a surface and map its properties on a

spatially resolved basis with a resolution of better than 1 μm (69). Such small size of indentation allows exact measurement of mechanical properties of fine microstructural features such as ultra fine grains, precipitates and phases. This also enables estimation of mechanical properties of "composite" materials. Another advantage offered by nanoindentation technique is its ability to measure the surface properties independent of the nature of the substrate (68). Since the indentation depth is very small (nm), plastic deformation of substrate is avoided and only surface properties are measured. Table 4.6 presents the experimental results of elastic modulus (E) and hardness (H) for LSE 1, LSE 2 and LSE 3 samples as obtained from load-displacement curve of nanoindenter. The experimental values for E and H were obtained from the loading-unloading curves using the analytical technique developed by Oliver and Pharr (71). The values of the elastic modulus of the "composite" coating obtained by nanoindentation technique will further be used to compute the interfacial strength/energy of the coating/substrate interface.

Table 4.6. Experimental Elastic Modulus (E) and Hardness (H) Values as Obtained from the Load-Displacement Curves of Nanoindenter

Sample	Volume Fraction of TiB_2	Volume Fraction of Matrix*	Elastic Modulus of TiB_2 (GPa)	Elastic Modulus of Matrix* (GPa)	Hardness of TiB_2 (GPa)	Hardness of Matrix (GPa)
LSE 1	0.52	0.48	558.6	326.4	33.2	7.1
LSE 2	0.66	0.34	556.9	306.4	32.8	7.0
LSE 3	0.69	0.31	560.3	292.4	33.9	6.5

a) Volume fraction of TiB_2 has been computed using quantitative microscopy (64).
b) E and H values represent average value of twenty indentations in each sample.
c) * Matrix implies Fe rich matrix containing ultra-fine dissolved boride particles and traces of metastable phase(s) such as Fe_aB_b and Ti_mB_n.

Volume fraction of TiB_2 increases with the laser traverse speed (Table 4.2). As explained earlier in section 4.2, this is attributed to the lesser interaction time of laser beam at higher speed of 200 cm/min for LSE 3 sample. At lower speeds, interaction time of laser beam with TiB_2 particles is large which causes disintegration into fine particles and also depth of melt zone increases. Thus, at lower laser traverse speed, there are less number of discernible TiB_2 particles in a large melt volume and hence volume fraction is low. The variation in experimental E and H values of TiB_2 is insignificant. On the contrary, E and H values for matrix change with laser speed. This fact is again attributed to the degree of dissolution of TiB_2 particles and phase transformation, if any. Hardness value is highest for the LSE 1 sample due to a higher degree of disintegration of TiB_2 particles at lower laser traverse speed.

Figure 4.32 shows representative load-displacement curves for an indentation on TiB_2 particle in coating region, Fe matrix in coating region and unaffected AISI 1010 steel substrate, respectively in LSE 3 sample. Sample LSE 3 has been considered for discussion purpose as it has highest volume fraction (69 vol. %) of TiB_2 particles. All indentations were made to a depth of 300 nm. Although TiB_2 is brittle in nature, load-displacement response from ceramic particle does not show any signs of cracking (Figure 4.32 (a) and Figure 4.33). TiB_2 particles show high degree of elasticity and recovers 140 nm of displacement. Figure 4.32b shows load-displacement curve for Fe matrix in coating region. Matrix is highly plastic as compared to TiB_2 particle and recovers 58 nm of displacement. Figure 4.32c shows load displacement curve from unaffected AISI 1010 steel substrate. It is even more plastic in nature with an elastic recovery of mere 20 nm of displacement. Figure 4.32b and 4.32c differentiate between the mechanical properties of

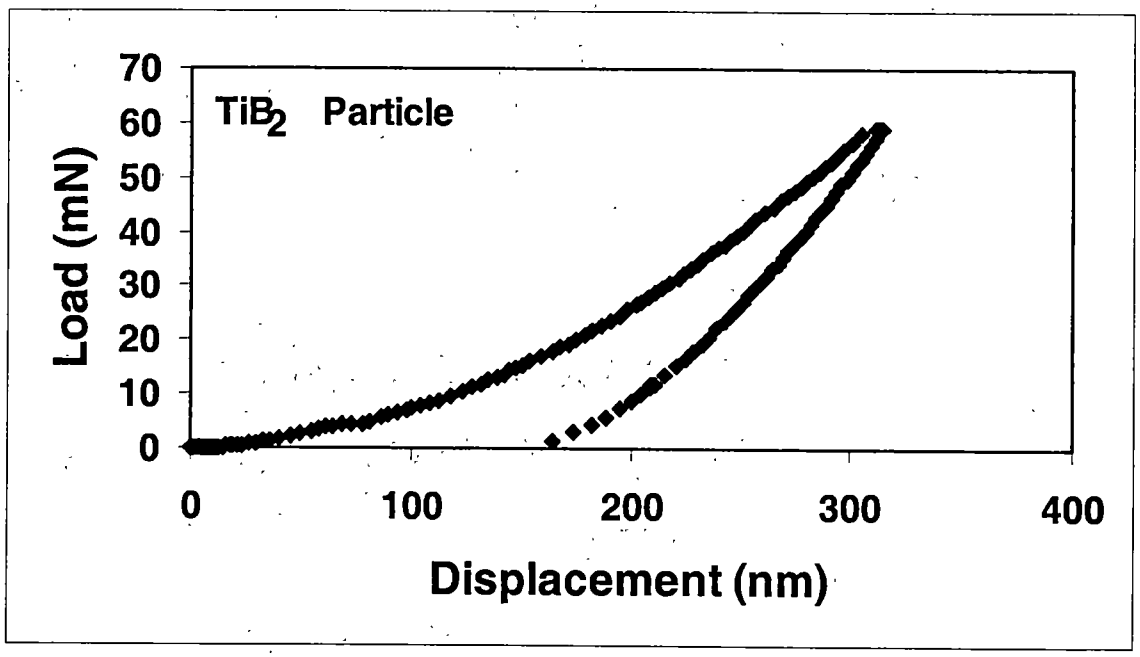


Figure 4.32(a). Load-displacement curve from the nanoindentation of TiB_2 particle in the "composite" coating zone.

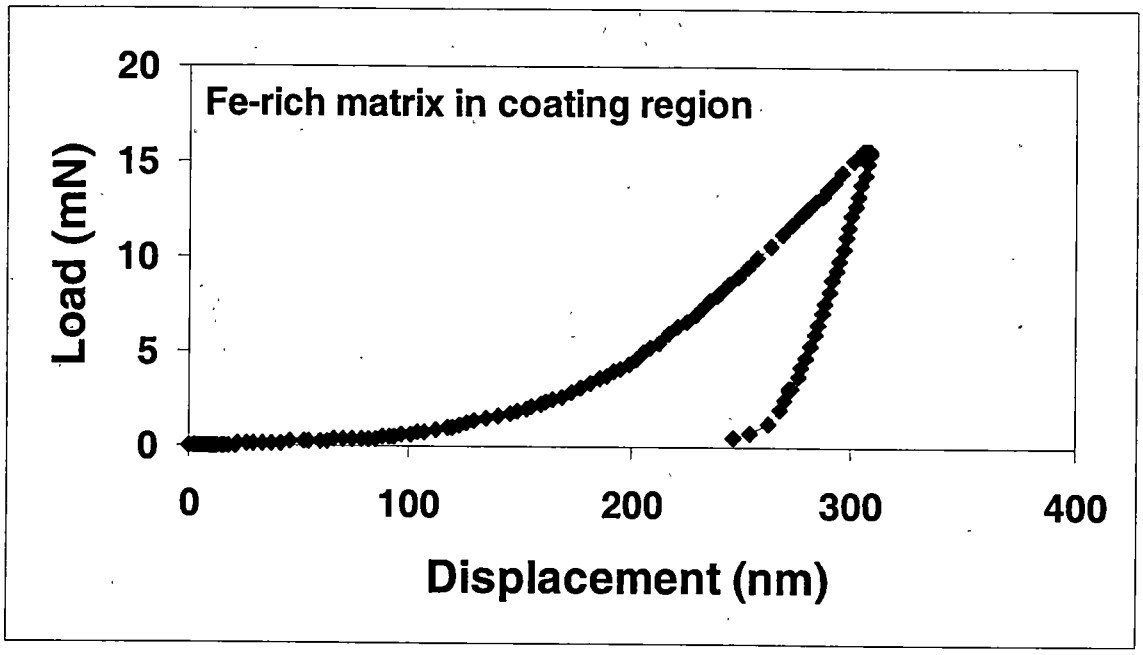


Figure 4.32 (b). Load-displacement curve from the nanoindentation of Fe-rich matrix region in the "composite" coating zone.

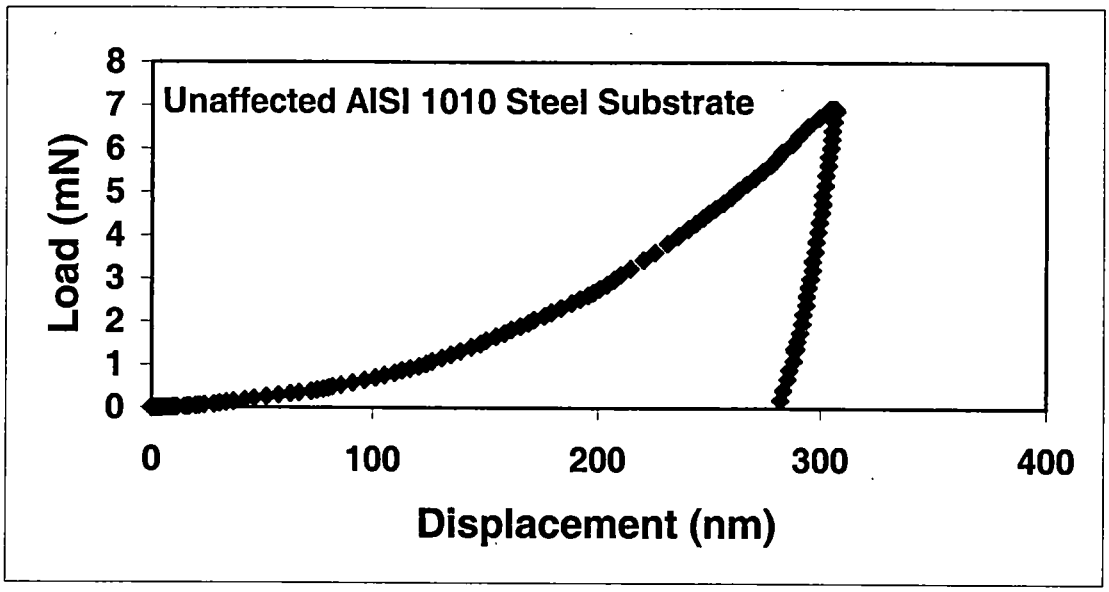


Figure 4.32 (c). Load-displacement curve from the nanoindentation of unaffected AISI 1010 steel substrate.

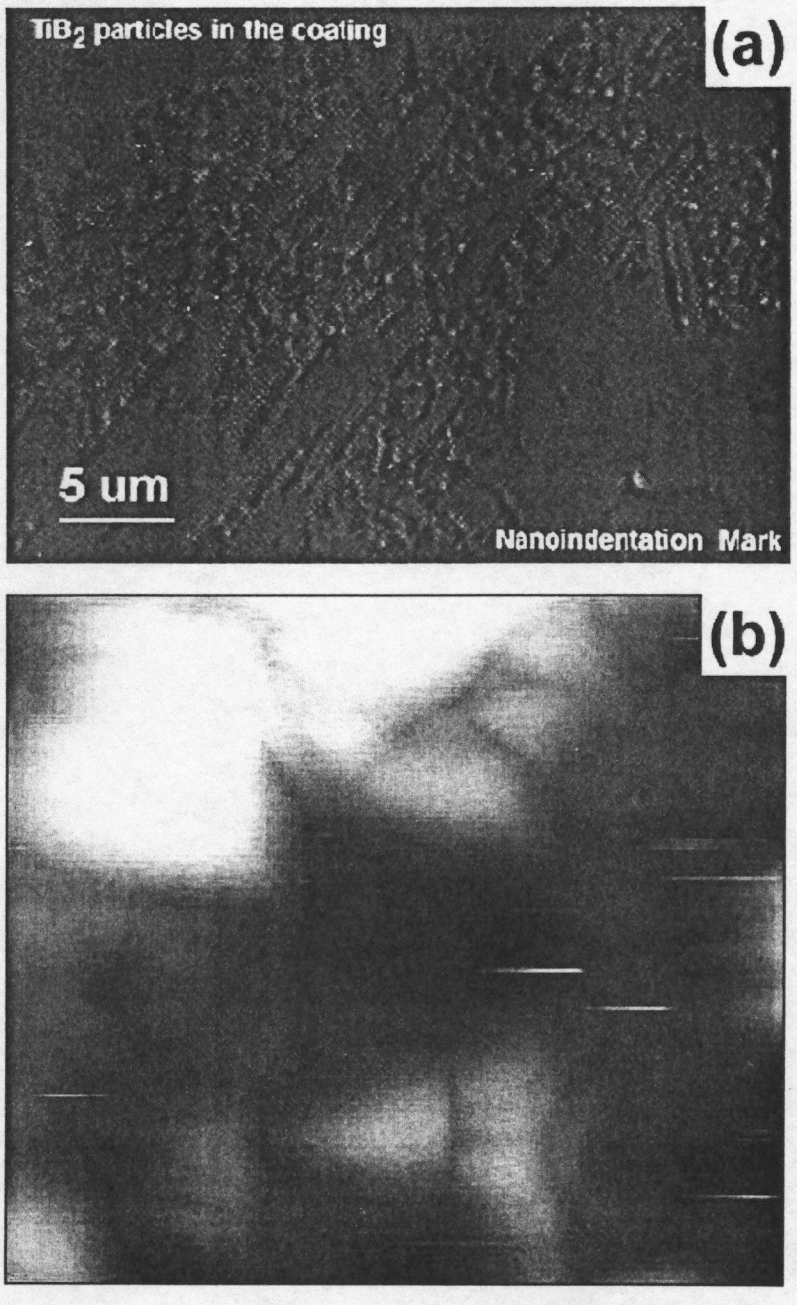


Figure 4.33. Nanoindentation marks on a cluster of TiB_2 particle: (a) low magnification view and (b) high magnification view. No crack is seen along the edges of indentation mark.

Fe (in unaffected steel substrate) and Fe matrix (in coating region) containing dissolved ultra-fine TiB_2 particles with traces of metastable phase(s) of type Fe_aB_b and Ti_mB_n. Hardness for Fe in unaffected substrate region is 2.7 GPa whereas it increases upto 6.5 GPa for Fe matrix in coating region. Elastic modulus, E for Fe (substrate) is 240 GPa and increases to 292.4 GPa for Fe matrix (in coating region). This further corroborates the fact that Fe matrix in coating region constitutes of dissolved TiB_2 particles and traces of metastable phase(s) apart from Fe. It is important to observe that Fe_aB_b phase have elastic modulus and hardness values of 305 GPa and 15 GPa, respectively, which are intermediate to mechanical properties of TiB_2 and unaffected 1010 steel (56). Table 4.7 lists the experimental and theoretical values of E and H for TiB_2, 1010 steel and Fe-rich matrix in the coating region (56,102). The values of the elastic modulus obtained from the each microstructural feature of the "composite" coating are employed to compute the overall elastic modulus of the "composite" coating. Elastic modulus of the "composite" coating will further be used to compute the interfacial strength/energy of the coating/substrate interface.

Table 4.7. Experimental and Theoretical Values of Mechanical Properties of TiB_2, Fe Matrix and AISI 1010 Steel Substrate

Location	Experimental E (GPa)	Theoretical E (GPa)	Experimental H (Gpa)	Theoretical H (GPa)
TiB_2 particle	560.3	551.5	33.9	33.1
Fe matrix (in coating region)	292.4	---	6.5	---
1010 steel	240	236.3	2.7	2.4

A. Elastic Modulus Computation for Composite Coating

Elastic modulus, E of the composite boride coating has been computed using rule of mixture (ROM) as shown by equation 4.11. The overall microstructure was "homogeneous" with uniform distribution of TiB_2 particles within the Fe-rich matrix (Figure 4.3). Such microstructural features suggest that rule of mixture (ROM) is a valid assumption to estimate the modulus of the "composite" coating (91). V_p and E_p represent volume fraction and elastic modulus of TiB_2 particles whereas V_m and E_m represents volume fraction and elastic modulus of Fe rich matrix in composite coating region.

$$E_{coating} = V_pE_p + V_mE_m \qquad (4.11)$$

Computations have been performed for various volume fractions (0.52, 0.66 and 0.69) of TiB_2 in the composite coating as the final volume fractions varied with the laser traverse speeds viz. 150, 175 and 200 cm/min. A comparison between theoretical and experimental E values has been made. For theoretical computations, it has been assumed that Fe rich matrix in composite coating region consists of only Fe from AISI 1010 steel substrate. On the contrary, for experimental computations, it was considered that Fe rich matrix in coating region consists of dissolved TiB_2 particles and traces of metastable phase(s) such as Fe_aB_b and Ti_mB_n. Tables 4.6 and 4.7 list all the experimental and theoretical values required for ROM computations. A comparison of E of the composite coating for various laser processing speeds (i.e volume fraction of TiB_2 particles) is shown in Figure 4.34 and Table 4.8. Experimental values (Table 4.6 and Figure 4.34) indicate that there exits a nonlinear relationship between laser traverse speed within the range considered in the present study and resulting volume fraction of TiB_2 particles in the "composite" coating.

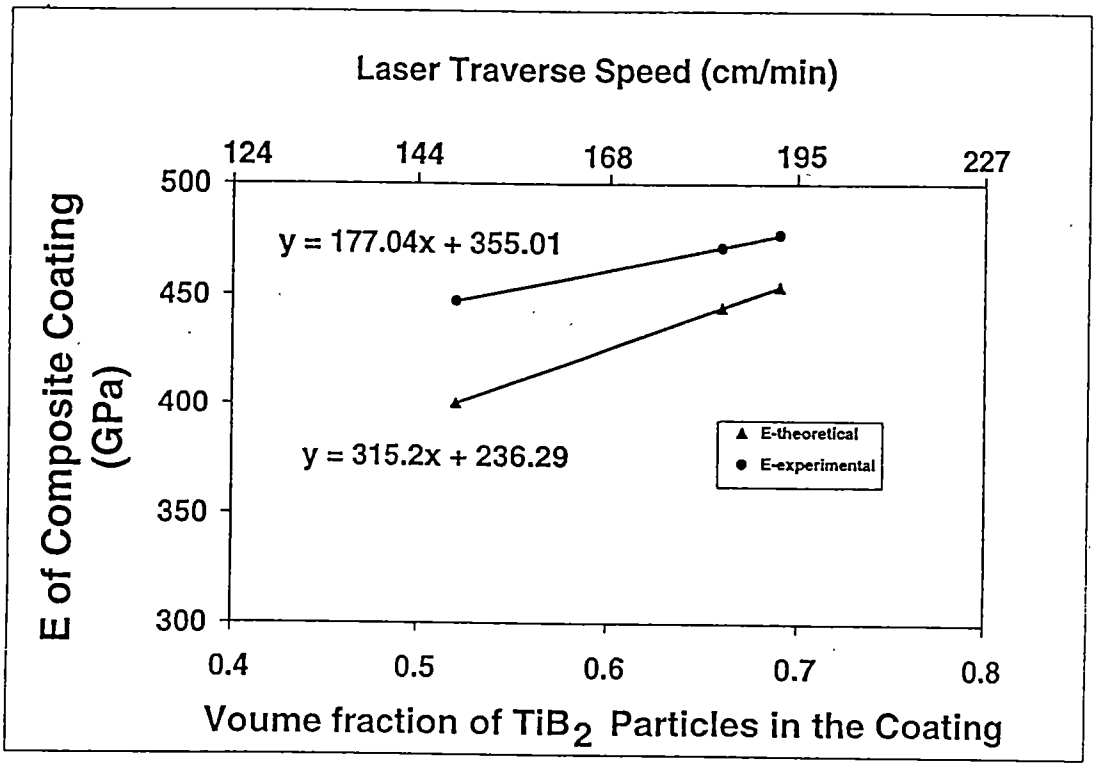


Figure 4.34. Theoretical and experimental elastic modulus of the "composite" boride coating for various laser traverse speeds.

Table 4.8. Theoretical and Experimental Elastic Modulus Values of Composite Boride Coating for Various Laser Processing Speed

Sample	Theoretical Elastic Modulus (GPa)	Experimental Elastic Modulus (GPa)
LSE 1	400.2	447.1
LSE 2	444.3	471.7
LSE 3	453.8	477.3

However, existence of this non-linear relationship is not a topic for the present study. Computed values of elastic modulus were higher than theoretical values for all the cases. This increased elastic modulus of the coating is attributed to the earlier observation that Fe-rich matrix in the coating region contains dissolved TiB_2 particles and traces of metastable phase(s). This is contrary to our assumption during theoretical computations where only Fe is present in matrix of "composite" coating. Regression analysis was performed on the experimental and theoretical results, which is shown by equation 4.12 and 4.13, respectively where $E^{C}_{coating}$ is the effective "computed" elastic modulus of the composite coating and $E^{T}_{coating}$ is the "theoretical" elastic modulus of the composite coating.

$$E^{C}_{coating} = 177.04\, V_p + 355.01 \qquad (4.12)$$

$$E^{T}_{coating} = 315.21\, V_p + 236.29 \qquad (4.13)$$

From equation 4.12, it can be evaluated that $E^C_{coating}$ is same as E^C_{matrix} for V_p equal to zero. Hence, E^C_{matrix} is 355.01 GPa, which is 1.5 times higher than theoretical E value, 236.3 GPa of AISI 1010 steel (Table 4.7). This pronounced effect on elastic modulus of coating is due to laser processing which causes dissolution of TiB_2 into Fe matrix and formation of metastable phase(s).

TEM investigations discussed in the earlier section (4.2) further confirms the presence of dissolved boride particles in Fe-rich matrix, reactivity between Fe and TiB_2, and formation of metastable phase(s). Some of the salient features of TEM investigations related to nanoindentation analysis are being briefly discussed again. The "composite" nature of boride coating where TiB_2 particles of various shapes and sizes are embedded in Fe matrix has been confirmed by TEM images in Figure 4.8 to 4.10. The presence of ultra-fine dissolved boride particles within fine Fe dendrites has been shown in Figure 4.12. EDS spectrum corresponding to spot A on dendrites show Fe peaks whereas spot B between dendrites reveals Fe and Ti peaks. Ti peaks are indicative of dissolved boride particles within Fe dendrites. This fact is further corroborated by diffraction pattern of the same area as shown in Figure 4.13. Diffraction pattern is a combination of hexagonal structure of TiB_2 along [0001] direction and BCC structure of Fe along $[\bar{1}\,11]$ direction. Such evidence confirms the presence of dissolved boride particles within Fe rich matrix that causes an increase in hardness and modulus of the matrix. The reactivity between Fe and TiB_2 particle and the nucleation of metastable phase(s) of type Fe_aB_b and Ti_aB_b and $(Fe,Ti)_xB_y$ has already been discussed in great detail in earlier sections of TEM analysis.

Even though the "composite" nature of the laser engineered TiB_2 coating provided a coating of sound interface with enhanced mechanical properties (hardness and elastic modulus), it will be highly functional only if the interface between the coating and the substrate is sound and strong. The following section, therefore, deals with the evaluation of the coating/substrate interface for its mechanical properties.

4.3.3 Interfacial Strength Evaluation by Four Point Bend Test

The theory behind four-point bend test is based on the assumptions made in linear elastic fracture mechanics (LEFM). It should be observed that two major assumptions are made for four-point bend test. Firstly, it is assumed that "mixed" mode of fracture prevails as the sample undergoes bending as well as tension. Also, plain strain conditions are assumed due to fixed ends of the sample during four-point bend test. The relevant physical quantities obtained using four-point bend method are critical elastic energy release rate, G_c and the critical stress intensity factor, K_c for the "composite" coating/metal interface. The elastic energy release rate is obtained by equating the elastic energy released on crack growth to the energy required for the crack to propagate. For a plate of unit thickness the condition for crack growth becomes (28):

$$G = \frac{d}{da}(Q-U) \geq \frac{dW}{da} = R \qquad (4.14)$$

where U is the elastic energy contained in the plate, Q is the work performed by the external force and W is the energy for crack formation i.e. surface free energy for brittle fracture. R is the crack resistance force and a represents crack length. If G becomes larger than R the crack will propagate. As failure of the material occurs by growth of

cracks the stress state at the crack tip is most important parameter rather than the far field applied stress. The stress σ_{yy} at the crack tip (on a crack plane y = 0) is characterized by the stress intensity factor K and failure under σ_f, failure stress occurs when K reaches a critical value. The critical energy release rate for bimaterial interfaces (i.e. coating-substrate system) can be expressed as equation 4.15 (28,104):

$$G_c = \frac{2\left(\frac{1-\upsilon_1}{\mu_1} + \frac{1-\upsilon_2}{\mu_2}\right)}{4\cosh^2(\pi\varepsilon)} K\bar{K} \qquad (4.15)$$

where μ_1 and μ_2 represents the shear modulus coating and substrate respectively, ν_1 and ν_2 are the corresponding Poisson's ratio. ε is known as bimaterial constant and K is complex because of mixed mode of fracture (104-105). Bimaterial constant, ε is computed as per following equations (105):

$$\varepsilon = \frac{1}{2\pi}\ln\left(\frac{1-\beta}{1+\beta}\right) \qquad (4.16)$$

where β (for plane strain condition) is defined as the measure of mismatch in the in-plane bulk modulus. It is given by equation 4.17

$$\beta = \frac{1}{2}\frac{\mu_1(1-2\upsilon_2) - \mu_2(1-2\upsilon_1)}{\mu_1(1-\upsilon_2) + \mu_2(1-\upsilon_1)} \qquad (4.17)$$

Table 4.9 lists theoretical and computed material properties (shear modulus and material constants such as ε and β) for TiB_2-Fe material system. These values have been computed using elastic modulus data obtained from nanoindentation and equations 4.16 and 4.17. The theoretical values of material properties for TiB_2 and AISI 1010 steel are taken from reference handbooks (56,102). Poisson's ratio for the "composite" coating has

been computed using rule of mixture (ROM) for LSE 3 sample (volume fraction of TiB_2 particles is 0.69). Poisson's ratio for TiB_2 and AISI 1010 steel is 0.11 and 0.33 respectively. Hence, Poisson's ratio for composite coating in LSE 3 sample is 0.18.

Table 4.9. List of Theoretical and Computed Material properties for TiB_2 coating/Steel Substrate System (LSE 3 sample)

Material Property/Constant	Theoretical Value	Computational Value
Elastic Modulus, E^* (GPa)	453.8	477.3
Shear Modulus, $\mu^{\#}$ (GPa)	192.3	202.2
Mismatch Constant, $\beta^!$	0.0185	0.0258
Bimaterial Constant, $\varepsilon^{\otimes}$	-0.0058	-0.0082

* These values have been taken from nanoindentaion data from Table 4.8

\# Shear modulus, μ has been computed using following equation: $\mu = \frac{E}{2(1+\upsilon)}$ where ν is the Poisson's ratio of the "composite" coating.

! Mismatch Constant, β has been computed using equation 4.17.

$\otimes$ Bimaterial Constant, ε has been computed using equation 4.16.

Cracks in the "composite" TiB_2 coating are oriented vertically through the entire coating thickness and as a consequence do not cause delamination of the coating. Figure 4.35 shows a cross sectional view of such sample. No crack has initiated from the precrack/notch that was created using a diamond saw (Figure 4.35a). However, precrack has blunted and broadened suggesting some plastic deformation. The vertical cracks are formed in the entire coating with 800-1000 μm spacing between two successive cracks

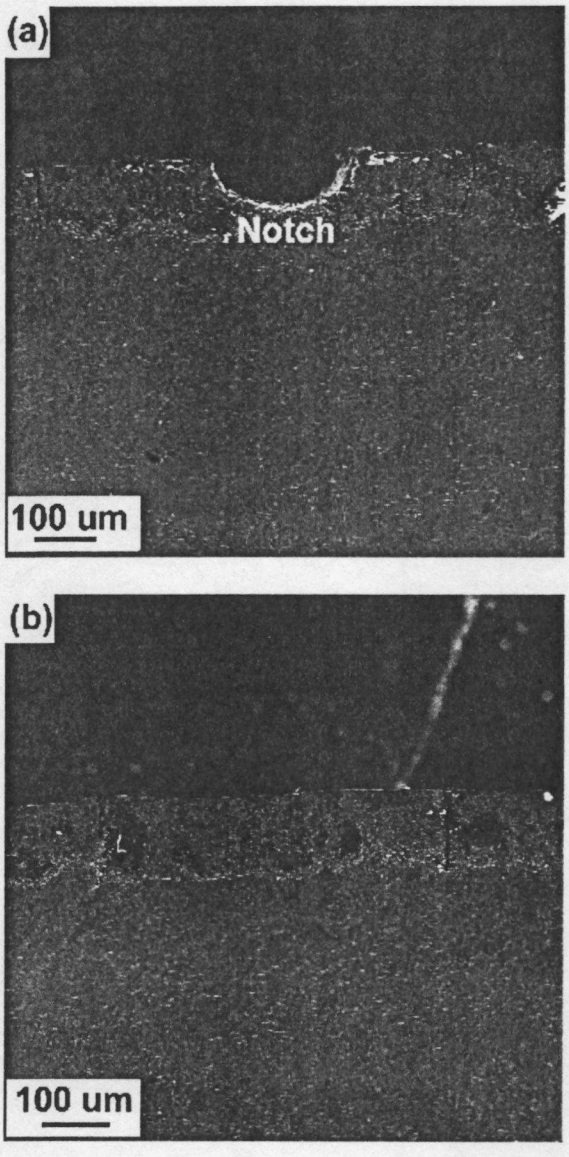


Figure 4.35. SEM micrographs of the cross section of the four-point bend test samples: (a) blunted precrack/notch suggesting plastic deformation and (b) vertical cracks throughout the coating thickness.

(Figure 4.35 b). Much of the crack propagates through brittle ceramic particle (TiB_2) rich region suggesting that crack energy was not dissipated fully leading to crack run all the way through coating and is deflected and blunted when they reach the substrate (Figure 4.36). The crack runs vertically through the regions of TiB_2 particles with a small deflection at certain places. This small deflection of the crack in the "composite" coating zone can be attributed to the interparticle region containing Fe-rich matrix. These cracks are opened by the plastic deformation in a very small zone.

As stated earlier, it should be noted that four-point tests were performed only for LSE 3 samples that were processed at the highest laser traverse speed. Also, LSE 3 sample contains the highest volume fraction (0.69) of TiB_2 particles. The critical load was determined when the crack reached the coating-substrate interface. Such observation was made when there was a small drop in the load. Moreover, microscopic observation at this stage also confirmed about the crack reaching coating-substrate interface. The critical bending moment, M corresponding to the delamination load was computed using equation 3.7 and was found to be 231 N/m. Critical energy release rate has been computed using equation 3.8 as shown below.

$$G_c = \frac{18M_c^{\,2}(1-\upsilon_2^2)^2 E_1}{(1-\upsilon_1^2)E_2^2}\frac{h_1}{h^4} \qquad (3.8)$$

It should be emphasized here that prefix 1 denotes composite TiB_2 coating and prefix 2 stands for AISI 1010 steel substrate. The various parameters needed to compute the critical strain energy release rate are Poisson's ratio (υ) of the coating and the substrate, elastic modulus (E) of the coating and the substrate apart from coating thickness (h_1), overall sample thickness (h) and critical bending moment (M_c). E for the

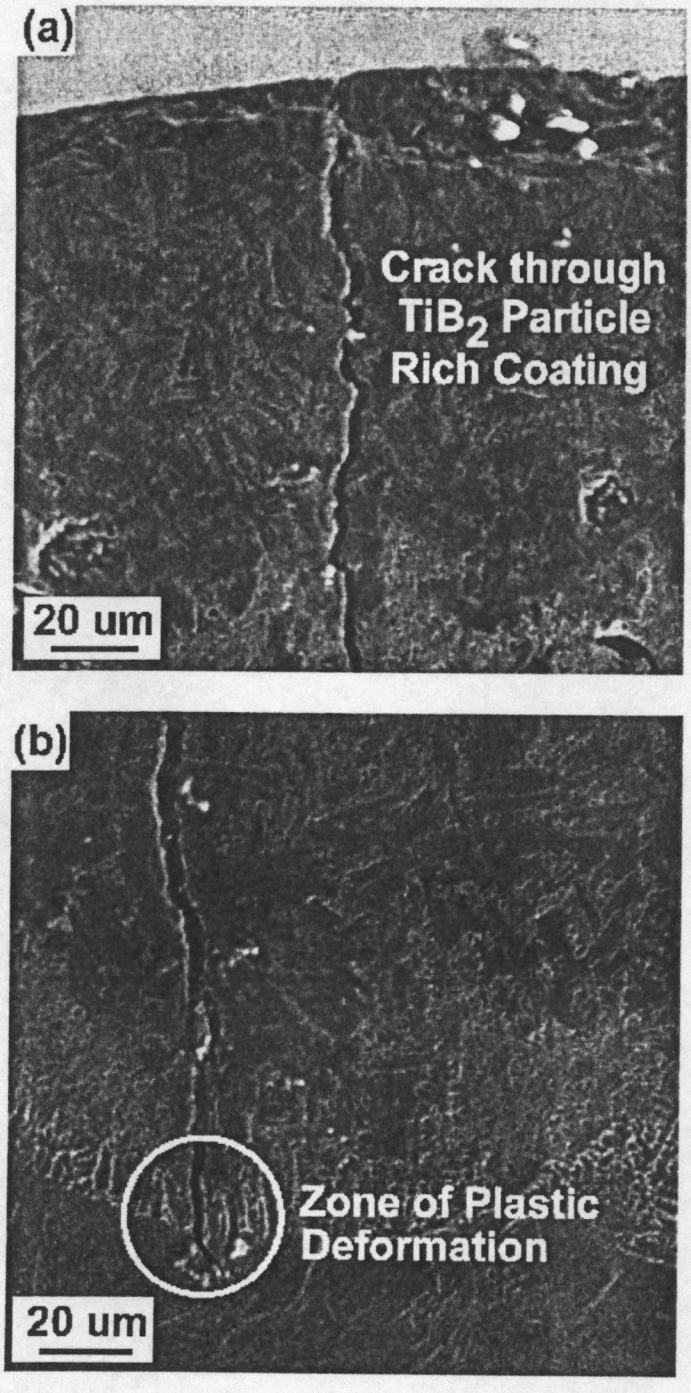


Figure 4.36. SEM micrographs of the cross-section of four-point bend samples showing (a) crack propagation through brittle TiB_2 particles and (b) crack blunting at the coating/substrate interface due to localized plastic deformation of the substrate.

coating has been obtained from the nanoindentaion data (Table 4.8) whereas Poisson's ratio for the composite coating has been computed using rule of mixtures (ROM) similar to equation 4.11. Coating thickness is 200 μm and the total thickness of the four-point bend sample is 1.5 mm. It should be recalled that theoretical as well as computed value of elastic modulus of the coating were determined in section 4.3.2 (Table 4.8) for LSE 3 sample. Theoretical and experimental values of critical energy release rate G_c has been computed using these parameters.

$$G_c^{\text{theoretical}} = 251 \text{ J/m}^2$$

$$G_c^{\text{experimental}} = 265 \text{ J/m}^2$$

The stress intensity factor characterizing the bimaterial interface is obtained from equation 4.15. All the parameters needed to compute stress intensity factor are listed in Table 4.9.

$$|K_c|^{\text{theoretical}} = 6.55 \text{ MPa m}^{1/2}$$

$$|K_c|^{\text{experimental}} = 6.63 \text{ MPa m}^{1/2}$$

It should be noted that the energy release rate for a perfectly brittle cleavage fracture is approximately 5 J/m^2 whereas the fracture energy for ductile steel is of the order of 300 J/m^2 (25). Critical energy release rate in our case is found to be very high suggesting a "composite" kind of strong interface. A similar behavior has been observed in an earlier study based on the laser-processed ceramic (Cr_2O_3) coating on steel substrate where critical energy rate of 270 J/m^2 and stress intensity factor of 8.5 MPa m$^{1/2}$ produced a very strong and adherent interface (28). Fracture toughness of the "composite" TiB_2 coating is nearly 6.5 MPa m$^{0.5}$, which is higher than the literature value (4-5 MPa m$^{1/2}$) of

monolitihic TiB_2 (56). An increase in the fracture toughness is attributed to the "composite" nature of the coating. It should be emphasized that the computed value of fracture toughness holds true for mixed mode of fracture whereas literature values are quoted for mode one failure. However, this is the nearest possible comparison between two values of fracture toughness, in lack of available data for such material systems.

Several researchers have tried to investigate the correlation between W_a, work of adhesion and fracture energy, G_c for ceramic metal interface (26). Table 4.10 summarizes the comparison between the work of adhesion and fracture energy for various ceramic/metal interfaces, which form a reaction product at the interface (26). A large discrepancy exists between the work of adhesion and the fracture energy, which is typically > 50 W_a (26). Similar behavior is seen for TiB_2/Fe interface in Table 4.10. The experimental values obtained for fracture energy, G_c (265 J/m^2) is nearly 90 times greater than W_a (2.85 J/m^2). Such differences are attributed to the nonplanarity of the interface at the atomic level and the possible plastic deformation within the bond layer (26). This nonplanarity causes surface roughness at the interface, which locally absorb stresses and results in higher value of fracture energy.

Four-point bend test appears to be an appropriate method to test the interfacial properties of bimaterials. The advantage of the four-point bend test lies in the independence of the method of microcracks present in the ceramic coating (25,28). However, there are few limitations to this test as well. Such a high-energy release rate is accounted by two additional factors other than the energy released by the coating viz. residual tensile stresses in the coating and plastic deformation/yielding of the substrate (25,28,106).

Table 4.10. Work of Adhesion (W_a) and Fracture Energy (G_c) of Metal/Ceramic Interfaces

Material System	Work of Adhesion, W_a (J/m^2)	Fracture Energy, G_c (J/m^2)
Nb/Al_2O_3	0.8	----
Au/Al_2O_3	0.5	----
Ni/Al_2O_3	0.2 -0.8	0-60
Cu/Al_2O_3	0.4-0.7	0-45
Fe/TiB_2	2.85	265

The thermal loading by the laser beam causes stresses to build up in the coating. Thermal strains are produced within the coating which affect the strain energy release rate. Thermal strain energy caused by laser processing is of the order of 30-40 J/m^2 in 100 μm thick Cr_2O_3/Fe interface (28). Thermal strain energy is a function of material properties, laser processing variables and is affected by the localized temperature fluctuations. Computation of the thermal strain energy involves a lot of tedious experimentation and computations, which was not the objective of the present study.

Another factor that could cause an increase in energy release rate is the plastic deformation and work hardening of the ductile substrate material (28). Since the laser produced interface is very strong and failure does not occur by delamination of the coating, crack propagates through the entire thickness of the coating and produces a localized work hardening/plastic deformation at the crack tip in the substrate zone (Figure

4.36b). For an accurate measurement of elastic energy release rate, these two factors should be accounted. But in lack of such accuracy and a suitable technique to determine the interfacial energy, four-point bend test is the most reliable available test to provide an indication of the quality of the interface in bimaterials.

In the real world, coatings are exposed to various external stresses that might cause damage. In particular, cracks are developed by the tensile stresses, which significantly deteriorate the coating property. Four-point bend tests have already been conducted to evaluate the response of coating under such tensile stresses. Uniaxial tensile stresses are another class of stress experienced by many material systems. Even though uniaxial tensile testing is not so common for the coatings, recently researchers have stressed to carry out uniaxial tensile test for ceramic coating (107-109). Hence, it was thought to investigate the deformation behavior of the composite TiB_2 coating under uniaxial tensile test. However, it should also be emphasized here that uniaxial tensile test of coating is not as significant as four-point bend test because it does not provide detailed and quantitative information about the coating/substrate interface, as obtained earlier in this section.

4.3.4 Deformation Behavior of Composite Coating under Uniaxial Tensile Test

The main aim of the uniaxial tensile test was to investigate the fracture response and morphology of the "composite" coating under uniaxial tensile stresses. The tensile test samples were made out of LSE 3 samples and had dimensions of 50 mm x 5mm x 0.3 mm. First, it was thought to carry out the tensile test of the coating material itself (200 μm thick), however, such samples were very fragile for uniaxial tensile testing. Hence,

total thickness of the tensile sample was maintained at 300 μm, which constituted of 200 μm thick coating and 100 μm thick substrate.

Figure 4.37 shows a stress-strain curve of the "composite" coating under uniaxial tensile stress. The curve shows a typical stress-strain curve obtained for a composite material. At a stress of 50 MPa, there is a change in the slope of the curve for a short while and it further increases suggesting load transfer from soft Fe matrix to high strength TiB_2 particles. The failure of the coating occurs at a stress of 282 MPa. It should be observed that failure of the "composite" coating is not catastrophic, which is a general response of the ceramic materials loaded under uniaxial tension (110). The several kinks obtained after the failure of the coating suggests load transfer from brittle TiB_2 particles to the softer Fe-rich matrix. The stress-strain curve does not show a completely graceful failure as obtained in fiber reinforced composites (110). Such behavior could be attributed to a very high volume fraction (0.69) of TiB_2 particles (ceramic) in the "composite" coating. Elastic modulus of the coating was computed from the slope of the stress-strain curve (till the fracture stress of 282 MPa). It was found to be 355.7 GPa, which is far, less than value of 477.3 GPa as obtained by nanoindentaion technique for LSE 3 sample. Such difference in the values of elastic modulus is attributed to the presence of 100 μm thick steel substrate in the tensile samples. AISI 1010 steel is very ductile and has a elastic modulus of 236.3 GPa (102). During the uniaxial tensile test, ductile steel substrate is also deformed resulting in the reduction of the elastic modulus of the "composite" coating. It is emphasized here that nanoindentation is a more realistic technique to measure elastic modulus of the coating, as it measures only surface properties and is not affected by the substrate properties.

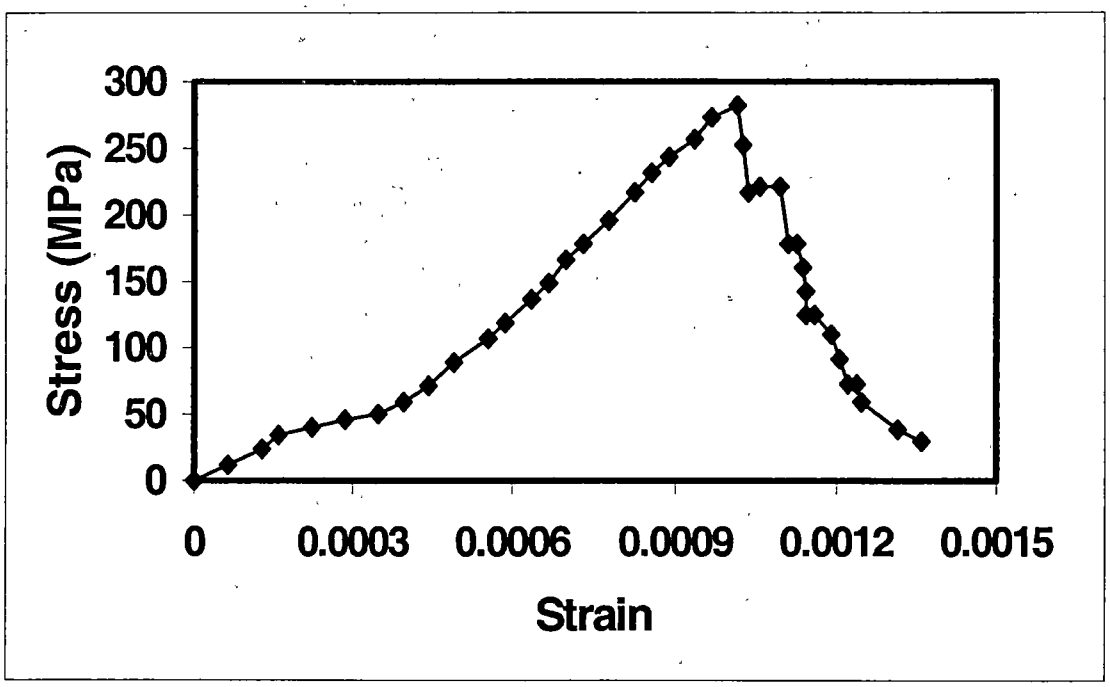


Figure 4.37. Stress-Strain curve showing deformation behavior of "composite" TiB_2 coating under uniaxial tensile stress.

Table 4.11 provides a comparison among the fracture stress values for various ceramic/metal systems under uniaxial test. In lack of standard test system, coating morphology and other material parameters, this comparison does not provide clear insight about the response of coatings under uniaxial test. However, it can be considered as a yardstick for the first approximation of failure stresses for various ceramic/metal systems. From Table 4.11, it can be inferred that for thick coatings (thickness >100 μm), "composite" TiB_2 coating fails at a reasonably high fracture stress, suggesting a stronger coating.

Table 4.11. Failure Stress for Various Ceramic Coating/Metal Substrate Under Uniaxial Tensile Stresses

Material System	Coating Method	Coating Thickness (μm)	Failure Stress (MPa)	Reference
Glass/Cu	Screen printing	100	35-50	(80)
TiN/304 steel	Arc-ion plating	6.5	350-400	(107)
Ni-P/1010 steel	Electroless	10	225-325	(108)
8 % Y_2O_3-ZrO_2	Plasma spray	250	150	(109)
TiB_2/1010 steel	LSE	200	282	Present Work

Fracture surfaces were observed in scanning electron microscope to understand the fracture morphology. Figure 4.38 is a low magnification view of the fractured surface. Coating/substrate interface is very strong and there is no sign of delamination. The strength of coating/substrate interface has already been evaluated using four-point

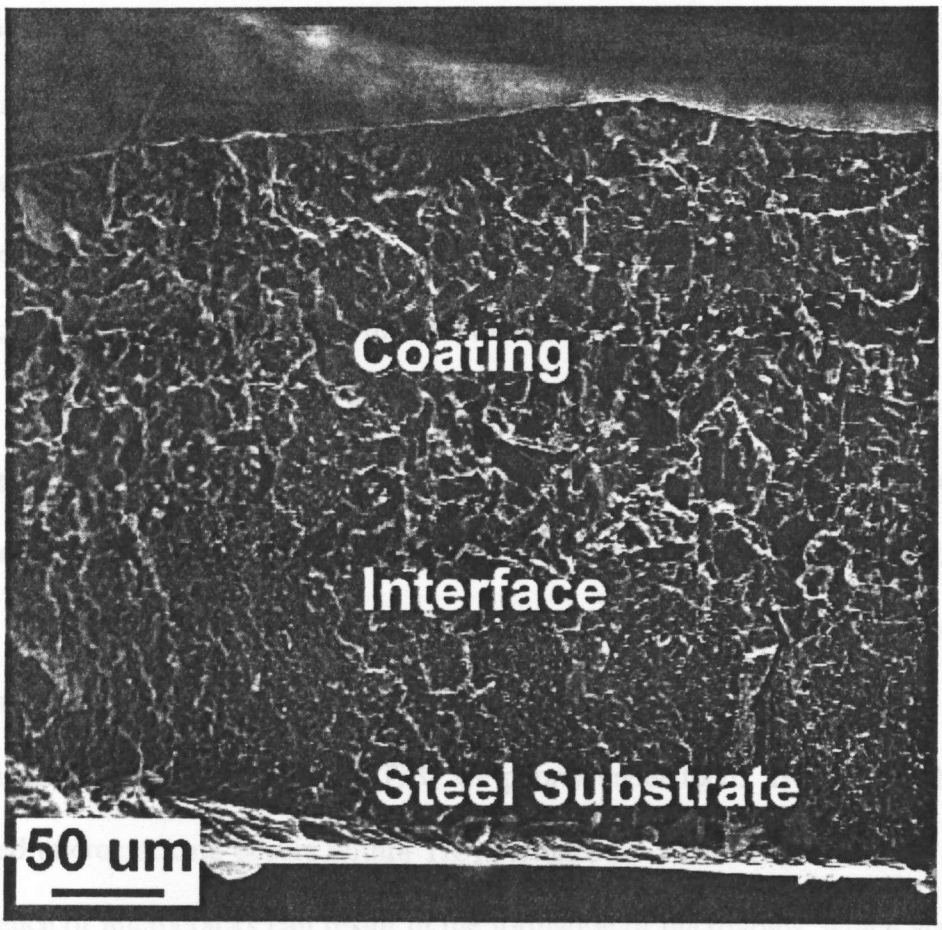


Figure 4.38. Low magnification view of the SEM micrograph showing overall fracture morphology of the composite TiB_2 coating under uniaxial tensile stresses.

bend test and has been discussed exhaustively in section 4.3.3. A high magnification view of the fracture surface of the composite coating is shown in Figure 4.39. Fracture occurs by mixed mode but is dominated by brittle fracture. The fracture in TiB_2 particles is essentially brittle and occurs by cleavage. Such phenomenon is evident from the faceted and cracked TiB_2 particles. Fe-rich matrix acts as a bridge/binder between these TiB_2 particles (marked by arrow). Fe is very soft and ductile as compared to TiB_2. The interlinking Fe bridges tend to fail in a ductile manner. But these bridge zones are very small in size and volume fraction and hence they are not able to support the load when cracking of TiB_2 occurs. The small kinks observed in the stress-strain curve are formed when these small zones of Fe tend to support the load but are not able to do it for longer periods. An additional feature observed in the fractured surface of some TiB_2 particles is the presence of few microvoids (marked by arrow). The details of the fracture mechanism occurring in monolithic TiB_2 are poorly understood. However, it has been concluded microcracking occurs within TiB_2 particles for a critical grain size (111-112). Coalescence of microcracks can result in the formation of microvoids, which are seen in some of the TiB_2 particles. The effects of microcracking on the mechanical properties of ceramic materials is highly debatable due to multiple and simultaneous deformation mechanisms operative in ceramic systems (56). However, based on a variety of mechanical characterization techniques, it can be deduced that ultrahard "composite" TiB_2 coating with a strong and adherent coating/substrate interface can be applied using laser surface engineering technique.

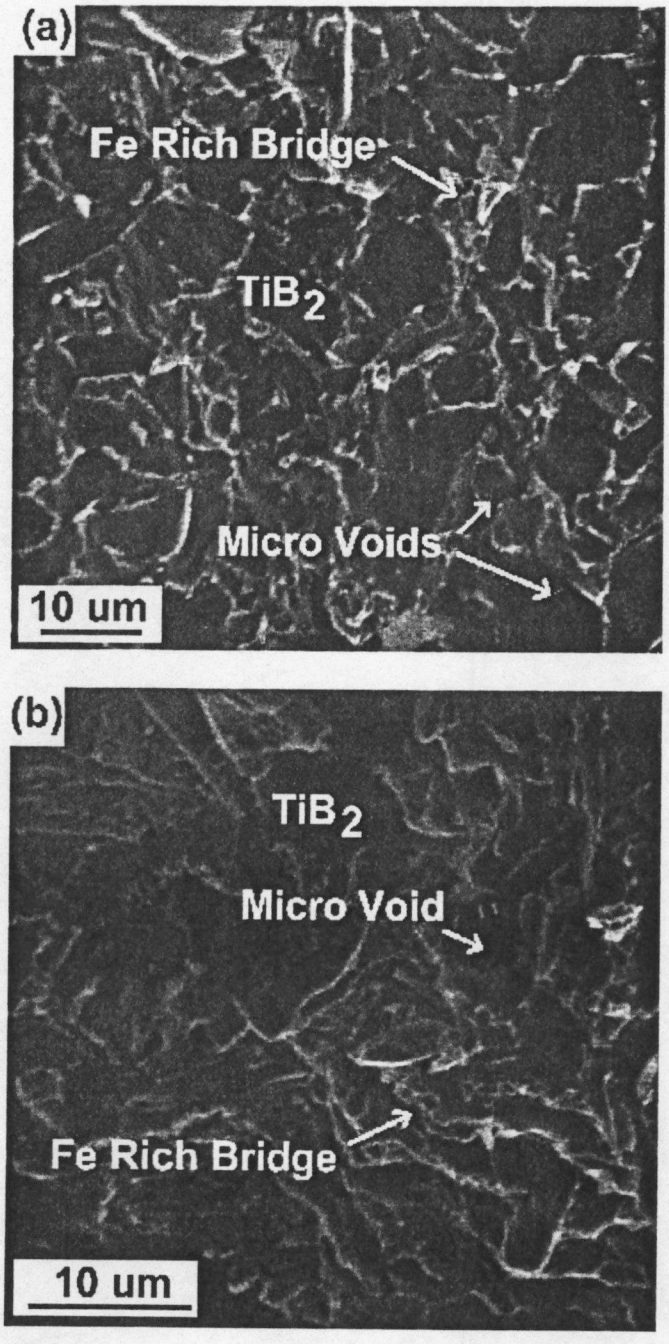


Figure 4.39. High magnification views of the fracture morphology showing mixed mode of fracture occurring in "composite" TiB_2 coating.

Such enhanced mechanical properties of "composite" TiB_2 coating synthesized using laser based technique is expected to perform in superior manner for wear applications. The most important application of ultrahard TiB_2 coating seems to be wear-resistant coating for various machine tools and parts. Hence, it was necessary to study the tribological characteristics (wear and friction) of such coating.

4.4 Tribological Characterization of the Composite TiB_2 Coating

Tribological properties of the ceramic coatings depend upon several factors such as hardness and thickness of the coating, coating material, type of the substrate, operating conditions and coating process. Based on these variables, several wear mechanisms have been proposed for different coating-substrate system viz. ploughing, flake formation, micropolishing, cohesive failure or fragmentation, spalling, plastic deformation, removal of hard particle phase and attrition (113). Surface topography of the laser-engineered surface is shown in Figure 4.40a. The surface is relatively smooth, flat and free from cracks. The profile of the LSE deposited TiB_2 surface is illustrated in Figure 4.40b. The average surface roughness, R_a for LSE coating is 6.39 μm. The importance of the surface roughness in wear phenomena will be elucidated in the following sections.

4.4.1 Mass Loss Analysis

The dry sliding wear tests were conducted using a block-on-disk tribometer (Figure 3.7). Wear test results are presented in Figure 4.41, which shows the weight loss over a 20-minute period.

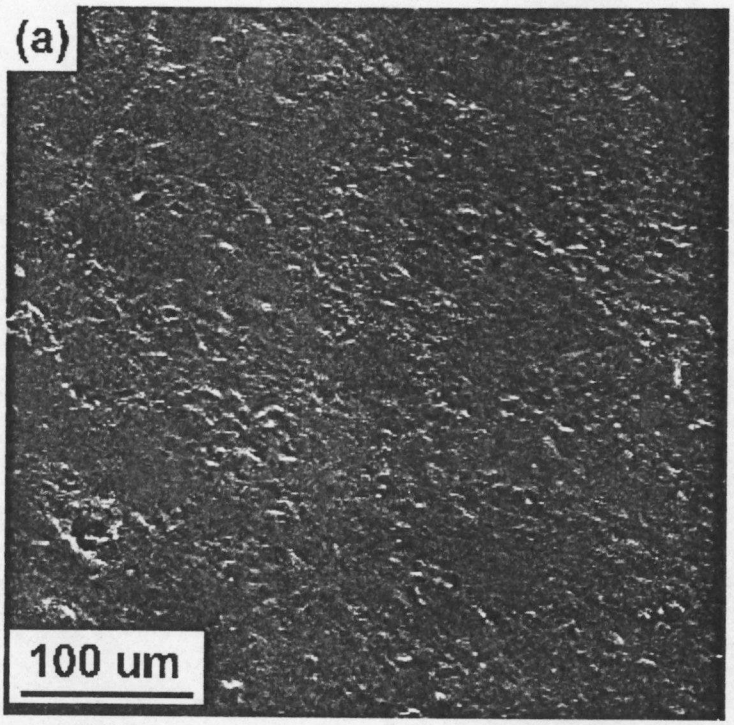


Figure 4.40 (a). SEM micrograph showing smooth surface topography of the laser engineered surface obtained in LSE 3 sample.

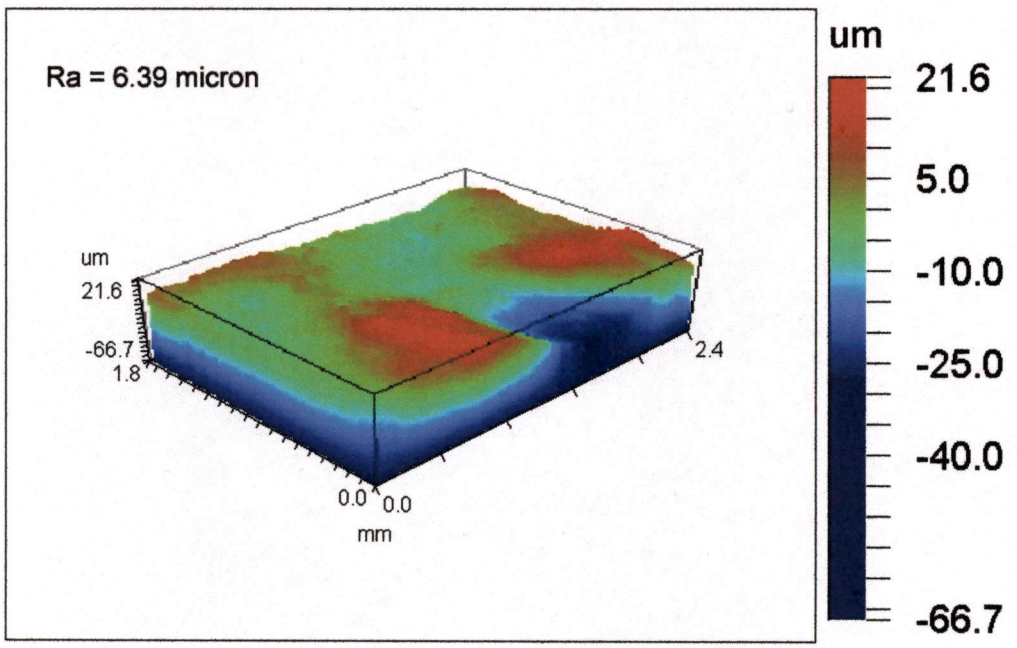


Figure 4.40 (b). Surface roughness profile of the laser engineered surface of LSE 3 sample.

SOUTHWORTH
PARCHMENT LINED
100% COTTON FIBER

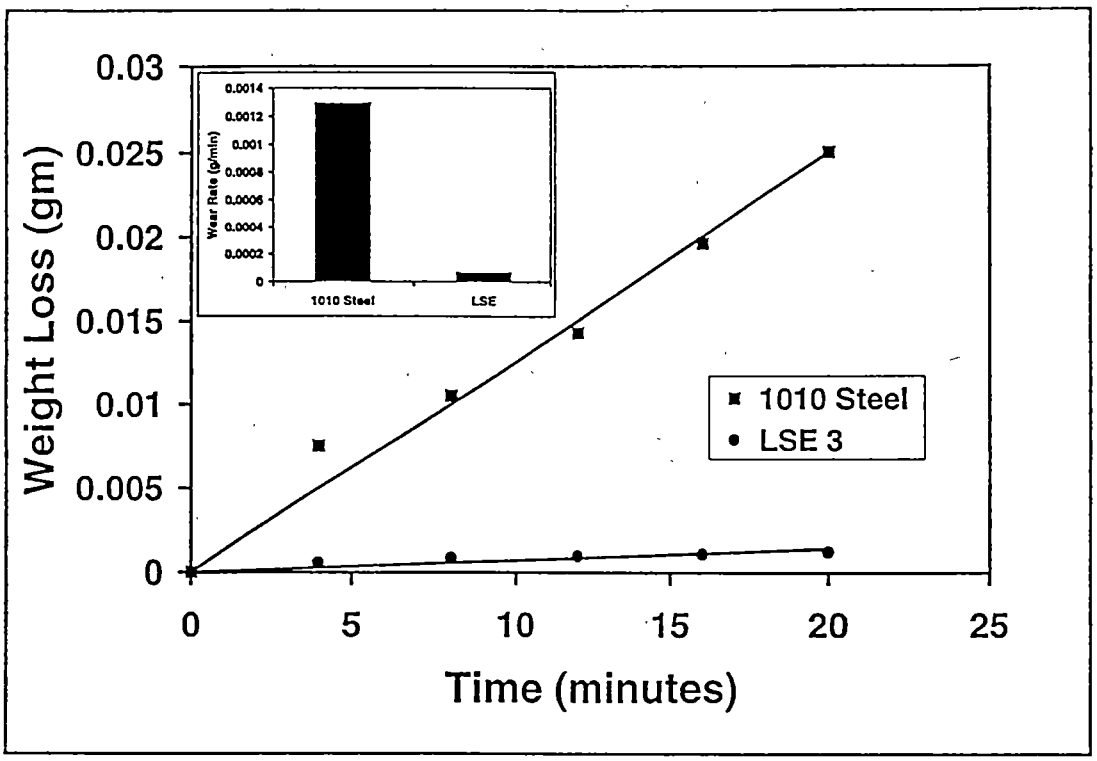


Figure 4.41. Cumulative weight losses over a 20-minute period during dry sliding wear block-on- disk test. Inset shows wear rates corresponding to various surfaces.

The comparative wear rates (obtained by the slope in Figure 4.41) for LSE surface and AISI 1010 steel are presented as bar diagram in inset. It can be easily observed that weight loss has drastically reduced for LSE coated in comparison to the AISI 1010 steel substrate. Wear rate for LSE surface has decreased by a factor of 15 in comparison to the uncoated AISI 1010 steel substrate. Moreover, wear rate for LSE coated surface tends to stabilize after an initial period of 4 minutes suggesting the smoothening and/or breaking off of hard asperities, thereby providing a flat contact with the "composite" composition. The worn surfaces of LSE coated samples were subjected to topographic observations in SEM.

Wear mechanism in such multiphase composite materials is very complex which depends upon several factors such as volume fraction, distribution and morphology of the ceramic particles (114). Under ideal conditions, monolithic ceramic such as TiB_2 is expected to fail in a brittle manner (56). However, presence of the softer matrix phase, Fe between hard ceramic particles alters the wear nature of monolithic TiB_2. It has been mentioned and validated earlier that Fe acts as an excellent binder for Ti based refractory ceramics (35,37,98). This prevents debonding at TiB_2 particle/Fe matrix interface (100). The strength of the TiB_2/Fe interface has been addressed at microstructural, chemical and atomic level in section 4.2. Under such materials conditions, Fe-based matrix phase(s) deforms plastically to accommodate the high stresses experienced by TiB_2 particles. This prevents brittle fracture and fragmentation of TiB_2 ceramic particles. Hence, chipping off is prevented and no lose debris is observed. A composite layer containing hard TiB_2 particles and soft Fe phase(s) cover the entire substrate, which assists in reducing the wear rate. It should be recalled from the TEM discussion that ultrafine boride particles

are dissolved within the Fe-rich matrix which further aid in increasing the wear resistance of such "composite" coating. Such microstructural features are elucidated in Figure 4.42 that shows TiB_2 particles embedded in Fe matrix. There is no crack formation observed within the worn area. The interface of the worn/unworn surface is the potential site for crack to be propagate and further increase the wear rate. Figure 4.43 shows such interface devoid of any crack or debris. This suggests that wear occurs mainly by the plastic deformation of the softer matrix Fe phase resulting in very little loss of material. Figure 4.44 is the surface roughness profile of the worn surface of the LSE coated sample. Wear surface is clearly indicated by the depressions (plastic deformation) caused by the rotating disk of the tribometer and relatively small change in the average surface roughness, R_a from 6.39 μm (as coated) to 4.56 μm.

The x-ray diffraction spectrum of the LSE coated surface before and after wear is shown in Figure 4.45. Within the limits of resolution of the x-ray diffractometer, the spectrum does not illustrate evolution of any new phase(s) during the wear process indicating that wear in LSE coated samples, is essentially physical in nature. Such new phase(s), if formed could influence the wear behavior of the coatings.

4.4.2 Coefficient of Friction Measurement

In the present work, the coefficient of friction is calculated by measuring the changes in voltage and current in the electrical circuit of the motor driving the block-on-ring tribometer during loading (115). Based on the principle of energy conservation, the frictional energy (W_f) equals to the change in the electrical work during loading, given by equation 4.18.

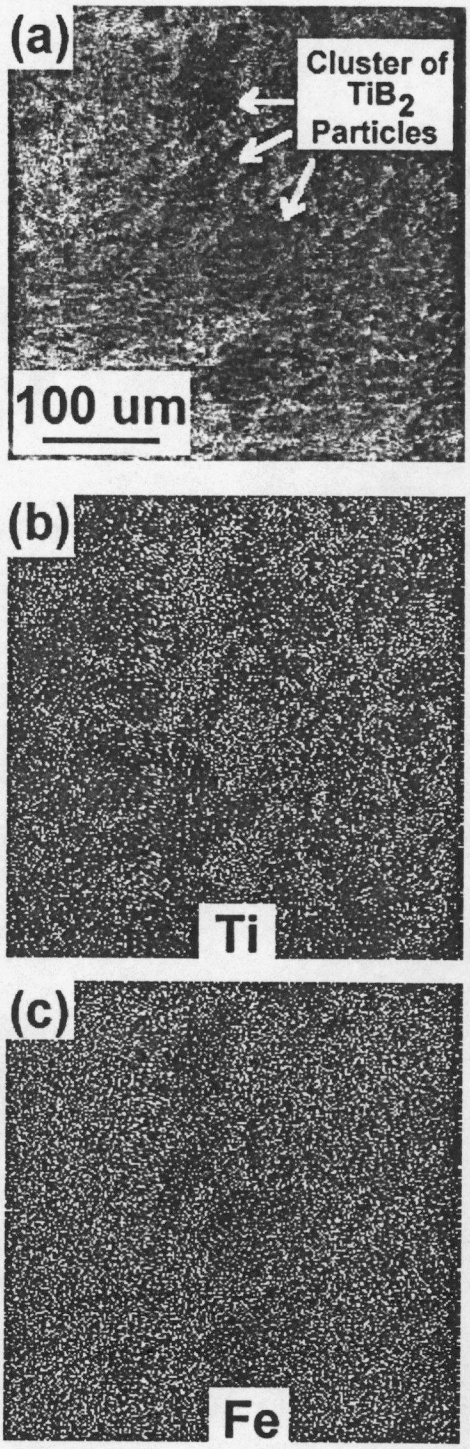


Figure 4.42. (a) SEM micrograph of the worn surface of TiB_2 coated sample and corresponding X-ray elemental maps for (b) Ti and (c) Fe.

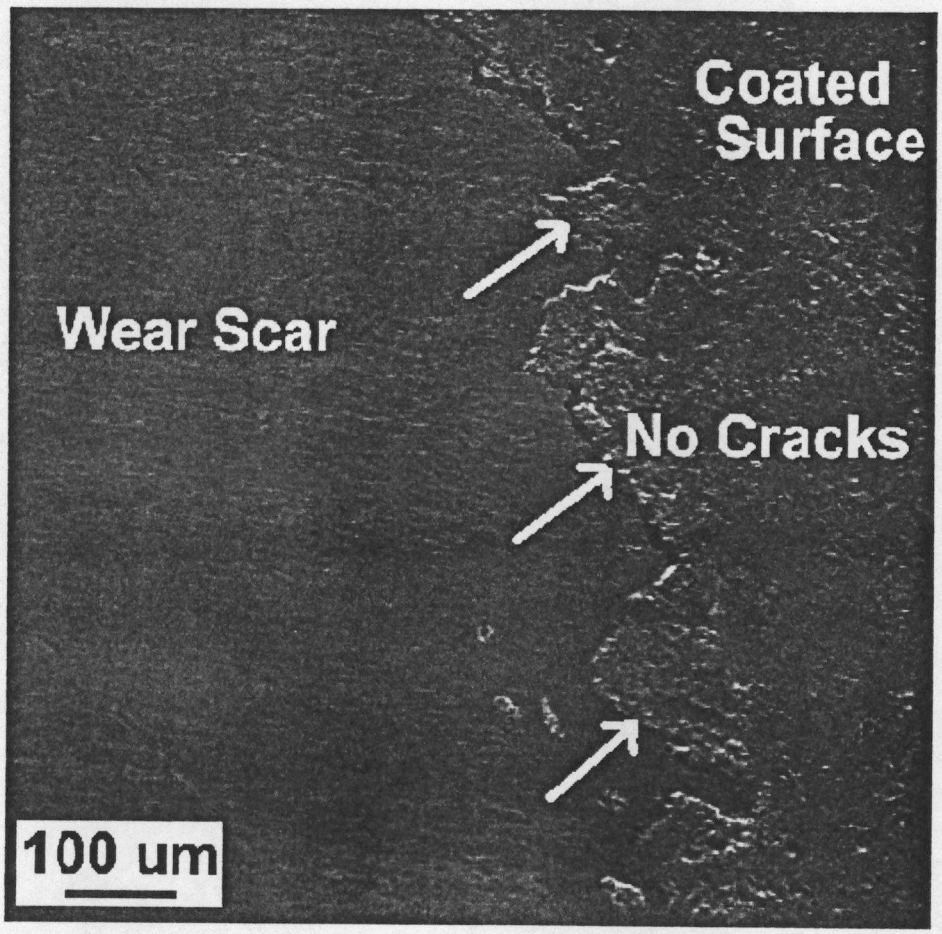


Figure 4.43. Low magnification SEM micrograph of the wear scar showing the absence of cracks at the worn/unworn interface.

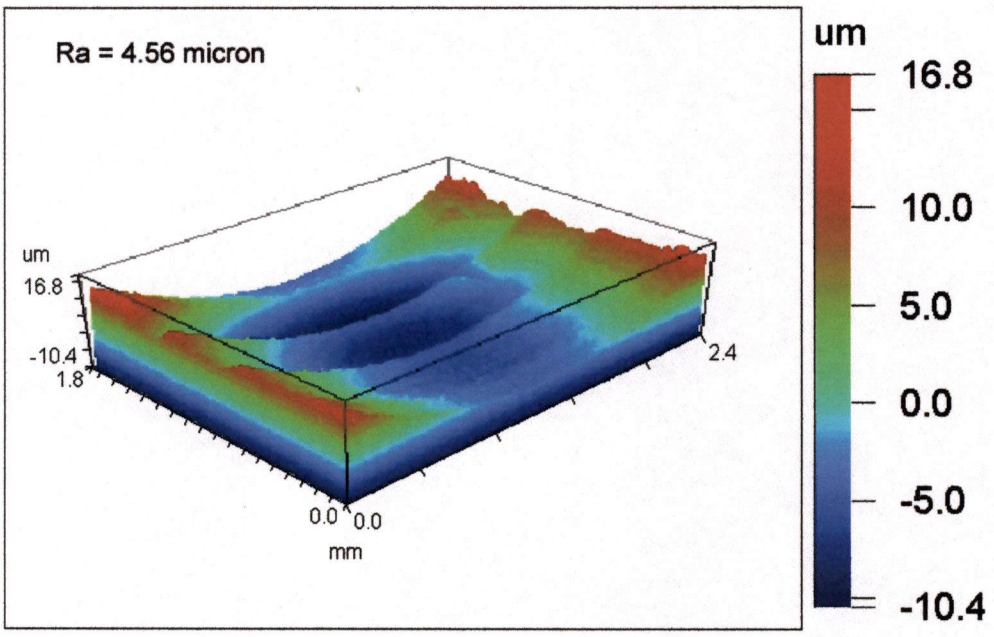


Figure 4.44. Surface roughness profile of the wear surface for the LSE sample.

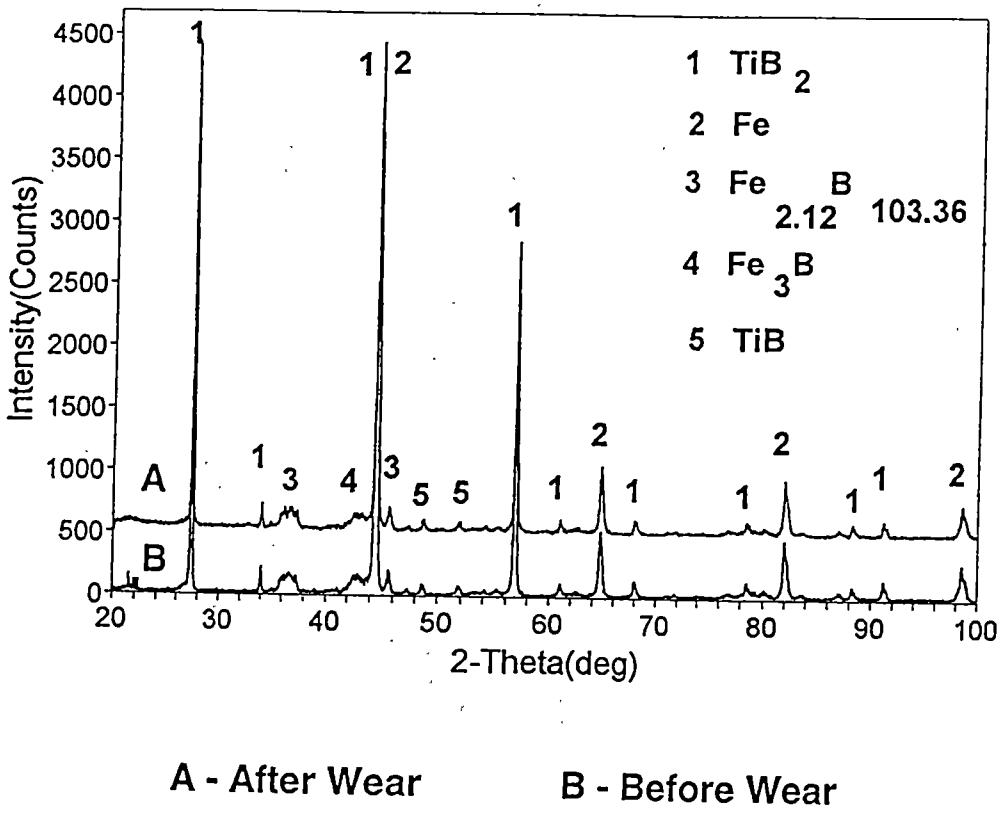


Figure 4.45. X-ray diffraction spectra of the TiB_2 coated surface: before and after wear.

$$W_f = Voltage(\Delta V) x Current(\Delta I) \qquad (4.18)$$

From friction theory, it is known that

$$W_f = \mu N v \qquad (4.19)$$

where N is the normal load, v is the linear speed of the disk and μ is the coefficient of friction. By equating above two equations, coefficient of friction is computed. The computed coefficient of friction for composite TiB_2 coating has been plotted for entire test time of twenty minutes (Figure 4.46). The best-fit line shows coefficient of friction to be 0.59 for TiB_2/steel coating. The low degree of fluctuations in friction value for LSE coated sample is accounted by the formation of a "composite" layer on the entire surface. The wear behavior of the "composite" coating is very complex, which could be explained by a model that elucidates frictional behavior of multiphase and /or composite materials (114). This model predicts that friction behavior of a composite/multiphase material is influenced by the relative amounts and friction coefficients of the constituent phase. Also, it is affected by the wear resistance of the individual constituent. In most wear situations, the more wear resistant phase(s) carry a disproportionately larger part of the load and hence have a larger influence on the friction of the composite. Hence, the friction coefficient of composite generally does not follow a linear rule of mixture, but is dominated by friction coefficient of the most wear resistant constituent. It is well understood that a refractory ceramic like TiB_2 has high wear resistance as compared to plain carbon steel. Hence, according to the model discussed above, TiB_2 particles in the coating tend to carry a larger load than Fe and contribute largely towards coefficient of

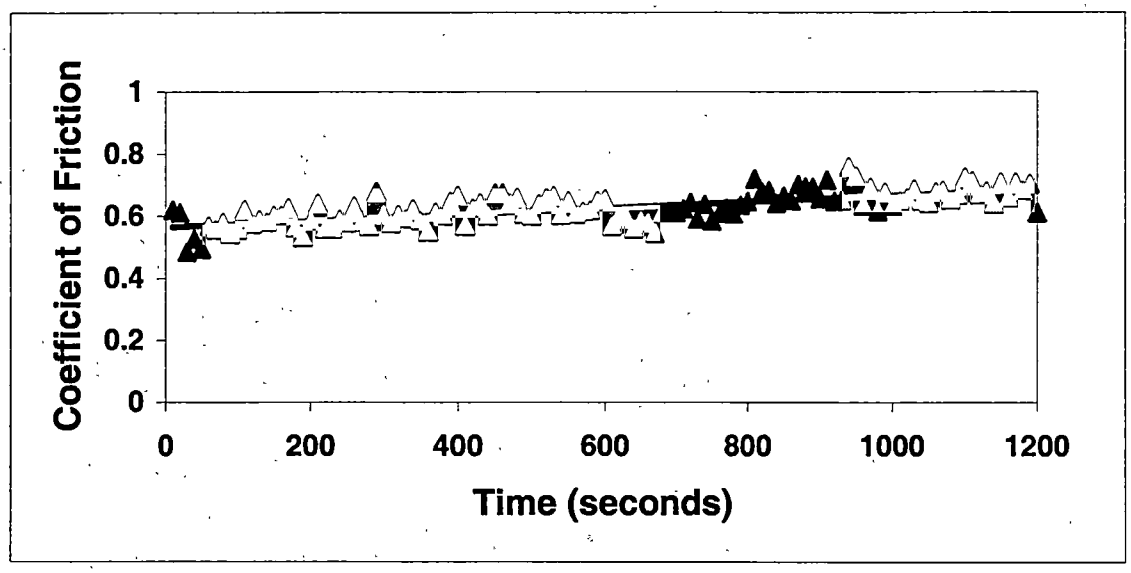


Figure 4.46. Variation in coefficient of friction with time during dry sliding test.

friction of the "composite" coating. However, in the present study, no such mathematical modeling has been done for this particular materials system. A summary of the features of coating and their tribological characteristics has been presented in Table 4.12.

Table 4.12. Summary of TiB_2 Coating and its Tribological Characteristics

Features	LSE Process
Energy Density Input (MW/m^2)	15.0
Nature of the Coating	Thick (200 μm) composite coating with embedded TiB_2 particles in the Fe-rich matrix
Surface Roughness, R_a (before wear)	6.39 μm
Surface Roughness, R_a (after wear)	4.56 μm
Wear Rate (g/min)	0.00005
Coefficient of Friction	0.59
Wear Mechanism	Plastic deformation

It can be concluded that "composite" TiB_2 coating has an excellent wear resistance with a strong coating/substrate interface. TiB_2 being a high temperature material, it is expected to perform superiorly at high temperature for various applications i.e. "composite" TiB_2 coating should have excellent high temperature oxidation resistance and corrosion resistance. It is envisaged that TiB_2 will be deposited on machine parts and various tools as wear and oxidation resistant coating. Another important application of TiB_2 is in the aluminum casting industry as protective coatings for dies and molds. Liquid aluminum is very corrosive that causes excessive damage to dies, mold and

molten metal handling tools. TiB_2 is corrosion resistant to liquid Al, making it an ideal candidate for protective coating on dies and molds. Such engineering components experience high temperature either due to processing or the environmental conditions. Hence, high temperature oxidation of laser deposited "composite" TiB_2 coating in air along with high temperature corrosion by liquid Al has been studied in the following sections.

4.5 High Temperature Oxidation of TiB_2 Coating in Air

Elevated temperature oxidation behavior of TiB_2 coating in air was evaluated by two procedures: (a) thermogravimetric analysis (TGA) to study oxidation kinetics and (b) long term exposure to study oxide scale growth and morphology.

4.5.1 Oxidation Kinetics

Oxidation behavior of "composite" TiB_2 coating has been characterized through measurements of their mass change per unit surface area ($\Delta m/a$) during exposure at various temperatures and time. Figure 4.47 illustrates mass gain per unit area during three-hour exposure for oxidation of the test samples at various temperatures. Oxidation rate is parabolic for all test temperatures during constant temperature exposures. Such parabolic rate of oxidation is represented by the following equation where t is oxidation time and k and C represent oxidation kinetic constants.

$$\left(\frac{\Delta m}{a}\right)^2 = kt + C \qquad (4.20)$$

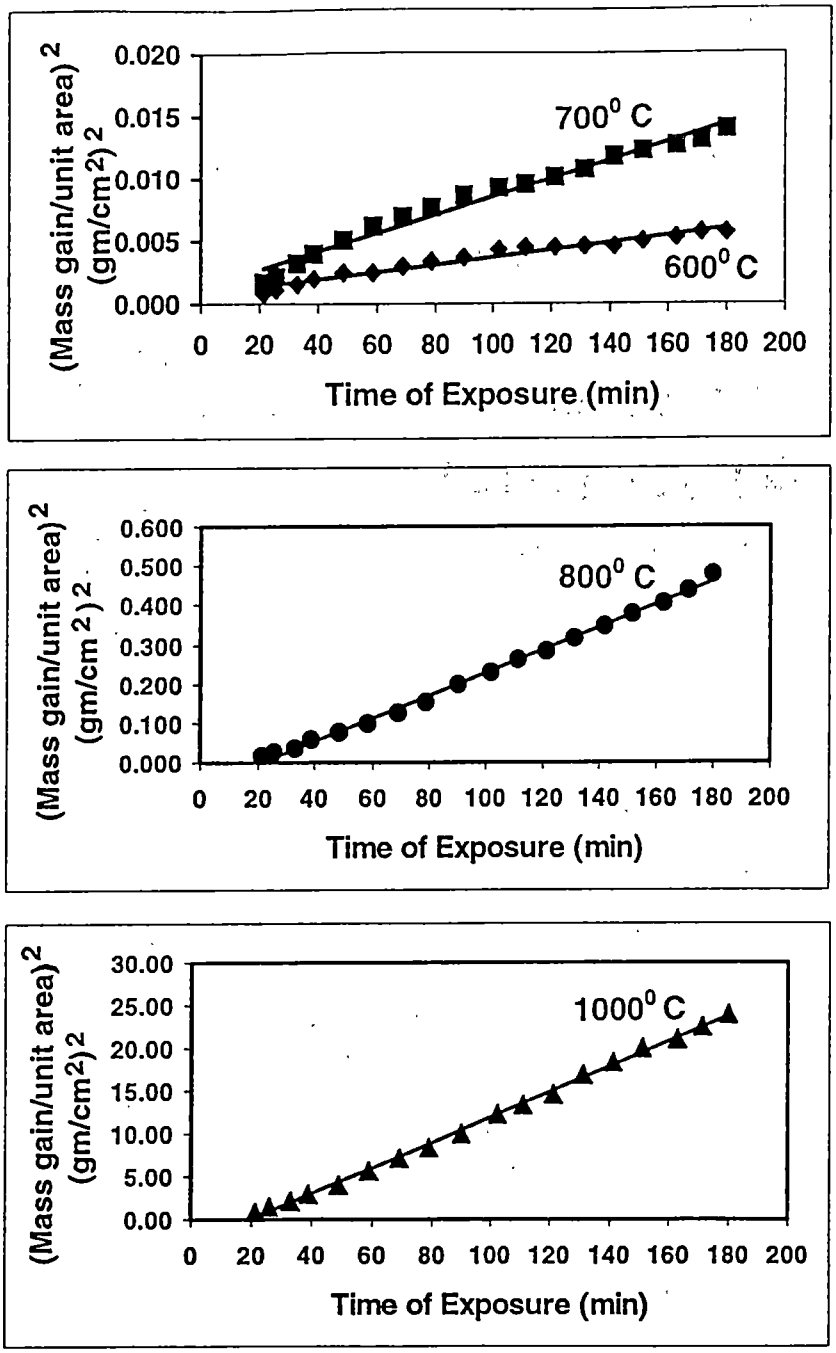


Figure 4.47. Oxidation kinetics for "composite" TiB_2 coating showing parabolic rate of reaction for 600, 700, 800 and 1000^{0}C.

Table 4.13 lists all the values of k and C for various test temperatures. It is evident from Figure 4.47 that the oxidation rate at 1000^0C is significantly higher than other test temperatures. Based on these k values for different test temperatures, Arrhenius type of plot (ln k vs.RT^{-1}) is constructed as shown in Figure 4.48. Activation energy, Q, for parabolic rate of oxidation of the composite TiB_2 coating determined from Figure 4.48 is 205 kJ/mol.

Table 4.13. Oxidation Kinetic Constants for Composite TiB_2 Coating for Various Constant Temperatures of Exposure

Test Temperature (^{0}C)	k ($gm^2 cm^{-4} min^{-1}$)	C ($gm^2 cm^{-4}$)
600	4×10^{-5}	0.0216
700	9×10^{-5}	0.0420
800	2.5×10^{-3}	0.2072
1000	0.1307	0.0128

Oxidation kinetics of composite TiB_2 coating are found to be parabolic for all the temperatures between 600^0C and 1000^0C. On the contrary, Irving and Worsley suggested parabolic rate of oxidation for pure TiB_2 powder samples for all temperatures except between 900 and 950^0C where rate was cubic (116). Barandika et al. found oxidation rate for TiB_2 based cermet (TiB_2 + 14 wt. % Fe + 6 wt. % Ni + 5 wt. % Al + 3 wt. % Ti) to be linear between 775 and 1000^0C and parabolic below 775^0C (117).

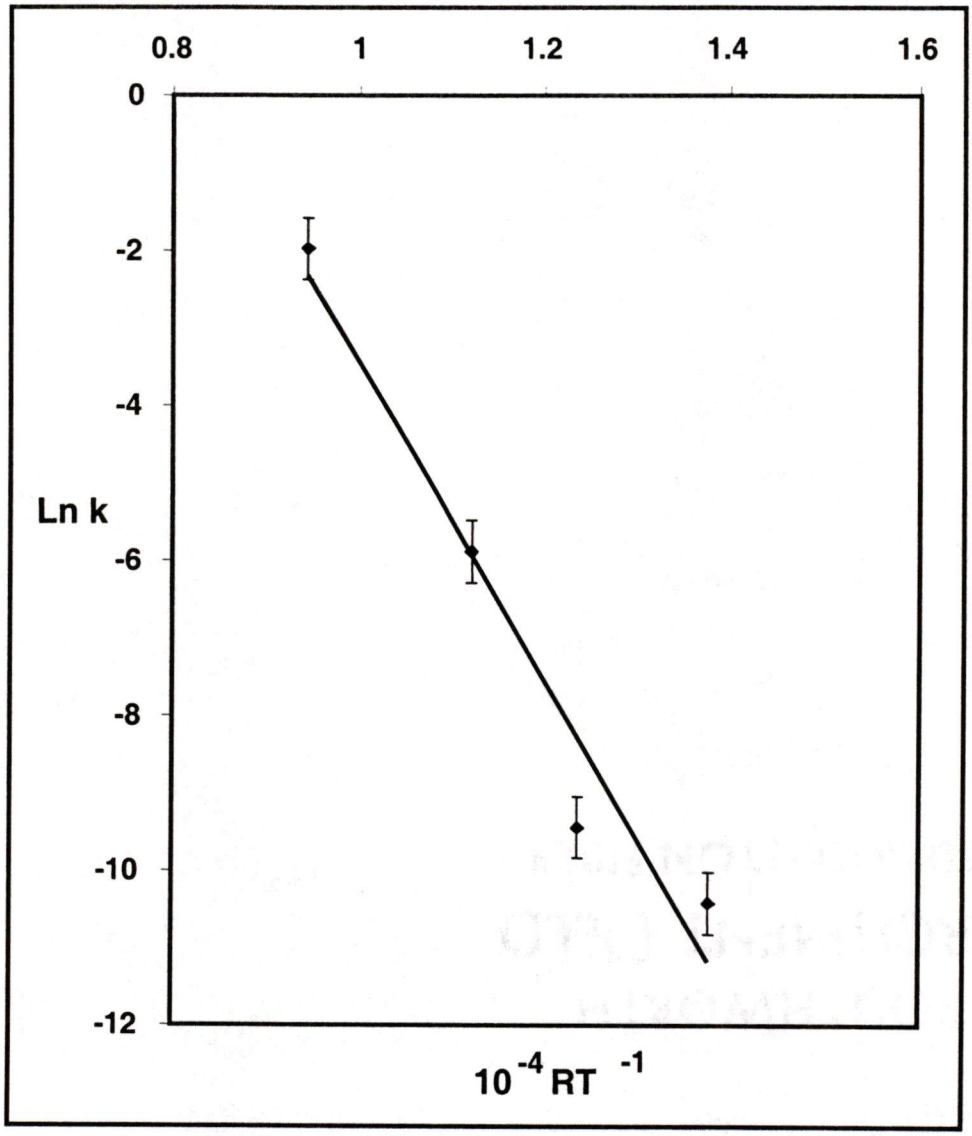


Figure 4.48. Arrhenius plot for the parabolic rate of oxidation of "composite" TiB_2 coating.

In all these studies, however, the physical and chemical nature of samples was far different from the "composite" coating sample under investigation in this work. Furthermore, activation energy for composite boride coating was found to be similar to the earlier study of TiB_2 based cermet (118). This could be attributed to some degree of similarity between physical nature of "composite" coating and TiB_2 based cermet.

The lower values of rate constant k, for 600 and 700^0C are indicative of very slow oxidation. Oxidation rate increases at 800^0C and reaches alarmingly high at 1000^0C (Figure 4.47b). Reaction rate constant k, for 1000^0C is 3 order of magnitudes higher than that of 600 and 700^0C (Table 4.13). A higher degree of oxidation is attributed to the combined effect of several reasons such as formation of non-protective oxide scales along with the rapid evaporation of B_2O_3 (117). The detailed mechanism of the oxidation reactions occurring within the "composite" TiB_2 coating/Fe system were understood by characterizing the oxide scales formed on the coating in accordance with the oxidation kinetics. Oxide scales formed on these samples were characterized cross-section morphology, structural features and surface morphology.

4.5.2 Oxide Scale Characterization

A. Cross-Sectional Morphology

Table 3.3 should be referred for the sample nomenclature for oxide scale characterization. Figure 4.49 shows the low magnification SEM micrographs of the cross section of A-series samples after long duration exposure at 600^0C. "Composite" TiB_2 coating is continuous and metallurgically adherent to the substrate. There is no oxide layer build up or porosity in the cross section. There are, however, few cracks in the

coating for A3 sample, which was oxidized for 50 hours at 600^0 C (Figure 4.49c). A similar view of B series samples is presented in Figure 4.50. B1 shows a thin oxide layer build up on the coating (Figure 4.50a). Coating is, however, still intact with no signs of delamination, cracks and porosity. Oxide layer grows thicker for B2 sample that was exposed at 800^0 C for longer period of 30 hours (Figure 4.50b). Even for such long time exposure, oxide layer is adherent to the coating and TiB_2 particles in the coating are still intact. A crack is however, seen in the coating, which passes through TiB_2 particles. Further, increasing severity of oxidation is evident from Figure 4.50c for sample B3 which was exposed for 50 hours at 800^0 C. Oxide layer has grown thicker and spalled off the coating from several locations. Weaker interface between oxide layer and composite coating is revealed much clearly later in this section Figure 4.53c. Although TiB_2 particles are intact in the coating, there is severe damage to coating by crack propagation through TiB_2 particles (Figure 4.50c). C series samples were exposed for oxidation at 1000^0 C (Figure 4.51). C1 sample, which was exposed for 10 hour shows a horizontal split in the "composite" boride coating (Figure 4.51a). Moreover, there is lot of porosity at the composite coating/steel substrate interface. Figure 4.52 presents the x-ray elemental maps for Ti and Fe distribution corresponding to split coating observed in Figure 4.51a. C2 and C3 samples behaved in a similar manner showing three distinct layers in Figure 4.51b and 4.51c. Top most layer shows oxidized boride coating whereas intermediate layer is iron oxide layer. Iron oxide layer separated from the steel substrate in both C2 and C3 samples. Although Figure 4.51 suggests delamination of the boride coating at boride coating/iron oxide interface, instead the separation after oxidation occurred at iron oxide/substrate interface. Delamination of boride layer from iron oxide

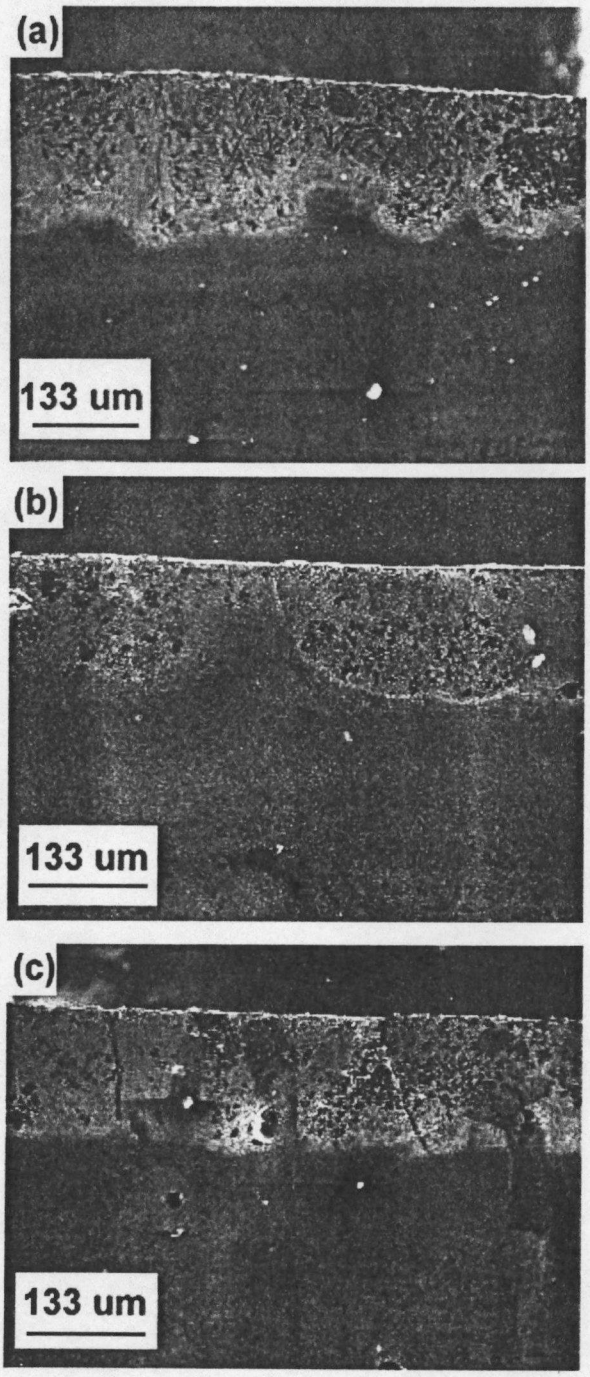


Figure 4.49. Low magnification SEM micrographs showing cross sectional view of (a) A1 sample (b) A2 sample and (c) A3 sample after long term exposure at 600^0C.

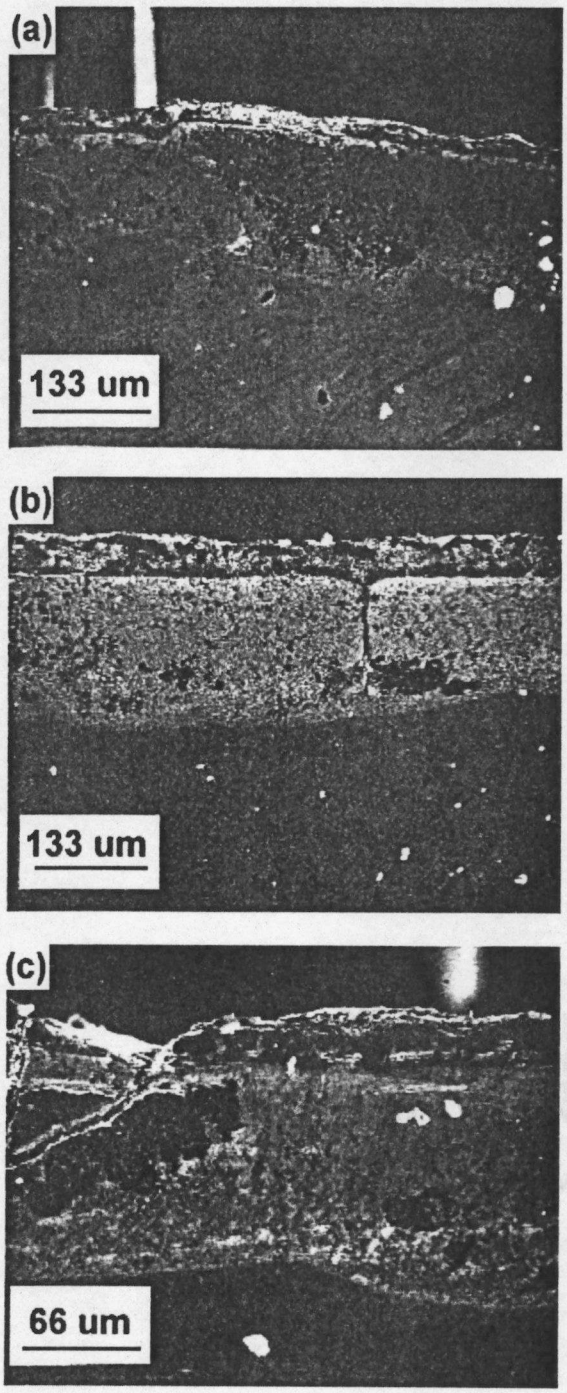


Figure 4.50. Low magnification SEM micrographs showing cross sectional view of (a) B1 sample (b) B2 sample and (c) B3 sample after long term exposure at 800^0C.

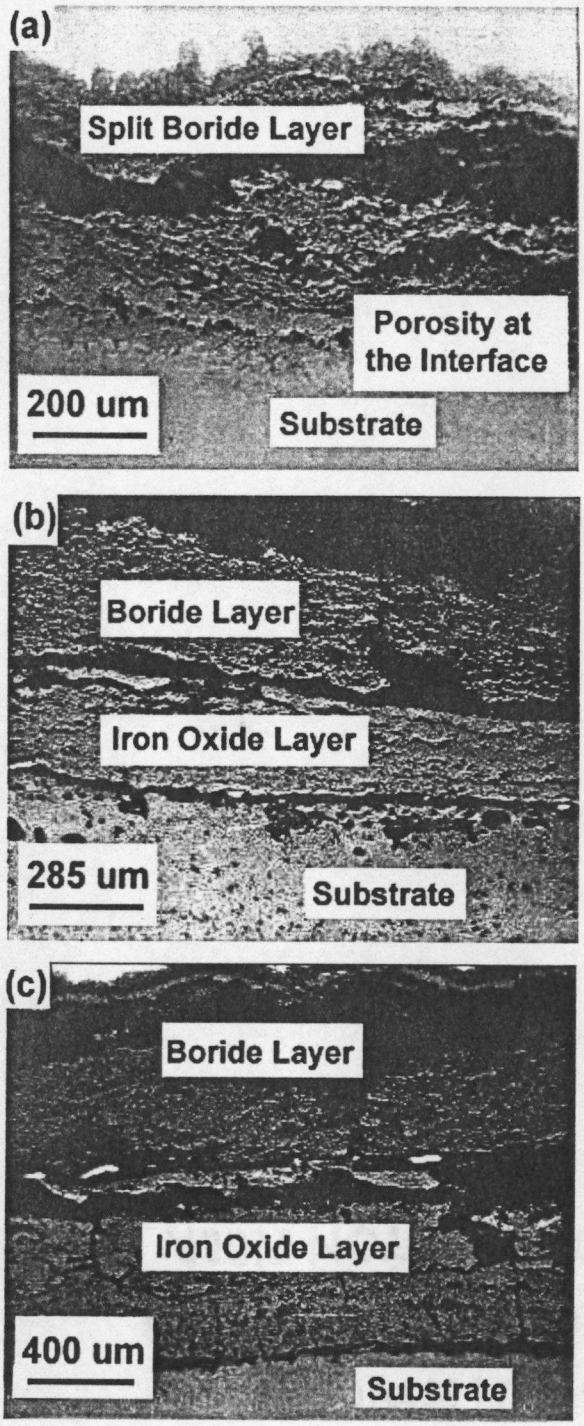


Figure 4.51. Low magnification SEM micrographs showing cross sectional view of (a) C1 sample (b) C2 sample and (c) C3 sample after long term exposure at 1000^0C.

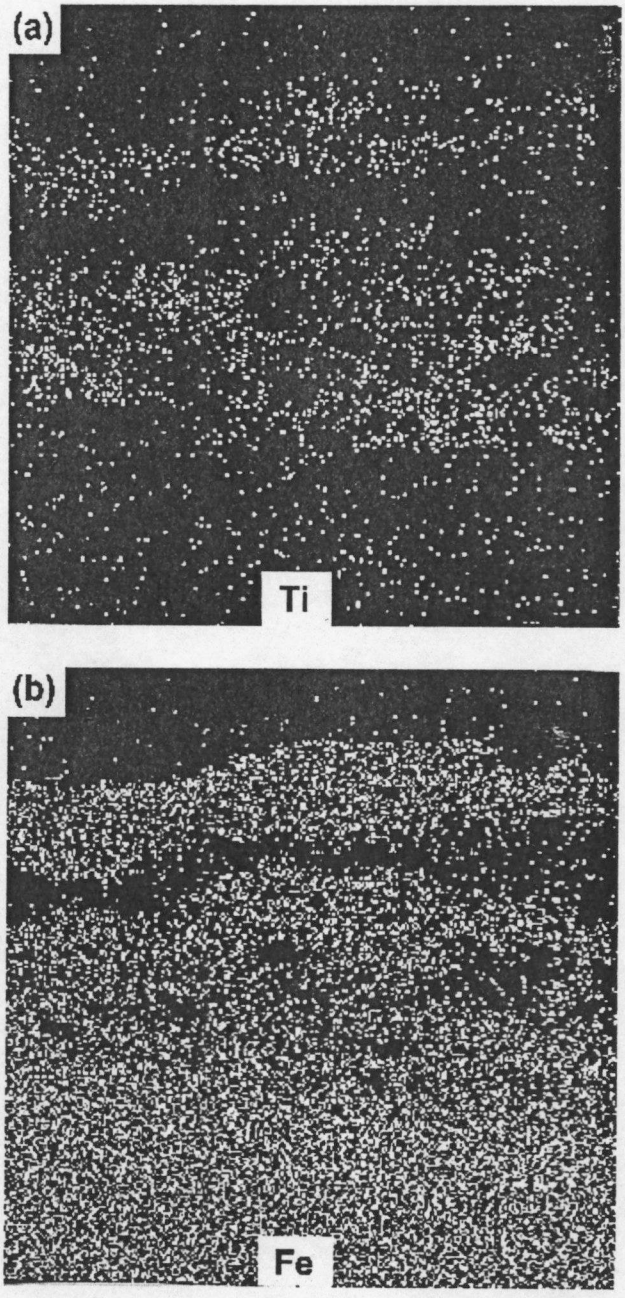


Figure 4.52. X-ray maps showing elemental distribution of Ti and Fe corresponding to Figure 4.51(a).

layer has occurred due to mechanical damage caused by grinding and polishing during preparation of metallographic sample. Delaminated layer was too fragile and brittle in nature. Intermediate iron oxide layer is infested with porosity and cracks along the entire length.

High magnification view of the oxide layer in the cross section of B series samples is shown in Figure 4.53. B1 sample shows intact acicular shaped TiB_2 particles within the coating with an adherent oxide layer of 15 μm thickness (Figure 4.53(a)). In Figure 4.53b, an adherent oxide layer on the B2 sample is 40 μm thick with a highly porous and lamellar structure. A crack propagated through the coating with oxides formed in the interspacing of the crack. Severely damaged TiB_2 coating in B3 sample is illustrated in Figure 4.53c. Even though individual TiB_2 particles are still intact, severe crack propagation has damaged the integrity of the coating. The top oxide layer has a weaker interface with TiB_2 coating in comparison to B1 and B2 samples that caused its spallation. A region of delamination of oxide layer from the coating is marked with an arrow in Figure 4.53c.

Figure 4.54 shows the high magnification cross sectional view of the oxidized boride layer in C1 sample and corresponding x-ray elemental maps for Ti and Fe distribution. Oxide is highly porous and lamellar with high iron content. Ti is uniformly distributed in the oxide. EDS analysis (spot A) at lamellar regions suggests 75 to 80 wt. % Fe and 20 to 25 wt. % Ti uniformly distributed in the composite oxide. Dark regions (spot B) are porosity in the oxide. High magnification cross sectional views of oxide morphology for sample C2 and C3 is not presented here as oxidized boride layer separated from steel substrate (Figure 4.50a and 4.50b).

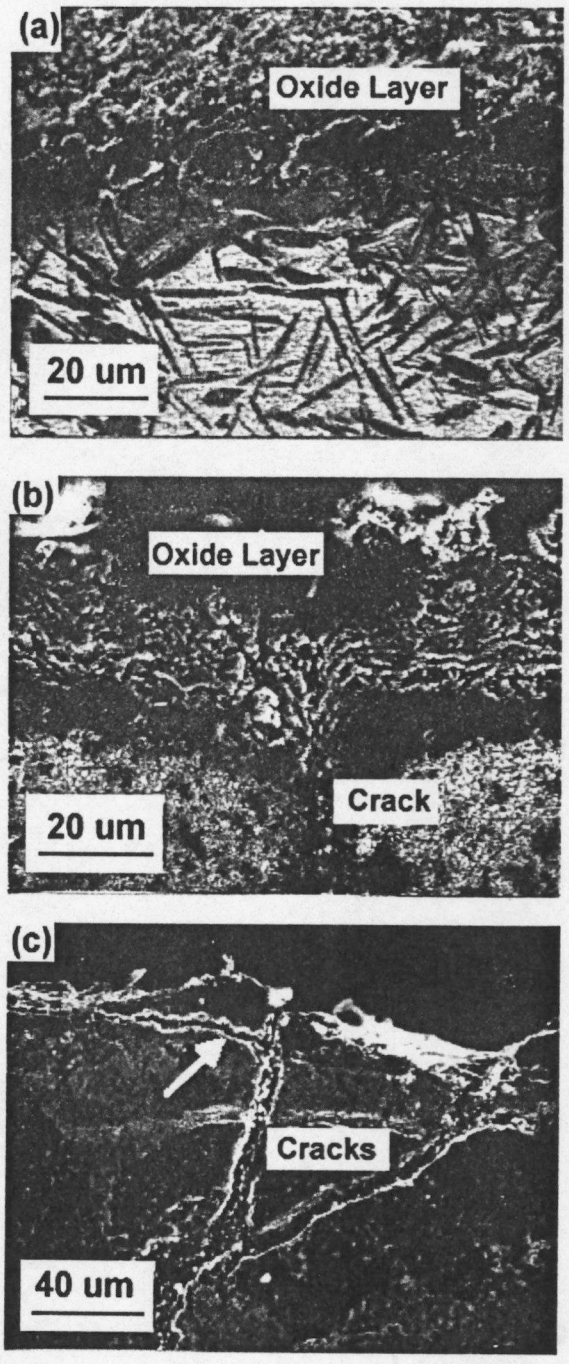


Figure 4.53. High magnification SEM micrographs showing cross sectional view of (a) B1 sample (b) B2 sample and (c) B3 sample after long term exposure at 800^0C.

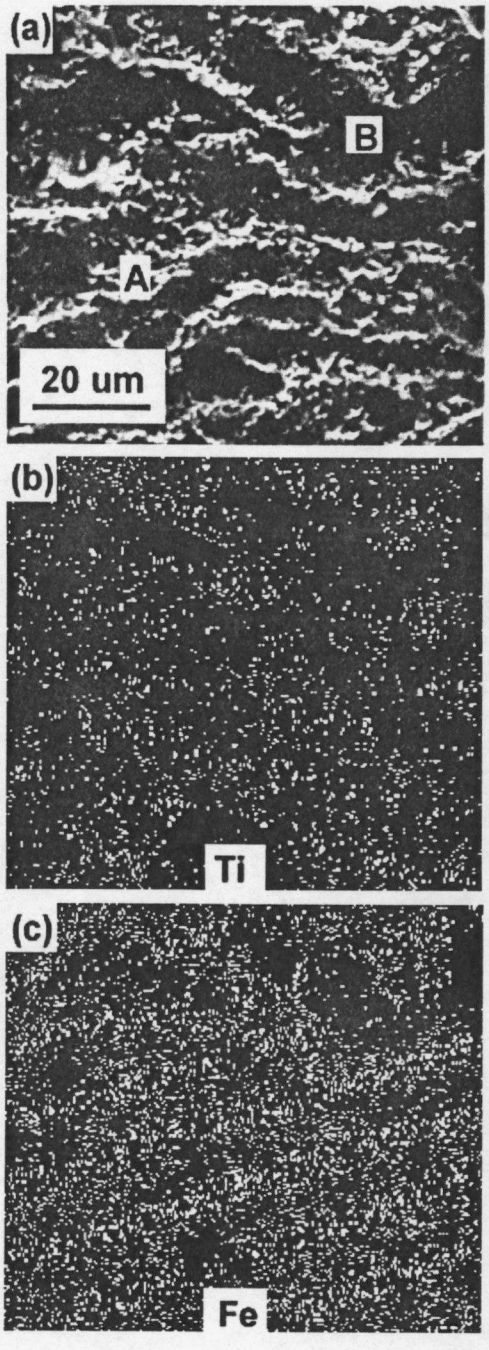


Figure 4.54. (a) SEM micrograph of the cross section of layer oxide formed on C1 sample and corresponding x-ray maps for (b) Ti and (c) Fe distribution.

B. Top Surface Oxide Morphology

Topographic features of oxide scale formed in A, B and C series samples are compared in Figure 4.55. A3 sample shows relatively smoother surface with nucleation of oxide islands on the coated surface (Figure 4.55a). Oxide growth accelerates at higher temperature of 800^0C for B3 sample. Figure 4.55b shows a very rough surface with highly porous and fibrous oxide. C1 sample shows oxide grains growing upwards from the coated surface (Figure 4.55c). Surface topography of oxide layers in C2 and C3 samples could not be observed due to extremely brittle nature of separated layer from the substrate. Figure 4.56 illustrates the surface roughness profiles corresponding to oxide scales observed in Figure 4.55 for A3, B3 and C1 samples. Average surface roughness, R_a of the oxide scales formed on A3, B3 and C1 sample is 9.54 μm, 14.39 μm and 23.37 μm respectively.

C. Structural Characterization of Oxide Scale

Structural characterization of oxide scales formed on the coated surface was performed using x-ray diffractometry. Several oxides of type Ti_aO_b, Fe_mO_n and $Fe_xTi_yO_z$ with various stoichiometries are formed. Table 4.14 presents a comprehensive list of all the major phases present in A, B and C series samples. X-ray diffraction spectra for A series samples are shown in Figure 4.57. TiB_2 is the major phase along with Fe and TiO_2, which is an oxidation product. In B series samples, TiB_2 peaks are not observed. TiO_2, $Fe_xTi_yO_z$ and Fe_3BO_6 are the prominent phases present in B series samples (Figure 4.58). The major phases present in C series samples are Ti_2O_3, Fe_2O_3 and $Fe_xTi_yO_z$.

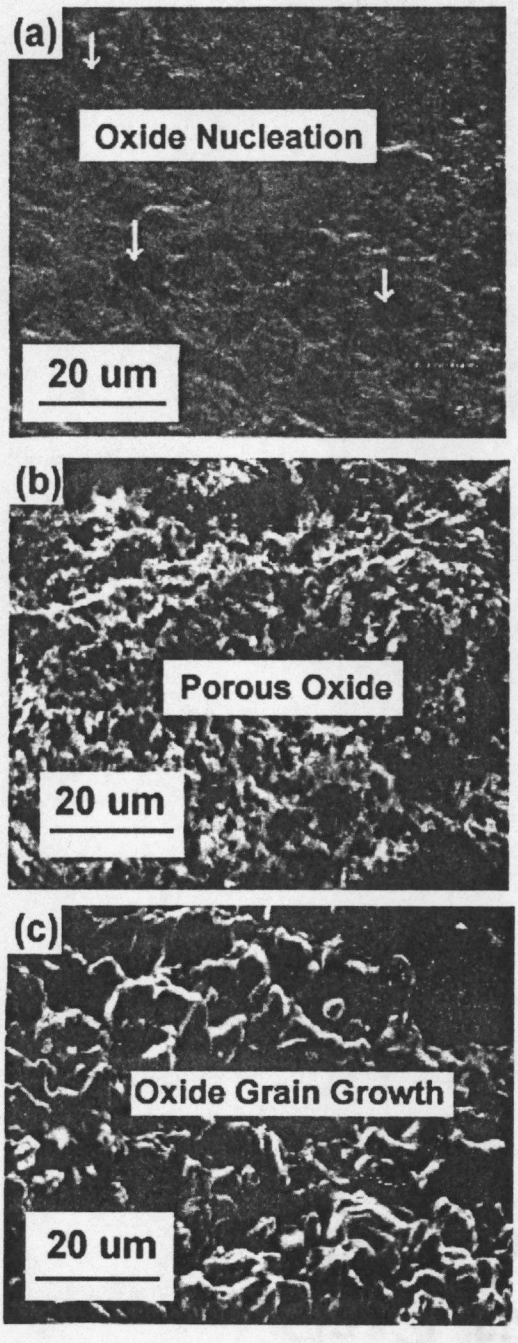


Figure 4.55. Top surface morphology indicating oxide growth in (a) A3, (b) B3 and (c) C1 samples.

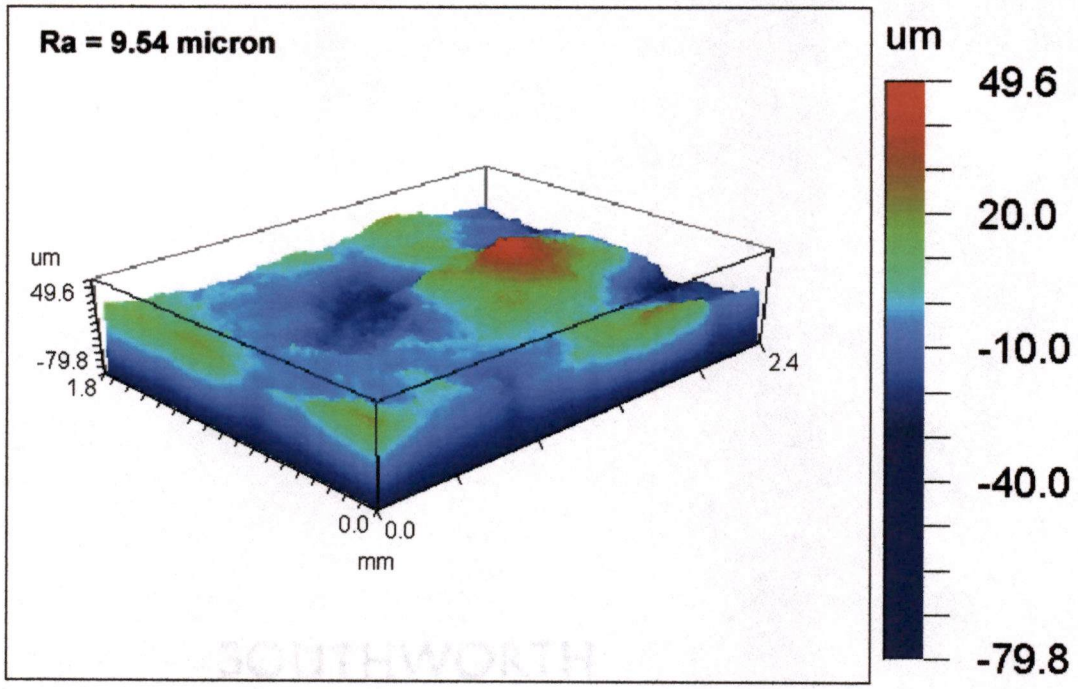


Figure 4.56(a). Roughness contours of the surface morphology of the oxide growth in A3.

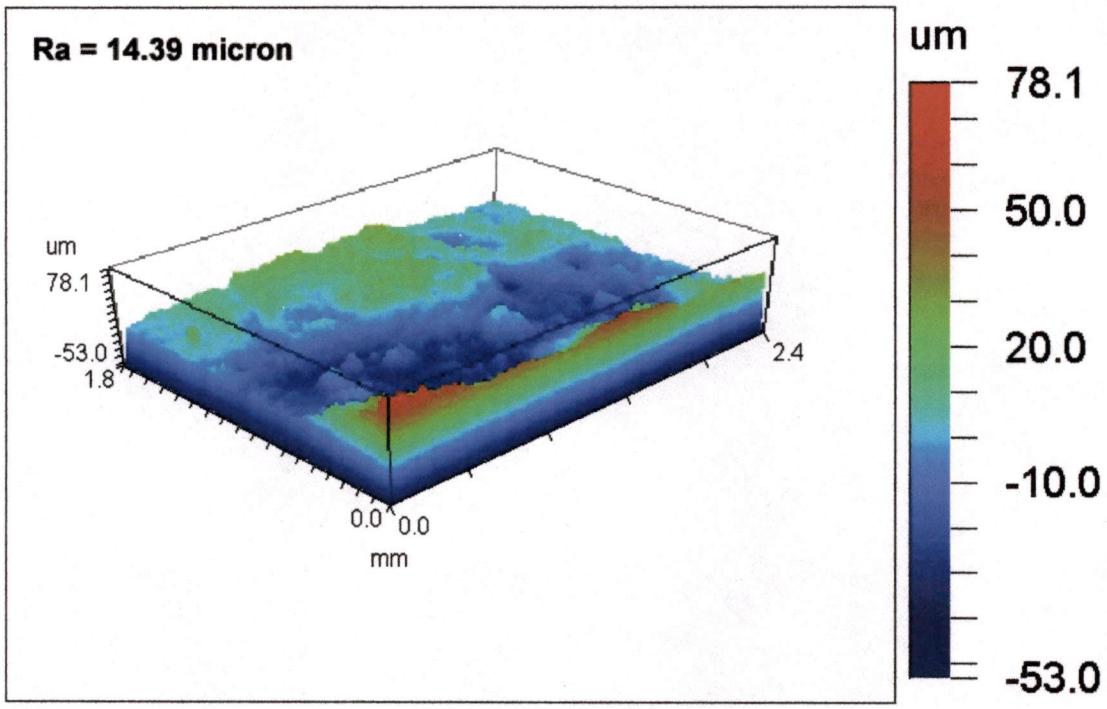


Figure 4.56(b). Roughness contours of the surface morphology of the oxide growth in B3.

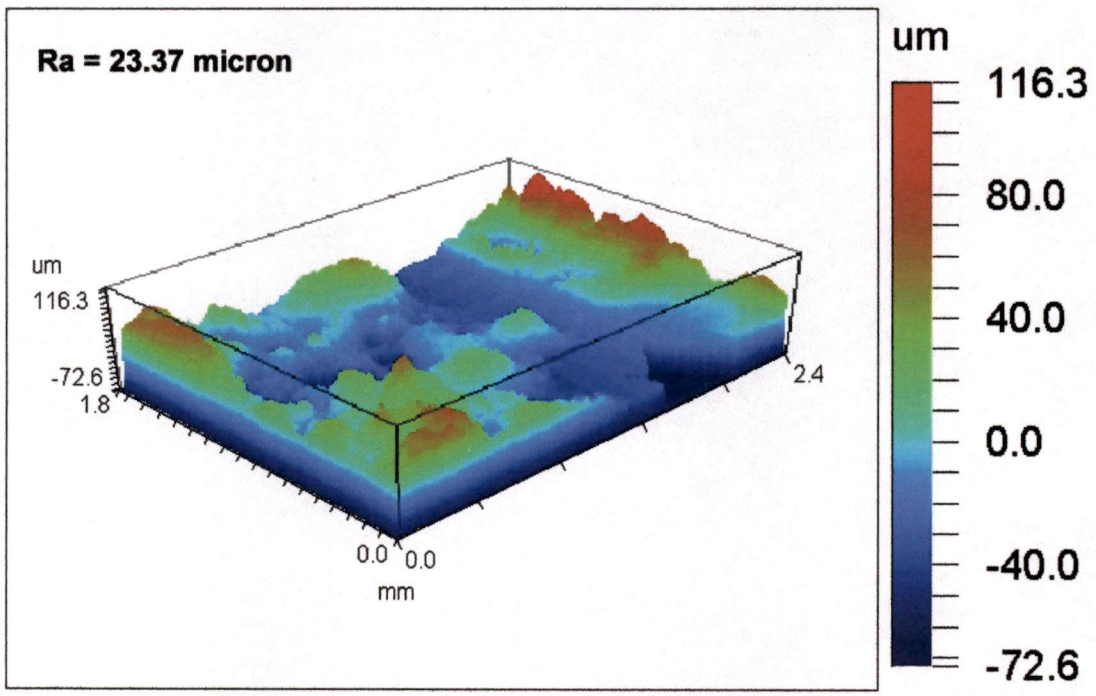


Figure 4.56(c). Roughness contours of the surface morphology of the oxide growth in C1.

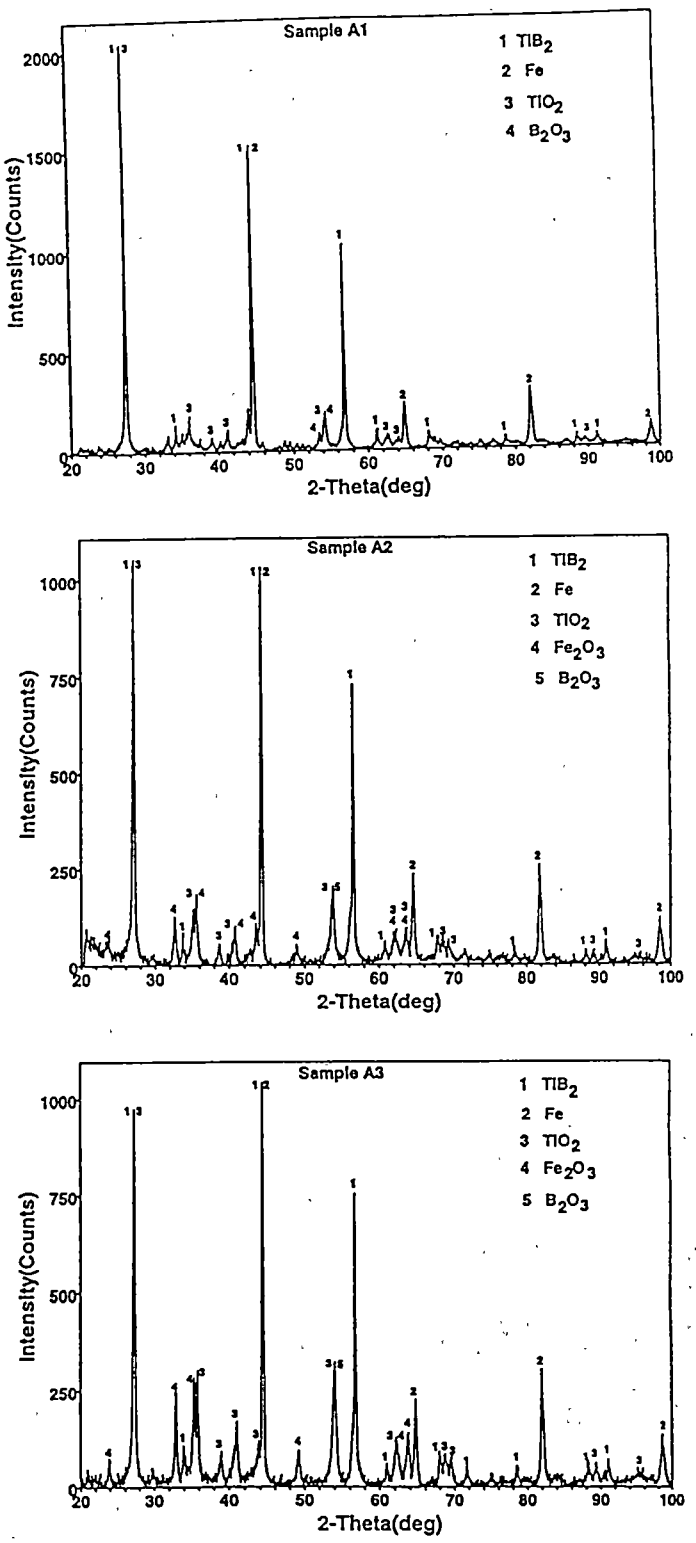


Figure 4.57. X-ray diffraction spectra for A series samples.

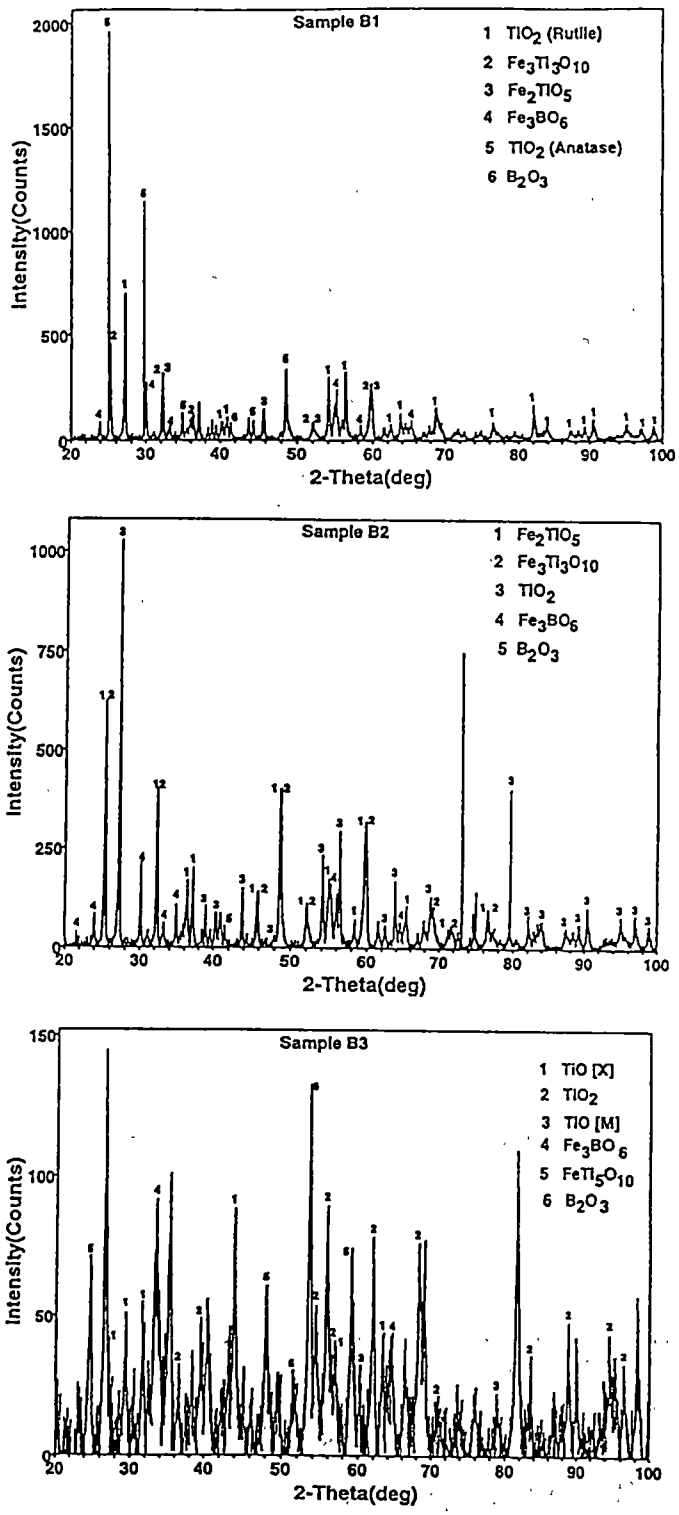


Figure 4.58. X-ray diffraction spectra for B series samples.

Table 4.14. Comprehensive List of Major Phases Present in the Oxide Scale

Phases Present	A1	A2	A3	B1	B2	B3	C1	C2 Top*	C2 Bottom!	C3 Top*	C3 Bottom!
Fe	X (*B*)	X (*B*)	X (*B*)	-	-	-	-	-	-	-	-
TiB_2	X (*H*)	X (*H*)	X (*H*)	-	-	X (*H*)	-	-	-	-	-
TiO_2	X (*R*)	X (*R*)	X (*R*)	X (*R*)	X (*R*)	X (*R*)	-	-	-	-	-
Ti_2O_3	-	-	-	-	-	-	X (*Rh*)	-	X (*Rh*)	-	X (*Rh*)
Fe_2O_3	-	X (*Rh*)	X (*Rh*)	-	-	-	X (*Rh*)	X (*Rh*)	X (*Rh*)	-	X (*Rh*)
B_2O_3											
$Fe_3Ti_3O_{10}$	-	-	-	X (*O*)	X (*O*)	-	-	-	-	-	-
$FeTi_5O_{10}$	-	-	-	-	-	X (*U*)	-	-	-	-	-
Fe_2TiO_5	-	-	-	X (*O*)	X (*O*)	-	-	-	-	-	-
$FeTiO_3$	-	-	-	-	-	-	-	X (*Rh*)	-	-	-
Fe_2Ti_4O	-	-	-	-	-	-	-	-	-	X (*C*)	-
Fe - Ti - O	-	-	-	-	-	-	-	X (*C*)	-	X (*C*)	-
Fe_3BO_6	-	-	-	X (*O*)	X (*O*)	X (*O*)	-	-	-	-	-

* Top (See Figure 3.9)
! Bottom (See Figure 3.9)
X indicates presence of the phase
( ) indicates crystal structure of the phase
B Body centered cubic
H Hexagonal
R Rutile
Rh Rhombohedral
O Orthorhombic
C Cubic
U Unknown

Since coating layer separated in C2 and C3 samples after oxidation, x-ray diffractomtery was performed on both top and bottom part of the separated layer (Figure 3.9). Such experimentation provided valuable information about oxidation mechanism and phase(s) formed in the top layer as well as the coating/substrate interface. Ti_2O_3 and Fe_2O_3 are formed on the bottom side of the separated oxide layer of C2 and C3 samples. X-ray diffraction spectra of C series samples are presented in Figure 4.59.

Oxidation of "composite" TiB_2 coating occurs in several ways as schematically illustrated in Figure 4.60. Oxidation of such "composite" coating is very complex as it leads to formation of several multiple oxides (Table 4.14). It is anticipated that glassy B_2O_3 formation occurs at 450^{0}C, which melts and covers the surface (117-118). B_2O_3 is an oxidation product of TiB_2 that occurs through the following reaction:

$$TiB_2 + 5/2\ O_2 = TiO_2 + B_2O_3 \qquad (4.21)$$

Figure 4.57 shows few B_2O_3 peaks in A-series samples. However, B_2O_3 was not detected as major phase by XRD analysis due to its glassy nature. At lower temperatures B_2O_3 have low oxygen diffusivity value and hence act as protective layer against oxidation (119). This fact is corroborated by Figure 4.47b that shows very slow oxidation rate for 600 and 700^{0}C. Figure 4.49 also does not show any oxide layer on the coating which further validates the slow oxidation rate at 600 ^{0}C. However, oxidation rate increases at 800^{0}C with a further rapid increase at 1000^{0}C (Figure 4.47b). Such oxidation behavior is attributed to the properties of oxides formed on the surface. It is noteworthy that although B_2O_3 has a boiling point of 1250^{0}C, it evaporates at a temperature much lower than its boiling point (117, 120). Evaporation of B_2O_3 starts at 750^{0}C which causes increase in oxidation rate at 800^{0}C (117). This fact is pronounced in

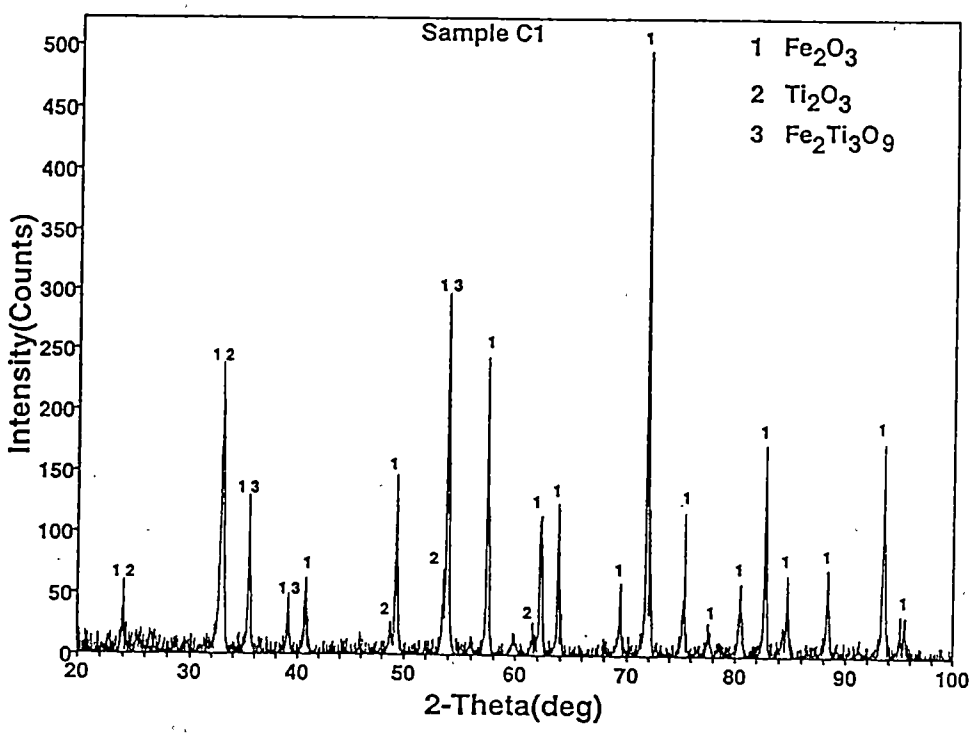


Figure 4.59 (a). X-ray diffraction spectra for C1 sample.

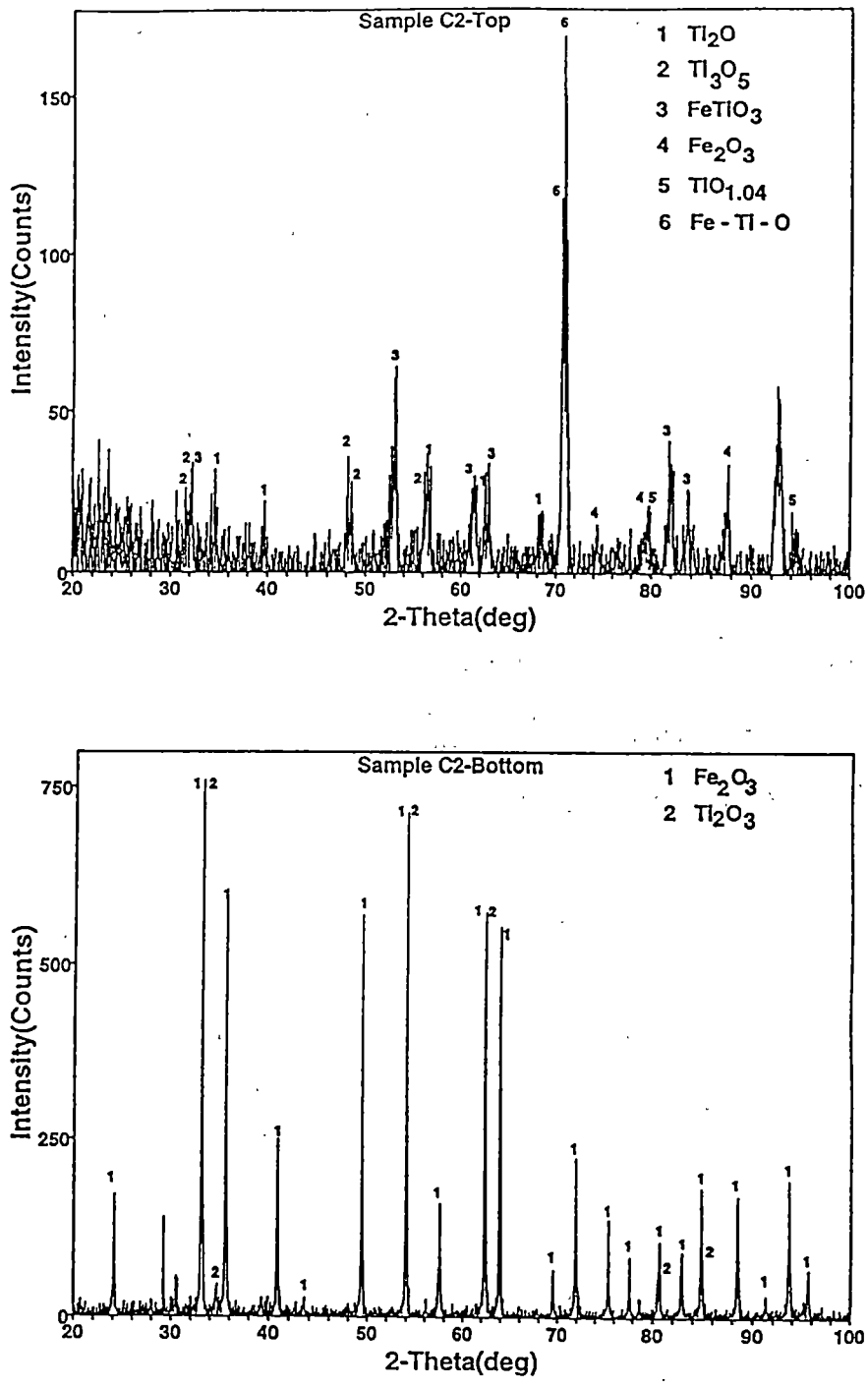


Figure 4.59 (b). X-ray diffraction spectra for C2 top and bottom sample.

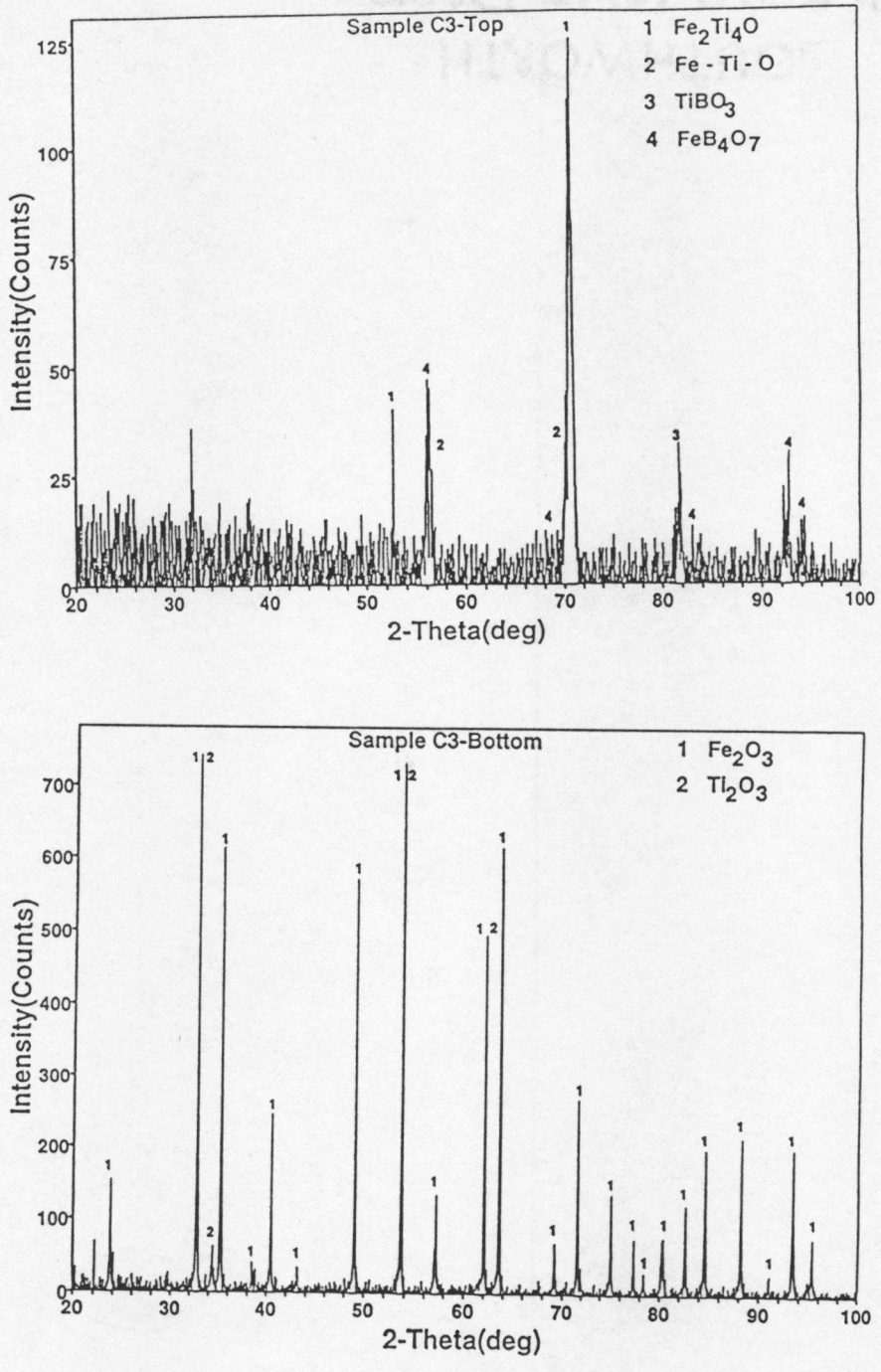


Figure 4.59 (c). X-ray diffraction spectra for C3 top and bottom sample.

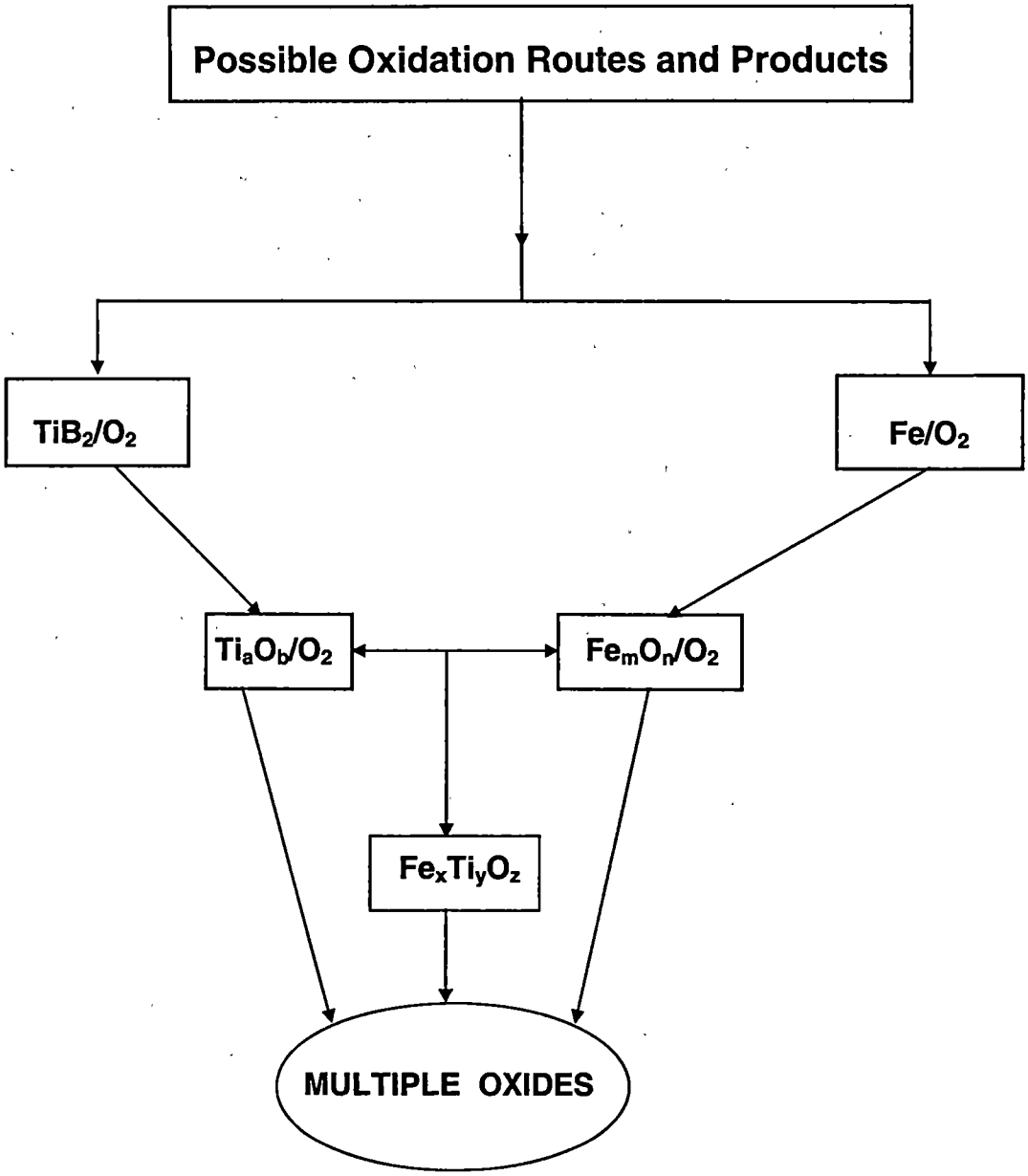


Figure 4.60. A schematic suggesting the possible oxidation routes and products occurring in "composite" TiB_2 coating.

Figure 4.50, which shows formation of oxide layer on the coating. Sharp increase in oxidation rate at 1000°C is attributed to rapid increase in evaporation rate of B_2O_3 at temperature higher than 950°C (117). Apart from evaporation of B_2O_3, there are other factors, which also contribute towards oxidation rate at 800 and 1000°C. After evaporation of entire B_2O_3, a thinner diffusion barrier layer of TiO_2 is left behind on the coated surface along with Fe_2O_3. Iron oxide forms due to oxidation of Fe, which is present as matrix material in the "composite" TiB_2 coating. Hence, now only a composite mixture of TiO_2 and Fe_2O_3 is present as the oxide scale on the surface that is indicated by XRD patterns for A series samples (Table 4.14 and Figure 4.57).

TiO_2 (rutile) is a non-stoichiometric, metal-excess, n-type oxide, which exhibits both titanium interstitial ions and oxygen vacancies. Due to such defect structure, TiO_2 is prone to oxidation by cationic as well as anionic movements (121). Moreover, TiO_2 has a high Pilling Bedworth ratio of 1.95, which causes microcracks and pores in the oxide scale due to compressive stresses in the oxide layer (121). Such microcracks and pores act as sites for oxygen diffusion and enhances the oxidation rate. On the contrary, Fe_2O_3 is a metal deficit, p-type oxide with a rhombohedral crystal structure. In such crystal structure, oxygen ion exists on a close packed hexagonal arrangement with iron ions in interstices that are more mobile (122). Oxidation in Fe_2O_3 occurs by outward cationic movement (122). Since Fe^{+3} ions are more mobile in Fe_2O_3 scale, oxide growth occur outwards at scale/gas interface leaving behind iron vacancies. Coalescence of such vacancies leads to formation of voids and pores, which provide new sites for direct oxidation by oxygen molecule. After long time, these voids and pores can combine and form deep cracks. Such phenomenon is clearly evident in Figure 4.51 for C series

samples. Figure 4.51a shows the porosity at coating/substrate interface. Migration of Fe^{+3} ions outward is clearly visible in Figure 4.52b, which shows vacant space in Fe zone. C2 and C3 samples were exposed for 30 and 50 hours respectively. Coating layer split apart from the substrate due to vacancy condensation and coalescence (Figure 4.51b and 4.51c). This is due to severe oxidation of steel substrate, which causes growth of Fe_2O_3 between boride layer and substrate. Formation of Fe_2O_3 between boride layer and substrate is further confirmed by XRD spectra of the bottom portion of the oxide layer of C2 and C3 samples (Figures 3.9 and 4.59).

In B series samples, some portion of B_2O_3 reacts with Fe_2O_3 to form Fe_3BO_6 as indicated in the following reaction.

$$B_2O_3 + 3Fe_2O_3 = 2\ Fe_3BO_6 \qquad (4.22)$$

Synthesis of borates through reaction of B_2O_3 with oxides has been reported earlier (120). Formation of borate further reduces protective covering layer of B_2O_3 and hence increases the oxidation rate. Fe_3BO_6 peaks are indicated in each of B series samples (Figure 4.58 and Table 4.13). There is, however, no Fe_3BO_6 formation at 1000^0C, which is probably due to lack of reaction time as B_2O_3 evaporates rapidly. Table 4.14 presents list of other phases present in the oxide scale of B series samples. Complex oxides such as Fe_2TiO_5 and $Fe_3Ti_3O_{10}$ form in B1 and B2 samples whereas $FeTi_5O_{10}$ forms in B3 sample. Physical identification of each of these phases is difficult as they form continuous and composite oxide layer. Formation of such complex multiple oxides is explained through various reactions occurring within the oxide scale. Fe_2TiO_5 forms on reacting with TiO_2 through equation 4.23

$$Fe_2O_3 + TiO_2 = Fe_2TiO_5 \qquad (4.23)$$

Equation 4.24 consists of two reactions which involves decomposition of Fe_2O_3 (Fe^{+3} to Fe^{+2}) and subsequent reaction with TiO_2 to form $Fe_3Ti_3O_{10}$.

$$3Fe_2O_3 + 6TiO_2 = (3\ Fe_2Ti_2O_7) = 2\ Fe_3Ti_3O_{10} + \tfrac{1}{2}\ O_2 \qquad (4.24)$$

Thermodynamically, reduction of Fe^{+3} to Fe^{+2} occurs at temperature greater than 777^0C (117). Such condition holds true in the present case as B series samples were oxidized at 800^0C. B3 sample forms another complex oxide $FeTi_5O_{10}$ that is shown by equation (4.25)

$$Fe_2O_3 + 10\ TiO_2 = 2FeTi_5O_{10} + 3/2O_2 \qquad (4.25)$$

Oxygen molecules are liberated within the complex oxide scale, which further increases the oxidation rate of B series samples by enhancing the oxidation internally (122-123). Such effect is pronounced in Figure 4.53b that shows highly porous oxide with a lamellar structure. Composite and complex nature of oxide is evident from Figure 4.54 which shows cross section of the oxide scale formed on C1 sample. At 1000^0C, oxidation of Fe in the steel substrate gets accelerated such that Fe_2O_3 is the major oxidation product. It also reacts with TiO_2 to form complex oxides such as $Fe_2Ti_3O_9$, $FeTiO_3$, Fe-Ti-O and Fe_2Ti_4O similar to B series samples. Reactions for such oxide formations are listed below.

$$Fe_2O_3 + 3TiO_2 = Fe_2Ti_3O_9 \qquad (4.26)$$

$$Fe_2O_3 + 2TiO_2 = 2FeTiO_9 + \tfrac{1}{2}\ O_2 \qquad (4.27)$$

C series samples also contain Ti_2O_3 oxide that reacts with Fe_2O_3 to form Fe_2Ti_4O through reaction 4.28

$$Fe_2O_3 + 2Ti_2\ O_3 = Fe_2Ti_4O + 4\ O_2 \qquad (4.28)$$

It should be understood that most of the oxides are nonstoichiometric in nature with variable compositions due to excess/deficiency of metal/oxygen ions (121). Such variance in chemical composition leads to formation of unconventional oxides, which causes the change in oxidation mechanism. Simultaneous presence of two or more oxides in the scale also causes change in oxidation kinetics (123). Hence, oxidation of "composite" TiB_2 coating is a very complex phenomenon in the presence of multiple oxides which can be schematically represented as in Figure 4.60.

Surface roughness profile of the top surface of the oxide scale is in accordance with the nature of the oxide formed in three samples A3, B3 and C1. Average surface roughness R_a is least for A3 sample (9.54 μm) as it does not show significant growth of oxide. Slow oxidation rate for A-series samples has already been discussed earlier. Oxide scale grows thicker and rougher with time as it forms several complex oxides. Hence, a higher average surface roughness (14.39 μm) is observed for B3 sample (Figure 4.56b). C1 shows upward growth of coarse Fe_2O_3 grains leading to very high level of roughness (22.37 μm). It has been shown earlier that Fe_2O_3 grows through compact Cr_2O_3 scale in Fe_2O_3-Cr_2O_3 rhombohedral oxide system and eventually forms an outermost layer (121-122). Similar situation holds true for C1 sample where Fe_2O_3-Ti_2O_3 rhombohedral oxide system coexists (Table 4.14) and eventually Fe_2O_3 protrusions cover the entire surface (Figure 4.55c). Fe_2O_3 grains/protrusions on the surface are the main cause for extremely rough surface for C1 sample (Figure 4.55c).

The high temperature oxidation behavior of the "composite" TiB_2 coating has been addressed very critically in terms of kinetics as well as structural morphology of the oxide growth. It was shown that oxidation of the composite coating begins in the

temperature range of 700-800 ^{0}C. The theory about evaporation of protective oxide, B_2O_3 has been discussed and correlated to the TGA experimental observations. However, to further confirm the evaporation of B_2O_3, a novel analytical approach based on neural networks was adopted (124).

4.5.3 Neural Network Application to High Temperature Oxidation

A. Background

Neural computing provides an approach that is closer to human perception and recognition than conventional computing. The special characteristics of neural computing such as learning by example, distributed associative memory, fault tolerance, pattern recognition and synthesis make them useful in a variety of applications (125-127). Neural computing has found its application in various fields like digital communication, environmental pollution analysis, sales forecasting, biomedical systems such as diagnosing coronary artery disease, jet engine diagnostic system and detect aircraft in synthetic aperture radar images (125). However, neural network has its own limitations in general. One of the limitations is that good results can be obtained only if the data to be tested is within the range of the trained data. Extrapolation of the test results beyond the trained data is likely to give errors. Secondly, there are always end effects in the trained and tested software, which cause increased error in the output data at the end points (127). To avoid the end effects in training the data, theoretical data points should be added to the input parameters.

In the present study, neural computing has been used to determine the oxidation kinetics of the composite TiB_2 coating. The use of neural network software reduces the

required extensive experimental study by learning the trend of the mass gain curves and predicting the effect of variables (temperature and time) within its region of learning. The "Professional II/ PLUS version 5.23" neural networks software was trained from the initial experimental results obtained from thermogravimetric analyzer (TGA). The trained software was used to obtain the required data for several intermediate temperatures. This simulated data in addition to the experimental data was used to determine rate constant (k) and activation energy (E) for the oxidation studies. This computational technique assisted in better understanding of the oxidation mechanism occurring in laser deposited "composite" TiB_2 coating.

B. Application of Professional II/Plus Software

Professional II/PLUS is a powerful and versatile neural network proto-typing and development system. It enables us to design, build, train, test and display paradigms that solve complex, real-world problems. The areas in which neural network solutions apply are limited only by the imagination. Professional II/Plus uses a graphical network display and mouse-driven user interface in each version of this product (Neural Ware, Inc., 1995). The Professional II/PLUS software was supplied with the results obtained from the thermogravimetric experiments as its input data. The software was trained with these input data using a Back Propagation (Back-prop) network paradigm. Back-prop calculates an error between the desired and the actual output and propagates the error information back to each node in the network. The back-propagated error drives the learning at each node. The network was built with one input layer, output layer and one or two hidden layers. Three input parameters were chosen for this network which

included one functional link. Usually functional links assist in a better classification of the given problem and in increasing the learning rate significantly. The experimental data was trained using the neural networks individually for every two temperature zones of the oxidation analysis. The reason is due to a large variation in the output values, determined as the gain in mass of the sample per unit area of the sample (m/A), for each temperature at which oxidation was carried out. The input parameters chosen were time (t) and temperature (T). The square root of time ($t^{1/2}$) was added as a functional link. The output parameter was obtained in the form of the mass gained per unit area of the sample undergoing oxidation i.e. m/A (gm/sq.cm). The number of hidden layers and the number of elements in each hidden layer for the three sets of trained data are tabulated in Table 4.15.

Table 4.15. List of Layers and Corresponding Elements used for Neural Computations

Trained data (Temp ^{0}C)	Input layer	Hidden layer 1	Hidden layer 2	Output layer
600 & 700	3	6	3	1
700 & 800	3	4	0	1
800 & 1000	3	4	0	1

All these parameters were chosen after repeated trials were performed with various permutations to get a learned system with the least root mean square error and a fast learning rate. A tanH (hyperbolic) type of activation function was used in this system. The system was trained using a Supervised Learning or Associative Learning where the input is provided and matched with the output. The software was trained using Delta-Rule for 100,000 cycles, where the root mean square error dropped to less than one percent of the initial values. In this type of learning rule, the error computed as the difference between the desired output and the actual output is transformed by the derivative of the transfer function. This error is then back propagated till it reaches the first layer.

The trained data, corresponding to the experimental results of the oxidation analysis at 600^0C, 700^0C, 800^0C and 1000^0C was used to obtain the output data in terms of the gain in mass/area of the sample at temperatures between these temperatures at steps of 50^0C. The data provided by the neural networks was tested for one of the intermediate points (at 900^0C) to test the consistency of the simulated values with the experimentally obtained results. To understand the kinetic behavior and observe any change in the oxidation mechanism, output data is required at intermediate temperatures. Applying neural networks to the existing data generated the required intermediate data. Such exercise obviates the need of performing additional experiments at intermediate temperatures.

The Professional II/Plus Software (version 5.23) was used to train the experimental data in three sets using the procedure stated in the previous section. The trained data obtained in each case gave less than 1% error from the experimental results.

The trained software for each set of data was then used to study the effect of temperature on oxidation at steps of 50^0C. The results obtained were plotted as a square of the output parameter, i.e. mass/area (gm/sq. cm) against the time provided for oxidation at different temperatures. The output data obtained between the temperature ranges, 600^0C to 700^0C, 700^0C to 800^0C and 800^0C to 1000^0C are represented in Figures 4.61, 4.62 and 4.63 respectively. These plots were divided into three temperature zones due to the wide range in the y-axis data i.e. $(\text{mass gain/area})^2$. In all these figures, hollow legends indicate the experimental data obtained from TGA whereas the filled legends represent the data simulated from neural networks. Due to very low errors (less than 1%) between the experimental and the trained data, the curves seem to merge at several points. The experimental and the trained neural network data are represented to show the consistency in the trained software. In Figure 4.61, the nature of the curves appear to be non-linear due to an enlargement in the y-axis values (in a small range of values) in comparison to Figure 4.62 and 4.63. However, all these curves show a linear fit with errors less than 10 %. An oxidation experiment was conducted in the TGA at 900^0C as a test run to obtain the consistency of the data that was simulated by the software. The output experimental curve is included in Figure 4.63 as a comparison to the simulated data. A linear fit of these data provided the rate constants of the oxidation reaction in the system. At 900^0C, though the experimental data deviated from the simulated data, the error in their rate constants was less than 10%. The relatively large error in the test run data in comparison to the trained data could possibly be because of large variation in the output data in the temperature range, 800^0C to 1000^0C. Moreover, less number of data points over a larger

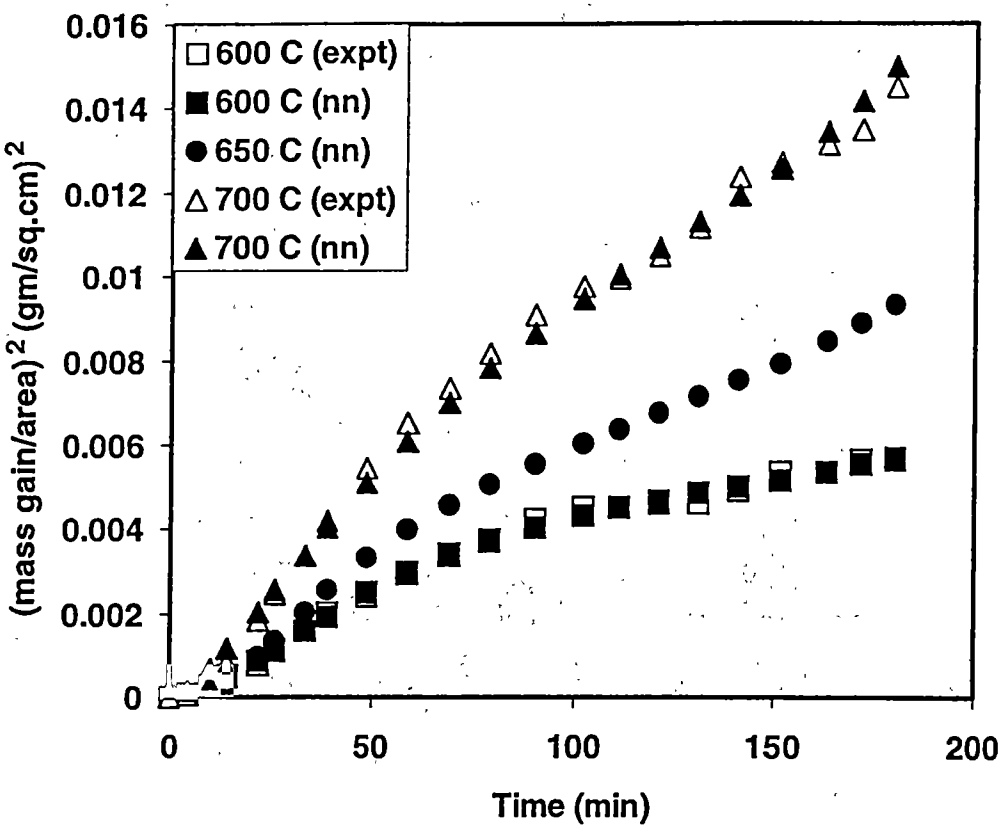


Figure 4.61. Oxidation kinetics for "composite" TiB_2 coating for trained and experimental data between 600-700^{0}C.

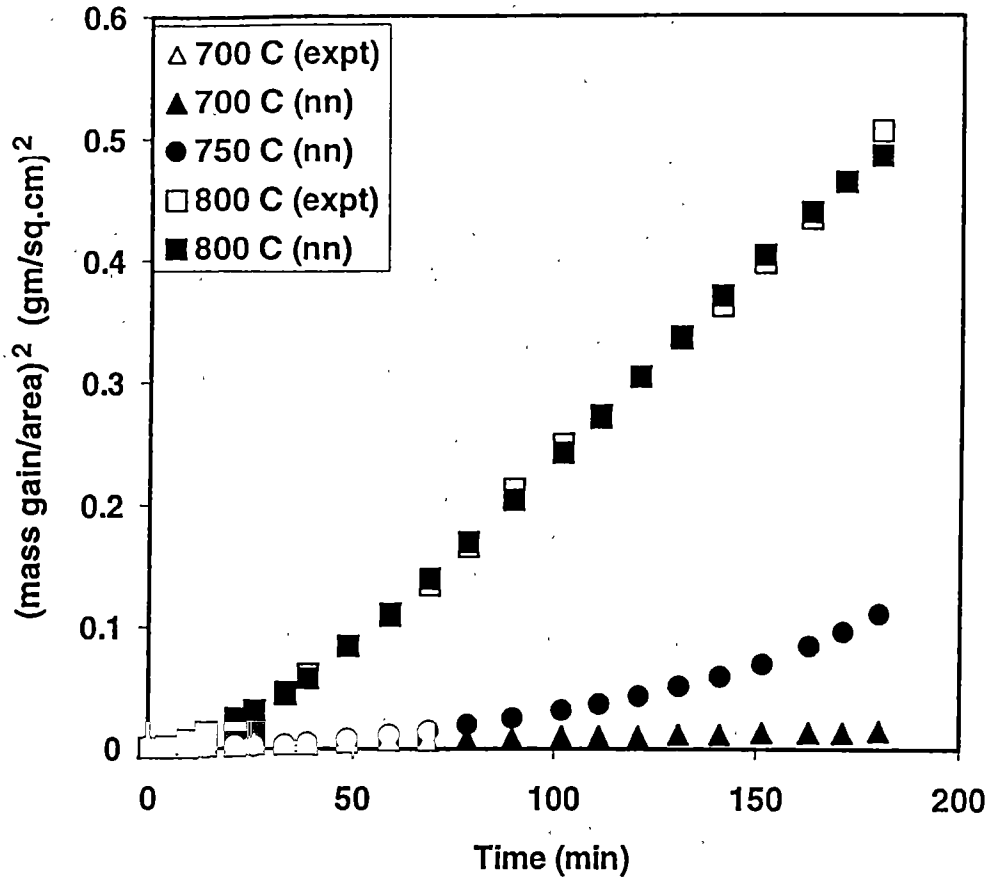


Figure 4.62. Oxidation kinetics for "composite" TiB_2 coating for trained and experimental data between 700-800^{0}C.

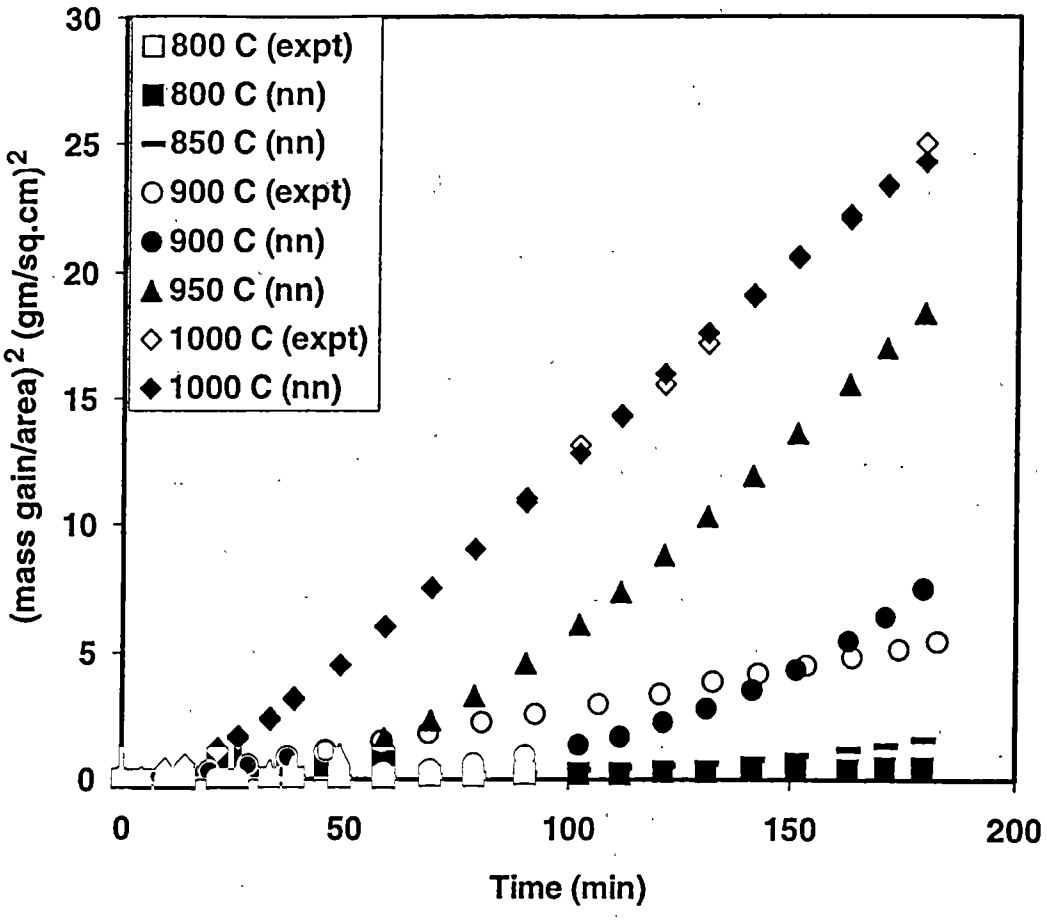


Figure 4.63. Oxidation kinetics for "composite" TiB_2 coating for trained and experimental data between 800-1000^{0}C.

range of temperatures were available to train the system, which could cause these errors. Table 4.16 lists rate constant (k) values for all these temperatures.

The lower values of rate constant k, for 600^0C and 700^0C are indicative of very slow oxidation (Figure 4.61 and Table 4.16). Oxidation rate increases at 750^0C and reaches alarmingly high values at 1000^0C (Figures 4.62 and 4.63). Reaction rate constant k, for 750^0 is an order of magnitude higher than that of 600^0C and 700^0C (Table 4.16).

Table 4.16. Oxidation Kinetic Constants for Composite-TiB_2 Coating using TGA Experiments and Interpolated Data using Neural Networks

Temperature, T (^{0}C)	Rate Constant, k ($gm^2\ cm^{-4}\ min^{-1}$)		Error (%)
	Experimental	Neural Network	
600	4×10^{-5}	4×10^{-5}	0
650	____	5×10^{-5}	____
700	9×10^{-5}	9×10^{-5}	0
750	____	4×10^{-4}	____
800	2.5×10^{-3}	2.5×10^{-3}	0
850	____	6×10^{-3}	____
900	0.0288	0.0263	8.7
950	____	0.0809	____
1000	0.1307	0.1304	0.23

In the earlier discussion it was proposed that evaporation of B_2O_3 start at 750^0C, which causes increase in oxidation rate at 800^0C (117). This fact is pronounced and validated in the ***simulated*** oxidation curve for 750^0C in Figure 4.62 that shows incipient increase in oxidation rate. Oxidation rate at 1000^0C is very high (Figure 4.63 and Table 4.15), which is attributed to the rapid increase in evaporation rate of B_2O_3 at temperature higher than 950^0C (117). Rapid evaporation of B_2O_3 at 950^0C is evident from the ***simulated*** curve in Figure 4.63. Hence, it could be seen that oxidation rate curves for 750^0C and 950^0C, which were simulated using neural networks are in accordance with the oxidation mechanism of "composite" TiB_2 coating. Details of these oxidation products and mechanism have been presented in earlier section 5.1.2. These values of the rate constant (k) were further used to obtain the activation energy of the oxidation reaction occurring at these temperatures. The Arrhenius plot for this system is shown in Figure 4.64. The activation energy was about 210 kJ/mol for this system in the temperature range, 600^0 to 1000^0C. It is very close in comparison to the experimental data, which resulted in activation energy of 205 kJ/mol (16). Also, such values of activation energy are similar to the earlier study of oxidation of TiB_2 based cermet (117). These observations suggest that interpolated data using neural networks is in close accordance with the experimental data. Moreover, it does not indicate any change in oxidation mechanism at intermediate temperatures.

In the present work, time and temperature were the major oxidation parameters that were varied during oxidation studies. Further work would be carried out to study the effect of environment (air or pure oxygen) and their flow rates on these TiB_2 coated samples exposed to oxidation tests. The same software can be used with changes in the

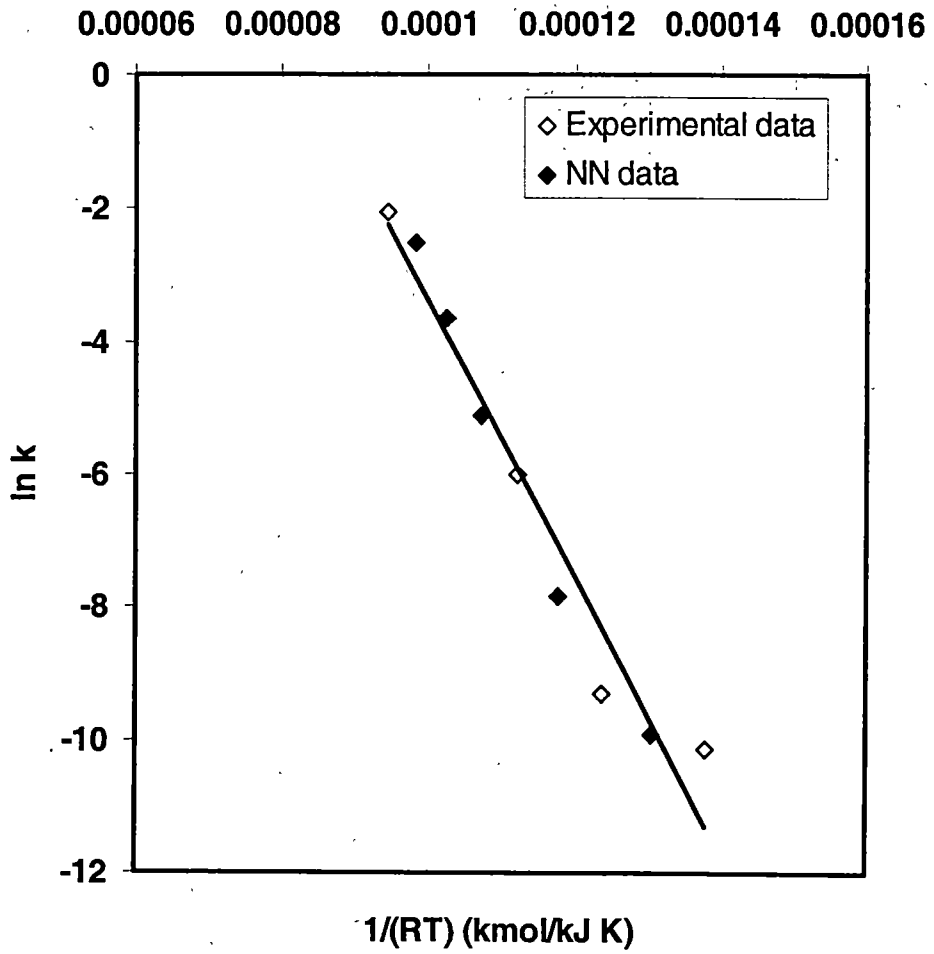


Figure 4.64. Arrhenius plot for parabolic rate of oxidation using the neural network data.

number of input and hidden layers and their corresponding elements to obtain the required output. This would help in reducing the extensive experimental work normally required to determine the effect of various process variables on the kinetics and mechanism of TiB_2 oxidation.

Before the advent of modern tools like neural networks, regression techniques were used to compute such interpolated data to provide expressions for reaction kinetics. In the present study, as a means of comparison with the application of neural networks, regression techniques were used to obtain a rate expression explaining the kinetics of the oxidation experiments. However, the results obtained by this method highly deviated from the experimental data. It could be due to a wide range of the output data with increase in the temperature of oxidation. By using the neural network software, the system can be trained in individual parts to avoid such errors as seen in regression analysis. Though a similar procedure can be used in regression analysis, with the increase in the number of input parameters (environment, gas flow rate) the analysis will become very complex unlike neural networks.

Apart from excellent wear and erosion resistance and significantly high oxidation resistance, Titanium diboride (TiB_2) has excellent corrosion resistance against metallic aluminum and cryolite, which makes it suitable candidate as a coating material for inert cathode used in Hall-Heroult cell for aluminum electrolysis (44,83). Moreover, TiB_2 is easily wetted by liquid aluminum due to low contact angle (128). Such unique combination of properties of TiB_2 makes it an ideal candidate to be used as mold coating material for aluminum casting industry.

4.6 High Temperature Corrosion Resistance Against Liquid Aluminum

The current operation in aluminum melting and casting facilities involves the application of sintered or bonded ceramic parts in molten aluminum delivery systems (e.g. in die casting and squeeze casting), as well as ceramic slurry coatings on metal and ceramic parts and molds (e.g. aluminum melting furnaces and tools, permanent and semi-permanent casting molds) for protection against corrosion by liquid aluminum (86). The ceramic slurry coatings on molds and tools have a short life and need frequent touch-up, resulting in high cost operation and frequent casting quality problems. Moreover, these slurry coatings are deposited using plasma spray technique, which does not promote metallurgical bond formation with the substrate. Hence, these coatings spall off and have a poor service life. In view of such requirements, it is essential to develop a suitable coating system (material and technique) for steel dies, molds and other parts that are subjected to liquid Al environment. Hence, "composite" TiB_2 coating deposited by laser based technique was evaluated for its corrosion resistance against liquid Al by carrying out "dip test" experiments. Details of such experimentation have been provided earlier in section 3.6.

Figure 4.65a shows the results of overall visual examination of the coated side of the surface. There is no peeling or spalling of the coating on the upper half (25 mm) of the samples. The lower half (25 mm) of the sample which was immersed in liquid A 356 Al shows differential attack for two samples viz. D4 and D24 that were immersed in liquid A356 Al for 4hr and 24 hr respectively. D24 shows a much severe attack in comparison to D4. Some sort of localized attack (necking) is also observed at the midway location of the D24 sample. Figure 4.65b shows similar features for the

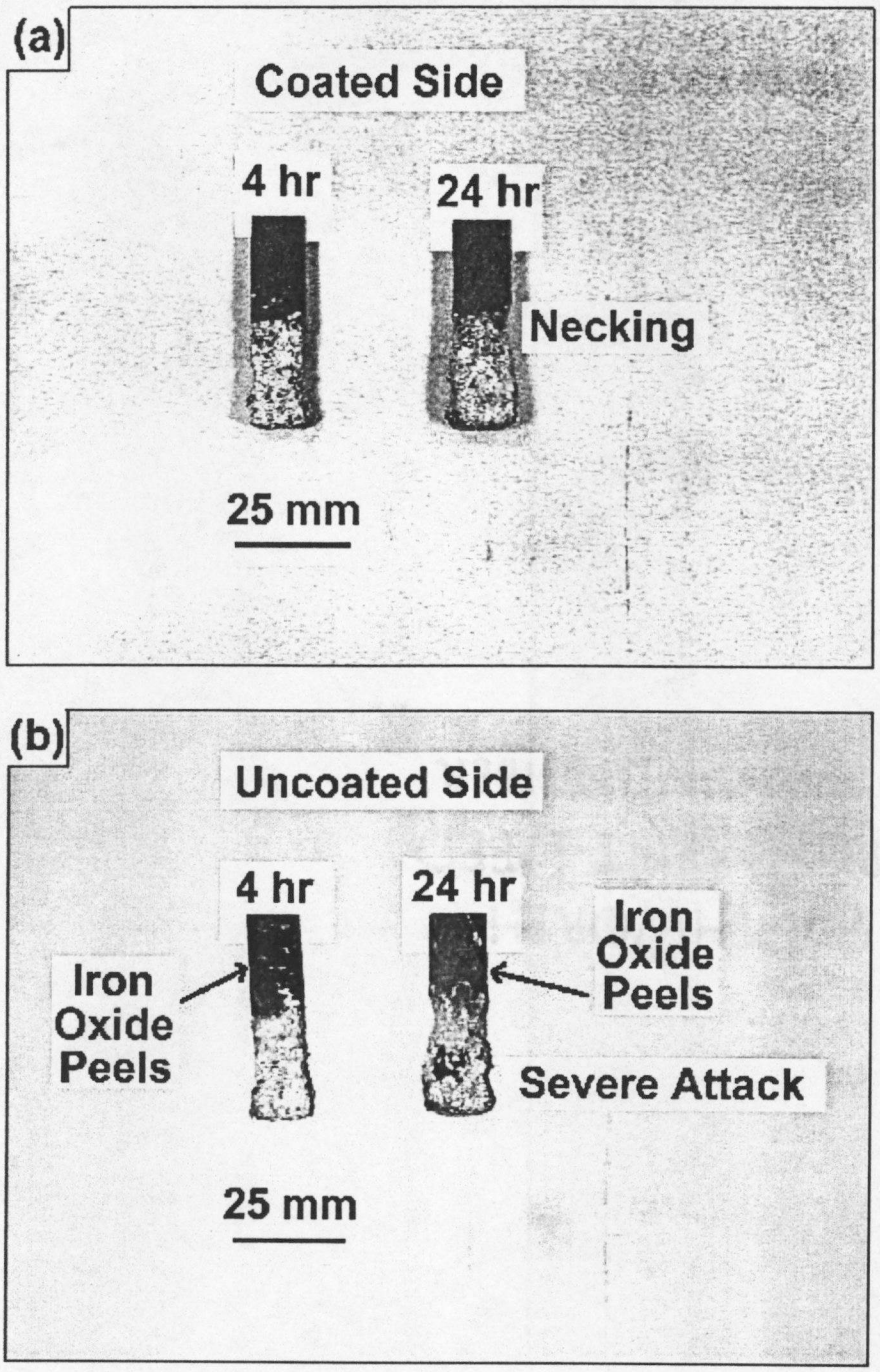


Figure 4.65. Overall view of D4 and D24 samples after dip test (a) coated side and (b) uncoated side.

uncoated side of these samples. In general, the attack by liquid metal is more severe as compared to coated side. This is prominently observed in D24 sample. Top half (25 mm) portion of the uncoated side of the samples show iron oxide layer with some peels. Such peel layers were not observed on the coated side, as TiB_2 is oxidation resistant in air upto 1000 ^{0}C (56).

Low magnification SEM micrographs of D4 and D24 samples are shown in Figure 4.66a and 4.66b respectively. Coating is metallurgically bonded in both cases. However, some cracks are observed through the thickness of the coating. Sample D4 does not show significant erosion due to liquid Al. Cracking is relatively severe and broader in D24 sample (Figure 4.66b). This fact will be further discussed later in this section. These cracks, however, do not run parallel to the coating/substrate interface and thereby avoid any chance of delamination of the coating. Figure 4.67a is high magnification view of one such crack in sample D4. The corresponding x-ray maps for Al, Ti and Fe distribution are also presented in Figure 4.67b, 4.67c and 4.67d respectively. It is clearly evident that there is no Al penetration into the crack. The crack formation is solely due to thermal shocking. It should be recalled that after dip test, samples were taken out from furnace at 780 ^{0}C and cooled in air. Although cooling was done on ceramic plate, it appeared to be rapid enough to cause thermal cracking. Moreover, coated samples were covered with a layer of A356 Al (Figure 4.65) which has very high thermal conductivity as compared to TiB_2 (56,102). Such features enhance the thermal shocking and promote crack forming in the coating.

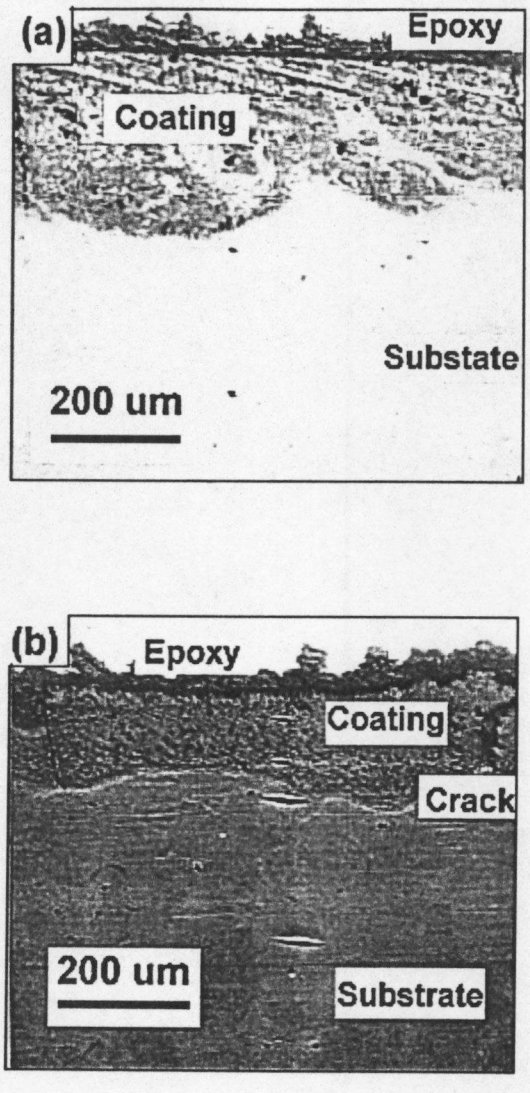


Figure 4.66. Low magnification SEM micrograph of the cross section of TiB_2 coated AISI 1010 steel (a) dipped in liquid A356 Al for 4 hours and (c) dipped in liquid A356 Al for 24 hours.

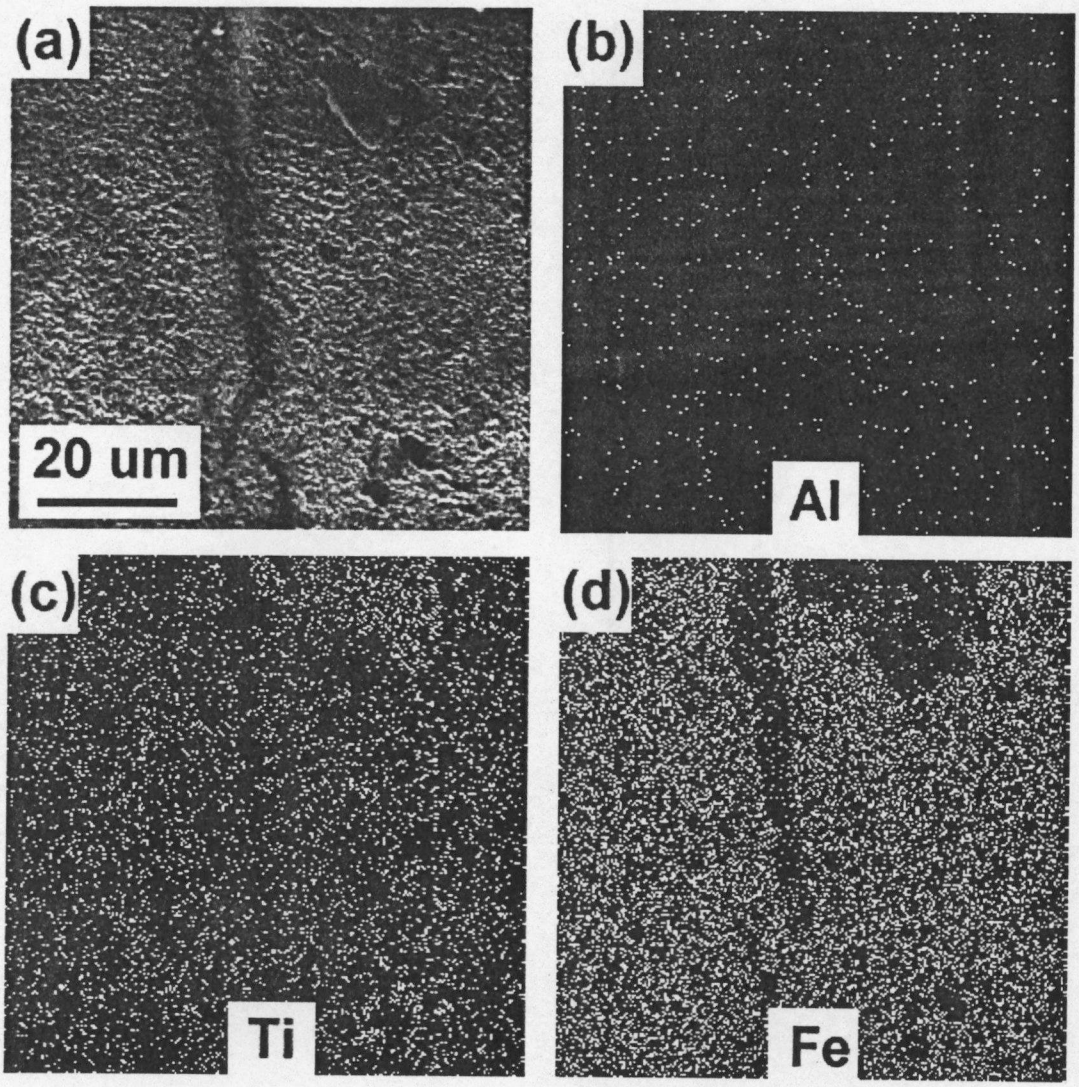


Figure 4.67. (a) High magnification SEM micrograph of the crack in the coating and corresponding X-ray elemental maps for (b) Al, (c) Ti and (d) Fe.

High magnification SEM micrographs shown in Figure 4.68 and 4.69 elucidate the nature of attack of liquid Al on TiB_2 coating in a more significant manner. It can be clearly observed that erosion of TiB_2 coating due to liquid Al attack on D4 sample was insignificant (Figure 4.68). X-ray maps show the presence of Al on top surface of the coating but it has not penetrated the coating (Figure 4.68a and 4.68b). Coating is intact, hard and "composite" in nature and free from Al. The relative hardness in the coating and the substrate can be observed from the indentation marks in Figure 4.68a. Figure 4.69a shows the eroded coating due to liquid Al in sample D24. It is clearly visible that nature of the attack is far more severe in comparison with D4 sample. Figures 4.69a and 4.69b show the penetration of liquid Al upto the depth 50 μm in the coating. A broad crack is also observed but it is free from Al. This further corroborates our earlier conclusion that cracks are formed due to thermal shocking rather than penetration by liquid Al. Erosion of the coating by liquid Al penetration is possible due to several factors. Liquid Al can attack Fe selectively which is present in the "composite" coating and in the process can dislodge TiB_2 particles. Also, TiB_2 particles get dissolved into smaller particles and to possibly decrease the corrosion resistance to liquid Al. Figure 4.70 is a high magnification view of the "composite" coating zone with a homogeneous distribution of fine TiB_2 particles. It is evident that TiB_2 particles have dissolved into finer particles after being subjected to liquid Al immersion at 780 ^{0}C for 24 hours. Figure 4.68a is a similar view of the D4 sample. TiB_2 particles are, however, larger in shape here as the degree of dissolution is not as high as observed for D24 sample. This observation supports the hypothesis that dissolution of TiB_2 particles assist in erosion of coating by liquid Al.

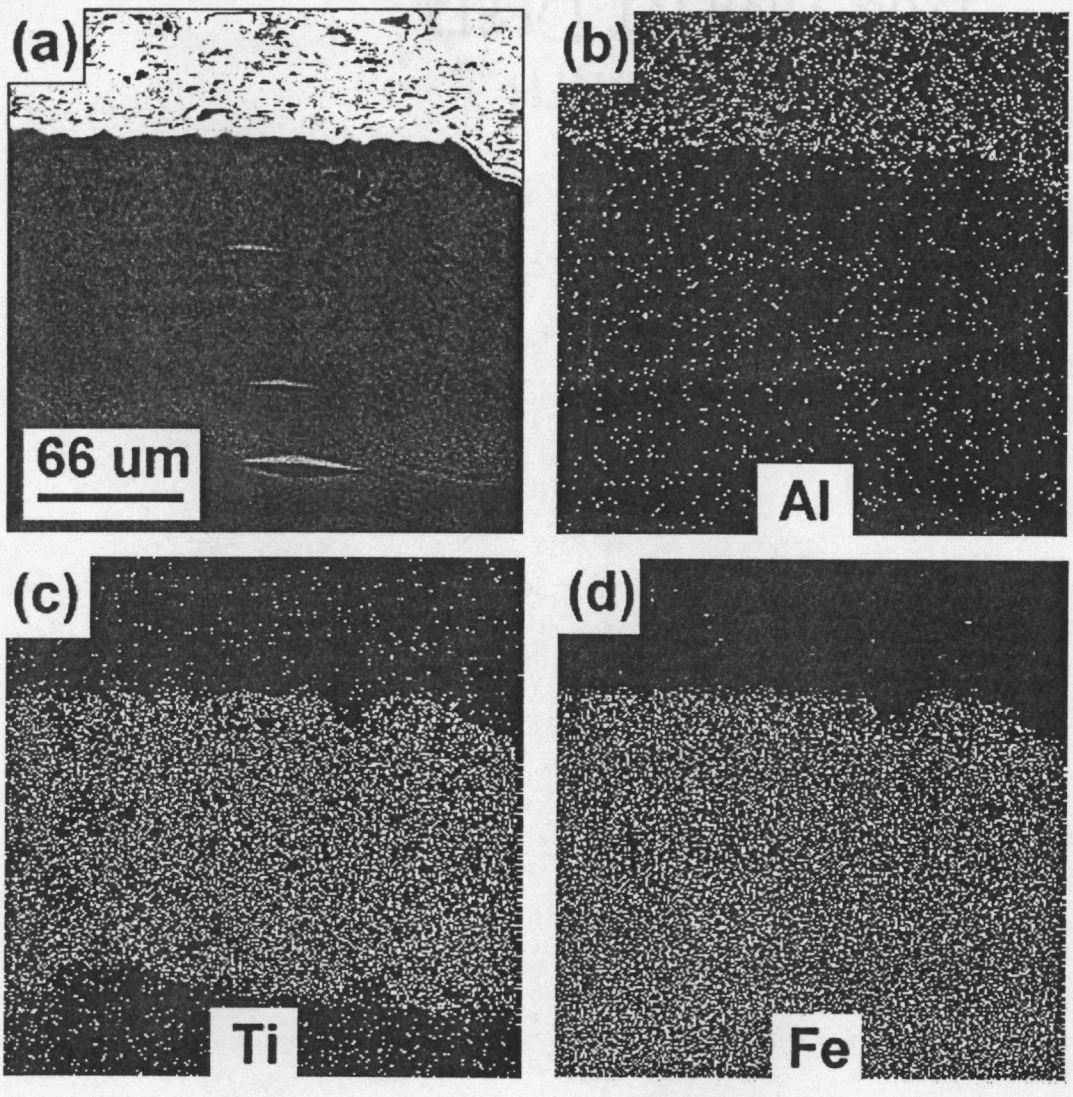


Figure 4.68. (a) High magnification SEM micrograph of the cross section of D4 sample and corresponding x-ray elemental maps for (b) Al, (c) Ti and (d) Fe.

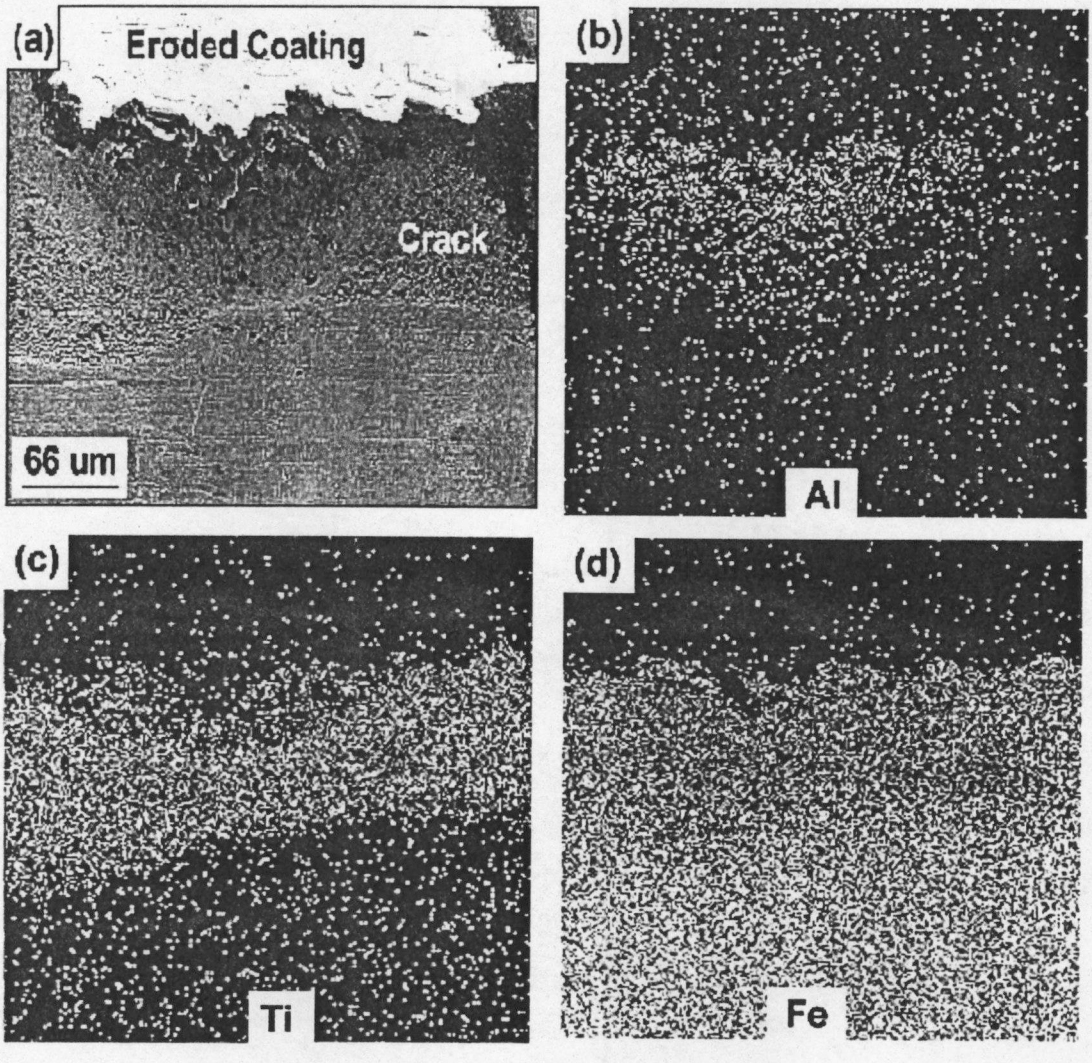


Fig 4.69. (a) High magnification SEM micrograph of the cross section of D 24 sample and corresponding x-ray elemental maps for (b) Al, (c) Ti and (d) Fe.

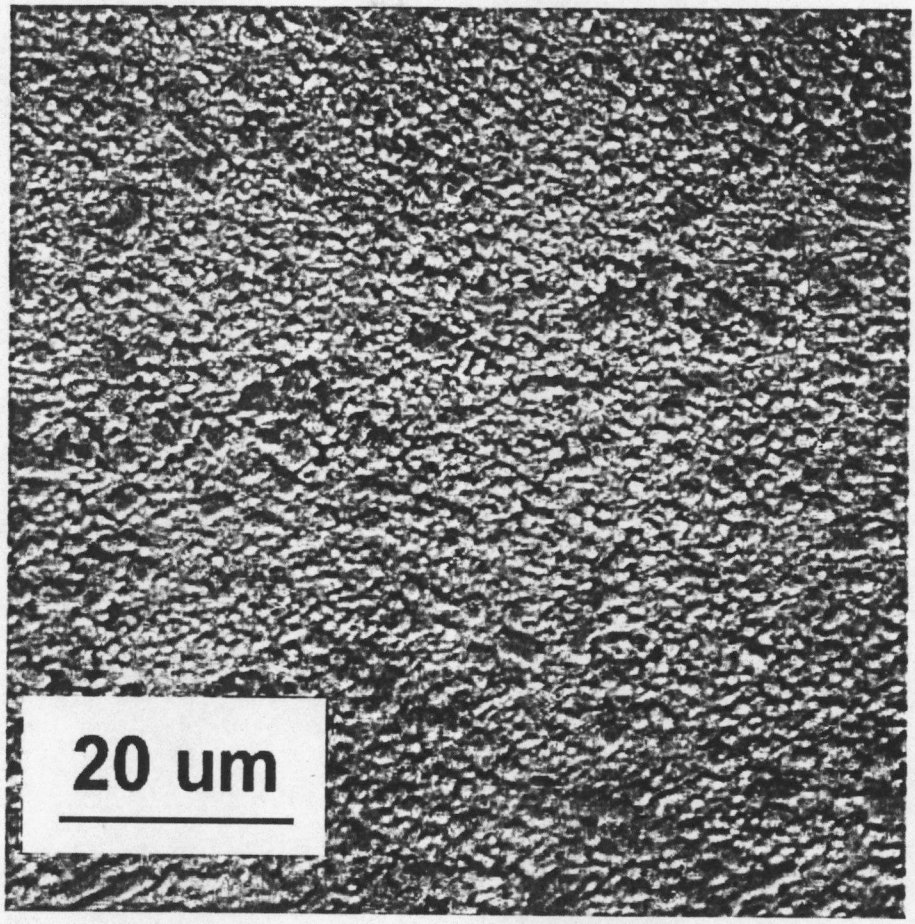


Fig 4.70. High magnification view of the dissolved TiB_2 particles in the laser melt zone in sample D 24.

Figures 4.71a, 4.71b and 4.71c show the x-ray diffraction spectra of the undipped, D4 and D24 samples respectively. Phase(s) present in various samples are listed in Table 4.17. Undipped sample shows all the major peaks of TiB_2 and Fe. Traces of metastable phase(s) such as Fe_aB_b and Ti_xB_y are also indicated which is a consequence of non-equilibrium synthesis experienced in laser processing. D4 sample also shows TiB_2 and Fe as major peaks along with few minor peaks of $Ti_{1.87}B_{50}$ phase. On the contrary, D24 reveals most of the peaks of this metastable phase $Ti_{1.87}B_{50}$. This observation suggests that some TiB_2 has transformed into $Ti_{1.87}B_{50}$. Also, degree of such transformation increases with time as observed for sample D24. It is quite possible that such phase transformation from TiB_2 to $Ti_{1.87}B_{50}$ also assists in accelerating the erosion of coating.

$Ti_{1.87}B_{50}$ is a low density (2.65 gm/cc) metastable phase with tetragonal crystal structure (129). $Ti_{1.87}B_{50}$ has cell dimensions of a = 8.83 Å and c = 5.07 Å. Such large size cell with low density suggests porous structure, which could be pervious to liquid Al when, subjected to prolonged period exposure. It has been observed earlier that TiB_2 often transforms to other metastable phase(s) of Ti_xB_y type with a porous crystal structure (130). D24 sample shows few Al_2O_3 peaks, which are present due to oxidation of top surface of liquid Al. Formation of brittle intermetallic phase such as FeAl is also indicated for the D24 sample that has been discussed below.

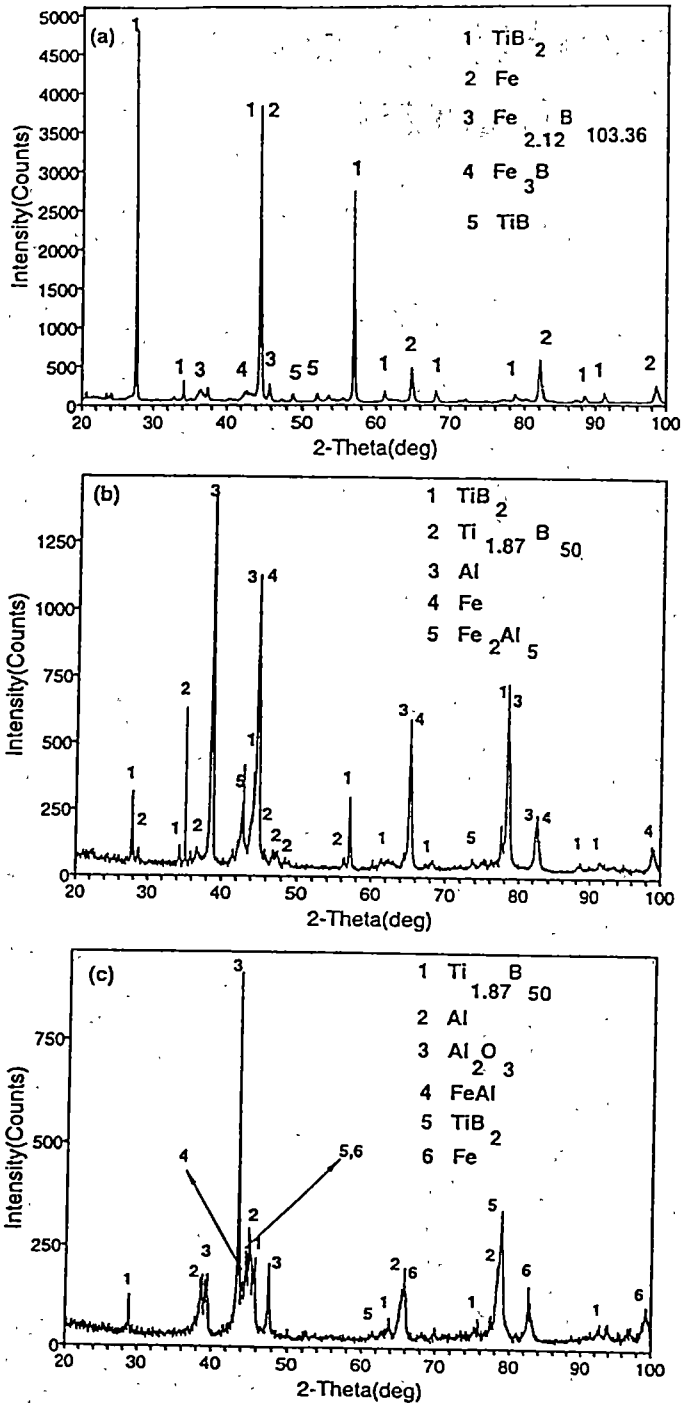


Figure 4.71. X-ray diffraction spectra from the top surface of TiB_2 coated AISI 1010 steel sample in (a) undipped condition, (b) after dipping in liquid A356 Al for 4 hours and (c) after dipping in liquid A356 Al for 24 hours.

Table 4.17. Crystal Structure of the Relevant Phases Present in Different Samples

Undipped Sample (Coated Side)		D4 Sample (Coated Side)		D24 Sample (Coated Side)	
Phase Observed	Crystal Structure	Phase Observed	Crystal Structure	Phase Observed	Crystal Structure
TiB_2	Hexagonal	TiB_2	Hexagonal	TiB_2	Hexagonal
Fe	BCC	Fe	BCC	Fe	BCC
TiB	Orthorhombic	Al	FCC	Al	FCC
Fe_3B	Tetragonal	$Ti_{1.87}B_{50}$	Tetragonal	$Ti_{1.87}B_{50}$	Tetragonal
$Fe_{2.12}B_{103.36}$	Rhombohedral	Fe_2Al_5	Orthorhombic	FeAl	Cubic (B2)
				Al_2O_3	Hexagonal

Figure 4.72a is a SEM micrograph illustrating of the attack of liquid Al on the uncoated side of AISI 1010 steel of D4 sample. Steel surface shows severe cracking and erosion of the material. Some of the eroded Fe has been trapped in Al as evident from corresponding x-ray maps in Figures 4.72b and 4.72c. The relative difference in the size of microhardness indentations elucidates the difference in hardness of various locations. Table 4.18 provides a comprehensive listing of microhardness values at various locations in different samples.

Spot C in Figure 4.72a suggests formation of some hard phase. It is possible that after prolonged hours of exposure to liquid Al, some Fe may react to form Fe-Al based

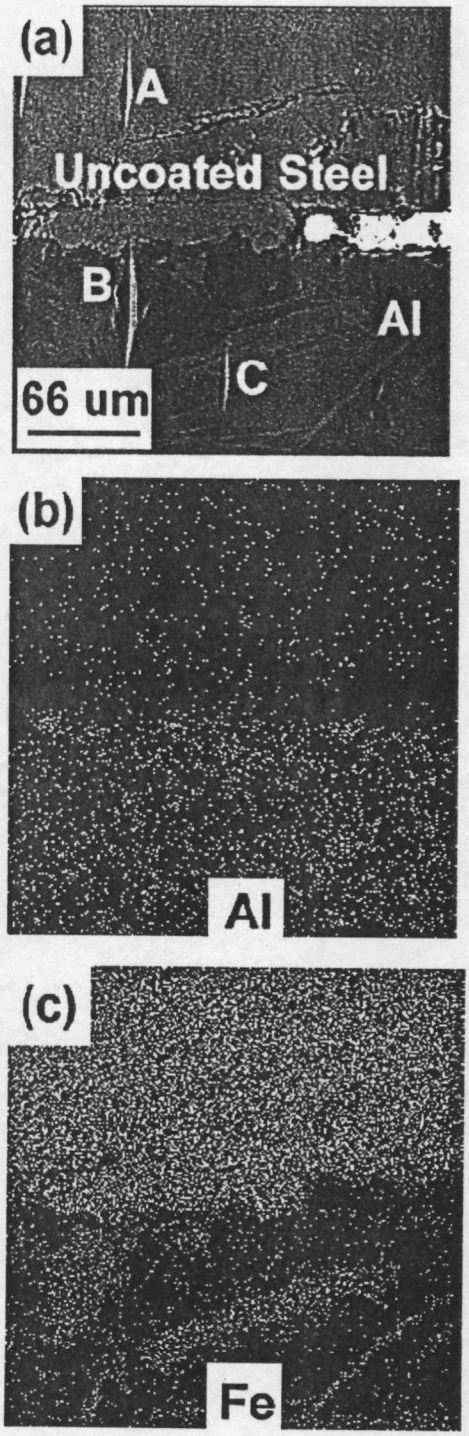


Figure 4.72 (a) SEM micrograph showing the attack of liquid A356 Al on uncoated side of D4 sample and corresponding x-ray elemental maps for (b) Al and (c) Fe.

intermetallics. Table 4.18 and x-ray diffraction spectrum (Figure 4.72b) of sample D4 suggests presence of Fe_2Al_5 intermetallic. In an earlier study based on reactive synthesis of Fe and Al, formation of Fe_mAl_n type hard intermetallics at a temperature lower than critical temperature has been indicated (131).

Table 4.18. Microhardness Values at Various Locations for D4 and D 24 Samples

Sample	Location	Microhardness (Knoop)
D4	1. Coating (Laser Melt Zone)	635 ± 38
	2. Heat Affected Zone	194 ± 21
	3. Uncoated Steel (spot A in Figure 4.73a)	179 ± 25
	4. Al rich side (spot B in Figure 4.73a)	104 ± 12
	5. Al rich side (spot C in Figure 4.73a)	595 ± 30
D24	1. Coating (Laser melt zone)	485 ± 28
	2. Heat Affected Zone	148 ± 18
	3. Uncoated Steel (spot A in Figure 4.75)	149 ± 21
	4. Al rich side (spot B in Figure 4.75)	532 ± 22

The attack of liquid A356 Al increases with time on uncoated steel. Such behavior is revealed in Figure 4.73 that shows the "severe attack" on uncoated side of D24 sample. Figure 4.73 shows a low magnification micrograph with the corresponding x-ray maps for Fe and Al elemental distribution. Liquid Al has attacked uncoated AISI 1010 steel

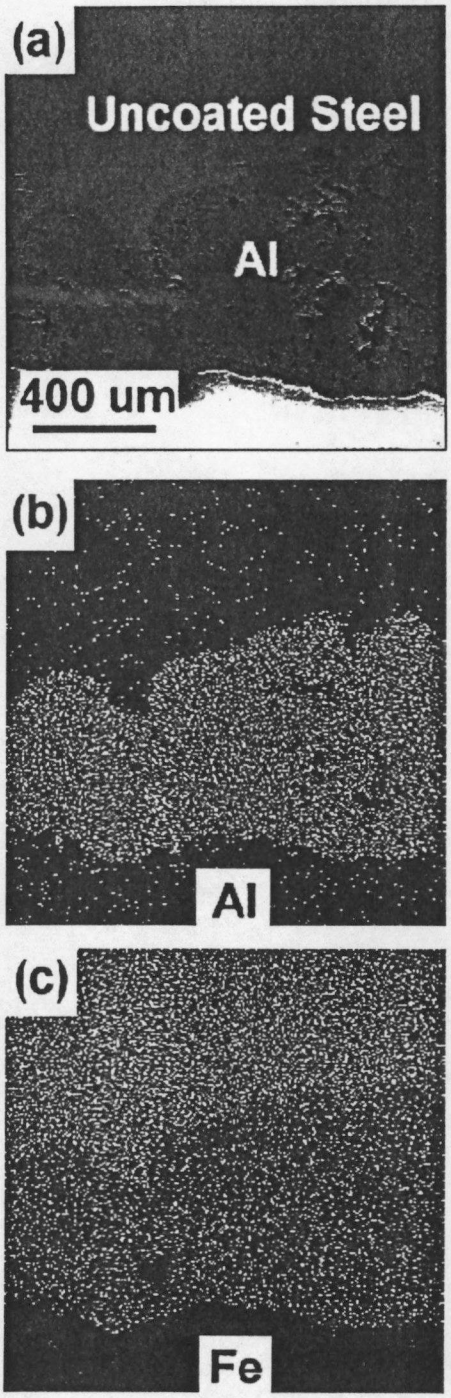


Figure 4.73 (a) Low magnification SEM micrograph showing the massive attack of liquid A356 Al on uncoated side of D 24 sample and corresponding x-ray elemental maps for (b) Al and (c) Fe.

and eroded Fe similar to D4 sample. However, degree of attack is far more severe for D24 sample as it was exposed to liquid Al for longer period. High magnification view of the eroded steel/Al interface is shown in Figure 4.74. Formation of hard and brittle phase in Al rich zone is indicated by the size of microhardness indentation. The brittleness of the phase is indicated by the cracks emanating from and near the edges of indentation (spot B in Figure 4.74(a)). X-ray diffraction spectrum of C24 sample (Figure 4.72c) also confirms formation of hard and brittle Fe-Al based intermetallic.

Laser deposited TiB_2 coating on AISI 1010 steel has shown significant corrosion resistance to liquid Al. However, it is envisaged that by proper control of processing parameters such as precursor composition, laser power and traverse speed, TiB_2 coating can be tailored with regard to morphology and content for further improvement in corrosion resistance to liquid Al.

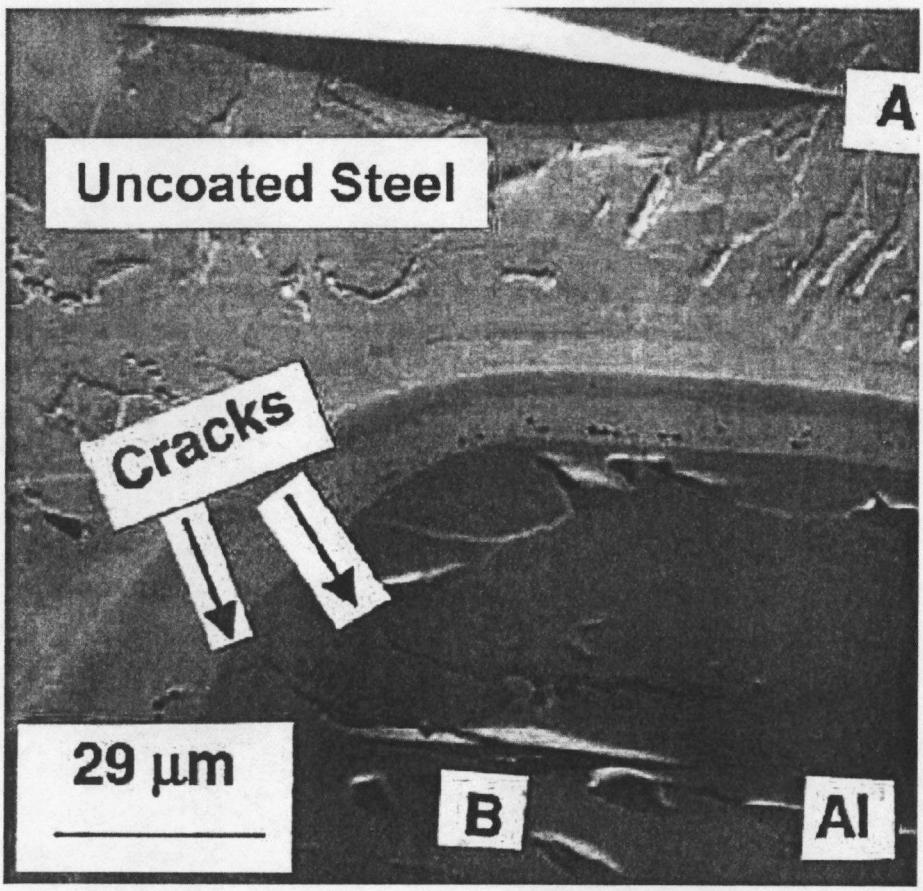


Fig 4.74. High magnification SEM micrograph showing the microhardness indentations and massive attack of liquid A356 Al on uncoated side of D 24 sample.

Part -5

CONCLUSIONS

5. CONCLUSIONS

A study on laser surface engineering of TiB_2 coating on AISI 1010 steel was carried out at Department of Materials Science and Engineering, Center for Laser Applications of The University of Tennessee Space Institute. Ultrahard and wear resistant TiB_2 was deposited on 1010 steel using industrial grade 2 kW Nd:YAG laser. Processing parameters were optimized within a fixed envelope to synthesize an adherent and defect free coating. A detailed characterization of the coating has been performed using electron microscopy (scanning and transmission), EDS and x-ray diffractometry. Several experiments were performed to evaluate the mechanical properties (e.g. hardness, elastic modulus, interfacial strength, fracture morphology), tribological properties (wear resistance, coefficient of friction) and high temperature oxidation and corrosion properties. The major conclusions derived from these investigations are listed below:

A. Microstructural Features

- TiB_2 has been deposited on AISI 1010 steel using laser surface processing. A uniform, continuous and crack free coating is obtained. Coating is "composite" in nature comprising TiB_2 particles and Fe from steel trapped in laser melt zone. Needle/acicular shaped boride particles are uniformly distributed in the melt zone. An adherent and metallurgically sound interface is obtained.
- Microstructure consists of various cellular dendrites and fine equiaxed dendrites indicative of complex solidification process and very high cooling rates within the melt zone.

- Existence of metastable phase(s) such as Fe_xB_y and Ti_mB_n is observed, which is characteristic feature of non-equilibrium synthesis by laser energy. The presence of metastable phase(s) has been confirmed by HRTEM and SAD patterns.
- A nano-size reaction zone occurs between TiB_2 particle and Fe suggesting formation of metastable phase(s) in trace amount. The size of reaction zone at the ceramic/metal interface is approximately 100 nm. The reaction products are nano-crystalline in nature.
- TiB_2/Fe interface is atomically smooth and sharp with very little mismatch. Also, interface is sound with no evidence of cracking or delamination.
- Defects such as stacking faults, twins and dislocations are observed within the TiB_2 particle.
- Coating is superhard in nature.

B. Mechanical Properties

- Elastic modulus, E of the composite boride coating increases with increasing laser processing speed. Highest E value of 477.3 GPa was achieved for coating in LSE 3 sample which was processed at the highest traverse speed of 200 cm/min.
- Theoretical elastic modulus values are lower than experimental elastic modulus as latter include effect of dissolution of ultra fine TiB_2 particles in Fe matrix and metastable phase formation such as Fe_aB_b and Ti_mB_n. Dissolution of ultrafine TiB_2 particles in Fe matrix in coating region has been corroborated by TEM micrograph and corresponding EDS analysis and SAD pattern.

- Elastic modulus of Fe rich matrix containing dissolved ultra fine TiB_2 particles and traces of metastable phase(s) of type Fe_aB_b and Ti_mB_n is 355 GPa, which is 1.5 times higher than elastic modulus of AISI 1010 steel.
- The interfacial energy for the coating/substrate system is very high (265 J/m^2) suggesting a strong and adherent interface. There is no crack propagation along the coating/substrate interface that confirms the high interfacial energy.
- $|K_c|^{experimental}$ is 6.63 MPa $m^{1/2}$ for the TiB_2/Fe interface , which is higher than the fracture toughness of TiB_2 ceramic.
- Four-point bend test is the most reliable technique to evaluate the interfacial strength of the laser engineered coatings.
- Fracture of the "composite" TiB_2 coating under uniaxial tensile stresses occurs by mixed mode but is dominated by brittle fracture. The fracture in TiB_2 particles is essentially brittle and occurs by cleavage. Fe-rich matrix acts as a bridge/binder between these TiB_2 particles.

C. Tribological Properties

- Wear resistance of TiB_2 coated surface is very high than AISI 1010 steel.
- Coefficient of friction values for LSE coated TiB_2 coating is 0.59.
- Wear in LSE deposited TiB_2 coating occurs by plastic deformation of the soft matrix phase, Fe from a "composite" layer on the surface.

D. High Temperature Oxidation

- Oxidation rate for "composite" TiB_2 coating was parabolic for all test temperatures of 600, 700, 800 and 1000^0C. Rate of oxidation was very slow for 600 and 700^0C whereas 800 and 1000^0C showed higher oxidation rates. Activation energy, Q, was computed as 205 kJ/mol.
- Long duration exposure of composite TiB_2 coating at 600^0C did not show significant oxide scale formation.
- A protective layer of B_2O_3 forms which evaporates at 775^0C causing an increase in rate of oxidation at 800^0C. A porous and lameller oxide scale forms on "composite coating and grows in thickness for longer duration of exposure. Several complex mixed oxides of type Ti_aO_b, Fe_mO_n and $Fe_xTi_yO_z$ are formed within the scale, which further complicates the oxidation mechanism.
- Oxidation is even more severe at 1000^0C due to rapid evaporation of B_2O_3. The attack is severe at coating/substrate interface due to formation of Fe_2O_3 that causes delamination of coating layer from the substrate. Oxide surface gets rough in nature as complex oxides nucleates and grow upwards on the surface.
- Neural network was successfully used to study the oxidation behavior of composite TiB_2 coating at intermediate temperatures of 750^0 and 950^0C. It minimizes the number of experiments and predicts the trend curves with acceptable errors.
- There was no change in the oxidation mechanism of TiB_2 coating in the temperature range of 600^0C to 1000^0C in comparison to earlier minimal experimental study. The activation energy for oxidation of composite TiB_2 coating was 210kJ/mol, which is

similar to earlier studies. Evaporation of B_2O_3 was suggested by the simulated curves at 750^0 and 950^0C without performing the experiments.

- Regression techniques, performed to compare with the neural network study, highly deviated results from the experimental results. This suggests that the application of neural networks is preferred over regression analysis in this study.

E. High Temperature Corrosion Resistance Against Liquid Aluminum

- Laser deposited ultrahard "composite" TiB_2 coatings on AISI 1010 steel has shown significant corrosion resistance to liquid A356 Al.
- Sample immersed in liquid A356 Al for 4 hr at 780 ^{0}C showed better resistance in comparison to the sample immersed for 24 hour. There was no attack/penetration of liquid Al in the coating layer. Few cracks through the thickness of the coating layer were observed as a consequence of thermal shock.
- Sample immersed in liquid A356 Al for 24 hr at 780 ^{0}C was attacked in a much severe way. Liquid Al has penetrated into top 50 μm of the coating. It has been attributed to dissolution of TiB_2 particles and its phase transformation to $Ti_{1.87}B_{50}$.
- Uncoated side of both samples (D 4 and D 24) have shown massive attack on AISI 1010 steel surface. Steel gets eroded by liquid Al and is trapped within solidified Al rich zone. It also forms hard and brittle Fe-Al based intermetallics.

Part - 6

RECOMMENDATIONS FOR THE FUTURE WORK

6. RECOMMENDATIONS FOR THE FUTURE WORK

As a continuation of the present work on the laser surface engineering of TiB_2 on AISI 1010 steel, following work is recommended:

- Particle shape of TiB_2 has changed from faceted polygons to acicular/needle shaped after laser surface engineering. The major phase present in these acicular shaped particles as obtained by x-ray diffraction was hexagonal TiB_2. The phenomenon behind the shape change of TiB_2 particles is not thoroughly understood. It is suggested that a detailed study is required to investigate the solidification and growth mechanism in TiB_2 particles as a consequence of LSE. Though, such study had been initiated by the author, it was beyond the scope of the present work to take it to the conclusive end.
- Thermal strains are present in the TiB_2 coating, which causes an increase in the value of estimated interfacial energy, G_{ss}. It is suggested that advanced mathematical modeling could be applied on the present material system to predict the measure of thermal strain energy in the laser processed TiB_2 coating.
- Mathematical modeling of wear and friction in composite coating could be studied.

LIST OF REFERENCES

REFERENCES

1. Mazumder, J., Laser Assisted Surface Coatings: in *Metallurgical and Ceramic Protective Coatings,* ed. Kurt H. Stern, Chapman and Hall, London (1996), 74 -111.
2. Steen, W. M., Surface Engineering with Laser, *Metals and Materials*, vol. 1 (12) (1995), 730-736.
3. Gnanamuthu, S., Laser Surface Treatment, *Optical Engineering*, vol. 19 (5) (1980), 783-792.
4. Molian, P. A., Principles and Applications of Lasers for Wear-Resistant Applications: in *Surface Modification Technologies,* T. S. Sudarshan and D.G. Bhat ed., The Metallurgical Society, Warrendale, PA, (1988), 237-265.
5. Folkes, J. A., Developments in Laser Surface Modification and Coating, *Surface and Coatings Technology*, vol. 63 (1994), 65-71.
6. Chande, T. and Mazumder, J., Mass Transport in laser Surface Alloying, *Appl. Phys. Lett.,* vol. 41 (1982), 42-53.
7. Molian, P.A., Non-equilibrium Phases in Laser Processed Fe-0.2 wt% C-20 wt% Cr Alloys, *Mater. Sci. Engg.,* vol. 50 (1983), 241-245.
8. Christodoulu, G. and Steen, W. M., *Lasers in Materials Processing* (ed. E. A. Metzbower) ASM, Metals Park, OH, (1983) 38-53.
9. Molian, P.A., Effect of Fusion Zone Shape on the Composition Uniformity of Laser Surface Alloyed Iron, *Scripta Metall.*, vol. 16 (1982), 65-68.

10. Schussler, A. and Zum Gahr, K-H., Laser Processing of Metal-Ceramic Composite Multilayer, *Journal De Physique IV*, vol. 1 (1991), c7.121- c7.126.

11. Beurs, H. De and De Hosson, J. Th. M., Wear Induced Hardneing of Laser Processed Chromium-Carbon Steel, *Scripta Metall.*, vol. 21 (1987), 627-632.

12. Hu, C. and Baker, T. N., Laser Processing to Create in-situ Al-SiC_p Surface Metal Matrix Composites, *J. Mater. Sci.*. vol. 30 (1995), 891-897.

13. Zhou, X. B. and De Hosson, J. Th. M., A Reaction Coating on Aluminum Alloys by Laser Processing, *Scripta Mater.*, vol.28, (1993), 219-224.

14. Hirose, A and Kobayashi, K. F., Formation of Hybrid Clad Layers by Laser Processing, *ISIJ International,* vol. 35 (6) (1995), 757-763.

15. Khedkar, J., Khanna A.S. and Gupt, K.M., Tribological Behavior of Plasma and Laser Coated Steels, *Wear,* vol. 205 (1997), 220-227.

16. Agarwal, A., Katipelli, L.R. and Dahotre, N. B., Elevated Temperature Oxidation of Laser Surface Engineered Composite Boride Coating on Steel, *Metal and Mater. Trans A.* (in press) (1999).

17. Katipelli, L.R., Agarwal, A. and Dahotre, N.B., Laser Surface Engineered TiC Coating on 6061 Al Alloy: Microstructure and Wear, *Appl. Surface Science* (in press) (1999).

18. Agarwal, A and Dahotre, N.B., Comparative Wear in Titanium Diboride Coatings on Steel using High Energy Density Processes, *Wear*, (communicated) (1999).

19. Agarwal, A and Dahotre, N.B., Laser Deposited Titanium Diboride Coating for Protection of Molten Aluminum Handling Tools and Molds, *Lasers in Engg.*, (in press) (1999).

20. Zhou, X. B. and De Hosson, J. Th. M., Spinel/Metal Interfaces in Laser Coated Steels: A Transmission Electron Microscopy Study, *Acta Metall.Mater*, vol.39 (10) 1991, 2267-2273.

21. Zhou X. B. and De Hosson, J. Th. M., Martensitic Transformations in Laser Processed Coatings, *Acta Metall. Mater*, vol. 42 (4) (1994),1155-1162 .

22. Hegge, H. J., Boetje, J and De Hosson, J. Th. M., Oxidation Effects During Laser Cladding of Aluminum with SiC/Al Powders, *J. Mater. Sci.*, vol. 25 (1990), 2335-2338.

23. Burg, M. van de and De Hosson, J. Th. M., Metal-Ceramic Interfaces in Laser Coated Aluminum Alloys, *Acta Metall. Mater*, vol. 41 (9) (1993), 2557-2564.

24. Schuster, J. C., Physical Chemistry of Ceramic-Metal Interface Formation, *Trans JWRI*, vol. 23(2) 1994,143-147.

25. De Hosson, J. Th. M., Laser Synthesis and Properties of Ceramic Coatings, in *Intermetallic and Ceramic Coatings*, eds. N. B. Dahotre and T.S. Sudarshan, Mercel and Dekker, New York. (1999), 307-439.

26. Evans A. G. and Rühle, M., Microstructure and Fracture Resistance of Metal/Ceramic Interfaces, *MRS Bulletin*, vol. 10 (1990), 46-50.

27. Nakahashi, M., Joining of Ceramics to Metals (1): Interfacial Reactions Between Ceramic and Metals, *Welding International*, vol.10 (10) (1996), 765-770.

28. Burg, M. van de and De Hosson, J. Th. M., Mechanical Performance of Metal-Ceramic Interfaces Produced by Laser Processing, *Interface Science*, vol.3 (1995), 107-118.

29. Li, J. G., Wetting of Ceramic Materials by Liquid Silicon, Aluminum and Metallic Melts Containing Titanium and Other Reactive Elements: A Review, *Ceramics International,* vol. 20 (1994), 391-412.

30. Laurent, V., Chatain, D. and Eustathopoulos, N., Wettability of SiC by Al and Al-Si Alloys, *J. Mater. Sci.,* vol.22 (1987), 244-250.

31. Zhou, X. B. and De Hosson, J. Th. M., Wetting Kinetics of Liquid Aluminum on an Al_2O_3 Surface, *J. Mater. Sci.,* vol. 30 (1995), 3571-3575.

32. Zhou, X. B. and De Hosson, J. Th. M., Reactive Wetting of Liquid Metals on Ceramic Substrates, *Acta. Mater.*, vol. 44(2) 1996, 421-426.

33. Kosolapova, Ya. T., *Handbook of High Temperature Compounds: Properties, Production, Application,* Hemisphere Publishing Corporation, New York (1990), 651-688.

34. Upadhyaya, G. S., Wetting of Ceramic by Metal Melts: An Electronic Approach, in *Sintered Metal-Ceramic Composites,* ed. G. S. Upadhyaya, Elsevier Science Publishers, Amsterdam (1984), 41-50.

35. Agarwal, A. and Dahotre, N. B., Pulsed Electrode deposition of Superhard Boride Coatings on Ferrous Alloys, *Surf. Coat. & Tech.*, vol. 106(2/3) 1998, 242-250.

36. Agarwal, A. Dahotre, N. B. and Sudarshan, T.S., Evolution of Interface in Pulsed Electrode Deposited Titanium Diboride on Copper and Steel, *Surf. Engg.*, vol.15(1) (1999), 27-32.

37. Agarwal, A. and Dahotre, N. B., Pulsed Electrode Surfacing of Steel with TiC Coating: Microstructure and Wear Properties, J. *Mater. Engg. Performance*, vol. 8(4) (1999), 479-486.

38. C. Mroz, Advanced Materials and Powders, *Ceramic Bulletin*, vol. 78 (6) (1999), 77-81.

39. Williams, W. S. and Kaloyeros, A. E., Synthesis, Characterization and Potential Applications of Amorphous Coatings of TiC and TiB_2 in Hard Coatings Based on Borides, Carbides and Nitrides, in *Hard Coatings Based on Borides, Carbides & Nitrides,* eds. A. Kumar, Y.W. Chung and R.W.J. Chia, Proc. TMS Annual Meeting, San Antonio, TX, (1998), pp. 269-280.

40. Yu, M. and Shivpuri, R., Characterization of Coatings for H13 Dies in Aluminum Die Casting by Accelerated Erosion and Corrosion Tests, in *Elevated Temperature Science and Technology I,* eds. N. B. Dahotre, J. M. Hampkian and J. J. Stiglich, The Minerals, Metals and Materials Society, (1995), 85-94.

41. Leuctner, R. E., Krzanowski, J. E. and Brock, W.F., Pulsed Laser Deposition of Mixed Metal Carbide Coatings, in *Hard Coatings Based on Borides, Carbides & Nitrides,* eds. A. Kumar, Y.W. Chung and R.W.J. Chia, Proc. TMS Annual Meeting, San Antonio, TX (1998), 233-247.

42. Brockmeyer, J.W., Williams, B. E. and Heng, S., Characterization and Testing of Layered HfC/SiC Protective Coatings, in *Hard Coatings Based on Borides, Carbides and Nitrides*, eds. A. Kumar, Y.W. Chung and R.W.J. Chia, Proc. TMS Annual Meeting, San Antonio, TX (1998), 259-268.

43. Herman, H. and Sampath, S., Thermal Spray Coatings, in *Metallurgical and Ceramic Protective Coatings,* ed. Kurt H. Stern, Chapman and Hall, London (1996), 261-289.

44. Billehaug, K. and Oye, H., Inert Electrodes for Hall-Heroult Process, *Aluminum Verlag* (Dusseldorf), vol. 56(100) (1981), 250-252.

45. Singh, J., Quli, F., Wolfe, D. E., Scriempf, J. T. and Singh, J., An Overview: Electron Beam-Physical Vapor Deposition Technology-Present and Future Applications in Surface Engineering, in *Science and Technology I*, eds. A. Kumar, Y.W. Chung. J.J. Moore and J.E. Smugeresky, Proc. TMS Annual Meeting, San Diego, CA (1999), 59-74.

46. Agarwal, A. and Dahotre, N. B., Insitu Synthesis of Intermetallic and Ceramic Coating Using Pulse Electrode Surfacing, *Scripta Mater.*, communicated (1999).

47. Barnett, S. A., Madan, A. and Kim, I. W., Structure and Mechanical properties of Nitride Based Superlattices with Immiscible Layers, *Hard Coatings Based on Borides, Carbides and Nitrides*, eds. A. Kumar, Y.W. Chung and R.W.J. Chia, Proc. TMS Annual Meeting, San Antonio, TX (1998), 189-201.

48. Kumar, A., Chan, H. L. and Shamsuzzoha, M.,Growth and Characterization of Crystalline Metal Nitrides Coatings Prepared by Pulsed Laser Deposition Method, *Hard Coatings Based on Borides, Carbides and Nitrides*, eds. A. Kumar, Y.W. Chung and R.W.J. Chia, Proc. TMS Annual Meeting, San Antonio, TX (1998), 219-230.

49. Doll, G. L., The Growth and Characterization of BN coatings, in *Hard Coatings Based on Borides, Carbides and Nitrides*, eds. A. Kumar, Y.W. Chung and R.W.J. Chia, Proc. TMS Annual Meeting, San Antonio, TX (1998), 129-142.

50. Feldermann, H., Sebastian, M., Merk, R., Restle, M., Ronning, C. and Hofasss, H., Synthesis and Properties of Cubic BN Thin Films, in *Hard Coatings Based on Borides, Carbides and Nitrides*, eds. A. Kumar, Y.W. Chung and R.W.J. Chia, Proc. TMS Annual Meeting, San Antonio, TX (1998), 143-152.

51. Richter, F., Pintaske, R., Hahn, J and Welzel, T., Deposition of Cubic BN by Magentron Sputtering: Process Diagnostics and Film Characterization, in *Hard Coatings Based on Borides, Carbides and Nitrides*, eds. A. Kumar, Y.W. Chung and R.W.J. Chia, Proc. TMS Annual Meeting, San Antonio, TX (1998), 153-168.

52. Wu, M. L., Lin, X. W., Dravid, and Y. W. Chung, Y. W., Structural Characterization of CN/ZrN Superlattice Coatings, in *Hard Coatings Based on Borides, Carbides and Nitrides*, eds. A. Kumar, Y.W. Chung and R.W.J. Chia, Proc. TMS Annual Meeting, San Antonio, TX (1998), 17-24.

53. Alexandrescu, R., Crunteanu, A., Cireasa, R., Cojocaru, S., Morjan, I and Kumar, A., Carbon Nitride Thin Films Synthesized from the Gas-Phase by laser-induced reactions: A Parametric study, in *Hard Coatings Based on Borides, Carbides and Nitrides*, eds. A. Kumar, Y.W. Chung and R.W.J. Chia, Proc. TMS Annual Meeting, San Antonio, TX (1998), 73-88.

54. Rabalais, J. W. and Marton, D., Hyperthermal Particle Enhanced Deposition of Materials, in *Hard Coatings Based on Borides, Carbides and Nitrides*, eds. A. Kumar, Y.W. Chung and R.W.J. Chia, Proc. TMS Annual Meeting, San Antonio, TX (1998), 25-34.

55. George, M.A., Weimer, J.J. and Kumar, A., Surface Characterization of TiN films Prepared by Sputter and Pulsed Laser Deposition Techniques, in *Hard Coatings Based on Borides, Carbides and Nitrides*, eds. A. Kumar, Y.W. Chung and R.W.J. Chia, Proc. TMS Annual Meeting, San Antonio, TX (1998), 203-209.

56. Cutler, R. A., Engineering Properties of Borides, in *Engineering Materials Handbook: Ceramic and Glasses*, ASM International, vol. 4 (1991), 787-803.

57. Dempsey, E., Bonding in Refractory Hard Metals, *Philos. Mag.*, vol. 3(86) (1963), 285-299.

58. Friedel, J., *The Physics of Metals,* ed. J. M. Ziman, Cambridge, Cambridge University Press, (1969).

59. Hagg, G., *Z. Phys. Chem*, vol. B6 (1929), 221-224.

60. Samsonov, G. V., and Vinitskii, I. M., *Handbook of Refractory Compounds,* IFI Plenum Data Company, New York, (1980), 441-442.

61. Akselsen, O. M., Advances in Brazing of Ceramics, *J. Mater. Sci.*, vol. 27 (1992) 1989-2000.

62. Komvopoulos, K., Effects of Process Parameters on the Microstructure, Geometry and Microhardness of Laser-Clad Coating Materials, *Materials Science Forum,* vol. 163-165 (1994), 417-422.

63. Komvopoulos, K and Nagarathnam, K., Processing and Characterization of Laser-Cladded Coating Materials, *J. Engg. Mater. Tech.*, vol. 112 (1990), 131-143.

64. Agarwal, A and Dahotre, N. B., Laser Surface Engineering of Steel for Hard Refractory Ceramic Composite Coating, *Inter. J. Refractory Mater. & Hard Metals,* vol. 17(4) 1999, 283-293.

65. DeHosson, J. Th. M. De and Burg, M. Van Den, Metal-Ceramic Interfaces Produced by Laser Melt Injection Processing, *Materials & Manufacturing Processes,* vol.10 (6) (1995), 1285-1294.

66. Oliver, W. C. and Pharr, G. M., An Improved Technique for Determining Hardness and Elastic Modulus Using Load and Displacement Sensing Indentation Experiments, *J. Mater. Res.*, vol. 7(6) (1992),1564-1583.

67. Mencik, J. and Swain, M. V., Design of Contact Loaded Components Using Data from Depth Sensing Microindentation Tests, *Surf. Engg.*, vol. 13(6) (1997), 498-504.

68. Vancoille, E., Celis, J. P. and Roos, J. R., Mechanical Properties of Heat Treated and Worn PVD TiN, (Ti, Al) N, (Ti, Nb) N and Ti(C,N) Coating as Measured by Nanoindentation, *Thin Solid Films*, vol. 224 (1993), 168-176.

69. Pharr, G. M., Harding, D. S. and Oliver, W. C., Mechanical Properties and Deformation Behavior of Materials having Ultra-fine Microstructures, eds. M. Nastasi et al., *Proc. NATO Advanced Study Institute on Mechanical Properties and Deformation Behavior of Materials having Ultra-fine Microstructures*, Porto Novo, Portugal, Kluwer Academic Publishers, (1993), 449-461.

70. Biswas, S. K., Venkatesh, K., Bobji, M. S. and Sebastian, K. S., Nanoindentation, *Trans. Indian Inst. Met*, vol. 49(5) (1996), 725-738.

71. Celis, J. P., Roos, J. R, Vancoille, E. and Franck, M., Characterization of Hard Ceramic Coatings by Nanoindentation, *Wear of Materials*, eds. K. C. Ludema and R. G. Bayer, Proc. Intl. Conf. On Wear of Materials, Orlando, vol. 2 (1991), 655-658.

72. Stone, D., LaFontaine, W. R., Alexopoulos, P., Wu, T.W. and Li, C.Y., An Investigation of Hardness and Adhesion of Sputter-Deposited Aluminum on Silicon by Utilizing a Continuous Indentation Test , *J. Mater. Res.*, vol. 3(1) (1988), 141-147.

73. Lawn, B. R., Evans, A.G. and Marshall, D.B., Elastic/Plastic Indentation Damage in Ceramics: The Median/Radial Crack System, *J. Amer. Cer. Soc.*, vol. 63 (1980), 574-579.

74. Hill, R., *The Mathematical Theory of Plasticity*, Oxford University Press, Oxford, (1950).

75. Ponton, C. B. and Dawlings, R.D, Vickers Indentation Fracture Toughness Test. I. Review of Literature and Formulation of Standardized Indentation Toughness Equations, *Mater. Sci. and Tech.*, vol.5 (1989), 865-872.

76. Rickerby, D., Measurement of Coating Adhesion, in *Metallurgical and Ceramic Protective Coatings,* ed. Kurt H. Stern, Chapman and Hall, London (1996), 306-331.

77. Elssner, G., Suga, T. and Turwitt, M., Fracture of Ceramic to Metals, *J. Phys. (Paris) Colloq. D4*, vol. 46 (1985), 597-612.

78. Howard, J. and Clyne, T. W., Interfacial Fracture Toughness of Vacuum-Plasma-Sprayed Coatings, *Surf. Coat. Tech.*, vol. 45(1-3) (1991), 333-342.

79. Rice, J. R., *Fracture: An Advanced Treatise*, ed. by H. Liebowitz, vol. 22 (1968), 191-197.

80. Ashcroft, I. A. and Derby, B., Adhesion Testing of Glass-Ceramic Thick Films on Metal Substrates, *J. Mater. Sci.*, vol. 28 (1993), 2989-2998.

81. Agarwal, A and Dahotre, N. B., Synthesis of Boride Coating on High Energy Density Processes: Comparative Study of Evolution of Microstructure, *Mater.Char.*, vol.42(1) (1999), 31-44.

82. Wang, W., Application of Ceramic Thermal Spray Coatings for Molten Metal Handling Tools and Molds, Presented at the Fall Meeting of ASM International in *Surface Modification Technologies* XII , Rosemont, IL, (1998).

83. Oye, H. and Sorlie, M., Cathodes in Aluminum Electrolysis, *Aluminum Verlag (Dusseldorf),* vol.2 (1992).

84. Samsonov, G. V., and Vinitskii, I. M., *Handbook of Refractory Compounds,* IFI Plenum Data Company, New York (1980), 140-144.

85. Kurz, W. and Fisher, D. J., *Fundamentals of Solidification*, Trans Tech Publications, Switzerland (1989), 63-92.

86. Flinn, J. E., *Rapid Solidification Technology for Reduced Consumption of Strategic Materials*, Noyes Publications, Park Ridge, NJ (1985), 42-64.

87. Guo, Z. X. and Derby, B., Chemistry Effects on Interface Microstructure and Reactions in Titanium-Based Composites, *Composites*, vol. 25(7) (1994), 630-636.

88. Guo, Z. X. and Derby, B., Stabilization of TiB_x-Coated SiC Fibers by Nitridation, *Scripta Mater.*, vol. 38 (11) (1998), 1629-1634.

89. Avner, S.H., *Introduction to Physical Metallurgy*, McGraw Hill Book Company, Singapore (1974), 65-106.

90. Weimin, S., Dudley, M., Pengxing, L. and Renjie, W.,Microstructure and Interfaces in TiB_2/Ti-46Al-3Cr Alloy Comopsites, in *Mat. Res. Soc. Symp. Proc.*, vol. 410, eds. A. F. Hepp, P. N. Kumta, J. J. Sullivan, G. S. Fischman and A. E. Kaloyeros, Materials Research Society, Pittsburgh, PA (1996), 405-410.

91. Agarwal, A and Dahotre, N. B., Mechanical Properties of Laser Deposited Composite Boride Coating using Nanoindentation, *Metal & Mater. Trans A*, (in press) (1999).

92. *De Hosson J. Th. M., Zhou X. B. and Van Den Burg M*, Metal-Ceramic Interfaces in Laser Coated Steels: A Transmission Electron Microscopy Study of a Mixture of Iron and Spinel Grains, *Acta Metall. Mater.* vol. 40 (1992), 139-142.

93. Murthy, A. S. and Goo, E., Triclinic Ni_2Al Phase in 63.1 Atomic Percent NiAl, *Metal & Mater. Trans*, vol. 25A (1994), 57-61.

94. Williams, D. B. and Carter, C. B., *Transmission Electron Microscopy, II: Diffraction*, Plenum Press, New York (1996), 237-263.

95. Ramqvist, L., Wettability of Metallic Carbides by Liquid Cu, Ni, Co and Fe, *Int. J. Powder Met.*, vol. 1(4) (1965), 2-21.

96. Ogwu, A. A. and Davies, T. J., Electronic Structure Basis for Selection of Metal Binders for Hardmetal Systems, *Mater. Sci. & Tech,* vol. 9 (1993), 231-217.

97. L. Brewer, *Electronic Structure and Alloy Chemistry of Transition Elements'*, ed. A. Beck, Interscience, New York (1963), 221-232.

98. Raghunath, C.,Bhat, M. S. and Rohatgi, P.K., In Situ Technique for Synthesizing Fe-TiC Composites, *Scripta Metall.*, vol. 32(4) (1995), 577-582.

99. Zhou, X. B. and De Hosson, J. Th. M., Influnece of Surface Roughness on the Wetting Angle, *J. Mater. Res.*, vol. 10(8) 1995, 1984-1992.

100. Agarwal, A., Dahotre, N. B. and Allard, L. F., Ceramic Metal Interface in Laser Deposited Hard Refractory Ceramic Composite Coating: Electron Microscopic Study, Pract. Metall., vol. 36 (3), (1999), 250-263.

101. Ning, X., G., Pan, J., Hu, K. Y. and Ye, H. Q., High Resolution Electron Microscopy Studies on the Microstructure of β-Si_3N_{4w}/Al Interfaces in a β-Si_3N_{4w}/6061 Al Composite, in *Mat. Res. Soc. Symp. Proc.,* eds. W. A. T. Clark, U. Dahmen and C. L. Briant (Ed.), Boston, MA (1991), 865-870.

102. *Metals Handbook*, American Society for Metals, vol. 1 (1978), 145-213.

103. Williams, D. B. and Carter, C.B., *Transmission Electron Microscopy, III: Imaging*, Plenum Press, New York (1996), 441-458.

104. Rice, J.R.., Elastic Fracture Mechanics Concept for Interfacial Cracks, *J. Appl. Mech.* vol. 55 (1988), 98-103.

105. Hutchinson, J. W. and Suo, Z., Mixed Mode Cracking in Layered Materials, in *Advances in Applied Mechanics*, eds. J. W. Hutchinson and T.Y. Wu, Academic Press Ltd, London, vol. 29 (1992), 64-78.

106. Brussel, B. A. Van and De Hosson, J. Th. M., Residual Stresses in the Surface Layer of Laser-Treated Steels, *Mater. Sci. & Engg,*. vol. A161 (1993), 83-89.

107. Yamamoto, K., Kawaguch, Y., Yasunaga, T. and Sato, T., Cracking Behavior of AIP-Coated Metal Nitrides Under Tensile Stress, *Surf. Coat. Tech.*, vol.113 (1999), 227-232.

108. Panagopoulos, C.N., Papachristos, V.D. and Sigalas, C., Tensile Behavior of as Deposited and Heat Treated Electroless Ni-P Deposits, *J. Mater. Sci.*, vol. 34 (1999), 2587-2600.

109. Rejda, Ed. F., Socie, D. F. and Itoh, T., Deformation Behavior of Plasma Sprayed Thick Thermal Barrier Coatings, *Surf. Coat. Tech.*, vol. 113 (1999), 218-226.

110. Chawla, K. K., *Ceramic Matrix Composites*, Kluwer Academic Publishers, Dordrecht (1993), 54-135.

111. Baumgartner, H. R. and Steiger, R.A., Sintering and Properties of Titanium Diboride made from Powder Synthesized in a Plasma Arc Heater, *J. Am. Ceram. Soc.* vol. 67(3) (1984), 207-212.

112. Ferber, M.K., Ferber, P.K. and Finch, C.B., Effect of Microstructure on the Properties of TiB_2 Ceramics, *J. Am. Ceram. Soc.*, vol. 66(1) (1983), C2-C4.

113. Bahadur, S. and Yang, C. N, Friction and Wear Behavior of Tungsten and Titanium Carbide Coatings, *Wear*, vol. 196 (1996), 156-163.

114. Axen, N., Hutchings, I. M. and Jacobson, S., A Model for Friction of Multiphase Materials in Abrasion, *Tribology Intl.*, vol. 29 (6) (1996), 467-475.

115. Rohatgi, P. K., Dahotre, N. B., Liu, Y., Yin, M. and Barr, T.L., Tribological Behavior of Al Alloy-Graphite and Al Alloy-Microcrystalline Carbon Particle Composites, in *Proc. Intl. Symposium on Advances in Cast Reinforced Metal Composites*, eds. S.G. Fishman and A.K. Dhingra, ASM International, Ohio 1988, 367-373.

116. Irving, R. J. and Worsley, I. G., The Oxidation of Titanium Diboride and Zirconium Diboride at High Temperatures, *J. Less-Common Metals*, vol. 16 (1968), 103-112.

117. Barandika, M. G., Echeberria, J.J., Sanchez, J. M. and Castro, F., Oxidation Resistance and Microstructure of the Oxide Layers for TiB_2-based Cermets, *J. Mater. Chem.*, vol. 8(8) (1998), 1851-1857.

118. Voitovich, V. B., Lavrenko, V. A and Adejev, V.M., High Temperature Oxidation of Titanium Diboride of Different Purity, *Oxidation of Metals,* vol. 42(1/2) (1994), 145-161.

119. Moeller, T., *Inorganic Chemistry,* John Wiley & Sons, New York (1972), 752-763.

120. Samsonov, G. V., *The Oxide Handbook*, Plenum Press, New York (1973), 348-360.

121. Birks, N. and Meier, G. H., *Introduction to High Temperature Oxidation of Metals,* Edward Arnold Ltd., London (1983), 91-130.

122. Fontana, M. G., *Corrosion Engineering,* McGraw Hill Inc., New York (1986), 505-541.

123. Gesmundo, F., Mathematical Modelling of Alloy Oxidation, *Mater. Sci. Forum*, vol. 251-254 (1997), 3-18.

124. Godavarty, A., Agarwal, A. and Dahotre, N. B., *Computational Materials Science* (submitted) (1999).

125. Jain, L. C. and Rao, V. V., *Industrial Applications of Neural Networks,* CRC Press LLC, (1999), 249-286.

126. Keller, P. E., Hashem, S., Kangas, L. J. and Kouzes, R. T., *Application of Neural Networks in Environment, Energy and Health*, Progress in Neural Processing-5, World Scientific Publishing Co, Pt. Ltd., Singapore, (1995),1-7.

127. NeuralWare, Inc., *Neural Computing – A Technology Handbook for Professional II/PLUS and Neural Works Explorer,* Technical Publications Group, Pittsburgh PA (1995), NC 63- NC 86.

128. Rhee, S. K., Presented at Fall Meeting of the Ceramic- Metal Systems Division of the American Ceramic Society, Fort Worth, TX (1968), 386-389.

129. JCPDS Files, PDF # 29-1356.

130. Hyman, M. E., McCullough, C., Valencia, J.J., Levi, C. G. and Mehrabian, R., Microstructure Evolution in TiAl Alloys With Boron Additions: Conventional Solidification, *Met. Trans,* vol. 20 (A) (1989), 1847-1859.

131. Shyam, A., Suwas, S. and Bhargava, S., Microstructural Features of Iron Aluminides Formed by the Reaction Between Solid Iron and Liquid Aluminum, *Pract. Metall.*, vol. 34(6) (1997), 264-277.

APPENDICES

APPENDIX I

INTRODUCTION TO PULSE ELECTRODE SURFACING TECHNIQUE TO DEPOSIT CERAMIC COATINGS ON METALS

I-1. Pulsed Electrode Surfacing Investigations

As a part of a multi-year US Air Force funded project (Contract No. F40600-96-C-0004) titled "Ultrahard Ceramic Coatings on Metals", author also investigated deposition of ceramic coatings by PES process. The purpose of these coatings was to provide the feasiblity study about coating arc-heater segments. Arc heater segments are made up of OFHC copper and steel and require effective dissipation of high heat flux from the inner bore while maintaining electrically non-conducting surfaces. Smooth and ultrahard coatings that have high thermal conductivity and little electrical conductivity can prevent these surfaces by preventing arc erosion. Various ceramics viz. TiB_2, TiC and AlN were deposited on metallic substrates such as AISI 1018 steel and oxygen free high conductivity (OFHC) copper. These investigations resulted in a series of technical articles in various journals. Some of these articles have already been published whereas some of them are in the publication process. *It was thought to put these collections of papers as appendices it will provide a wide base for the reader of this thesis.* Three of these publications are about TiB_2 coatings deposited by PES process. Such publications will provide the reader a comparative idea about the TiB_2 coating deposited by two high energy density processes i.e. pulsed electrode surfacing (PES) and laser surface

engineering (LSE). There are total of six publications related to PES and ceramic coatings, which are being added here as Appendix II-VII.

I-2. Pulse Electrode Surfacing

Pulse electrode deposition (PES) is an effective process for depositing ceramic coatings on metals for demanding environments. This process is a micro-welding process and makes use of electrical pulses of short duration and high current to deposit coatings from a consumable electrode on to the metallic substrate. The variables in the PES process are substrate and electrode materials and power settings. The primary requirement for the electrode material is that it should be electrically conductive and thus capable of being melted in an electric arc.

In a PES control system, the coating thickness and the quality of coating is directly related to the electrical parameters like voltage, current, capacitance, pulse width and duration. A PES power system transforms the AC power into pulsed DC power. The pulsed DC power source consists of a pulse generator and a power controller. The pulse controller sets a time basis and controls the on and off states of the power controller. The power controller, which consists of an electronic switch and a current limiting circuit, delivers the pulse to the gap with the required power. The power controller will effectively control the discharge time of the capacitor. The discharge energy is determined by both the capacitance and the voltage. When the ceramic electrode, having a positive polarity is brought close to the work piece surface (metallic substrate), which has a negative polarity, spark is generated. The intensity of the spark is directly

proportional to the voltage across the two electrodes, the amount of current and the duration of current flow, which is called pulse duration.

$$\text{Energy of Spark (E)} \propto \text{Voltage (V)} \times \text{Current (I)} \times \text{Pulse time (t)}$$

The energy of the spark in term decides the amount of material being deposited and the bond strength between the deposited material and the substrate or work piece. The dielectric medium, which is air in most of the cases, provides a path for the discharge and the region between electrode remains ionized, enabling continuous flow of current.

The PES process poses a lot of advantages over other coating techniques such as plasma spray, detonation gun, PVD and CVD. Since the process requires very little total heat input, it minimizes the chance of thermal distortion. The bulk substrate remains near ambient temperature and acts as heat sink. Thus, there are no thermal stress effects or metallurgical changes in areas other than fusion zone. Since the bulk material acts as huge heat sink, heat is rapidly dissipated leading to a rapid solidification of the molten pool. This result in an extremely fine grained coating layer, which has high density, hardness and strength. The coating is metallurgically bonded to the substrate and forms an alloy with it. This ensures excellent adhesion properties of the PES coatings with high spalling resistance. Other advantage of the PES process includes use of a relatively inexpensive and portable equipment. PES coatings can be deposited in air at room temperature. This prevents the need for expensive environmental chambers required in several other types of coating processes. PES coatings also offer excellent resistance to oxidation, corrosion, sulfidation, erosion and are used in hostile environments.

APPENDIX II

PULSE ELECTRODE DEPOSITION OF SUPERHARD BORIDE COATING ON FERROUS ALLOY

(published in ***Surface & Coatings Technology*** journal)

ELSEVIER

Surface and Coatings Technology 106 (1998) 242–250

SURFACE & COATINGS TECHNOLOGY

Pulse electrode deposition of superhard boride coatings on ferrous alloy

Arvind Agarwal *, Narendra B. Dahotre

Center for Laser Applications, Department of Materials Science and Engineering, University of Tennessee Space Institute, Tullahoma, TN 37388, USA

Received 18 November 1997; accepted 2 June 1998

Abstract

Pulse electrode surfacing (PES) is an effective process for depositing ultrahard, corrosion- and erosion-resistant ceramic coatings on metals. In the present work, a titanium diboride coating deposited on 1018 steel using PES technique has been investigated. An attempt has been made to correlate the thermodynamic predictions and experimental observations. The role of the ceramic–metal interface in the development of these coatings has been studied. A thick, adherent, metallurgically bonded and crack-free coating is obtained. It has been found that Fe intermixes with TiB_2 layer and acts as an excellent binder for TiB_2. It promotes the composite effect of both hardness and toughness in these coatings and, hence, provides a crack-free coating with the sound interface. © 1998 Elsevier Science S.A.

Keywords: Pulse electrode surfacing (PES); Superhard coating; Thermodynamics; Titanium diboride; Transition metal/compound

1. Introduction

Surface modification processes play a unique role in the development of exotic materials for the sophisticated purposes. It has been observed that alteration of the surface of most engineering materials leads to an improvement in properties such as hardness, wear resistance, high-temperature strength and corrosion resistance. Pulse electrode deposition (PES) is one such surface modification technique that utilizes high current electrical pulses of short duration to modify the metal surface [1–3]. A unique combination of high current and short pulse time via discharge capacitance and voltage results in melting of the electrode and deposition of the material on the substrate. The primary requirement for the electrode material is that it should be electrically conductive and thus capable of melting in an electric arc.

The main advantage of this process is its ability to apply metallurgically bonded coatings with a low heat input to the substrate at ambient temperature. This reduces the heat-affected zone (HAZ) and minimizes the changes in the properties of the substrate material [2]. The PES process poses several advantages over other coating techniques such as plasma spray, detonation gun, PVD, CVD and laser-assisted coatings. Since the process requires very little total heat input, it minimizes the chance of thermal distortion. The bulk substrate material remains near ambient temperature and acts as a heat sink. Thus, there are no thermal stress effects or metallurgical changes in areas other than the fusion zone. Since the bulk material acts as a huge heat sink, heat is rapidly dissipated leading to rapid solidification of the molten pool. This results in an extremely fine-grained coating of high density, hardness and strength. Since the coating is metallurgically bonded to the substrate, it ensures excellent adhesion properties of the PES coatings with a high spalling resistance [4]. Another advantage of the PES process is that relatively inexpensive and portable equipment can be used. PES coatings can be deposited in air at room temperature. This obviates the need for expensive environmental chambers required in several types of other coating processes. PES is a micro-welding process that can be used to deposit even ultrahard ceramic coatings on a metallic substrate [2,5]. These ultrahard ceramic coatings are used for several applications such as nuclear, fossil and geothermal energy environments, high-temperature turbine coatings for aerospace applications, industrial cutting tools, waste reclamation and water treatment plants, wear-resistant surfaces on large agricultural and textile equipment, high-temperature sensors, systems used in petrochemical and pharmaceutical industry and for modern sport equipment.

* Corresponding author. Tel: +1 931 393 7255; Fax: +1 931 454 2271; e-mail: aagarwal@utsi.edu

0257-8972/98/$19.00 © 1998 Elsevier Science S.A. All rights reserved.
PII S0257-8972(98)00545-3

The present work deals with the deposition of TiB_2 on 1018 steel using the PES technique. This investigation of TiB_2-coated steel using the PES method is based upon two aspects, viz. thermodynamic predictions and experimental analysis. The chemistry of the ceramic–metal system at the interface plays an important role in the properties of these coatings [6]. The chemical reactions occurring at the interface lead to the formation of various stoichiometric and non-stoichiometric compounds that in turn determine the adherent strength and other properties of the coating.

Although a chemical equilibrium may never be attained in the real sense because of kinetics considerations, this paper presents thermodynamic calculations of a ceramic–metal (TiB_2–Fe) system based on the equilibrium assumption. An attempt is made to predict the possibility of formation of various phases and compounds of the TiB_2–Fe system at the interface and in the coating. Thermodynamic predictions are coupled with an experimental analysis to characterize the TiB_2–Fe interface and coating morphology.

2. Experimental

2.1. Materials

In the present investigation, TiB_2 has been deposited on 1018 steel using PES method. TiB_2 is the hardest and lightest refractory material with excellent oxidation-resistant properties at temperatures up to 1673 K [7]. TiB_2 is chemically inert in corrosive environments. The electrical conductivity of TiB_2 is high, which makes it a suitable choice for deposition by the PES technique [2,5,7]. The salient physical properties of TiB_2 and 1018 steel are listed in Table 1 [7–9].

2.2. Coating process

TiB_2 coatings were deposited on 1018 steel coupons using PES method at Materials Modifications Inc. (MMI, Fairfax, VA). Coupons of 1018 steel with dimensions of 25 mm × 10 mm were mechanically polished on emery paper of grit 240 and then rinsed with acetone. A sintered electrode of TiB_2 was used to deposit a coating on these steel coupons. TiB_2 electrode had Ni in the range of 1–3 wt% as binder. Deposition was carried out using a hand-held gun in air at room temperature. Pulsed electrode deposition was carried out at a voltage of 50 V and a spark time of 10 μs. The discharge capacitance used for the PES process was 450 μF with a current of 50 A. It should be recalled that a high current is needed for deposition by the PES technique [1,10].

2.3. Characterization

Coating and interface characterizations were carried out using a scanning electron microscope (SEM), X-ray diffractometer (XRD) and microhardness tester. Samples for metallography were prepared by polishing on a Buehler TEXMET 2000 cloth during the initial stages of polishing. This minimized the damage to any dissimilar interface (ceramic/metal) during polishing. Nital was used as the etchant for the TiB_2-coated steel sample. The coating morphology and interface were investigated using an ISI Super III-A scanning electron microscope. EDAX and X-ray mapping were coupled with SEM to characterize the elements in a semi-quantitative analysis. A Philips Norelco X-ray diffractometer with CuKα radiation, operating at 30 kV and 40 mA, was used for phase(s) identification. Microhardness measurements were performed on Buehler Micromet II microhardness tester using a Knoop indenter with a load of 200 g applied for 15 s.

3. Results and discussion

3.1. Thermodynamic predictions

The chemical reactions occurring in the coating and interface are of immense significance as they assist in predicting the nature and properties of the coatings. For a ceramic–metal system, the application of thermodynamics requires the consideration of all possible reactions occurring in the system [11]. This is essential in the absence of a ternary phase diagram such as Fe–Ti–B

Table 1
Physical properties of Fe and TiB_2

Properties	Fe (1018 steel)	TiB_2
Crystal structure	b.c.c.	h.c.p.
Melting point (°C)	1538	3225
Density (g cm^{-3})	7.8	4.5
Hardness (kg mm^{-2})	250	3000
Electrical resistivity (μΩ·cm)	12	30
Thermal conductivity (W m^{-1} K^{-1})	55	65
Coefficient of thermal expansion (10^{-6} K^{-1})	12.2	4.6

as in the present study. For our material system of TiB_2–Fe, the reactions between Ti–B, Fe–B and Ti–Fe are being considered. From the binary phase diagrams of the above mentioned systems, the following reactions are possible.

Ti–B system:

$$Ti + B = TiB$$

$$Ti + 2B = TiB_2$$

$$3Ti + 4B = Ti_3B_4.$$

The thermodynamic data for this metastable phase Ti_3B_4 are unknown. Henceforth, only TiB and TiB_2 will be considered for further analysis and discussion.

Fe–B system:

$$Fe + B = FeB$$

$$2Fe + B = Fe_2B$$

Fe–Ti system:

$$Fe + Ti = FeTi$$

$$2Fe + Ti = Fe_2Ti.$$

Gibbs free energies and enthalpies of formation of the borides of Ti and Fe for various temperatures are presented in Table 2 [12]. These data are based upon the borothermic reduction of oxides as carried out by Samsonov and Vinitski [12]. However, the lack of thermodynamic data for the formation of Ti_3B_4, FeTi and Fe_2Ti and other compounds makes stability predictions difficult for many systems.

Fig. 1 shows the free energy of formation of borides as a function of temperature. It is evident from the graph that the free energy of formation is almost independent of temperature up to 2000 K. This implies that entropy (obtained from the slope of the curve) for the formation of above borides is almost negligible. Thus, it is reasonable to assume that the free energy of formation of the above borides varies in a similar nature, even at the temperature attained during arc formation in PES process. It is evident from Table 2 that TiB_2 is the most stable boride in the Fe–Ti–B system.

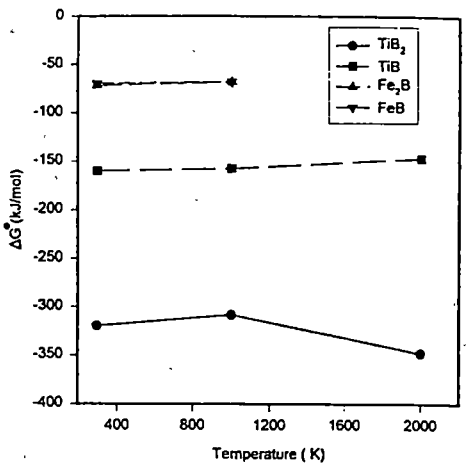


Fig. 1. Free energy of formation of borides of Ti and Fe as a function temperature.

3.2. Microstructural characterization

Fig. 2(a) shows the topographical features of the top surface of TiB_2 deposited on the steel substrate. The surface is irregular with several islands of a globular shape and a splash-like appearance. This is a characteristic feature of the PES technique. In the present work, the PES process is carried out in air, and it supports a globular mass-transfer mechanism. This is attributed to the fact that dissociable gases like nitrogen and air form a plasma of high thermal conductivity that promotes globular mass transfer [1]. A molten globular droplet forms at the TiB_2 electrode tip and impinges on the steel substrate. This produces a splash appearance on the top surface. The elemental distribution of Ti and Fe on the top surface is illustrated by X-ray maps in Fig. 2(b and c) that confirm island formation of TiB_2 in the PES technique. Globular mass transfer provides high deposition rates that can assist in the deposition of thick coatings [1].

Fig. 3 shows SEM micrographs of the cross- section of the TiB_2-coated steel at various magnifications. It

Table 2
Thermodynamic properties of borides of titanium and iron

Phase (K)	ΔG^0 (kJ mol^{-1})			ΔH^0 (kJ mol^{-1})		
	298	1000	2000	298	1000	2000
TiB	−159.7	−157.4	−160.3	−160.3	−165.3	−186.0
TiB_2	−319.7	−308.3	−347.9	−323.8	−326.6	−347.9
FeB	−69.5	—	—	−71.1	−72.9	—
Fe_2B	−71.8	—	—	−71.1	−77.9	—

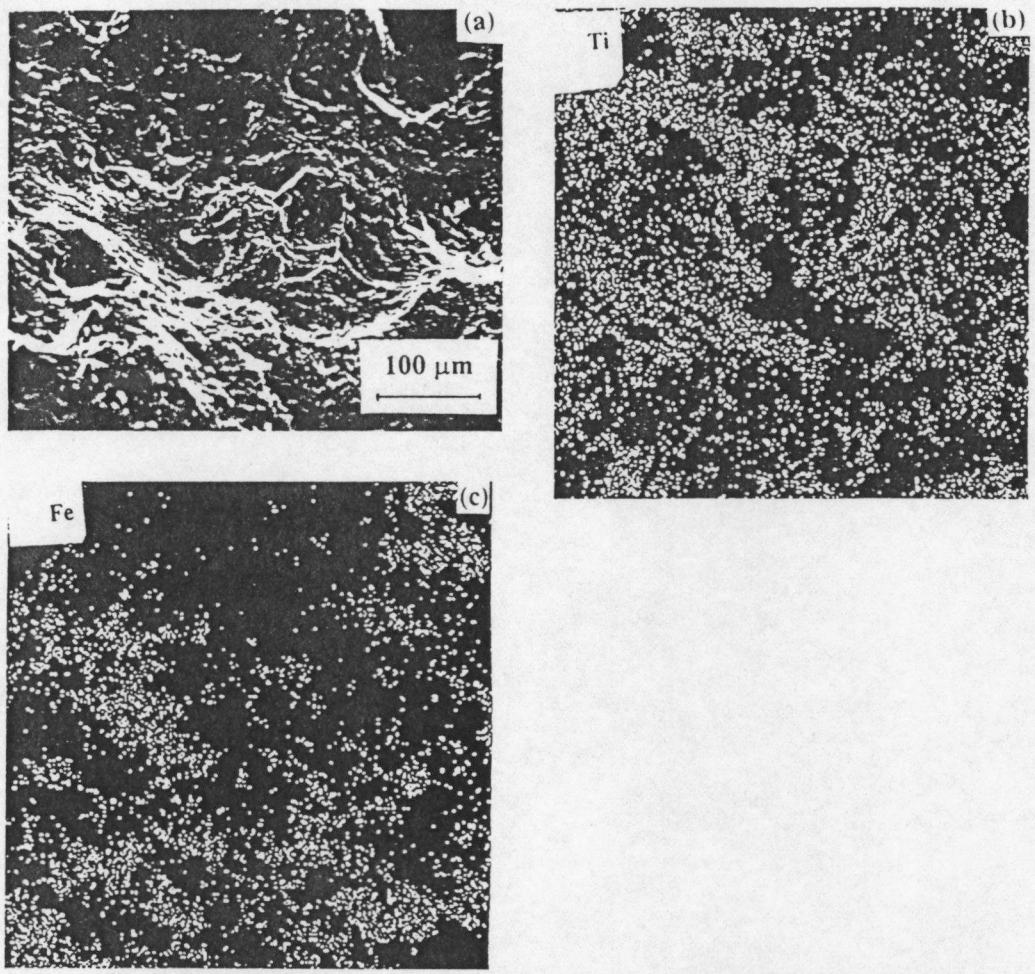


Fig. 2. TiB_2-deposited steel coupon (a) topographical features, (b) X-ray elemental map for Ti and (c) X-ray elemental map for Fe.

can be seen in Fig. 3(a) that the coating is thick, dense, adherent and free of defects such as cracks. A few crack-like features are artifacts created during polishing. Fig. 3(b) shows the cross-section of the same sample at a different location. It can be seen that the coating thickness is not very uniform throughout the cross-section. This is in accordance with the nature of PES process as described above and as observed earlier in the topographical features of the same sample in Fig. 2(a). Also, a strong and continuous interface along with the heat-affected zone (HAZ) can be seen in Fig. 4(a). There is no delamination at the interface of the coating and the substrate. Also, the presence of a continuous interface explains the formation of a metallurgical bond between TiB_2 and steel. The formation of metallurgical bond suggests that there is some intermixing that has occurred between Fe and TiB_2. Elemental X-ray maps of the cross-section corresponding to the Ti and Fe distribution are shown in Fig. 4(b and c). This clearly shows the Ti-rich zone in the coating, whereas the base material is rich in Fe. Fig. 5 shows concentration profiles for Ti and Fe in the coating and substrate. Ti varies from 20 wt% to 15 wt% in the coating and 15 wt% to a negligible amount in the interfacial region and substrate. However, there is a high concentration of Fe in the coating (80 wt%) and the interfacial region (>80 wt%). This provides evidence that Fe has migrated into the TiB_2 layer. This occurs during solidification of the localized melt pool of the TiB_2 layer and steel substrate. The reason for the high Fe content is the large difference between the melting points of the TiB_2 coating and the Fe substrate. The lower melting

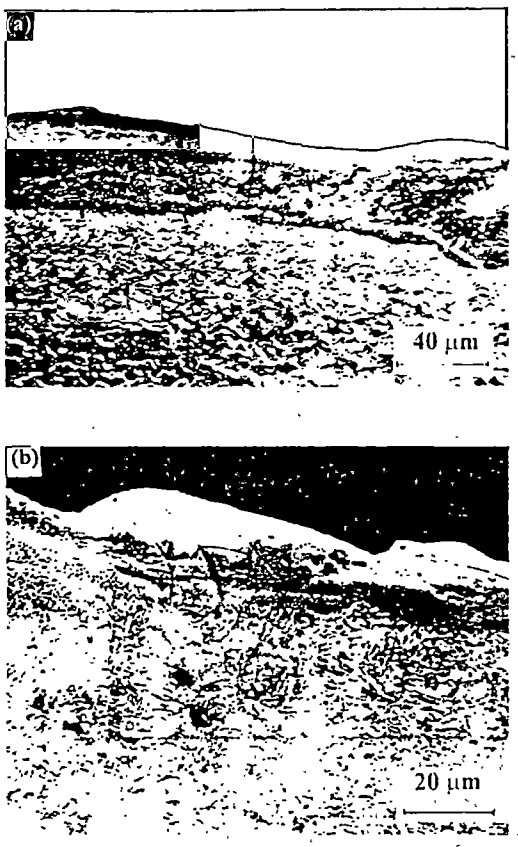


Fig. 3 SEM micrographs of the cross-section of the TiB_2-deposited steel coupon

point constituent (the Fe substrate in the present case) forms a larger volume of molten material as compared to the TiB_2 electrode. Hence, the resulting coating layer has a higher concentration of Fe.

It is important to consider the nature of possible reactions occurring within both the coating and the interface. This would reveal the nature of the interaction whether it is chemical or physical. All the possible chemical reactions for Fe–Ti–B system have been considered earlier, and it was found that the formation of TiB_2 is the most thermodynamically favorable reaction. However, there is some possibility of formation of some metastable phase(s) such as Fe_xTi_y and Ti_aB_b due to the kinetics of the PES process. It should be recalled that PES is a high-energy-density process that leads to rapid solidification of the melt pool. Hence, it could promote the formation of some metastable phase(s) in the coating and interface. The X-ray diffraction spectrum of the coated surface shown in Fig. 6 reveals the present phase(s) in the coating and interface: it shows all the major peaks for TiB_2 and Fe. However, a couple of low-intensity peaks could not be identified, which may be attributed to some metastable phase(s). This supports our earlier thermodynamic prediction of the formation of TiB_2 being the most favorable reaction in the Fe–Ti–B system. Moreover, based on the Fe–Ti phase diagram, there is a possibility of formation of intermetallic Fe_2Ti at an 80 wt% Fe composition. However, the absence of Fe_2Ti, FeTi, FeB and Fe_2B is supported by thermodynamics as well as the X-ray diffraction spectrum. It could be inferred, therefore, from the above discussion that Fe does not chemically react within the layer but performs a role like a binder in the TiB_2–Fe system.

The wetting phenomenon of the ceramics by the metal has been addressed by several researchers [13–17] It is shown that a Ti-based ceramic easily wets Fe at high temperatures, and wetting progresses further with time [13]. The wetting phenomenon has been attributed to the unfilled d-orbitals in transition metals and their compounds such as borides and carbides [14,15]. This has also been proved experimentally during the in-situ synthesis of Fe–TiC composite [18]. Furthermore, a detailed analysis of the role of metals as binders for ceramics and their wetting characteristics based on the electronic structure has been addressed elsewhere [14].

TiB_2 is a transition metal-based ceramic, and it has a partly covalent and partly metallic bonding [15,17,19]. The metallic nature of the bonding is also revealed by the electrical conductivity of TiB_2, which is high and similar to that of the metals (Table 1). It is theoretically postulated that if the ratio of the size of the non-metal atom to that of the metallic atom is less than 0.59, then bonding is partly covalent and partly metallic [19]. Further, it is also confirmed and postulated for the transition-metal-based ceramics that the covalent bonding in such compounds is not as important as metallic bonding [15]. A d-band substructure similar to that of transition metals also exists in transition-metal-based ceramics, which leads to metallic bonding in such ceramics [15]. A value has been assigned to the number of d electrons present in these transition metals and their compounds. Electrons in the d-band substructure participate in the formation of a metallic bond, and accordingly, TiB_2 has 5.5 d electrons available for bonding [15].

Based on the theoretical and experimental results, an empirical rule for the suitable choice of binder used in sintering of transition metal based ceramics has been proposed [14]. For a transition metal or compound with an unfilled inner d shell in the state d^x, a transition metal in the state d^y would be the most suitable binder (x and y denoting the number of electrons in the unfilled d shells) if the following condition is satisfied.

$$x+y=11. \quad (1)$$

It is also suggested that a selection of a material system

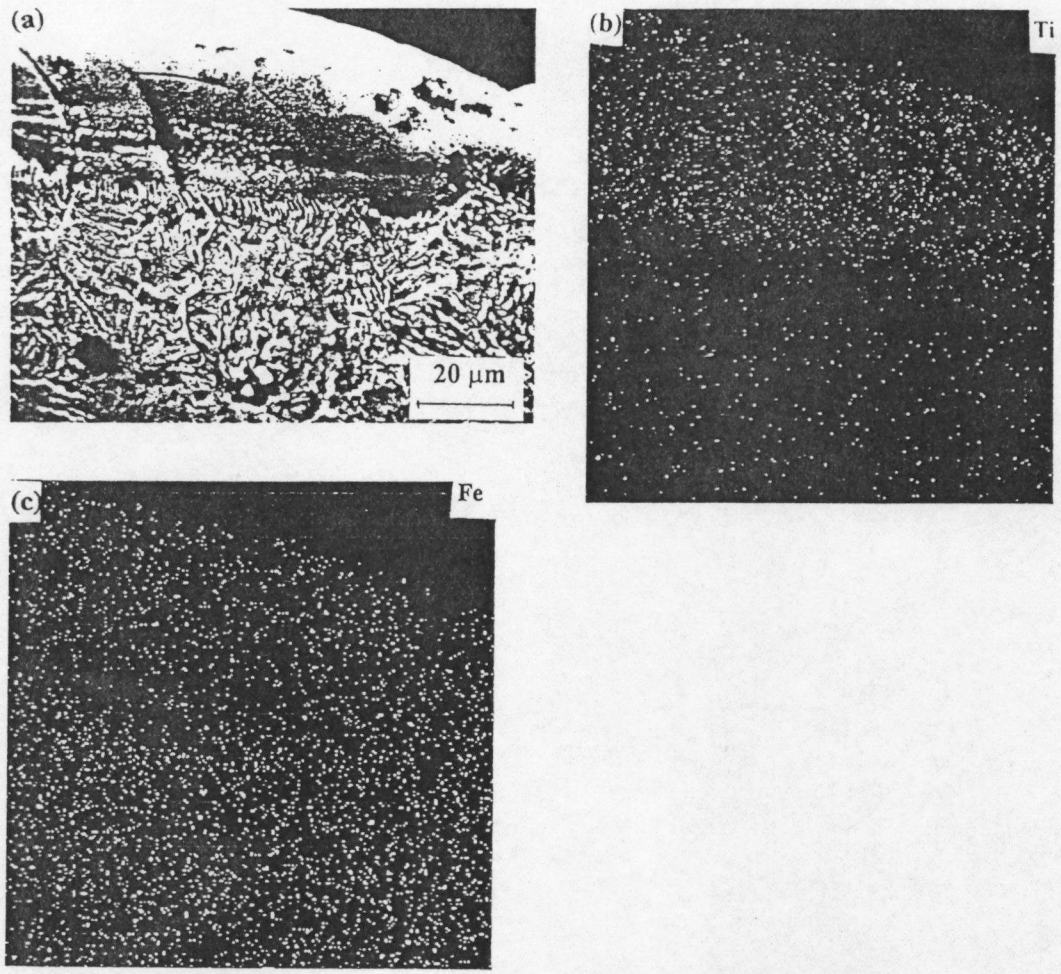


Fig. 4. Cross-section of TiB_2-deposited steel coupon (a) SEM micrograph, (b) X-ray elemental map for Ti and (c) X-ray elemental map for Fe

that gives $x+y=10$ or $x+y=12$ would also provide good bonding, but it would be inferior to the system satisfying the $x+y=11$ condition.

In the material system TiB_2–Fe of the present study, Fe has an unfilled d subshell with six electrons (d^6s^2 configuration), and TiB_2 has 5.5 d electrons, as assigned previously [15]. This satisfies the above hypothesis [14] of Eq. (1):

$$(x=5.5)+(y=6)=11.5. \quad (2)$$

The Fe does not react with the TiB_2 layer but remains as a binder similar to Co in the WC–Co system. This fact has been earlier corroborated in the analysis based on the electronic configuration that states that bonding in such material systems does not promote compound formation [15]. Further, this hypothesis has been verified and confirmed in another experimental study based on a Cu–TiB_2 system where Cu acts as a poor binder for TiB_2 due to its completely filled d subshell [20].

3.3. Mechanical characterization

Mechanical characterization of the coating and interface has been performed using a microhardness tester. Fig. 7 shows the microhardness variation in the coating, heat-affected zone and substrate material. There is a gradual decrease in microhardness values going down from the coating to the substrate. The microhardness values (Knoop) in the coating are high with an average value of 1124 kg mm^{-2}, whereas it decreases to 182 kg mm^{-2} in the base material. The microhardness value at the interface and in the heat-affected zone is

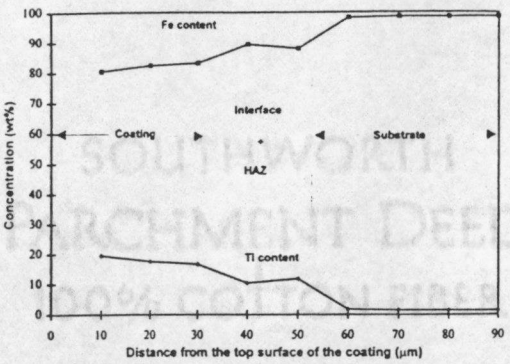


Fig. 5. Elemental depth profile of Ti and Fe in the coating and substrate.

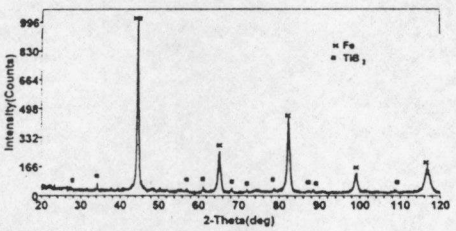


Fig. 6. X-ray diffraction spectrum of TiB_2-deposited steel coupon.

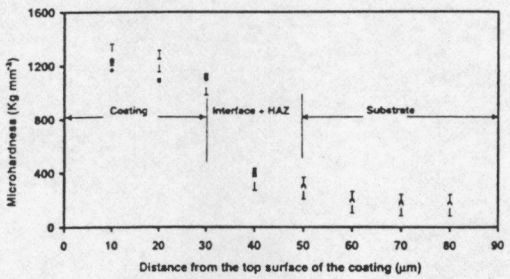


Fig. 7. Microhardness (Knoop) profile in the coating layer, interface and substrate.

384 kg mm^{-2}. The gradual change in the microhardness values is attributed to the presence of a transition zone. Fig. 8 shows an SEM micrograph of a cross-section of the coating and the substrate with microhardness indentations. The relative difference in the size of microhardness indentations elucidates the variation in hardness in the coating and substrate. Fig. 8(a) shows the coherent and defect-free nature of the coating. No crack initiation or propagation is seen at any of those indentation sites. A mechanically strong interface is observed in Fig. 8(b). The microhardness indentation at the interface (marked by an arrow) does not show any sign of delamination

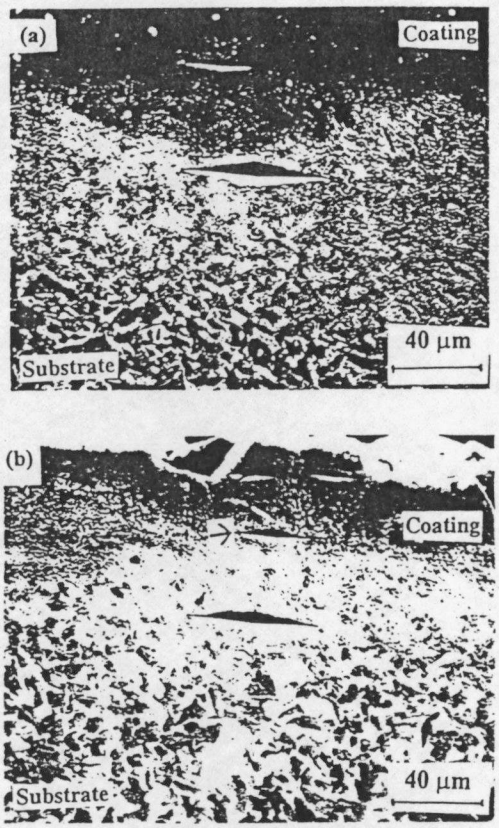


Fig. 8. SEM micrographs of the cross-section showing microhradness indentations in the coating, interface and the substrate.

of the coating. A magnified view of the coating, interface and heat-affected zone is shown in Fig. 9. There is no crack initiation or delamination at the interface which supports the high cohesive strength observed. Moreover, coating is free from defects such as microcracks and voids. However, some surface porosity is present that could be possibly due to the entrapment of air during successive deposits of TiB_2 globules. It should be recalled that TiB_2 deposition occurs via a globular-mass-transfer mechanism in air. Fig. 9 also reveals the fine-grained nature of the coating, which is a consequence of the rapid solidification occurring during the PES process [1,2]. Generally, microcracking does not occur in fine-grained TiB_2 [21]. Hence, it can be concluded that the fine grain size contributes to freedom from microcracks in the TiB_2 deposit.

Another aspect of the strong interfacial strength is obtained from the fact that inspite of a threefold difference between the coefficients of thermal expansion of

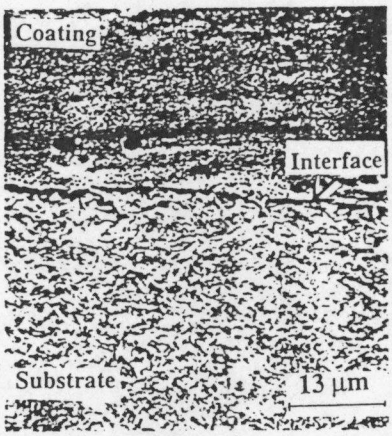


Fig. 9. SEM micrograph of the cross-section at a higher magnification, revealing an adherent and continuous interface and crack-free coating.

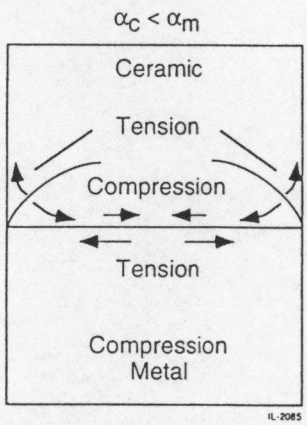


Fig. 10. Schematic drawing illustrating the phenomenon of crack initiation and interface delamination due to a mismatch in the coefficient of thermal expansion.

TiB_2 and steel (Table 1), there is no delamination at the interface. It is well known that if the coefficient of thermal expansion of a ceramic material (α_c) is less than that of the metallic material (α_m), then the differential tensile and compressive stresses are generated at the interface, as shown in Fig. 10 [22]. These stresses lead to interface decohesion and crack formation in the coating. However, none of these failures is observed in the present study. This is explained as being due to the presence of Fe in TiB_2, which provides toughness to the ceramic coating layer. Thus, Fe mixed in the TiB_2 layer provides a composite effect of hardness and toughness similar to that of the WC–Co system.

4. Conclusions

TiB_2 has been deposited on the steel substrate using the PES technique. A dense, adherent, fine-grained and defect-free hard ceramic coating is obtained. There is no delamination or crack initiation at the interface which accounts for the high interfacial cohesive strength. Fe migrates into the TiB_2 layer and acts as a binder. It does not react chemically with TiB_2 but acts as a binder for the ceramic and imparts a composite effect of both hardness and toughness. The possibility of formation of a metastable phase was explored, based on the thermodynamics and experimental conditions. TiB_2 was the most stable phase formed in the layer.

Acknowledgement

The authors wish to express their sincere appreciation to Dr T.S. Sudarshan at Materials Modifications Inc., Fairfax who provided the samples for the present work. The support extended by Mr K. Muralidhar and Mr S. Krupashankara at MMI, in depositing the coating by the PES technique, is highly acknowledged. The authors acknowledge the financial support from the US Air Force (Contract No. F40600-96-C-0004) for this work.

References

[1] R.N. Johnson, in: T.S. Sudarshan, D.G. Bhat (Eds.), Surface Modification Technologies, The Metallurgical Society, Warrendale, PA, 1988, pp. 189–213.
[2] R.N. Johnson, in: N.B. Dahotre, J.M. Hampkian, J.J. Stiglich (Eds.), Elevated Temperature Science and Technology I, The Minerals, Metals and Materials Society, 1995, pp. 264–277.
[3] E.A. Brown, G.L. Sheldon, A.E. Bayoumi, Wear 138 (1990) 137–151.
[4] R.N. Johnson, Thin Solid Films 118 (1984) 31–47.
[5] G.V. Samsonov, A.D. Verkhoturov, V.S. Sychev, A.I. Bezykornov, Fiziko-Khimicheskaya Mekhanika Materialov 7 (5) (1971) 3–6.
[6] J.T. Klomp, in: S.D. Petevers (Eds.), Ceramic–Ceramic and Ceramic–Metal Joining, Elsevier Applied Science, New York, 1989, pp. 127–144.
[7] N.B. Dahotre, M.H. McCay, T.D. McCay, Mater. Manufac. Process. 9 (1) (1994) 1–36.
[8] R.A. Cutler, Engineering Materials Handbook: Ceramic and Glasses, ASM International, OH, Vol. 4, 1991, pp. 787–803.
[9] Metals Handbook, American Society for Metals, Materials Park, OH, Vol. 1, 1978, pp. 145–213.
[10] A.I. Bushik, V.A. Shilov, Elektronnaya Obrabotka Materialov 1 (1991) 22–25.
[11] J.T. Klomp, in: Y. Ishida (Ed.), Fundamentals of Diffusion Bonding, Elsevier, Amsterdam, 1987, pp. 3–25.
[12] G.V. Samsonov, I.M. Vinitskii, Handbook of Refractory Compounds, IFI Plenum Data Company, New York, 1980.
[13] L. Ramquist, Int. J. Powder Met. 4 (1965) 1–4.
[14] A.A. Ogwu, T.J. Davies, Mater. Sci. Technol. 9 (1993) 231–237.
[15] E. Dempsey, Philos. Mag. 3 (86) (1963) 285.
[16] L. Brewer, in: A. Beck (Ed.), Electronic Structure and Alloy

Chemistry of Transition Elements, Interscience, New York, 1963 p. 221
[17] J. Friedel, in J.M. Ziman (Ed.), The Physics of Metals, Cambridge University Press, Cambridge, 1969
[18] C. Raghunath, M.S. Bhat, P.K. Rohatgi, Scripta Metallurgica 32 (4) (1995) 577–582
[19] G. Hagg, Z. Phys. Chem. B 6 (1929) 221.
[20] A. Agarwal, N.B. Dahotre, T.S. Sudarshan, Surf. Eng. (accepted)
[21] M.K. Ferber, P.F. Becher, C.B. Finch, J. Am. Ceram. Soc. 66 (1) (1983) C2–C4
[22] T. Tanaka, H. Morimoto, H. Homma, Nippon Steel Tech. Rep. 37 (1988) 36

APPENDIX III

EVOLUTION OF INTERFACE IN PULESD ELECTRODE DEPOSITED TITANIUM DIBORIDE ON COPPER AND STEEL

(published in ***Surface Engineering*** journal)

EVOLUTION OF INTERFACE IN PULSED ELECTRODE DEPOSITED TITANIUM DIBORIDE ON COPPER AND STEEL

A. Agarwal, N. B. Dahotre, and T. S. Sudarshan

Pulsed electrode surfacing (PES) is a microwelding surfacing process for the successful deposition of ultrahard wear and erosion resistant ceramic coatings on metals. The present study investigates titanium diboride deposition on oxygen free high conductivity Cu. A thin and irregular coating with cracks was obtained on the Cu substrate, with the ceramic/metal interface distinct in TiB_2 deposited on Cu leading to decohesion at the interface. The present work has been compared with an earlier study on TiB_2 coatings deposited on 1018 steel using the PES technique. The difference in nature of the interfaces has been related to wettability, and the role of copper and iron as binders for TiB_2 ceramics has been addressed. Iron acts as an excellent binder for TiB_2, providing a crack free coating and a strong interface, whereas Cu is a poor binder, leading to a weak ceramic/metal interface.

Mr Agarwal and Dr Dahotre are in the Center for Laser Applications, Department of Materials Science and Engineering, University of Tennessee Space Institute, Tullahoma, TN 37388, USA, and Dr Sudarshan is with Materials Modification Inc., 2929-P1 Eskridge Road, Fairfax, VA 22301, USA. *Manuscript received 20 March 1998; in final form 3 August 1998.*

© 1999 IoM Communications Ltd.

INTRODUCTION

The applications of high performance ceramic coatings have increased in recent years, leading to the need for development of coatings with high hardness, high temperature strength, wear and erosion resistance, and corrosion resistance in hostile environments. Various surface modification processes including chemical vapour deposition (CVD), physical vapour deposition (PVD), and plasma spraying are currently used to deposit various coatings. However, the use of these techniques has been limited by several factors, such as the need for high input energy, cost of a vacuum chamber, size of the workpiece, poor bond strength, and environmental hazards.

Pulsed electrode surfacing (PES) is a surface modification technique which has several advantages over coating techniques such as plasma spray, detonation gun, PVD, CVD, and laser deposition. The prime advantage of this process is its ability to apply metallurgically bonded coatings with low heat input to the substrate at ambient temperature. A sound metallurgical bond between coating and substrate ensures excellent adhesion with high spalling resistance.[1] Moreover, the low heat input reduces the heat affected zone (HAZ) and minimises changes in properties of the substrate material.[2] In addition, because of its very small total heat input, the PES process minimises the chance of thermal distortion. The bulk substrate material remains near ambient temperature and acts as a heat sink, thus there are no thermal stress effects or metallurgical changes in areas other than the fusion zone. Other advantages of the PES process include the use of relatively inexpensive and portable equipment, as PES coatings can be deposited in air at room temperature, eliminating the need for the expensive environmental chambers required in many other coating processes. In addition, PES employs a unique combination of high current and short pulse time via a discharge capacitance–voltage circuit, resulting in melting of the electrode and deposition of material on the substrate.[2–4] An important requirement for the electrode material is that it should be electrically conductive and thus capable of melting in an electric arc.

In the present study, TiB_2 was deposited on oxygen free high conductivity (OFHC) Cu using the PES technique. OFHC Cu is used in arc heater segments for heating air in large industrial chambers, where it experiences high temperature oxidation. The high operating temperature enhances oxide formation on OFHC Cu. Copper does not form a protective oxide layer, and the oxide layer falls off readily, exposing a fresh metal surface to the oxidising environment, resulting in a greater loss of material from the system. Another problem encountered by these Cu segments and heating chamber walls occurs as a result of electrical arcing. An electric arc is produced in the chamber to heat the air, causing arc erosion of the wall of the chamber. An effective way of protecting the walls from arc erosion and high temperature oxidation is to coat the exposed metal surface with an adherent film which should possess high temperature strength, high oxidation and erosion resistance, and high electrical and thermal conductivity. In view of these requirements, TiB_2 was chosen to be deposited on OFHC Cu using the PES method. A detailed microstructural characterisation was carried out in the present investigation. In addition, a comparison was made with TiB_2 coated 1018 steel, which is also used in some parts of the arc heater. A detailed study of TiB_2 coated 1018 steel based on thermodynamic predictions and experimental analysis has been presented elsewhere.[5]

EXPERIMENTAL

Materials

Titanium diboride was deposited on to OFHC Cu using the PES process. Titanium diboride is a low density, hard refractory material which is chemically inert in corrosive environments and which has

ISSN 0267-0844

excellent oxidation resistance properties to 1673 K.[6] Wear resistance and abrasion resistance of TiB_2 coatings are high. In addition, the electrical conductivity of TiB_2 is high, making it suitable for deposition by PES.[2,6,7] The salient physical properties of TiB_2, OFHC Cu, and 1018 steel are listed in Table 1.[6,8,9]

Coating process

Titanium diboride coatings were deposited on to OFHC Cu coupons using the PES system at Materials Modification Inc. (Fairfax, VA, USA). Coupons of OFHC Cu having dimensions 25 × 10 mm were mechanically polished using 240 grit emery followed by an acetone rinse. A sintered TiB_2 electrode containing Ni in the range 1–3 wt-% as a binder was used to deposit coatings on these coupons. Deposition was performed using a handheld electrode in air at room temperature. The processing of the OFHC was carried out with a current of 30 A and a capacitance of 450 μF, while the processing of the 1018 steel was carried out with a current of 50 A and a capacitance of 450 μF.

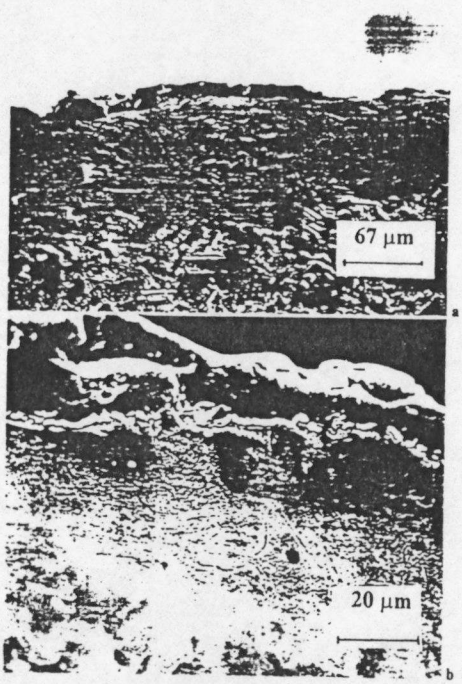
Characterisation

Microstructural and interfacial characterisation was performed using scanning electron microscopy (SEM), energy dispersive X-ray (EDX) analysis, X-ray diffractometry (XRD), and microhardness analysis. Metallographic specimens were prepared by polishing using Buehler Texmet 2000 cloth initially in order to inhibit damage to the dissimilar ceramic/metal interface during polishing. An aqueous saturated solution of CrO_3 was used as an etchant for OFHC specimens. The coating morphology and interfacial properties were investigated using the ISI Super III–A SEM. Spot analysis by EDX and X-ray mapping were coupled with SEM to characterise elemental distribution in a semiquantitative analysis. Phase identification was conducted using a Philips Norelco X-ray diffractometer with Cu K_α (1·54 μm) radiation operating at 30 kV and 40 mA. Microhardness measurements were performed using a Buehler Micromet II microhardness tester with a normal load of 200 g applied for 15 s.

RESULTS AND DISCUSSION

Microstructural characterisation

Scanning electron micrographs of the cross-section of the TiB_2 coated OFHC Cu at low and high magnifications are shown in Fig. 1. It can be seen in Fig. 1*a* that the coating is thin, irregular, and does not completely cover the entire Cu substrate. Figure 1*b* shows the same specimen at higher magnification. The coating thickness is irregular throughout the cross-section, in agreement with the nature of the PES process, as seen with a TiB_2 coating deposited on 1018 steel.[5] However, the degree of irregularity of coating thickness is higher in Cu specimens than in steel specimens. This is attributed to poor wetting of TiB_2 on the Cu substrate and to a large difference in thermal conductivities and coefficients of thermal expansion (CTE). The contact angle of TiB_2 for Cu is 143° whereas the contact angle of TiB_2 on steel is 100°.[10] Thus, there is better wetting for TiB_2 on steel than on Cu, leading to a more uniform ceramic coating on steel.



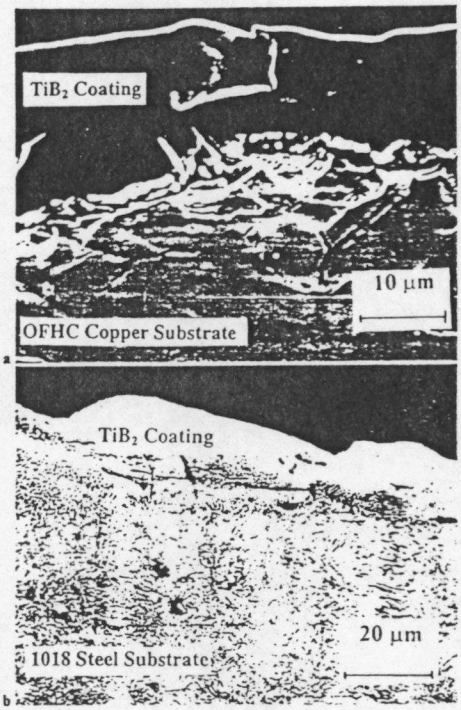
a shows thin, irregular coating; *b* detail, shows high degree of irregularity in coating thickness

1 *Cross-sectional SEM images of OFHC Cu coupon coated with TiB_2*

A sharp, distinct, and weak interface between TiB_2 and OFHC Cu is shown in Figs. 2*a* and 3*a*, suggesting that there is no metallurgical bond between the coating and the substrate. In contrast, Figs. 2*b* and 3*b* illustrate the strong interface of TiB_2 deposited on steel. The formation of a metallurgical bond depends on the chemical reaction or intermixing of two species at the interface. The elemental X-ray maps in Fig. 4

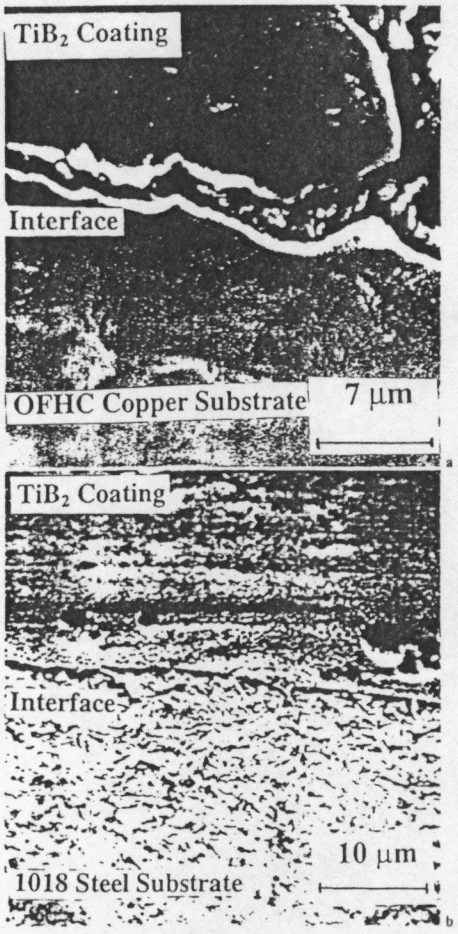
Table 1 Physical properties of OFHC Cu, 1018 steel, and TiB_2

Material	Crystal structure	Melting point, °C	Density, g cm^{-3}	Hardness, kg mm^{-2}	Electrical resistivity, μΩ cm	Thermal conductivity, W m^{-1} K^{-1}	Thermal expansion coefficient, × 10^{-6} K^{-1}
OFHC Cu	fcc	1085	8·8	55	2	390	17·8
1018 steel	bcc	1538	7·8	250	14	55	12·2
TiB_2	hcp	3225	4·5	3225	30	65	4·6



a OFHC Cu; *b* 1018 steel

2 *Cross-sectional SEM images of TiB_2 coating on given substrates*

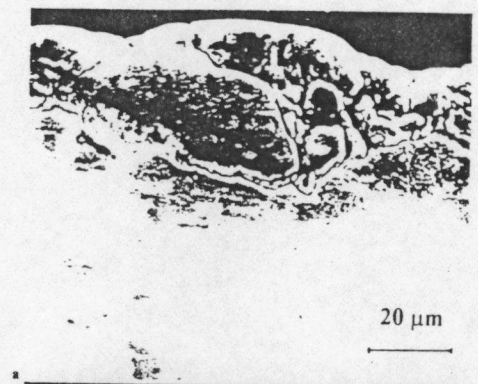


a OFHC Cu; *b* 1018 steel

3 *High magnification cross-sectional micrographs showing interface between TiB_2 and given substrates*

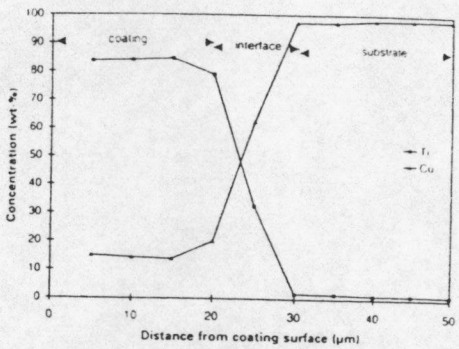
show Ti and Cu distribution in the coating and substrate. The high concentration of Ti within the coating and a sharp interface are evident in Fig. 4*b*. The concentration profiles for Ti and Cu in the coating and substrate are presented in Fig. 5. Coating thickness is estimated to be approximately 20 μm. The Ti content varies from 83 to 78 wt-% within the coating, while there is an insignificant amount in the substrate. The Cu concentration is nearly 15 wt-% in the coating and 100 wt-% in the substrate, suggesting poor mixing between TiB_2 and Cu. The presence of 15 wt-%Cu in the TiB_2 layer can be attributed to instantaneous wetting and to defects, including porosities, filled by liquid Cu as a result of capillary action during pulsed electrode deposition. It is a well known fact that metal is a more mobile species than ceramic in a ceramic–metal mixture.[11] However, it was seen that nearly 80 wt-%Fe was present in the TiB_2 layer in TiB_2 deposited on 1018 steel.[5] Thus, intermixing of Cu and TiB_2 is limited as compared to Fe and TiB_2. This is a prime reason for the lack of a chemical bond between TiB_2 and Cu and results in a weaker interface.

In the case of TiB_2 deposited on steel, the physical nature of the interaction between Fe and TiB_2 was defined. All possible reactions within the Fe–Ti–B system were considered, and it was found that TiB_2 is the most stable compound and that Fe acts as a binder.[5] Figure 6 shows the XRD spectrum of TiB_2 coated Cu, revealing all the major peaks of TiB_2 and Cu. An absence of peaks corresponding to other compounds in the XRD spectrum further confirms poor mixing and a lack of chemical reaction between Cu and TiB_2. Earlier, it was seen that TiB_2 is the most stable compound in the Fe–Ti–B system. In the Cu–Ti–B system, formation of any borides of Cu is not shown in the Cu–B phase diagram.[12] However, the possibility of formation of a metastable phase, i.e. $CuTi_2$, does exist, as shown in the Cu–Ti phase diagram with 20 wt-%Cu.[12] No such phase formation is indicated however in the XRD spectrum of this specimen. In view of these observations, it can be concluded that the presence of 15 wt-%Cu in a TiB_2 coating is only physical in nature. Copper acts as a binder similar to Fe in the Fe–TiB_2 system. However, it should be noted that Fe acts as an excellent binder, while Cu is not a suitable binder for a hard ceramic like TiB_2. The role of Fe as an excellent binder for Ti based hard ceramics has been shown experimentally in various studies,[5,13,14] as discussed below.



a scanning electron micrograph; *b* X-ray elemental map of Ti; *c* X-ray elemental map of Cu

4 *Images of TiB_2 deposited on OFHC Cu*



5 *Elemental depth profile of Ti and Cu in coating and substrate*

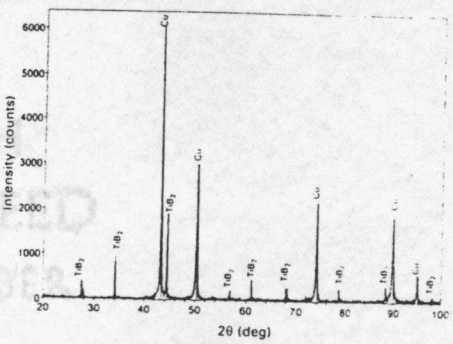
The roles of Cu and Fe as binders for ceramics are explained on the basis of their wetting characteristics. Several researchers have addressed the phenomenon of wetting of hard ceramics by metals.[15–19] It has been shown that Ti based ceramics easily wet Fe at high temperatures, and that wetting increases with time.[15] The wetting phenomenon has been attributed to unfilled d orbitals in transition metals and their compounds, including borides and carbides.[16,17] A detailed analysis of the role of metals as binders for ceramics and their wetting characteristics, based on electronic structure, has been addressed elsewhere.[16]

Titanium diboride is a transition metal based ceramic with partly covalent and partly metallic bonding.[16,19–20] The metallic nature of the bonding is suggested by the electrical conductivity of TiB_2, which is high and similar to that of the metals in Table 1. Moreover, the importance of metallic bonding over covalent bonding in these transition metal based ceramics has been postulated and confirmed.[17] A d band substructure similar to that of transition metals also exists in transition metal based ceramics, leading to metallic bonding in such ceramics.[17] A value has been assigned to the number of d electrons present in these transition metals and their compounds. Electrons in the d band substructure participate in the formation of a metallic bond. Accordingly, TiB_2 has 5·5 d electrons available for bonding.[15]

Based on theoretical and experimental results, an empirical rule has been proposed for the choice of binder used in sintering of transition metal based ceramics.[16] For a transition metal or compound having an unfilled inner d shell in the state d^x, a transition metal in the state d^y would be the most suitable binder (x and y represent the number of electrons in the unfilled d shells) if the following condition is satisfied

$$x + y = 11 \quad \ldots\ldots\ldots\ldots\ldots\ldots \quad (1)$$

This has been explained on the basis of an early model proposed by Friedel.[19] It is envisaged that the



6 *X-ray diffraction pattern for TiB_2 deposited on OFHC Cu*

physical interface between the hard ceramic and binder will have a bonding similar to a low melting point group IB element, i.e. a filled d shell of 10 electrons and one s shell electron. According to Friedel's hypothesis, such bonding would have lower cohesive energy and a low melting point.[19] Such properties are good for binders in these ceramics which are partly metallic and partly covalent in nature. As the deviation from equation (1) increases, bonding behaviour will also change. Nevertheless, a material selection system which gives $x + y = 10$ or $x + y = 12$ would also provide good bonding, though it would be inferior to a system satisfying the $x + y = 11$ condition because of deviation from the empirical rule mentioned in equation (1).

In the present study of the TiB_2–Cu material system, Cu has completely filled the d subshell with 10 electrons ($d^{10}s$ configuration) and TiB_2 has 5·5 d electrons, as assigned earlier.[17] Comparing with the hypothesis[16] in equation (1)

$$x(=5{\cdot}5) + y(=10) = 15{\cdot}5 \quad \ldots\ldots (2)$$

The results of equation (2) are very different from the hypothesis in equation (1), illustrating that Cu is a poor binder for TiB_2. However, Fe has 6 d subshell electrons (d^6s^2 configuration) and satisfies the hypothesis in equation (1) as shown by

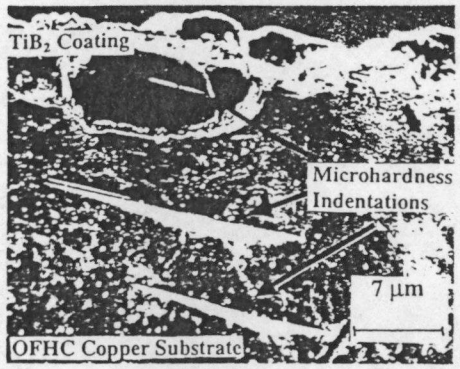
$$x(=5{\cdot}5) + y(=6) = 11{\cdot}5 \quad \ldots\ldots (3)$$

This accounts for the variation in wetting characteristics of Cu and Fe. It has been shown that Cu does not react with the TiB_2 layer but remains as a binder similar to Fe in Fe–TiB_2 and Co in WC–Co systems. This fact has been corroborated in an analysis based on electronic configuration which shows that bonding in such a material system does not promote compound formation.[17]

Mechanical characterisation

Mechanical characterisation of the coating and interface was carried out using a microhardness tester. Figure 7 is a cross-sectional SEM image of the coating and the substrate with microhardness indentations. The relative difference in size of the microhardness indentations demonstrates the hardness variation in the coating and substrate. Knoop microhardness values in the coating are very high, with an average value of 980 kg mm^{-2}, dropping to 78 kg mm^{-2} in the OFHC Cu substrate. The microhardness value at the ceramic/metal interface could not be measured in the absence of a significant transition region.

Figure 3*a* and *b* reveals the nature of interfaces developed in TiB_2–Cu and TiB_2–Fe respectively. It can be seen that interfacial decohesion occurs with TiB_2 deposited Cu whereas TiB_2 deposited on to steel has a strong interface with no signs of decohesion. Interfacial decohesion in the TiB_2–Cu system is attributed to the fourfold difference between the thermal expansion coefficient of TiB_2 and that of Cu (Table 1). It is well known that if the thermal expansion coefficient of a ceramic material α_c is less than that of a metallic material α_m, differential tensile and compressive stresses are generated at the interface.[21] These stresses lead to interfacial decohesion and crack formation in the coating, clearly shown in Fig. 3*a*. On the other hand, none of these failures are observed for TiB_2 coated steel (Fig. 3*b*). The presence of Fe in TiB_2 increases the toughness of the ceramic coating layer.[5]



7 *Cross-sectional SEM image showing microhardness indentations in TiB_2 coating and OFHC Cu substrate*

Thus, Fe mixed in the TiB_2 layer provides both hardness and toughness similar to the WC–Co system, whereas poor mixing between Cu and TiB_2 prevents similar effects. Instead, Cu acts as a poor binder for TiB_2. The degree of thermal expansion coefficient mismatch at the interface is higher in the TiB_2–Cu system, leading to delamination of the coating. Moreover, coating cracks are prominent in TiB_2–Cu as a result of a lack of toughness.

CONCLUSIONS

Titanium diboride was deposited on to oxygen free high conductivity (OFHC) Cu using the PES technique and test results were compared with those of a similar investigation on the TiB_2–Fe system. A thin, irregular, hard ceramic coating is obtained on OFHC Cu. Copper has poor wettability with TiB_2 and does not intermix significantly with the ceramic layer, and as a result is a poor binder for TiB_2. As a consequence, the TiB_2 coating shows interfacial decohesion and crack formation. Iron mixes easily with TiB_2 and acts as a suitable binder for ceramic, increasing both hardness and toughness. Titanium diboride is the most stable coating phase on an OFHC Cu substrate. No other metastable phase formation was found.

ACKNOWLEDGEMENTS

The authors wish to express their sincere appreciation to R. Raman, K. Muralidhar, and S. Krupashankara at Materials Modification Inc., Fairfax, VA, USA, who assisted in coating the specimens using the PES technique for the present work. The authors acknowledge financial support from the US Air Force (Contract F40600-96-C-0004) for this work.

REFERENCES

1. R. N. JOHNSON: *Thin Solid Films*, 1984, **118**, 31–47.
2. R. N. JOHNSON: in 'Elevated temperature science and technology I', (ed. N. B. Dahotre *et al.*), 264–277; 1994, Warrendale, PA, TMS.
3. R. N. JOHNSON: in 'Surface modification technologies II', (ed. T. S. Sudarshan and D. G. Bhat), 189–213; 1988, Warrendale, PA, TMS.

4 E. A. BROWN, G. L. SHELDON, and A. E. BAYOUMI: *Wear*, 1990, 138, 137–151.
5. A. AGARWAL and N. B. DAHOTRE: *Surf. Coat. Technol.*, 1998, 106, 242–250.
6. N. B. DAHOTRE, M. H. McCAY, and T. D. McCAY: *Mater. Manuf. Process.*, 1994, 9, 1–36.
7. G. V. SAMSONOV, A. D. VERKHOTUROV, V. S. SYCHEV, and A. I. BEZYKORNOV: *Fiz. Khim. Mekh. Mater.*, 1971, 7, 3–6.
8. R. A. CUTLER: in 'Engineering materials handbook: ceramic and glasses', Vol. 4, 787–803; 1991, Materials Park, OH, ASM International.
9. 'Metals handbook', Vol. 1, 145–213; 1978, Metals Park, OH, American Society for Metals.
10. G. V. SAMSONOV and I. M. VINITSKII: in 'Handbook of refractory compounds'; 1980, New York, NY, Plenum Data.
11. J. T. KLOMP: in 'Designing interfaces for technological applications: ceramic–ceramic and ceramic–metal joining', (ed. S. D. Petevers), 127–144; 1989, New York, NY, Elsevier Applied Science.
12. 'Metals handbook', Vol. 3, (ed. H. Baker); 1992, Materials Park, OH, ASM International.
13. C. RAGHUNATH, M. S. BHAT, and P. K. ROHATGI. *Scripta Metall.*, 1995, 32, 577–582.
14. A. AGARWAL and N. B. DAHOTRE. *Int. J. Refract Met. Hard Mater.*, to be published.
15. L. RAMQUIST: *Int. J. Powder Metall.*, 1965, 4, 1–4.
16. A. A. OGWU and T. J. DAVIES: *Mater. Sci. Technol.*, 1993, 9, 213–217.
17. E. DEMPSEY: *Philos. Mag.*, 1963, 3, 285.
18 L. BREWER: in 'Electronic structure and alloy chemistry of transition elements', (ed. A. Beck), 221; 1963, New York, NY, Interscience.
19. J. FRIEDEL: in 'The physics of metals', (ed. J. M. Ziman); 1969, Cambridge, Cambridge University Press.
20. G. HAGG: *Z. Phys. Chem.*, 1969, B6, 221.
21. T. TANAKA, H. MORIMOTO, and H. HOMMA: *Nippon Steel Tech. Rep.*, 1988, 37, 36.

IIW Commission IX
Working Group:

'Mathematical Modelling of Weld Phenomena'

Call for Papers

5th International Seminar on Numerical Analysis of Weldability

Graz, Austria — 4–6 October 1999

The 'International Seminar on Numerical Analysis of Weldability' has become a leading conference in the growing field of the development of methods for predicting the microstructure and properties of welds. It is of both practical and academic interest and supports the philosophy of computer methods which help optimise the welding process and consumables as well as the service behaviour of weld components.

Scope

- melt pool phenomena
- microstructure and mechanical properties
- post-weld heat treatment
- modelling tools
- solidification
- microstructural modelling in weld metal and heat affected zone
- residual stresses and distortion
- computer programs

Schedule

1 April 1999	**Deadline for abstracts**
1 May 1999	Notification of acceptance
1 September 1999	Deadline for manuscripts

Peer reviewed papers will be published by in book form by IOM Communications Ltd.

Further information from:

Bernhard Schaffernak, TU Graz, Institute for Materials Science, Welding and Forming, Kopernikusgasse 24, A–8010 Graz, Austria, tel. +43 873 7182, fax +43 873 7187, email bernie@weld.tu-graz.ac.at, Internet http://www.cis.tu-graz.ac.at/weld/seggau.html

APPENDIX IV

SYNTHESIS OF BORIDE COATING ON STEEL USING HIGH ENERGY DENSITY PROCESSES: COMPARATIVE STUDY OF EVOLUTION OF MICROSTRUCTURE

(published in ***Materials Characterization*** journal)

ELSEVIER

Synthesis of Boride Coating on Steel using High Energy Density Processes: Comparative Study of Evolution of Microstructure

Arvind Agarwal and Narendra B. Dahotre
Department of Materials Science and Engineering, Center for Laser Applications, University of Tennessee Space Institute, Tullahoma, TN 37388, USA

Ultrahard titanium diboride (TiB_2) coatings are deposited on plain carbon steel substrate using two high energy density processes, viz. pulsed electrode surfacing (PES) and laser surface engineering (LSE). These two processes are entirely different in physical nature and hence result in dissimilar microstructures. In the present investigation, a comparative study has been made between the evolved microstructures. Both processes produced a surface layer which is adherent and metallurgically bonded to the substrate. PES produced relatively thinner and less uniform coating than LSE process. The PES coating was, however, homogeneous and very fine grained. The laser-assisted coating was "composite" in nature with TiB_2 particles embedded in Fe matrix. Mechanical characterization of these coatings has been performed using microhardness measurements. © Elsevier Science Inc., 1999. All rights reserved.

INTRODUCTION

Superhard boride coatings are very useful for extending the service life of the surfaces that undergo severe conditions of wear, abrasion and erosion [1]. These ultrahard ceramic coatings are used for several applications. These include nuclear, fossil and geothermal energy environments [2–4], high temperature turbine coatings for aerospace applications [5], industrial cutting tools such as milling cutters and drills [6], wear resistant surfaces on large agricultural and textile equipment, high temperature sensors [6], systems used in the petrochemical and pharmaceutical industries, and modern sports equipment [7].

Conventionally, there have been several processes, such as chemical and physical vapor deposition, thermal spray, and detonation gun technique, for depositing ceramics on metals. However, there exists a need for the development of a coating technique that can successfully deposit a hard ceramic material such as TiB_2 on metallic substrates to produce a coating with a metallurgically sound interface. Such coating process should also obviate the need for a vacuum chamber, which often leads to restriction in size of work-piece and increases the cost of process. High energy density techniques such as Pulse Electrode Surfacing (PES) and Laser Surface Engineering (LSE) are two such effective processes used to deposit ultrahard ceramic coatings on metals. These processes can be performed in air to produce an adherent ceramic coating.

PULSE ELECTRODE SURFACING

Pulse Electrode Surfacing utilizes high current electrical pulses of short duration to modify the metal surface. A high current, short duration pulse via discharge capacitance and voltage circuit results in melting the electrode and depositing the material on the substrate [1, 8–9]. The process is very similar to the arc-welding process with the exception of little total heat input. Hence, PES is also referred as a mi-

MATERIALS CHARACTERIZATION 42:31–44 (1999)
© Elsevier Science Inc., 1999. All rights reserved.
655 Avenue of the Americas, New York, NY 10010

1044-5803/99/$-see front matter
PII S1044-5803(98)00054-0

cro-welding process. The main advantage of this process stems from the fact that metallurgically bonded coatings with an adherent interface can be produced with little heat input to the substrate at ambient temperature [10]. This minimizes the changes in the metallurgical properties of the substrate material and also reduces distortion due to thermal stresses [2, 7]. Since the bulk material remains near ambient temperature and acts as a heat sink, heat is rapidly dissipated, leading to rapid solidification of the molten pool which, in turn, results in an extremely fine grained coating of high density, hardness and strength. Furthermore, the PES process obviates the need for the expensive environmental chambers required in several other types of coating processes.

The primary requirement and the limitation for the PES process is that electrode material should be electrically conductive and thus be capable of melting in an electric arc. The consumable electrode having a positive polarity is brought close to the substrate, which has a negative polarity. This leads to the generation of spark and intense heat. The intensity of the spark is directly proportional to the voltage across the gap between the electrode and the substrate, the amount of current, and the duration of current flow, which is known as pulse time:

$$\text{Energy of the spark } (E) \propto \text{Voltage } (V) \times \text{Current } (I) \times \text{Time } (t)$$

The energy of the spark in turn decides the amount of electrode being deposited and the bond strength between the deposited material and the substrate. The dielectric medium, which could be air, argon or any other environment, provides a path for the discharge plasma and the region between the electrodes remains ionized, enabling continuous flow of current. The applied voltage should be higher than discharge voltage, which is dependent on the choice of electrode-dielectric system. At present, most of the researchers assume that major erosion of electrode in an arc discharge is of a thermal nature [10] and hence depends upon thermophysical properties of the electrodes. Thus, a suitable choice of processing parameters will lead to incipient melting of the electrode tip and material transfer will occur through discharge plasma. Several of such discharges are repeated with a frequency from tens to hundreds of hertz to deposit the coatings [8].

It has been successfully argued that material transfer from electrode tip to substrate occurs in the liquid state [9]. The choice of the gas environment influences the mechanism of transfer of material [2, 7]. Disassociable gases like air and nitrogen form a plasma of high thermal conductivity that promotes globular mass transfer. In globular mass transfer, a molten droplet forms at the end of the consumable electrode and is accelerated towards the substrate by the discharge plasma. These droplets impact the surface with a splash appearance leading to a rough and thick coating surface. However, argon ionizes easily producing a plasma of relatively low thermal conductivity that tends to produce a fine spray of molten material [2, 7]. Spray transfer produces a smoother and uniform deposit in comparison with globular mass transfer.

Thus in the PES process, apart from raising the temperature of the electrode to melting point, substantial electrical energy is also consumed in interacting with the environmental atoms above the substrate. Radiation is produced as a consequence of interaction of electrical energy with environmental atoms. This radiation interacts with substrate atoms to raise their temperature. However, this interaction of discharge electrons is "indirect" in nature and hence it does not raise the temperature of the substrate high enough to melt it significantly or cause substantial microstructural changes. Moreover, molten droplets also lose temperature during the flight period from the electrode tip to the substrate. This results in a transitory melting of the substrate and the formation of a small heat-affected zone (HAZ). Most probably, the reason for the shallow melt zone in the substrate is the much greater thermal sink in the substrate, and the pulsed nature of the spark. The time between sparks is very long relative to

the duration of the sparks themselves, thus allowing the substrate heat to dissipate rapidly. The transitory melting of cathode/substrate in the PES process can also be explained by thermal micro-explosions occurring on the substrate [11].

LASER SURFACE ENGINEERING

Laser surface engineering is a non-equilibrium synthesis involving techniques such as surface alloying, heat-treatment, composite layer formation and texturing. High cooling rates of 10^3 to 10^8 K/sec associated with the process result in the formation of novel, metastable phases and a variety of microstructures by exceeding the solid solubility limit beyond equilibrium phase diagram [12].

In contrast to the PES technique, the laser beam is a coherent energy source with low divergence and high energy density [13]. The majority of the laser beam energy is consumed in interacting "directly" with the precursor and the substrate, resulting in an intense rise in temperature and heat. A very small amount of laser beam energy is used in interaction with the environment above the substrate. Hence, in the present study, energy transfer in LSE process is much more efficient than in the PES process, resulting in the formation of a large melt zone and a significant HAZ.

Energy transfer from laser beam to the substrate also depends upon material properties such as absorptivity and thermal conductivity [13]. The interaction between laser and metal is explained by the free electron model of materials. Materials such as metals have free electrons and these oscillate with high energy leading to a plume/plasma formation. A suitable choice of laser and material system decides the frequency of such plasma, which, in turn, is associated with the absorption coefficient of the irradiated metal. In the present case, the surface of AISI 1010 steel has a good absorption coefficient for Nd: YAG laser, which assists in formation of a melt zone [14]. Fig. 1 and Table 1 provide a direct comparison between the PES and the LSE processes.

The thermodynamics and chemistry of the ceramic-metal system play an important role in the properties of these coatings. The chemical reactions occurring at the interface and within the coating lead to the formation of various stoichiometric and non-stoichiometric compounds that decide the adherent strength and other properties of the coating. Thermodynamic predictions, coupled with quantitative characterization of the evolved microstructure in the TiB_2-Fe material system, have been presented elsewhere [15–16].

In this study, hard TiB_2 ceramic has been deposited on two different plain carbon steel substrates using the PES technique and a continuous wave Nd:YAG laser, respectively. The processing parameters have been chosen on the basis of earlier works [7–9, 17–18]. An attempt has been made to

Table 1 Salient Physical Features of the PES and LSE Processes

Features	*PES Process*	*LSE Process*
Energy/Beam Source	Incoherent	Coherent beam with less divergence
Interaction with Dielectric	Significant interaction with dielectric atoms present between the electrode and the substrate	Minimal interaction with dielectric atoms present as an environment above the substrate
Energy Transfer to the Substrate	Indirect transfer through molten electrode droplet and radiation from the dielectric atoms	Direct interaction with the substrate forming a plume/plasma
Energy Density Input (MW/m^2)	0.10	15.0

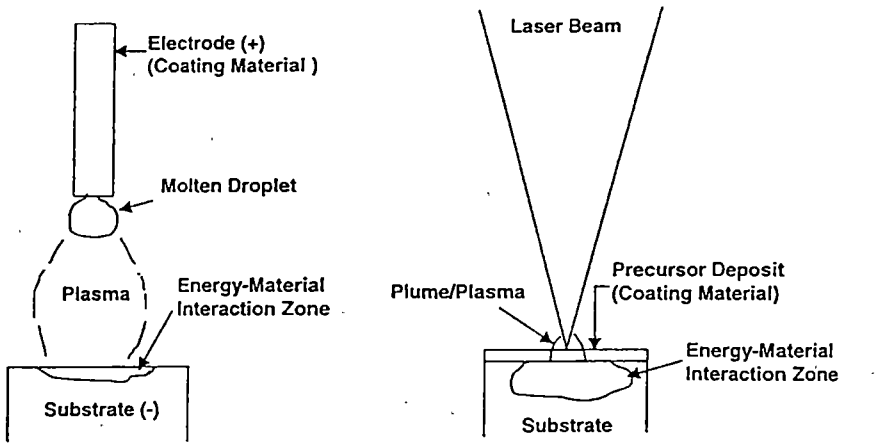


FIG. 1. A schematic drawing illustrating the physical processes of Pulsed Electrode Surfacing (PES) and Laser Surface Engineering (LSE).

reveal the differences in the microstructures evolved in such material systems processed using these high-energy beam techniques of different physical nature.

EXPERIMENTAL PROCEDURE

PULSE ELECTRODE SURFACING

TiB_2 coatings were deposited on AISI 1018 steel coupons using PES method as described elsewhere in detail [15]. TiB_2 is the hardest and lightest refractory material, and has excellent wear and oxidation resistant properties at temperatures up to 1673 K [19]. TiB_2 is chemically inert in corrosive environments. The electrical conductivity of TiB_2 is high which makes it suitable choice for deposition by the PES technique [2, 9, 19].

Coupons of AISI 1018 steel of dimensions 25mm x 10mm were mechanically polished on emery paper of grit 240 and then rinsed with acetone. A sintered electrode of TiB_2 containing Ni in the range of 1–3wt% as binder was used to deposit coating on these steel coupons. Deposition was done using a hand-held gun in air at room temperature. Pulsed electrode deposition was carried out at 50V and a spark time of 10 μs. The discharge capacitance used for the PES process was 450μF with a current of 50A. Thus, the energy density input for the PES process is $0.10 MW/m^2$.

LASER SURFACE ENGINEERING

Commercially available TiB_2 and Ti powders were obtained from CERAC, Milwaukee, WI and used as precursors for this study. Both powders had a purity of 99.5%. The average particle size range was 5.5μm ± 1μm. Thin plates of AISI 1010 steel of size 7.5 cm x 15cm were cleaned using sand blasting. The precursor of a powder mixture of composition 2wt% Ti and 98wt% TiB_2 was sprayed on these coupons using a spray gun. The average preplaced powder bed had a thickness of 150 ± 15μm. Sprayed coupons were dried at 70°C for 1 h prior to laser processing. The addition of 2wt% Ti to TiB_2 was made on the assumption that Ti increases the wetability in the melt zone [20]. It was also anticipated that additional Ti would recombine with any boron that might disassociate during the laser processing.

A 2.5kW Hobart HLP 3000 continuous wave Nd:YAG laser (1.06μm wavelength) equipped with a fiber optic beam delivery system was employed for synthesis of la-

ser-assisted TiB_2 coatings. In order to provide a large sweeping coverage (i.e. rapid processing speed) and to reduce and/or to eliminate overlap between the successive laser passes, the laser optics were configured to provide a 3.5mm wide line beam in spatial distribution onto the sample surface. The processing parameters were optimized in accordance with earlier reported literature [17–18]. It has been established that for effective laser surface modification processes such as cladding/alloying/infiltration, the beam power should be greater than 1kW [21]. In the present study, laser beam power and traverse speed were kept constant at 1.5kW and 33mm/s, respectively. Thus, the energy density input for LSE is $15MW/m^2$, a couple of orders of magnitude higher than PES process.

CHARACTERIZATION

Coating topography and microstructural characterization was performed using a scanning electron microscope (SEM) and a transmission electron microscope (TEM). Metallographic samples for scanning electron microscopy were prepared by polishing on Buehler TEXMET 2000 cloth during initial stages of polishing. The etchant used for TiB_2 coated steel sample was Nital. Laser treated samples required longer etching time as compared to PES samples. Such behavior could be explained by the nature of the coatings obtained in the two processes. ISI Super III-A scanning electron microscope coupled with EDAX was employed for investigating the microstructural morphology and chemical characterization of the coating and interface. The surface topography of the coated samples was conducted using the SEM. Structural characterization for phase(s) identification was carried out on a Philips Norelco x-ray diffractometer with CuK_α radiation operating at 30kV and 40mA. Microhardness measurements were performed on Buehler Micromet II microhardness tester using a Knoop indenter with a load applied for 15s. The normal load applied was 200g for PES samples and 300g for LSE samples. A Teclock AM-1201 dial gauge equipped with a fine diamond-tipped stylus was used for measuring surface roughness of the coated surfaces.

TRANSMISSION ELECTRON MICROSCOPE SAMPLE PREPARATION

Only LSE samples were investigated at the Oak Ridge National Laboratory (ORNL) using a Hitachi HF-2000 Field Emission transmission electron microscope operated at 200kV. PES samples could not be analyzed using the TEM because the discontinuous nature of PES coatings made it difficult to prepare samples for TEM observations.

For the TEM, the steel samples were coated with TiB_2 then sectioned using a slow-speed Buehler Isomet diamond saw. These samples were further mechanically ground to a thickness of approximately 300μm. A 2 mm square section of this sample was mounted on an epoxy stub and was further ground and polished to a thickness of approximately 150μm using a Buehler Isomet Minimet Polisher. A Gatan 656 dimple grinder was used for thinning the sample down to 20μm. The sample was very fragile at this stage. It was mounted on a carbon ring for support and then ion milled for 6–8h at setting of 6.5kV on a twin gun Gatan 691 Precision Ion Polishing System. Due to the "composite" nature of the laser assisted coating, where hard TiB_2 particles were embedded in plain carbon steel matrix, ion milling was very critical as it required differential level of milling.

RESULTS AND DISCUSSION

MICROSTRUCTURAL CHARACTERIZATION

The topographical features of the top surface of TiB_2 deposited on the steel substrate using the PES technique are illustrated in Fig. 2. The surface is rough and irregular with several islands of globular shape and a splash appearance. As mentioned earlier (section 1.1), this is a characteristic feature

SOUTHWORTH
PARCHMENT DEED
100% COTTON FIBER

of the PES technique. The present study of the PES process is being conducted in air, which supports a globular mass transfer mechanism. This is attributed to the fact that dissociable gases like nitrogen and air form a plasma of high thermal conductivity which promotes globular mass transfer [7]. A molten globular droplet forms at the TiB_2 electrode tip and impinges on the steel substrate. This produces a splash appearance on the top surface. Fig. 2(b) shows a higher magnification view of the top surface, indicating globular droplets on steel substrate. Globular mass transfer provides high deposition rates that can assist in deposition of thick coatings [15]. Fig. 3 shows the top surface of the laser-engineered surface. The surface is relatively smooth, flat and free from cracks. The surface roughness, R_a, is quantitatively characterized in Fig. 4. The surface roughness values are higher for PES samples, in correspondence with its topographical features observed in Fig. 2.

Fig. 5 presents the SEM micrographs of the cross-sectional views of the TiB_2 coated steel using the PES and LSE processes. It can be seen in Fig. 5(a), from the PES sample, that the coating is homogeneous, dense, adherent and free of defects like cracks. The few crack-like features are the artifacts created during polishing. It is evident that the coating thickness is not very uniform throughout the cross section. This is in accordance with the nature of the PES process as described above (section 1.1) and as earlier observed in the topographical features of the same sample in Fig. 2(a). Fig. 5(b) shows a continuous, adherent and crack-free laser deposited TiB_2 coating on AISI 1010 steel substrate. The coating/laser melt zone is "composite" in nature. It is an inhomogeneous mixture of TiB_2 ceramic particles of different morphologies (polygonal and acicular) and Fe. A thin layer of steel substrate melts and mixes with TiB_2 due to convection currents within the melt zone, resulting in a composite coating. Within the laser melt zone, the distribution of TiB_2 particles is uniform and their content is very high (volume fraction = 0.67). Such a microstructure is a consequence of relatively higher processing speed. At high laser

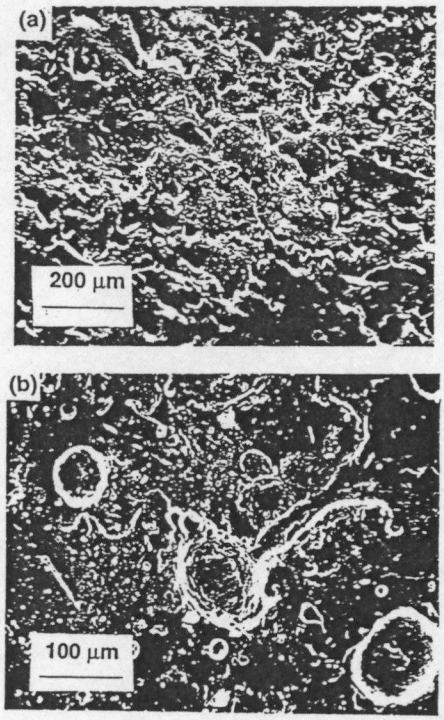


FIG. 2. SEM micrographs of the top surface of the AISI 1010 steel coated with TiB_2 using the PES process (a) indicating splash appearance and (b) globular mass transfer from electrode tip to the substrate.

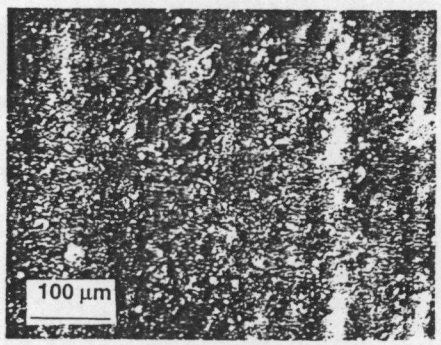


FIG. 3. SEM micrograph showing the topological features of laser coated surface.

SOUTHWORTH

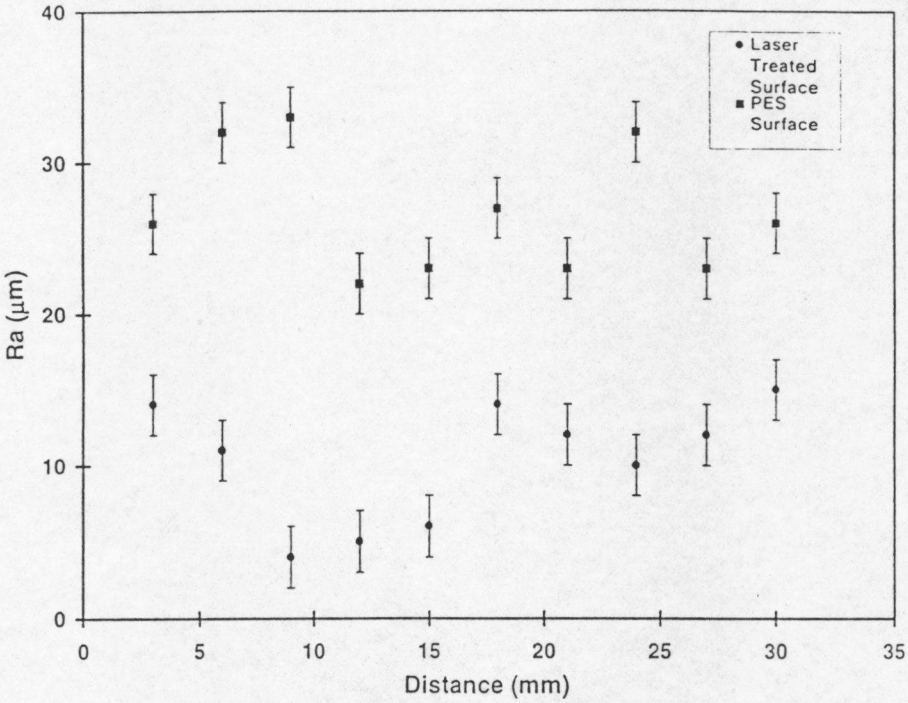


FIG. 4. Surface roughness profiles for the PES and LSE samples.

traverse speed, there is lesser dwell time for the sweeping laser beam to interact with the substrate and precursor. This results in a melt pool of low depth but with a higher concentration of TiB_2 particles. A detailed quantitative analysis of microstructural evolution as a function of various processing parameters has been elucidated in a separate study [16].

Fig. 6 is high magnification cross-sec-

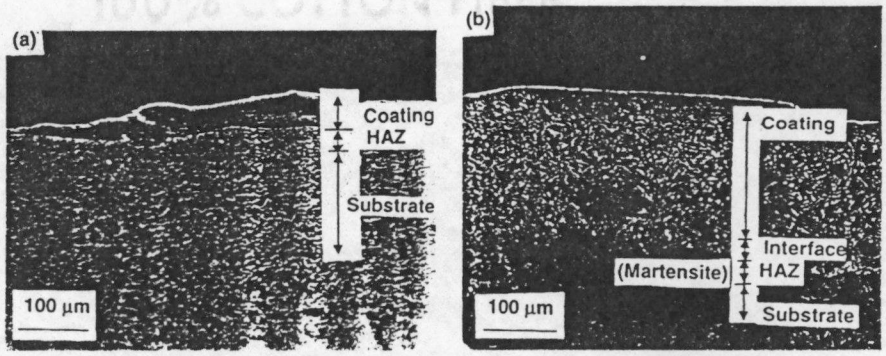


FIG. 5. SEM micrographs of cross sectional views of (a) PES sample and (b) LSE sample.

tional view of a PES sample, revealing a strong and continuous interface along with a HAZ. There is no delamination or existence of cracks at the interface of the coating and the substrate. The presence of such a continuous interface indicates formation of a metallurgical bond between TiB_2 and steel. Fig. 7(a) shows interfacial microstructure in LSE sample. A continuous, adherent and metallurgically sound interface with a dendritic and/or cellular structure is obtained. The interfacial region shows dendritic/cellular growth into the coating and martensitic structure in the substrate. Such a microstructure is attributed to the rapid heating and cooling rates attained during laser surface treatment. The temperature at the interfacial region of the AISI 1010 steel substrate reaches high enough to cause complete austenitization which then transforms to martensite due to high quenching rates.

The high magnification view of the dendritic/cellular interface obtained in LSE sample is shown in Fig. 7(b). The solidification structure of the melt zone depends upon the degree of constitutional supercooling. The rapid kinetics within the laser melt zone lead to variations in temperature at various locations due to the existence of different phases such as TiB_2, Fe and other metastable phases. Consequently, such differences in temperature result in variations in the degree of constitutional supercooling, leading to a complex solidification structure in both the interfacial region and the laser melted zone. It should also be observed that initial growth at the interface is towards the coating with a coarse cellular morphology. These coarse cellular dendrites transform into finer dendrites on going further into the melt zone. This feature is prominent in Fig. 7(b). This could again be attributed to the increasing cooling rates on going away from the interface into the melt zone. A higher cooling rate suggests refinement of microstructure such as cellular to coarse dendrites which could be further refined into equiaxed dendrites [22–23]. It should be recalled that LSE process has very high energy density input ($15MW/m^2$) compared with the PES process ($0.10MW/m^2$). Thus, the microstructures obtained by these two processes are significantly different.

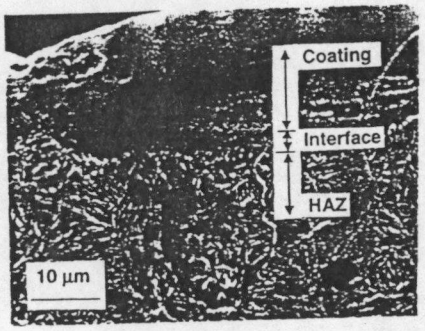


FIG. 6. High magnification SEM micrographs showing a continuous and adherent interface in the PES sample.

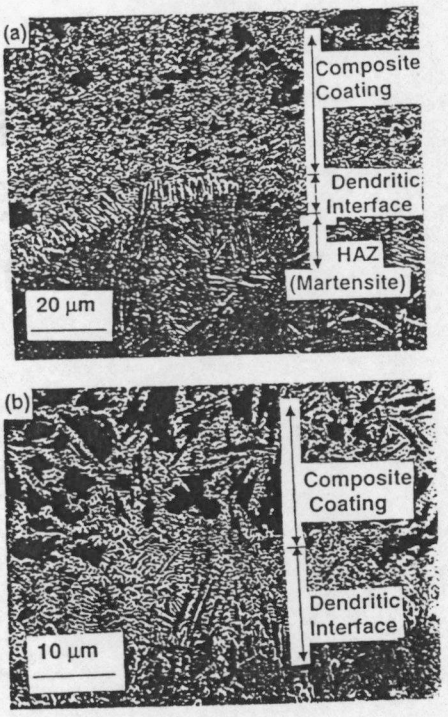


FIG. 7. SEM micrographs of the LSE sample (a) low magnification view of the interface and HAZ and (b) high magnification view showing cellular dendrites at the interface.

Fig. 8(a) shows the coating structure obtained in the PES sample The coating is homogeneous, dense and fine grained (approximately 2–3μm) with some surface porosity. There are no cracks with in the coating layer, suggesting its tough nature. It has been earlier mentioned that the substrate acts as a heat sink in the PES technique, leading to rapid solidification of the coating. Such very fine grained TiB_2 coating can be attributed to the high cooling rates. On the contrary, the structure within the laser melted zone of the LSE sample [Fig. 8(b)] is made up of a composite structure of needle-shaped TiB_2 particles within a fine (approximately size 1–2 μm) equiaxed dendritic matrix of Fe. Such a fine microstructure of equiaxed dendrites in the melt zone is also corroborative of very high cooling rates involved in laser surface modification. There are no cracks or delamination within the laser melt zone. Thus, the layer produced by the LSE process is also tough in nature.

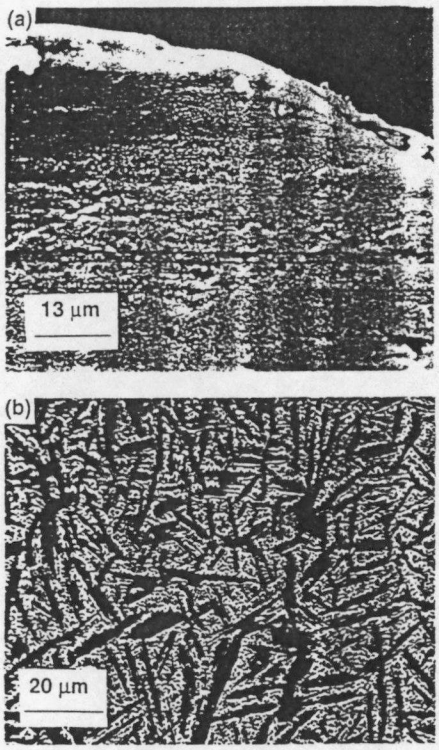


FIG. 8. SEM micrographs showing coating morphology in (a) PES sample and (b) LSE sample.

The formation of metallurgical bonds within both the PES and LSE samples indicates that there is some chemistry change at the interface and within the coating. EDAX analysis of the PES and LSE samples suggests intermixing of TiB_2 and Fe in the layer [15–16]. It has been shown earlier that in the PES sample, mixing was purely physical in nature where Fe acts as an excellent binder for TiB_2 [15]. This has been explained on the basis of wetting phenomena in refractory based ceramics [15, 24–25]. Moreover, it has been shown thermodynamically that TiB_2 is the most stable phase [15]. This fact is further corroborated in Fig. 9, which shows the x-ray spectrum for the PES sample. It reveals all the major peaks of TiB_2 and Fe. There is no discernible peak of any other phase(s), further confirming our analysis that there is no chemical reaction within the layer. Fig. 10 shows the x-ray spectrum of the LSE sample. TiB_2 is the most prominent phase present. However, some peaks of metastable phase(s) of the type Fe_xB_y and Ti_aB_b are also observed in the laser-processed sample. The formation of such non-stoichiometric and metastable phase(s) is explained by the non-equilibrium synthesis during laser surface engineering. It is possible that laser surface alloying, which has a high energy density, may cause some chemical reaction between Fe and TiB_2.

TEM work is under way to precisely understand the reactions occurring in the laser melt zone. The preliminary TEM investigations suggest the formation of a small reaction zone at the TiB_2 particle/Fe matrix interface (Fig. 11). Such a reaction zone is expected to provide strong bonding between the particle and the surrounding matrix [26]. The bright field TEM image of the composite coating produced by the LSE process is illustrated in Fig. 12. It clearly illustrates the "composite" nature of the coating due to TiB_2 particles of various

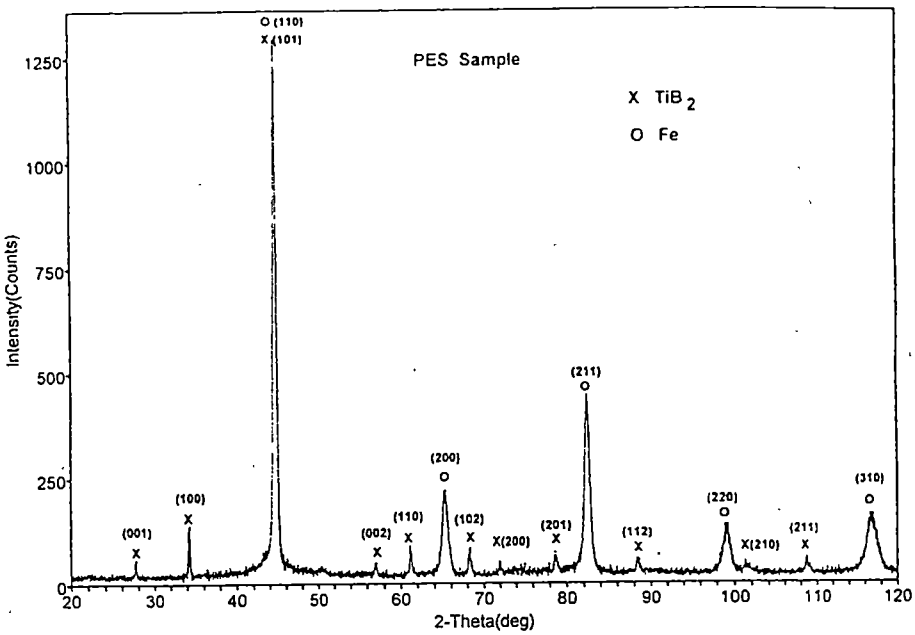


FIG. 9. X-ray diffraction spectrum of PES-coated sample

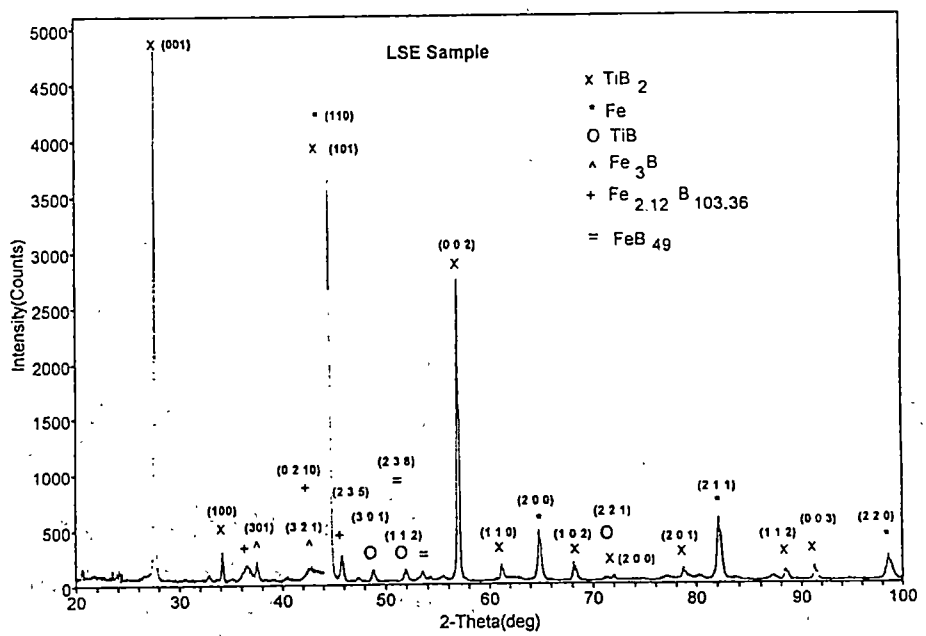


FIG. 10. X-ray diffraction spectrum of LSE-coated sample.

SOUTHWORTH
PARCHMENT DEED
100% COTTON FIBER

shapes embedded in the Fe matrix. However, the mode and nature of the reactions occurring within the laser melt zone are still not clearly understood. It is expected that further TEM investigations, such as high resolution lattice imaging, selected area diffraction pattern and microanalysis, will enable a better understanding of the novel phase(s) formed as a consequence of non-equilibrium synthesis.

MICROHARDNESS

Preliminary mechanical characterization of the coating and interface has been conducted using a microhardness tester. Fig. 13 shows the microhardness variations in the coating, the HAZ and the substrate material for the PES and LSE samples. For the PES sample, there is a gradual decrease in the microhardness values on going through the coating to the substrate [Fig. 13 (a)]. The relative difference in size of the microhardness indentations makes clear the hardness variation in coating and the substrate. Knoop microhardness values in the coating are high (average value 1124 ± 94 at Spot A), while they drop down to 182 ± 10 in the base material (Spot C). The microhardness value at the interface and in the HAZ is 384 ± 21 (Spot B). Fig. 13(a) shows the coherent and defect-free nature of the coating. No crack initiation or propagation is seen at any of the indentation sites, which supports the high cohesive strength of the interface and the toughness of the coating. This is attributed to the presence of Fe in the TiB_2 layer which provides toughness to the ceramic coating layer. Thus, mixing the Fe in the TiB_2 layer provides a composite effect of hardness and toughness. The microhardness variations in the LSE sample are significantly different from those in the PES sample due to the nature of the microstructure in the laser melt zone. Fig. 13(b) shows the microhardness indentations amid a cluster of TiB_2 particles (spot A), at the TiB_2 particle/steel interface (spot B) and in the HAZ in the steel substrate (spot C). Knoop microhardness values are extremely high within the clustered zone of TiB_2 particles, having an average value of 1742 ± 306. Spot B in Fig. 13(b) corresponds to an average Knoop microhardness value of 622 ± 37, whereas spot C, located in the HAZ (martensitic zone) of the steel substrate, has an average value of 407 ± 21. By comparison, the microhardness value in the unaf-

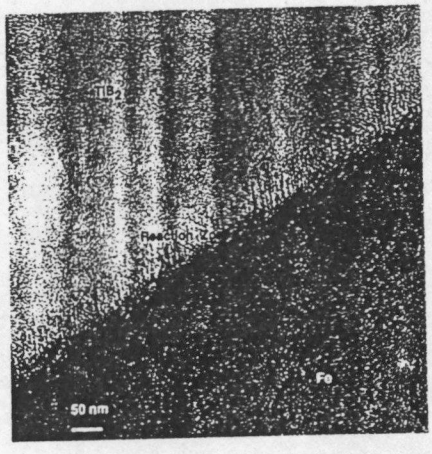


FIG. 11. TEM micrograph showing a reaction zone between TiB_2 particle and Fe matrix in the LSE sample.

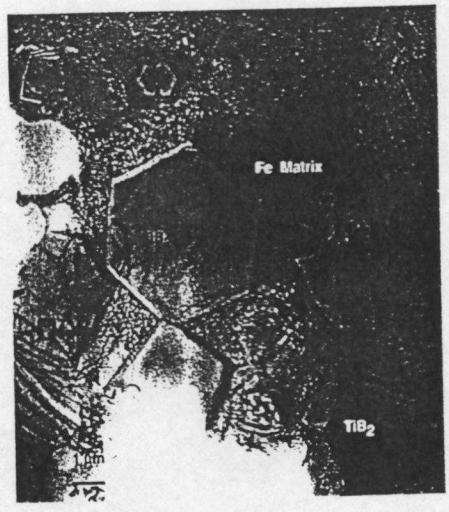


FIG. 12. Bright field TEM image illustrating embedded TiB_2 particles in Fe matrix, suggesting composite nature of laser deposited coatings.

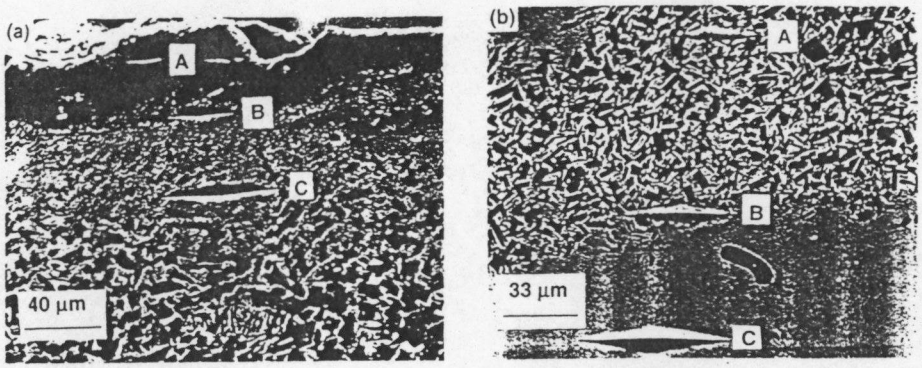


FIG. 13. SEM micrographs of cross-sections showing microhardness indentations in (a) PES sample and (b) LSE sample.

fected steel substrate was 140 ± 25. Pure TiB_2 has extremely high hardness of 33 GPa (3300Kg/mm^2) whereas phases such as Fe_xB_y and Ti_aB_b have hardness values (13–22 GPa), lower than TiB_2 but higher than 1010 steel [27]. The hardness variation in the melt zone is consistent with the fact that the microstructure in the laser melt zone is composite in nature, comprising of various phases and different sized particles. Microhardness indentations of such a large size provide a combined average hardness value of the various phases and particles. It is expected that nanoindentation studies will

Table 2 Summary of the Microstructural Features, Microhardness Measurements and Phase(s) Present in TiB_2 Coatings Deposited by PES and LSE Processes

Features	*PES Process*	*LSE Process*
Average Surface Roughness 'R_a' (μm)	23.8	10.9
Nature of Coating	Thin (35–40μm), homogeneous, dense and very fine grained (2–3μm)	Thick (200μm) Composite Coating with embedded TiB_2 particles in fine equiaxed Fe matrix
Type of Interface	Adherent and continuous with a small heat affected zone (25–30μm)	Dendritic/Cellular interface with a large heat affected martensitic zone (100μm)
Microhardness (Knoop) in Coating (kg/mm^2)	1124 ± 38	1742 ± 306
Microhardness (Knoop) at Interface (kg/mm^2)	384 ± 13	622 ± 37
Microhardness (Knoop) in Heat Affected Zone (HAZ) (kg/mm^2)	384 ± 13	407 ± 21
Microhardness (Knoop) in Substrate (kg/mm^2)	185 ± 10	140 ± 25
Phase(s) Present	TiB_2, Fe	TiB_2, Fe, TiB, Fe_3B, FeB_{49} and $Fe_{2.12}B_{103.36}$

provide a better estimation of the hardness values of the individual phases in a more precise manner.

Table 2 provides a list of the comparative differences in the evolved microstructures, microhardness measurements and phase(s) observed as a consequence of the PES and LSE processes. Such differences can be further instantaneously and clearly understood through reference to Table 1 and Fig. 1, which describe individual features of physical nature and mode of energy-material interaction in the two processes.

CONCLUSIONS

TiB_2 has been successfully deposited on a steel substrate using high-energy density processes such as PES and LSE. Both techniques have produced crack-free coatings with an adherent and metallurgically sound interface.

A homogeneous, dense, adherent, very fine grained and defect-free hard ceramic coating is obtained through the PES process. The coating produced by LSE is "composite" in nature, comprising TiB_2 particles and Fe from the steel substrate trapped in laser melt zone. Needle/acicular shaped boride particles are uniformly distributed in the melt zone.

The interfacial microstructure in the LSE sample is significantly different from that in the PES sample. The microstructure in the LSE sample consists of various cellular dendrites and fine equiaxed dendrites indicative of a complex solidification process and very high cooling rates within the melt zone.

In the PES process, Fe migrates into the TiB_2 layer and takes up the role of a binder. It does not react chemically with TiB_2 but acts as a binder for the ceramic and provides a composite effect of both hardness and toughness. TiB_2 was the most stable phase formed in the layer. However in the LSE process, the existence of metastable phases such as Fe_xB_y and Ti_mB_n is observed which is characteristic feature of non-equilibrium synthesis by laser energy. A small reaction zone at the TiB_2/Fe interface was observed in the TEM investigation.

A coating with a high hardness value is obtained from the PES process. However, hardness values are very high in LSE coatings. TEM studies coupled with nanoindentation analysis would give a precise correlation between the formation of novel metastable phases and hardness values in LSE samples.

The authors wish to express their sincere appreciation to Dr. T. S Sudarshan, Materials Modifications Inc., Fairfax who provided the samples for the present work. The authors would also like to express their sincere thanks to Dr. Lawrence Allard at ORNL for his help and guidance with the TEM work. This work was sponsored by the Assistant Secretary for Energy Efficiency and Renewable Energy, Office of Transportation Technologies, as part of the High Temperature Materials Laboratory User Program. ORNL is managed by Lockheed Martin Energy Research Corp. for the U. S. Department of Energy under contract number DE-AC05-96OR22464. The authors also acknowledge partial financial support from the US Air Force (Contract No. F 40600-96-C-0004).

References

1. R. A. Alfintseva, I. G. Bodrova, and A. D. Verkhoturov: The applications of refractory metal borides as electrodes in electrospark machining. *J. Less Common Metals* 67:443–448 (1979).
2. R. N. Johnson: Principles and applications of electro-spark deposition. In *Surface Modification Technologies*, T. S. Sudarshan and D. G. Bhat, eds. The Metallurgical Society, Warrendale, PA. pp 189–213 (1988).
3. K. Natesan and R. N Johnson: Corrosion resistance of chromium carbide coatings in oxygen-sulfur environment. *Surf. Coating Tech.* 33:341–351 (1987).
4. R. N. Johnson: Coatings for fast breeder reactor components. *Thin Solid Films* 118:31–47 (1984).
5. S. Raghunathan, J J. Stiglich, and T. S. Sudarshan: Characterization of Ir/Re duplex coatings on Ta/10W deposited by pulsed electrode surfacing (PES). In *Elevated Temperature Science and Technology I*, N. B. Dahotre, J. M. Hampkian, and J. J. Stiglich, eds. The Minerals, Metals and Materials Society, pp. 303–312 (1995).

6 E A Brown, G. L Sheldon, and A. E. Bayoumi A parametric study of improving tool life by electro-spark deposition. *Wear* 138:137–151 (1990).

7 R. N. Johnson: Electro-spark deposited coatings for high temperature wear and corrosion applications. In *Elevated Temperature Science and Technology I.* N. B. Dahotre, J. M. Hampkian, and J J Stiglich, eds. The Minerals, Metal and Materials Society, pp. 265–277 (1995).

8. A. I. Bushik and V. A. Shilov: some variants of the method of electrospark alloying of surfaces. *Elektronnaya Obrabotka Materialov* 1:22–25 (1991)

9. G. V. Samsonov, A. D. Verkhoturov, V. S. Sychev, and A. I. Bezykornov: Investigation of some of the laws governing the formation of a hardened layer during the process of electro-spark alloying. *Fiziko-Khimicheskaya Mekhanika Materialov* 7(5) 3–6 (1971).

10. V. V. Kantsel, T. S. Kurakina, V. S. Potokin, V I. Rakhovskii, and L. G. Tkachev: Thermophysical parameters of a material and electrode erosion in a high-current vacuum discharge. *Soviet Physics-Technical Physics* 13(6):814–817 (1968).

11. R. A. Basharov, E. N. Gavrilovskaya, O. A. Malkin, and E. S. Trekhov: Erosion of cathode in a pulsed discharge between parallel electrodes. *Soviet Physics-Technical Physics* 12(10):1383–1390 (1968).

12 J. Mazumder: Laser assisted surface coatings In *Metallurgical and Ceramic Protective Coatings.* Kurt H. Stern, ed. Chapman and Hall, London pp. 74—111 (1996).

13. P. A. Molian: Principles and applications of lasers for wear-resistant coatings. In *Surface Modification Technologies.* T. S. Sudarshan and D. G. Bhat, eds The Metallurgical Society, Warrendale, PA, pp 237–265 (1988).

14. W. W. Duley: *Laser Processing and Analysis of Materials,* Plenum Press, New York, pp 69–80 (1983).

15. A. Agarwal and N. B. Dahotre: Pulsed electrode deposition of superhard boride coatings on ferrous alloy. *Surf. Coating Tech.* (in press).

16. A. Agarwal and N. B. Dahotre: Laser surface engineering of steel for hard refractory ceramic composite coating. *Intl J Refractory Metals and Hard Matls* (submitted) (1998)

17. J. Th M. De Hosson and M Van Den Burg: Metal-ceramic interfaces produced by laser melt injection processing. *Materials and Manufacturing Processes* 10(6):1285–1294 (1995).

18. E. Ramous, L Giordano, A. Tiziani, B. Badan, and M. Cantello: Laser cladding of ceramic and metallic coatings on steel. In *Surface Engineering with High Energy Beams.* A. P Loureiro, O. Conde, L. Guerra-Rosa, and R. Vilar, eds. Trans Tech Publications, Switzerland, pp 425–434 (1990).

19. N. B. Dahotre, M. H. McCay, and T. D. McCay: Diamond materials for electromagnetic railguns. *Materials and Manufacturing Processes,* 9(1):1–36 (1994).

20. O. M. Akselsen: Advances in brazing of ceramics. *J Mater. Sci.* 27:1989–2000 (1992).

21. K. Komvopoulos and K. Nagarathnam: Processing and characterization of laser-cladded coating materials. *J. Eng. Materials and Technology,* 112:131–143 (1990).

22. W. Kurz and D. J. Fisher: *Fundamentals of Solidification.* Trans Tech Publications, Switzerland pp. 63–92 (1989).

23 J. E. Flinn: *Rapid Solidification Technology for Reduced Consumption of Strategic Materials.* Noyes Publications, Park Ridge, NJ pp. 42–64 (1985).

24. A. A. Ogwu and T. J. Davies: Electronic structure basis for selection of metal binders for hardmetal systems. *Matls. Sci. and Tech.* 9:231–237 (1993).

25. C. Raghunath, M. S. Bhat, and P. K. Rohatgi: In situ technique for synthesizing fe-tic composites. *Scripta Metallurgica* 32(4):577–582 (1995).

26. N. B. Dahotre, M. H. McCay, T. D. McCay, S. Gopinathan, and L. F. Allard: Pulse laser processing of a SiC/Al-alloy metal matrix composite. *J. of Mater. Res* 6(3):514–529 (1991).

27. R. A. Cutler: Engineering properties of borides. In *Engineering Materials Handbook: Ceramic and Glasses.* ASM International, OH, pp. 787–803. (1995).

APPENDIX V

PULSED ELECTRODE SURFACING OF STEEL WITH TITANIUM CARBIDE COATING: MICROSTRUCTURE AND WEAR PROPERTIES

(published in *Journal of Materials Engineering & Performance*)

JMEPEG (1999) 8:479-486 ©ASM International

Pulsed Electrode Surfacing of Steel with TiC Coating: Microstructure and Wear Properties

A. Agarwal and N.B. Dahotre

(Submitted 30 October 1998; in revised form 22 January 1999)

In the present study, pulse electrode surfacing (PES) technique was employed to deposit ultrahard and wear-resistant titanium carbide (TiC) coating on AISI 1018 steel. Wear resistance of the coated surface increased significantly. An attempt was made to correlate the thermodynamic predictions and experimental observations. A composite coating that is adherent, crack free, and defect free in nature was obtained, with TiC being the most stable phase. Islands of TiC of various shapes and sizes are present in the Fe-rich matrix in the coating. Microhardness measurements suggest high hardness values in the coating region. Tribological properties such as wear resistance and coefficient of friction were also measured. The coefficient of friction data do not show significant fluctuations. Wear and friction phenomena in such a coating have been explained on the basis of a model based on composite/multiphase material.

Keywords 1020 steel, pulse electrode surfacing, surface engineering, TiC, wear resistance

1. Introduction

Surface engineering of the metallic substrates plays a vital role in enhancing their application in hostile environments. The monocarbides of group 4 such as TiC, ZrC, and HfC are ideal materials for increasing hardness, wear and erosion resistance, and corrosion and oxidation resistance of the metallic surfaces (Ref 1). Surface properties can be altered by depositing monocarbide ceramic coatings on the component without making changes in the bulk properties. Several techniques such as plasma spray, chemical vapor deposition (CVD), physical vapor deposition (PVD), detonation gun, laser-assisted processes, and electrolytic deposition are used to carry out these surface modifications (Ref 2-4). Pulse electrode surfacing (PES) is one of such surface modification techniques that utilizes high current electrical pulses of short duration to modify the metal surface (Ref 5-8). A unique combination of high-current and short-duration pulse by discharge capacitance-voltage circuit results in melting the ceramic electrode and depositing the material on the substrate. The primary requirement for the electrode material is that it should be electrically conductive and thus capable of melting in an electric arc.

The main advantage of this process is its ability to apply metallurgically bonded coatings with low heat input to the substrate at ambient temperature. This reduces the depth of the heat-affected zone (HAZ) and thermal distortion, hence minimizing the changes in the properties of the substrate material (Ref 6). The bulk substrate material remains near ambient temperature and acts as heat sink. Thus, there are no thermal stress effects or metallurgical changes in areas other than in the fusion zone. Since the bulk material acts as huge heat sink, heat is rapidly dissipated leading to rapid solidification of the molten pool. Such a high energy-density coating process results in a fine grained coating of high density, hardness, and strength. Since the coating is metallurgically bonded to the substrate, excellent adhesion properties of the PES coatings with high spalling resistance are achieved (Ref 9). Another advantage of the PES process includes the use of relatively inexpensive and portable equipment. PES coatings can be deposited in air at room temperature. This prevents the need for expensive environmental chambers required in several types of other coating processes. These ultrahard ceramic coatings are used for several applications such as nuclear, fossil, and geothermal energy environments, high temperature turbine coatings for aerospace applications, solid lubricants for high-vacuum industrial cutting tools, waste reclamation, water treatment plant, wear-resistant surfaces on large agricultural and textile equipment, high-temperature sensors, systems used in petrochemical and pharmaceutical industry, and modern sports equipment (Ref 2, 5-7, 9-11).

In the present study, TiC has been deposited on AISI 1018 steel using PES technique. Thermodynamic predictions were coupled with experimental analysis to characterize the TiC-Fe interface and coating morphology. Dry sliding wear tests were performed to evaluate the tribological properties of TiC coating deposited by PES technique.

2. Experimental Procedures

2.1 Materials

In the present study, TiC has been deposited on AISI 1018 steel using PES technique. TiC is a very hard refractory material finding increasing usage for wear-resistant applications such as bearings, nozzles, cutting tools, and jet engine blades. It has relatively low electrical resistivity and can be used as a conductor for electricity, especially at elevated temperatures. Thus, TiC is a suitable choice for deposit on a structural

A. Agarwal and N.B. Dahotre, Center for Laser Applications, Department of Materials Science and Engineering, University of Tennessee Space Institute, Tullahoma, TN 37388, USA.

material such as AISI 1018 steel using PES method. The salient properties of TiC and AISI 1018 steel are listed in Table 1 (Ref 1, 12).

2.2 Coating Process

TiC coatings were deposited on AISI 1018 steel coupon using PES method at Materials Modifications Inc. (MMI, Fairfax, VA). Coupons of AISI 1018 steel with dimensions of 25 by 25 mm were mechanically polished on emery paper of grit size 240 and then rinsed with acetone. A sintered electrode of TiC was used to deposit a coating on these steel coupons. The TiC electrode had 3 to 5 wt% Ni and 1 to 3 wt% Fe as binder. Deposition was carried out using a handheld gun in air at room temperature. Pulsed electrode deposition was carried out at a voltage of 50 V and spark time of 10 μs. The discharge capacitance used for the PES process was 450 μF with a current of 25 A.

2.3 Characterization

Coating morphology, interface, and surface topography were studied using a ISI Super III-A scanning electron microscope (SEM). Samples for metallography were prepared by polishing on a Buehler TEXMET 2000 cloth during initial stages of polishing. This reduced the damage to the dissimilar ceramic/metal interface during polishing. Nital (nitric acid + 10 vol% methanol) was used as the etchant for TiC-coated steel samples. Energy dispersive spectroscopy (EDS) analysis and x-ray elemental mapping were coupled with SEM to characterize the distribution of elements in a semiquantitative analysis.

Structural characterization was performed using a Philips Norelco x-ray diffractometer with Cu Kα radiation (1.54 Å), operating at 20 kV and 40 mA. Microhardness measurements were performed on a Buehler Micromet II microhardness tester using a Knoop indenter with normal load of 200 gm applied for 15 s. Tribological properties were measured using a block-on-disk tribometer. Coated coupons of dimension 25 by 25 mm were tested for dry sliding wear against a hardened steel ring rotating at a linear speed of 270 m/min. Weight loss measurements were made after successive 2 min. The dry sliding wear test was conducted for 10 min with an applied normal load of 2 kg. The coefficient of friction (μ) was also recorded simultaneously by an interfaced computer, which acquired data in the form of electrical output power of the motor. Even though data were recorded at a frequency of 1 Hz for a total test time of 10 min, an average of 10 successive points was taken for computing the coefficient of friction, μ.

Table 1 Salient physical properties of TiC and 1018 steel

Properties	TiC	Fe (1018 steel)
Crystal structure	*B*1 NaCl (cubic)	bcc
Melting point, °C	3065	1538
Density, g/cm^3	4.9	7.8
Lattice parameter, Å	4.33	2.89
Hardness, kg/mm^2	2800	250
Electrical resistivity, μΩ cm	60	12
Thermal conductivity, W/m · K	27	55
Coefficient of thermal expansion, 10^{-6}/K	7.2	12.2

3. Results and Discussion

3.1 Thermodynamic Analysis and Predictions

The chemistry of the coating and interface is affected by the chemical reaction occurring within the deposited layer. These reaction products influence the mechanical and chemical properties of the coating. In the present study, therefore, attempts were made first to thermodynamically predict the possible reactions and secondly to verify the existence of these reaction products using analytical techniques such as energy dispersive x-ray spectrometry (EDS) and x-ray diffractometry.

For thermodynamic predictions, it is essential to consider all possible reactions for a ceramic-metal system. Thermodynamics of Fe-Ti-C system has been studied by several researchers (Ref 13-15). Even though to date, much work continues toward understanding Fe-Ti-C interaction, far from a thorough understanding has been achieved (Ref 15). It has been concluded that Fe-Ti-C is a very active and complex system due to several factors (Ref 13-15). This is mainly due to the presence of carbon, which easily migrates from TiC to Fe and vice versa depending upon reaction conditions such as temperature and activities of the elements (Ref 13-14, 16). This is further corroborated by the Ti-C phase diagram, which shows that TiC_x (x is ≤1) exists as a single homogeneous carbide phase for a wide range of stoichiometry (Ref 1). Hence, it provides a variable activity of carbon in the melt, which, in combination with temperature, influences the possible reactions in the melt zone. However, in an earlier similar study where TiB_2 was deposited on AISI 1018 steel using PES technique, it was found that unlike the Fe-Ti-C system, the Fe-Ti-B is not an active system (Ref 17). For the Fe-Ti-C system, possible reactions between Ti-C, Fe-Ti, and Fe-C are being considered. From the binary phase diagrams (Ref 18), the following reactions are possible. Thermodynamic data such as free energy of formation are extracted from various sources (Ref 19).

Ti-C system:

$$Ti + C = TiC_x$$

$$\Delta G = -182.9 + 0.01\,T \text{ kJ/mol} \quad (298\text{ K} < T < 1155\text{ K})$$

$$\Delta G = -186.4 + 0.013\,T \text{ kJ/mol} \quad (1155\text{ K} < T < 2000\text{ K})$$

The existence of Ti_2C and TiC_2 has not been confirmed (Ref 1).

Fe-C system:

$$3Fe + C = Fe_3C$$

$$\Delta G = 25.92 - 0.023\,T \text{ kJ/mol} \quad (298\text{ K} < T < 463\text{ K})$$

$$\Delta G = 26.67 - 0.025\,T \text{ kJ/mol} \quad (463\text{ K} < T < 1115\text{ K})$$

$$\Delta G = 10.34 - 0.01\,T \text{ kJ/mol} \quad (1155\text{ K} < T < 1808\text{ K})$$

$$2Fe + C = Fe_2C$$

$$\Delta G = 19.86 - 0.01\,T \text{ kJ/mol} \quad (298 \text{ K} < T < 1115 \text{ K})$$

$$\Delta G = 18.42 - 0.01\,T \text{ kJ/mol} \quad (1155 \text{ K} < T < 1808 \text{ K})$$

Fe-Ti system:

$$Fe + Ti = FeTi$$

$$2\,Fe + Ti = Fe_2Ti$$

Gibbs free energy data are not available for FeTi and Fe_2Ti. Lack of such data makes thermodynamic stability predictions difficult for many systems. Henceforth in this article, discussion is limited to TiC, Fe_2C, and Fe_3C. Figure 1 shows the free energy of formation of carbides as a function of temperature. It is evident from the graph that TiC is the most stable carbide, and free energy of formation does not change significantly with temperature. This implies that the entropy (obtained from the slope of the curve) of formation of carbides is almost negligible. Hence, it is reasonable to assume that free energy of carbides varies in a similar manner even at the temperature attained during arc formation in PES process. It is also evident from Fig. 1 that some possibility of formation of Fe_3C exists at temperatures higher than 1100 K. It is noteworthy that apart from temperature, activity of carbon also plays an important role in formation of various reaction products (Ref 13-16). In the earlier work it has been shown that at higher temperatures TiC dissociates into Ti and C increasing the activity of carbon in the melt (Ref 14-16). This results in some of the carbon diffusing into the Fe melt to form Fe_3C whereas the remaining carbon recombines with Ti to reprecipitate stoichiometric TiC.

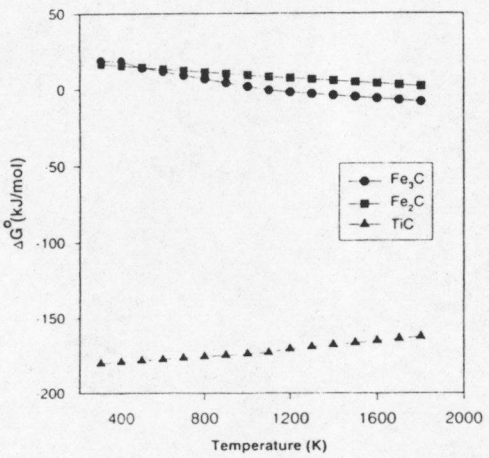


Fig. 1 Gibbs free energy of formation of carbides of Fe and Ti as a function of temperature

However, excess Ti remains in the Fe melt as Fe-Ti eutectic or solid solution (Ref 14-16).

3.2 Microstructural Characterization

The topographical features of the top surface of TiC deposited on AISI 1018 steel are shown in Fig. 2. The surface is irregular with a splash appearance. It is a characteristic feature of PES process. Electrical energy melts the TiC electrode and forms a molten globular droplet on the tip of the electrode. Molten droplet impinges on the steel substrate and produces a splash like appearance. Such process of mass transfer from electrode to substrate is supported by the fact that the PES process was carried out in air. Dissociable gases like air and nitrogen form a plasma of high thermal conductivity, which promotes globular mass transfer (Ref 5).

Figure 3 shows the SEM micrograph of the cross-section of TiC coated 1018 steel. Although coating thickness is not

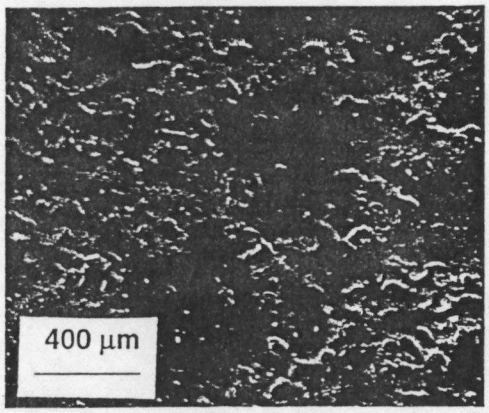


Fig. 2 SEM micrograph showing the topographical features of pulse electrode surfacing (PES) deposited TiC coating on steel

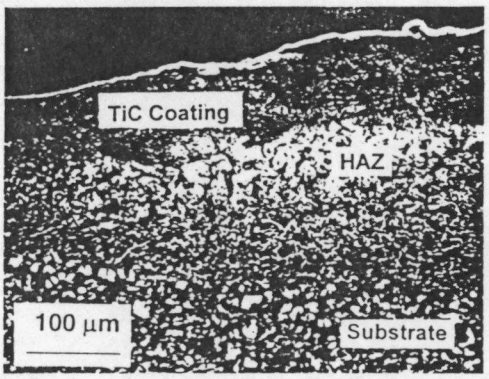


Fig. 3 SEM micrograph of the cross section of TiC deposited steel coupon

uniform, it is dense, adherent, and free from defects such as cracks and porosities. The irregular coating thickness is in accordance with the nature of the PES process as observed in the topographical features shown in Fig. 2. A strong, continuous and adherent interface along with the HAZ is illustrated in Fig. 4(a). Lath-shape martensite is also formed in the HAZ. Islands (particles) of TiC of various size and shape within the coating are observed in Fig. 4(a) and 5. The coating is composite in nature with TiC islands acting as hard reinforcement in a matrix of Fe and Ti. Most of these TiC islands have irregular morphology. It has been postulated that some of TiC particles dissociate and reprecipitate from the melt, leading to in situ formation of islands of TiC of various shape and size (Ref 13-14, 16).

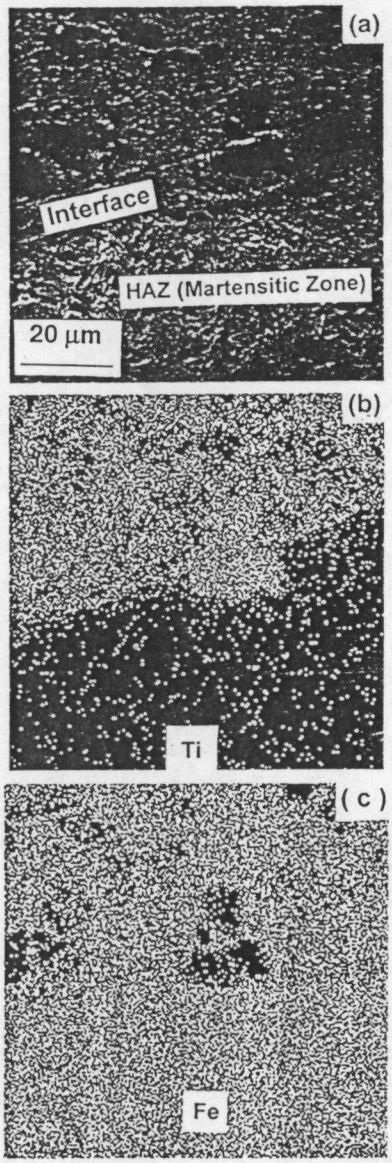


Fig. 4 (a) SEM micrograph of the interfacial region of TiC-deposited steel coupon and corresponding x-ray elemental map for (b) Ti and (c) Fe

The presence of Ti and Fe in the coating is evident from elemental x-ray maps of the cross section corresponding to Ti and Fe distribution in Fig. 4(b, c), respectively. TiC islands (particles) are shown by a Ti-rich zone in the x-ray maps, whereas the matrix contains mostly Fe and a small amount of Ti. EDS quantitative analysis shows the presence of up to 5 to 25 wt% Ti in the matrix at various locations. Figure 6 is the EDS spectrum corresponding to matrix location within the composite coating region. The reason for high Fe content is due to the large difference between the melting points of TiC coating and the Fe substrate. The lower melting point constituent (i.e., Fe) forms a larger volume of molten material as compared to the TiC electrode. This results in high concentration of Fe in the deposited layer (Ref 17).

Fe has excellent wetting and binding properties for refractory ceramic like TiC and TiB_2 (Ref 20, 21). Based upon electronic configuration of *d* electron subshells in transition metals and their hard refractory alloys, an empirical rule has been suggested that allows selection of a suitable binder for given refractory material (Ref 20). This has been corroborated by several researchers for several material systems such as (Ti,Ta)C-Mo and TaC-Ni (Ref 22). Also, in an earlier study conducted by the present authors where TiB_2 was deposited on AISI 1018 steel using PES method, it was observed that Fe acts as an excellent binder for TiB_2 (Ref 17). This further validates the hypothesis of empirical rule suggested for the choice of binder for transition metal based refractory ceramic. Moreover, TiC particles wet Fe easily at high temperatures and wetting increases at high temperatures (Ref 14, 23). All these factors illustrate the role of Fe as an excellent binder for TiC.

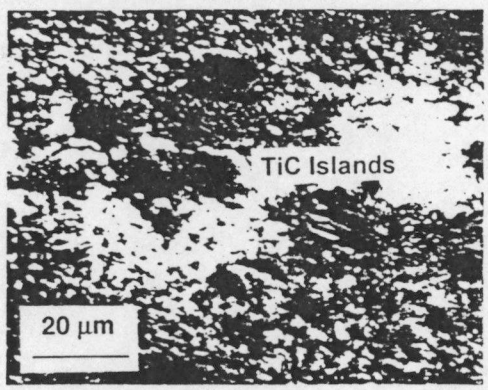


Fig. 5 High magnification SEM micrograph showing TiC islands of various shapes and sizes in the coating region

SOUTHWORTH
PARCHMENT DEPT
100% COTTON FIBER

The presence of Ti in the matrix could possibly be due to the following reasons. Excess Ti from TiC_x gets dissolved in the Fe melt and remains as Fe-Ti solid solution or Fe-Ti-C eutectic (Ref 16). However, the presence of 5 to 25 wt% Ti in the melt exceeds the solid solubility limits, which could be attributed to the nonequilibrium processing experienced during PES processing. Such higher compositions under nonequilibrium processing have also been observed earlier (Ref 24). Figure 7 illustrates the x-ray diffraction spectrum of the coated surface. It shows all the peaks of TiC, Fe (ferrite), and Fe (austenite). There is also an indication of possible FeTi formation, as FeTi peak overlaps with Fe (austenite) peak. Formation of such phase also accounts for high weight percent of Ti present in the matrix. FeTi formation in Fe-Ti-C system has also been observed in earlier studies (Ref 24). Austenite peaks exist because Fe melt retains excess carbon due to rapid solidification. On the contrary, carbon contents might not be high enough to form Fe_4C. This is also corroborated by the absence of Fe_3C peaks in Fig. 7. Furthermore, it has been shown earlier in thermodynamic predictions of Fig. 1 that free energy of formation of Fe_3C does not support its formation. Thus, TiC is the major phase in the coating in addition to Fe.

3.3 *Mechanical Characterization*

Mechanical characterization of the coating and interface was performed using a microhardness tester. Figure 8 shows a SEM micrograph of the cross section of the coating and the HAZ with microhardness indentations. The relative difference in the size of microhardness indentations explains the variation in hardness. Microhardness values (Knoop) in the coating are high with an average value of 1235 ± 86, and they drop down to 352 ± 32 in the HAZ. Microhardness in unaffected base material is 172 ± 12. Such variation in hardness is attributed to the presence of TiC particles in the coating and martensite in the HAZ as observed in Fig. 8. There is no crack initiation or delamination at the site of indentation, which indicates the tough nature of the coating. It should also be observed that though TiC and Fe show considerable differences in their coefficients of thermal expansion, still there is no delamination at the TiC/Fe interface. Such toughness combined with high hardness is attributed to the composite nature of the coating. Thus, TiC particles embedded in an Fe-rich matrix produces an effect similar to that of the WC-Co system.

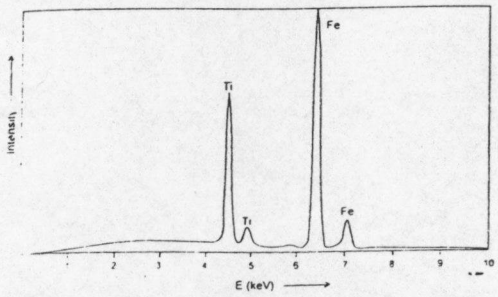


Fig. 6 EDS spectrum of the matrix region within the composite coating

3.4 *Tribological Characterization*

Wear Test (Weight Loss Analysis). Wear test results are presented in Fig. 9, which shows the weight loss over a 10 min period. It can be easily observed that the coated surface shows excellent wear resistance in comparison to uncoated AISI 1018 steel substrate. Wear rate (g/min) of the coated surface has reduced by almost a factor of 4, and it tends to stabilize after an initial period of 4 min. This suggests a formation of wear-resistant film over the entire substrate. The worn surface was subjected to topographic observations in SEM. Figure 10(a) shows a low magnification SEM micrograph of the worn surface of TiC coated AISI 1018 sample. Elemental x-ray maps corresponding to Ti and Fe distribution in Fig. 10(a) are presented in Fig. 10(b, c), respectively. These show Ti presence all over the surface along with Fe, which is in accordance with the composite

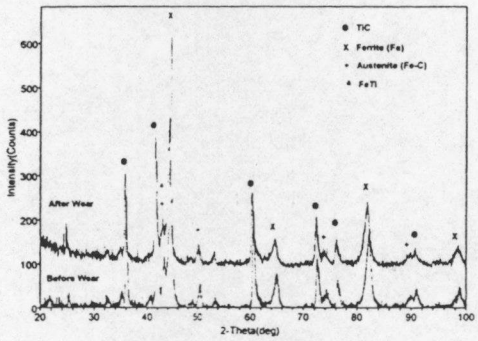


Fig. 7 X-ray diffraction spectra before and after wear of TiC deposited steel coupon

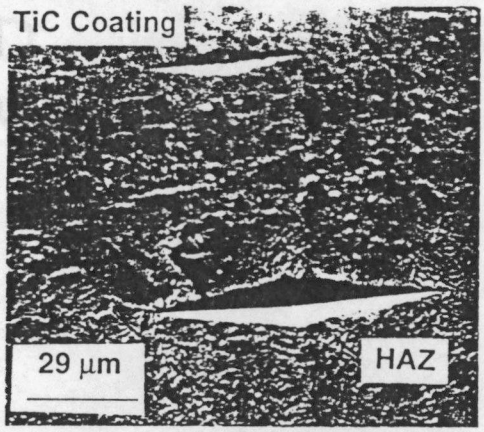


Fig. 8 SEM micrograph of the cross section showing microhardness indentations at different locations

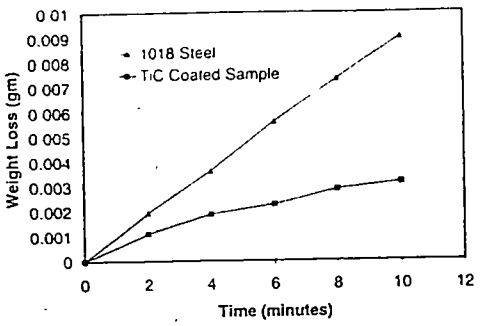


Fig. 9 Variation in cumulative weight loss as a function of time during dry sliding test

nature of the coating, as discussed earlier. There is no indication of brittle failure or loose debris formation of the TiC ceramic phase. The wear phenomenon in such multiphase composite materials is fairly complex, depending on several factors such as volume fraction, distribution, and morphology of the carbide particles (Ref 25). Under ideal conditions, monolithic ceramics such as TiC are supposed to fail in a brittle manner under wear conditions (Ref 26). However, the presence of softer phases such as ferrite and austenite (as observed in x-ray diffraction spectrum in Fig. 7) between hard ceramic particles alters the wear nature of monolithic TiC. It has been mentioned earlier that Fe acts as an excellent binder for Ti-base refractory ceramics (Ref 17, 20). This prevents debonding at the TiC particle/Fe matrix interface. Also, as mentioned earlier, several of the TiC islands in Fe matrix are formed in an in situ manner during the coating process, providing a coherent interface between these islands and the matrix (Fig. 4a and 5). Under such wear conditions, Fe-base matrix phases deform plastically to accommodate the high stresses experienced by TiC particles. This prevents brittle fracture and fragmentation of TiC ceramic particles. Hence, chipping off is prevented, and no loose debris is observed in Fig. 10 A composite film containing hard TiC particles and soft Fe phases covers the entire substrate, which assists in reducing the wear rate. The x-ray diffraction spectrum of a worn surface is shown in Fig. 7. Within the limits of resolution of the x-ray diffractometer, the spectrum does not indicate evolution of any new phases during the wear process. Such new phases, if formed, could influence the wear behavior of the coatings.

Coefficient of Friction Measurement. In the present work, the coefficient of friction is calculated by measuring the changes in voltage and current in the electrical circuit of the motor driving the block-on-ring tribometer during loading (Ref 27). Based on the principle of energy conservation, the frictional energy (W_f) equals the change in the electrical work during loading, as given by Eq 1.

$$W_f = \text{voltage } (\Delta V) \times \text{current } (\Delta I) \quad \text{(Eq 1)}$$

From friction theory, it is known that,

$$W_f = \Delta N v \quad \text{(Eq 2)}$$

where N is normal load, v is the linear speed of the disk, and μ is the coefficient of friction. By equating above the two equations, the coefficient of friction is computed. The measurement of coefficient of friction provides direct information about the work done to deform (elastically and/or plastically) the surface material. However, it is not necessarily a direct indication of material loss or separation as loose debris from the surface. Also, high friction does not necessarily imply high wear rate (Ref 28).

The computed coefficient of friction for TiC coating has been plotted for the entire test time of 10 min (Fig. 11). Coefficient of friction values are constant and do not fluctuate significantly. The best fit line shows the coefficient of friction to be 0.58. Such behavior of the composite coating could be explained by a model that illustrates frictional behavior of multiphase and /or composite materials (Ref 25).

This model predicts that friction of a composite/multiphase material is influenced by the relative amounts and friction coefficients of the constituent phase. Also, friction is affected by the wear resistance of an individual constituent. In most wear situations, the more wear resistant phases carry a disproportionately larger part of the load and hence have a larger influence on the friction of the composite. Hence, the friction coefficient of the composite generally does not follow a linear rule of mixture but is dominated by the friction coefficient of the most wear-resistant constituent. It is well understood that a refractory ceramic like TiC has high wear resistance as compared to that of plain carbon steel. Hence, according to the model discussed above, TiC particles in the coating tend to carry a larger load than Fe and contribute largely toward the coefficient of friction of the composite coating. It has been proposed earlier that TiC coatings have a low coefficient of friction and are ideal candidates as solid lubricants for high vacuum applications (Ref 2). Because TiC has a high wear resistance and low coefficient of friction, it dominates the friction of the composite. Such a hypothesis is supported by Fig. 10, which shows a composite film of TiC and Fe on the worn surface. Formation of such a film leads to an earlier stabilization of coefficient of friction, which is evident from Fig. 11.

4. Conclusions

- An ultrahard TiC coating has been successfully deposited over AISI 1018 steel using a high energy density process such as PES. The coating is adherent, crack free, and defect free. However, coating thickness is not uniform, which is a characteristic feature of PES process.
- The coating is composite in nature with TiC being the most stable phase in a Fe-rich matrix Islands of TiC of various sizes and shapes are present in the coating. Such coating morphology is due to the highly active and complex Fe-Ti-C material system.
- A coating with high hardness value is obtained.
- Wear resistance of the coated surface has increased significantly. The wear behavior of the TiC coated surface is explained by formation of a composite film, which accommodates stresses by plastic deformation of softer phases.
- A coefficient of friction has been computed and explained on a model based on the composite/multiphase material.

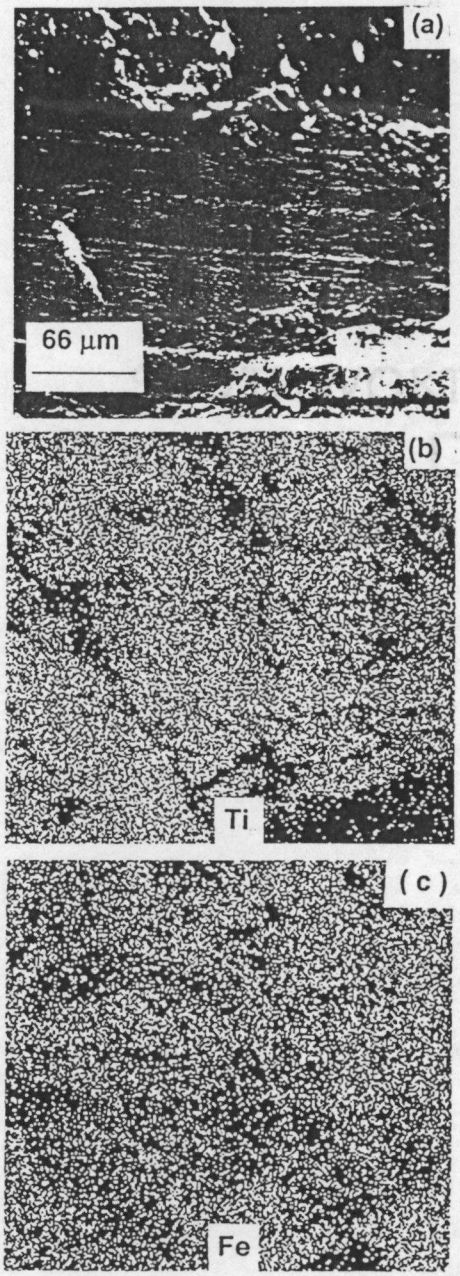


Fig. 10 (a) SEM micrograph of the worn surface of TiC coated steel coupon and corresponding x-ray elemental map for (b) Ti and (c) Fe

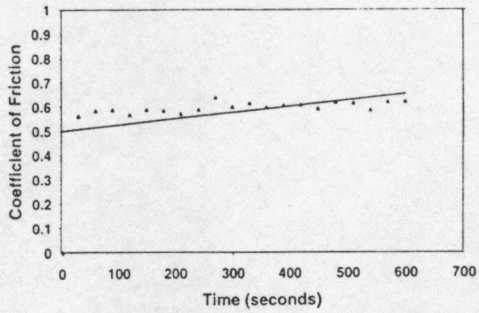


Fig. 11 Variation in coefficient of friction with time during dry sliding test

Acknowledgments

The authors thank Dr. T.S. Sudarshan at Materials Modifications Inc. (MMI), Fairfax for supplying the coated samples and Mr. R. Raman and Mr. S. Krupashankar, also at MMI, who extended support in depositing the coating by PES technique. The authors acknowledge financial support from the U.S. Air Force (contract No. F 40600-96-C-0004) for this work.

References

1. T.Y. Kosolapova, *Carbides: Properties, Production and Applications*, Plenum Press, New York, 1971, p 97-122
2. K. Upadhya, Properties and Performance of Plasma-Assisted Physically Vapor Deposited TiC Coatings, *Mater. Sci. Eng. A*, Vol 140, 1991, p 549-553
3. S. Kinkel, G.N. Angelopoulos, and W. Dahl, Formation of TiC Coatings on Steel by a Fluidized Bed Chemical Vapor Deposition Process, *Surf. Coat. Technol.*, Vol 64, 1994, p 119-125
4. M.L.F. Parames and O. Conde, Structure and Morphology of Laser Assisted Chemical Vapor Deposited TiC Coatings, *J. Phys. (France) IV*, Vol 3, 1993, p 217-224
5. R.N. Johnson, Principles and Applications of Electro-Spark Deposition, *Surface Modification Technologies*, T.S. Sudarshan and D.G. Bhat, Ed., The Metallurgical Society, 1988, p 189-213
6. R.N. Johnson, Electro-Spark Deposited Coatings for High Temperature Wear and Corrosion Applications, *Elevated Temperature Science and Technology I*, N.B. Dahotre, J.M. Hampkian, and J.J. Stiglich, Ed., The Minerals, Metal and Materials Society, 1995, p 265-277
7. E.A. Brown, G.L. Sheldon, and A.E. Bayoumi, A Parametric Study of Improving Tool Life by Electrospark Deposition, *Wear*, Vol 138, 1990, p 137-151
8. G.V. Samsonov, A.D. Verkhoturov, V.S. Sychev, and A.I. Bezykornov, Investigation of Some of the Laws Governing the Formation of a Hardened Layer during the Process of Electric-Spark Alloying, *Fiziko-Khimicheskaya Mekhanika Materialov*, Vol 7 (No. 5), 1971, p 3-6
9. K. Natesan and R.N. Johnson, Corrosion Resistance of Chromium Carbide Coatings in Oxygen-Sulfur Environment, *Surf. Coating Technol.*, Vol 33, 1987, p 3411-3451
10. R.N. Johnson, Coatings for Fast Breeder Reactor Components, *Thin Solid Films*, Vol 118, 1984, p 31-47
11. S. Raghunathan, J.J. Stiglich, and T.S. Sudarshan, Characterization of Ir/Re Duplex Coatings on Ta/10W Deposited by Pulsed Electrode Surfacing (PES), *Elevated Temperature Science and Technology I*, N.B. Dahotre, J.M. Hampkian, and J.J.

Stiglich, Ed., The Minerals, Metals and Materials Society, 1995, p 303-312

12. N.B. Dahotre, M.H. McCay, and T.D. McCay, Diamond Materials for Electromagnetic Railguns, *Mater. Manuf. Process.*, Vol 9 (No. 1), 1994, p 1-36
13. N. Frage, L. Levin, E. Manor, R. Shneck, and J. Zabicky, Iron-Titanium-Carbon System. I. Equilibrium Between Titanium Carbide (TiC_x) of Various Stoichiometries and Iron-Carbon Alloys, *Scr. Mater.*, Vol 35 (No. 7), 1996, p 791-797
14. C. Raghunath, M.S. Bhat, and P.K. Rohatgi, In Situ Technique for Synthesizing Fe-TiC Composites, *Scr. Metall.*, Vol 32 (No. 4), 1995, p 577-582
15. S. Jonsson, Assessment of the Fe-Ti-C System, Calculation of the Fe-Ti-N System and Prediction of the Solubility Limit of Ti (C,N) in Liquid Fe, *Metall. Mater. Trans. B*, Vol 29, 1998, p 371-384
16. N. Frage, L. Levin, E. Manor, R. Shneck, and J. Zabicky, Iron-Titanium-Carbon System. II. Microstructure of Titanium Carbide (TiC_x) of Various Stoichiometries Infiltrated with Iron-Carbon Alloy, *Scr. Mater.*, Vol 35 (No. 7), 1996, p 799-803
17. A. Agarwal and N.B. Dahotre, Pulse Electrode Deposition of Superhard Boride Coating on Ferrous Alloy, *Surf. Coat. Technol.*, Vol 106 (2/3), 1998, p 242-250
18. *Alloy Phase Diagrams*, Vol 3, *ASM Handbook*, ASM International, 1992
19. G.V. Samsonov and I.M. Vinitskii, *Handbook of Refractory Compounds*, IFI Plenum Data Company, New York, 1980, p 138-140
20. A.A. Ogwu and T.J. Davies, Electronic Structure Basis for Selection of Metal Binders for Hardmetal Systems, *Mater. Sci. Technol.*, Vol 9, 1993, p 231-217
21. G.S. Upadhyaya, Wetting of Ceramic by Metal Melts. An Electronic Approach, *Sintered Metal-Ceramic Composites*, G.S. Upadhyaya, Ed., Elsevier Science Publishers, Amsterdam, 1984, p 41-50
22. S. Economou, M. De Bonte, J.P. Celis, J.R. Ruos, R.W. Smith, E. Lugscheider, and A. Valencic, Tribological Behavior of TiC/TaC-Reinforced Cermet Plasma Sprayed Coatings Tested Against Sapphire, *Wear*, Vol 185, 1995, p 93-110
23. L. Ramquist, *Int. J. Powder Metall.*, Vol 4, 1965, p 1-4
24. P.H. Booker, Ph.D. thesis, Oregon Graduate Center, 1979
25. N. Axen, I.M. Hutchings, and S. Jacobson, A Model for the Friction of Multiphase Materials in Abrasion, *Tribol. Int.*, Vol 29 (No 6), 1996, p 467-475
26. W.A. Glaeser, Friction and Wear of Ceramics, *Friction, Lubrication, and Wear Technology*, Vol 18, *ASM Handbook*, ASM International, 1992
27. P.K. Rohatgi, N.B. Dahotre, Y. Liu, M. Yin, and T.L. Barr, Tribological Behavior of Al Alloy-Graphite and Al Alloy-Microcrystalline Carbon Particle Composites, *Proc. International Symposium on Advances in Cast Reinforced Metal Composites*, S.G. Fishman and A.K. Dhingra, Ed., ASM International, 1988, p 367-373
28. J. Halling, Tribology, *Surface Treatment for Protection: Spring Review Course*, The Institution of Metallurgists, Great Britain, Series 3 (No. 10), 1978, p 118-129

APPENDIX VI

COMPARATIVE WEAR IN TITANIUM DIBORIDE COATINGS ON STEEL USING HIGH ENERGY DENSITY PROCESSES

(This paper is under review in *Wear* journal)

Comparative Wear in Titanium Diboride Coatings on Steel Using High Energy Density Processes

Arvind Agarwal and Narendra B. Dahotre
Department of Materials Science and Engineering
Center for Laser Applications
University of Tennessee Space Institute
Tullahoma, TN 37388
USA

Abstract

A comparison between the tribological properties of titanium diboride (TiB_2) deposited using high energy density processes such as Pulse Electrode Surfacing (PES) and Laser Surface Engineering (LSE) has been made. The wear resistance of TiB_2 coated surface is higher than AISI 1010 steel. Wear resistance of the LSE coated TiB_2 coating is even better than PES deposited TiB_2 coating. Coefficient of friction values for LSE coated TiB_2 coating (μ=0.59) is lower than PES deposited TiB_2 coating (μ=0.68). Wear occurs in PES deposited TiB_2 coating by brittle fracture and attrition type mechanisms whereas wear in LSE deposited TiB_2 coating occurs by plastic deformation of the soft matrix phase, Fe from a "composite" layer on the surface.

Keywords: TiB_2 coating, Pulse Electrode Surfacing (PES), Laser Surface Engineering (LSE), Wear resistance, Coefficient of friction.

1. Introduction

Tribological properties of the ceramic coatings depend upon several factors such as hardness and thickness of the coating, coating material, type of the substrate, operating conditions and coating process. Based on these variables, several wear mechanisms have been proposed for different coating-substrate system viz. ploughing, flake formation, micropolishing, cohesive failure or fragmentation, spalling, plastic deformation, removal of hard particle phase and attrition [1]. In the present study, wear and friction characteristics of TiB_2 coating has been investigated.

Titanium diboride (TiB_2) is a transition metal based refractory ceramic which has unique properties of extremely high hardness, high melting point, wear resistance, corrosion resistance and electrical conductivity [2]. It also has excellent corrosion resistance against metallic aluminum and cryolite, which makes it suitable candidate as a coating material for inert cathode used in Hall-Heroult cell for aluminum electrolysis [3-4]. Conventionally, TiB_2 ceramics are processed by hot-pressing and sintering which are very expensive, as it requires high temperature processing [5]. Moreover, near net shape forming is also impossible. However, surface engineering seems to be an alternate way to modify the surface properties similar to that of TiB_2 without altering the bulk properties of the engineering component or structure. In the present study, TiB_2 has been deposited on plain carbon steel using high energy density processes, Pulse Electrode Surfacing (PES) and Laser Surface Engineering (LSE) techniques. A comparative study of wear and friction behavior of TiB_2 coating deposited by these two processes has been presented. For a better understanding of the comparative wear mechanisms, it is essential to understand the main features of the two coating processes. The detailed comparison of

the two coating processes and the resulting coating morphology has been presented elsewhere [6-9].

Pulse Electrode Surfacing (PES)

Pulse Electrode Surfacing (PES) technique utilizes a high current, short duration pulse via discharge capacitance and voltage circuit which results in melting the electrode and depositing the material on the substrate [10-13]. This process is very similar to arc-welding process with the exception of little total heat input. Hence, PES process is also referred as micro-welding process. The main advantage of this process stems from the fact that metallurgically bonded coatings with an adherent interface can be produced with little heat input to the substrate at ambient temperature [14]. Since the bulk material remains near ambient temperature and acts as heat sink, heat is rapidly dissipated leading to rapid solidification of the molten pool which in turn results in an extremely fine grained coating of high density, hardness and strength. Furthermore, PES process obviates the need of expensive environmental chambers required in several types of other coating processes. The primary requirement and the limitation for the PES process are that electrode material should be electrically conductive and thus capable of melting in an electric arc.

Laser Surface Engineering (LSE)

Laser surface engineering (LSE) is one of the surface modification processes where preplaced ceramic powder precursor is melted along with a thin layer of the substrate to produce a laser melt zone of desired composition [8]. The most important advantage stems from the fact that laser surface modification is a non-equilibrium synthesis. Laser surface modification involves high cooling rates (10^3 to 10^8 K/sec)

which produces metastable phases by exceeding the solid solubility limit beyond equilibrium phase diagram [15]. This leads to development of wide variety of microstructures with novel properties, which can not be produced by any conventional processing technique. Moreover, these coatings are metallurgically bonded providing a sound and adherent interface between the coating and substrate. The surface structure can be tailored to the surface requirement of the application by varying process variables such as laser traverse speed, power, beam size and type and composition of the precursor [16]. Also, laser beam has an excellent spatial resolution that makes it ideal for depositing coating on miniature size components such as electronic sensors for high temperature applications. Another advantage of laser surface modification comes from the fact that laser beam can be transported to any remote location through fiber optics. This allows deposition of coatings on components or parts that are complex in shape and remotely located.

2.0 Experimental Procedures

2.1 Pulse Electrode Surfacing (PES) Coating Procedure

Coupons of AISI 1018 steel of dimensions 25 mm x 10 mm x 3 mm were mechanically polished on emery paper of grit 240 and then rinsed with acetone. A sintered electrode of TiB_2 containing Ni in the range of 1-3 wt % as binder was used to deposit coating on these steel coupons. Deposition was done using a hand held gun in air at room temperature. Pulsed electrode deposition was carried out at 50 volts and spark duration of 10 μs. The discharge capacitance used for the PES process was 450 μF with

a current of 50 amperes. Such processing parameters provide an input energy of 0.10 MW/m^2.

2.2 Laser Surface Engineering (LSE) Coating Procedure

Commercially available TiB_2 and Ti powders obtained from CERAC, Milwaukee, WI were used as precursor material for this study. Both powders had a purity of 99.5 %. The average particle size range was 5.5 μm ± 1 μm. Thin plates of AISI 1010 steel of size 75 mm x 150 mm x 3mm were cleaned using sand blasting. The precursor of a powder mixture of 2 wt % Ti and 98 wt % TiB_2 composition in a water based organic vehicle was sprayed on these coupons using a paint spray gun. The average preplaced powder bed had a thickness of 150 ± 15 μm. Sprayed coupons were dried at 70^0C for 1 hour prior to laser processing. The addition of 2 wt. % Ti to TiB_2 was made on the assumption that Ti increases the wettability in the melt zone [17]. It was also anticipated that additional Ti would recombine with any boron, which may disassociate during laser processing. A 2.5 kW Hobart HLP 3000 continuous wave Nd:YAG laser (1.06 μm wavelength) equipped with a fiber optic beam delivery system was employed for synthesis of laser assisted TiB_2 coatings. In order to provide a large sweeping coverage (i.e. rapid processing speed) and to reduce and/or to eliminate overlap between the successive laser passes, laser optics were configured to provide a 3.5 mm long line beam in spatial distribution (TEM_{01}) onto the sample surface. The processing parameters were optimized in accordance with earlier reported literature [8-16]. In the present study, laser beam power and laser traverse speed were kept constant at 1.5kW and 33 mm/s, respectively. Thus, the energy density input for LSE is 15 MW/m^2, which is couple of orders of magnitude higher than PES process.

2.3 Microstructural Characterization

Coating morphology and wear surface topography was studied using a ISI Super III-A scanning electron microscope (SEM) coupled with EDAX. Metallographic samples for scanning electron microscopy were prepared by polishing on Buehler TEXMET 2000 cloth during initial stages of polishing. The etchant used for TiB_2 coated steel sample was Nital. Laser treated samples required longer etching time as compared to PES samples. Such behavior could be explained by the nature of the coatings obtained in two processes. Structural characterization for phase(s) identification was carried out on a Philips Norelco x-ray diffractometer with CuK_α radiation (1.54 Å) operating at 40kV and 20 mA. Surface roughness of the wear surface was examined using a WYKO VISION RST 500 optical profilometer.

2.4 Tribological Characterization

Tribological properties of the TiB_2 coating were measured using a block-on-disk tribometer. Coated coupons of dimension 25 mm x 25 mm x 3 mm were tested for dry sliding wear against a hardened steel ring rotating at a linear speed of 4.4 m/s. Weight loss measurements were made after successive 2 minutes. The dry sliding wear test was conducted for a total of 20 minutes duration with an applied normal load of 2 kg. Coefficient of friction (μ) was also recorded for a 10-minute period by an interfaced computer, which acquired data in the form of electrical output power of the motor. Even though data was recorded at a frequency of 1Hz for a total test time of 10 minutes, an average of 10 successive points was taken for computing the coefficient of friction, μ.

3.0 Results and Discussion

3.1 Coating Morphology

Coating morphology and surface roughness play a crucial role in influencing the tribological properties of the coating. Figure 1(a) shows the topographical features of the top surface of TiB_2 deposited on the steel substrate using PES technique. The surface is rough and irregular with several islands of globular shape and a splash appearance. This is a characteristic feature of the PES technique. In the present study, PES process was conducted in air, which supports globular mass transfer mechanism. This is attributed to the fact that dissociable gases like nitrogen and air form a plasma of high thermal conductivity, which promotes globular mass transfer [13]. A molten globular droplet forms at the TiB_2 electrode tip and impinges on the steel substrate. This produces a splash appearance on the top surface. The corresponding surface profile of the coated surface is illustrated in Figure 1(b). Surface is very rough in nature with several peaks and valleys. The average surface roughness, R_a for PES coating is high (16.91 μm) in tune with its topographical features observed in Figure 1. Surface topography of the laser-engineered surface is shown in Figure 2(a). The surface is relatively smooth, flat and free from cracks. The profile of the LSE deposited TiB_2 surface is illustrated in Figure 2(b). The average surface roughness, R_a for LSE coating is low (6.39 μm) in comparison to PES surface. The importance of the surface roughness in wear phenomena will be elucidated in the following sections. Figure 3 presents the SEM micrographs of the cross-sectional views of the TiB_2 coated steel using PES and LSE processes. It can be seen in Figure 3(a) that PES deposited TiB_2 coating is homogeneous, dense, adherent and free of defects like cracks. However, the coating thickness is not very uniform

throughout the cross section. This is in accordance with the nature of PES process as described above and as earlier observed in the topographical features of the same sample in Figure 1. Figure 3 (b) is a continuous, adherent and crack free laser deposited TiB_2 coating on AISI 1010 steel substrate. Coating/laser-melt-zone is "composite" in nature. It is a mixture of uniformly distributed TiB_2 ceramic particles of different morphologies (polygonal and acicular) and Fe. During laser processing, a thin layer of steel substrate melts and mixes with TiB_2 due to convection currents within the melt zone resulting in a composite coating. Within the laser melt zone, the distribution of TiB_2 particles is uniform and their content is very high (volume fraction ≈ 0.67).

3.2 Tribological Properties of TiB_2 Coating

3.2.1 Weight Loss Analysis

Wear test results are presented in Figure 4, which shows the weight loss over a 20-minute period. It can be easily observed that LSE coated surface shows least weight loss in comparison to the PES coated surface and AISI 1010 steel substrate. Wear rate (gm/min) of the PES coated surface has reduced by almost a factor of 3 whereas for LSE surface, wear rate has decreased by a factor of 15 in comparison to the uncoated AISI 1010 steel substrate. Moreover, wear rate for LSE coated surface tends to stabilize after an initial period of 4 minutes suggesting the smoothening and/or breaking off of hard asperities, thereby providing a flat contact with the "composite" composition. The worn surfaces of PES and LSE coated samples were subjected to topographic observations in SEM. Figure 5 (a) shows a low magnification SEM micrograph of the worn region in PES deposited TiB_2 sample. Elemental x-ray maps corresponding to Ti and Fe

distribution in Figure 5 (a) are presented in Figures 5 (b) and (c), respectively. Wear mechanism in PES deposited TiB_2 coating is essentially brittle in nature. Because of the inherent brittleness of the ceramic material, wear can occur by chipping [18]. Also, surface and subsurface cracks form, join and release small chips of material. These chipped off particles are further crushed into finer particles leading to formation of wear debris [18]. Such wear mechanism has been termed as attrition type of wear. A combination of brittle fracture and attrition wear mechanism is observed in PES coated TiB_2 sample. As observed earlier, PES surface is very rough in nature showing peaks and valleys in the TiB_2 coating (Figure 1). Under sliding conditions of wear, peaks of TiB_2 coating act as asperities and regions of high stress concentration. The interfacial strength between two successive droplets of a refractory ceramic like TiB_2 is not high and prone to crack formation. These small cracks tend to join leading to formation of a major crack. Such phenomenon is clearly evident in Figure 6 which shows small and thin cracks merging together to form a wide crack. Such wide crack formation results in chipping of TiB_2 coating as particles from the steel substrate. Chipping of TiB_2 particles suggest a high wear rate which is evident in Figure 4. Figure 5(a) shows denuded steel substrate after the chipping of particles of TiB_2 coating. Some of these chipped off particles are further crushed and form wear debris, which is indicated by the presence of Ti over the denuded steel substrate (Figure 5(b)) and bare regions with loss of TiB_2 coating on steel substrate (Figure 5(c)). Chipping of TiB_2 particles is further corroborated by the surface profile of the worn surface shown in Figure 7. TiB_2 coating have chipped off at several locations, which is indicated by the deep craters formed on the surface. Average surface roughness, R_a, of the worn surface has reduced from 16.91

μm (as coated) to 6.27 μm, which is attributed to the flattening of the surface after sliding wear for twenty-minute period.

The wear phenomenon in LSE coated sample is significantly different from the PES coated sample. As stated earlier, LSE deposited TiB_2 coating is "composite" in nature. Wear mechanism in such multiphase composite materials is very complex which depends upon several factors such as volume fraction, distribution and morphology of the ceramic particles [19]. Under ideal conditions, monolithic ceramic such as TiB_2 is expected to fail in a brittle manner [2]. However, presence of the softer matrix phase, Fe between hard ceramic particles alters the wear nature of monolithic TiB_2. It has been mentioned earlier that Fe acts as an excellent binder for Ti based refractory ceramics [7,20]. This prevents debonding at TiB_2 particle/Fe matrix interface [9]. Under such materials conditions, Fe-based matrix phase(s) deforms plastically to accommodate the high stresses experienced by TiB_2 particles. This prevents brittle fracture and fragmentation of TiB_2 ceramic particles. Hence, chipping off is prevented and no lose debris is observed. A composite layer containing hard TiB_2 particles and soft Fe phase(s) covers the entire substrate, which assists in reducing the wear rate. Such microstructural features are elucidated in Figure 8 that shows TiB_2 particles embedded in Fe matrix. There is no crack formation observed. Wear occurs mainly by plastic deformation of the softer matrix Fe phase resulting in very little loss of material (Figure 4). Figure 9 is the surface roughness profile of the worn surface of the LSE coated sample. Wear surface is clearly indicated by the depressions (plastic deformation) caused by the rotating disk of the tribometer and relatively small change in the average surface roughness, R_a from 6.39 μm (as coated) to 4.56 μm.

The x-ray diffraction spectrum of the PES and LSE coated surfaces before and after wear is shown in Figure 10. Within the limits of resolution of the x-ray diffractometer, the spectrum does not indicate evolution of any new phase(s) during the wear process indicating that wear in both PES and LSE coated samples, is essentially physical in nature. Such new phase(s), if formed could influence the wear behavior of the coatings.

3.2.2 Coefficient of Friction Measurement

In the present work, the coefficient of friction is calculated by measuring the changes in voltage and current in the electrical circuit of the motor driving the block-on-ring tribometer during loading [21]. Based on the principle of energy conservation, the frictional energy (W_f) equals to the change in the electrical work during loading, given by equation (1).

$$W_f = \text{Voltage } (\Delta V) \times \text{Current } (\Delta I) \qquad (1)$$

From friction theory, it is known that

$$W_f = \mu N v \qquad (2)$$

where N is normal load, v is the linear speed of the disk and μ is the coefficient of friction. By equating above two equations, coefficient of friction is computed.

The computed coefficient of friction for TiB_2 coating for both processes has been plotted for entire test time of ten minutes (Figures 11 and 12). For PES process, the fluctuations in coefficient of friction values are higher in comparison to the LSE process. The best-fit line shows coefficient of friction to be 0.68 for PES process and 0.59 for LSE process. Such difference in the friction behavior can be attributed to the coating morphology and prevailing wear mechanisms in two coatings. In PES process, surface is

inherently rough with peaks and valleys due to the nature of the process supporting a higher friction value. Moreover, fluctuations in coefficient of friction values for PES process are higher, insinuating chipping off TiB_2 particles (Figures 11). Such fluctuations are larger for first 2 minutes of the test. The degree of fluctuation decreases with time, which is attributed to the relative smoothening of the surface. In LSE process, the coated surface is inherently smoother than the PES surface, leading to a lower coefficient of friction value (Figure 12). The lower degree of fluctuations in friction value for LSE coated sample is accounted by the formation of a "composite" layer on the entire surface. A comparison between the coatings produced by two processes and their tribological characteristics has been summarized in Table 1.

Table 1. Summary of the TiB_2 Coatings and their Tribological Characteristics Deposited by PES and LSE Processes

Features	PES Process	LSE Process
Energy Density Input (MW/m^2)	0.10	15.0
Nature of the Coating	Thin (35-40 μm), homogeneous, dense and very fine grained (2-3 μm)	Thick (200 μm) Composite Coating with embedded TiB_2 particles in the Fe-rich matrix
Surface Roughness, R_a (before wear)	16.91 μm	6.39 μm
Surface Roughness, R_a (after wear)	6.27 μm	4.56 μm
Wear Rate (g/min)	0.0005	0.00005
Coefficient of Friction	0.68	0.59
Wear Mechanism	Brittle failure in addition to attrition	Plastic Deformation

The wear behavior of the "composite" coating is very complex, which could be explained by a model that elucidates frictional behavior of multiphase and /or composite materials [19]. This model predicts that friction behavior of a composite/multiphase material is influenced by the relative amounts and friction coefficients of the constituent phase. Also, it is affected by the wear resistance of the individual constituent. In most wear situations, the more wear resistant phase(s) carry a disproportionately larger part of the load and hence have a larger influence on the friction of the composite. Hence, the friction coefficient of composite generally does not follow a linear rule of mixture, but is dominated by friction coefficient of the most wear resistant constituent. It is well understood that a refractory ceramic like TiB_2 has high wear resistance as compared to plain carbon steel. Hence, according to the model discussed above, TiB_2 particles in the coating tend to carry a larger load than Fe and contribute largely towards coefficient of friction of the "composite" coating. However, in the present study, no such mathematical modeling has been done for this particular materials system.

4.0 Conclusions

1. Wear resistance of TiB_2 coated surface is higher than AISI 1010 steel. Wear resistance of the LSE coated TiB_2 coating is even better than PES deposited TiB_2 coating.
2. Coefficient of friction values for LSE coated TiB_2 coating (μ=0.59) is lower than PES deposited TiB_2 coating (μ=0.68).
3. Wear occurs in PES deposited TiB_2 coating by brittle fracture and attrition type mechanisms.

4. Wear in LSE deposited TiB_2 coating occurs by plastic deformation of the soft matrix phase, Fe from a "composite" layer on the surface.

Acknowledgments

The authors wish to express their sincere appreciation to Dr. T. S. Sudarshan at Materials Modifications Inc., Fairfax who provided the PES samples for the present work. The support extended by Mr. R. Raman and Mr. S. Krupashankara at MMI, in depositing coating by PES technique is highly acknowledged. The authors acknowledge the financial support from the US Air Force (Contract No. F40600-96-C-0004) for this work. The authors would like to thank Ms. Lalitha Reddy Katipelli for her assistance with image processing.

References

[1] S. Bahadur and C. N. Yang, *Wear, 196* (1996) 156.

[2] R. Cutler, *Engineering Materials Handbook: Ceramic and Glasses*, ASM International, OH, *4* (1995) 787.

[3] K. Billehaug and H. Oye, *Aluminum Verlag* (Dusseldorf), *56* (1980) 642.

[4] H. Oye and M. Sorlie, *Aluminum Verlag* (Dusseldorf), *2* (1994) 147.

[5] C. Mroz, *Ceramic Bulletin, 78(6)* (1999) 77.

[6] A. Agarwal and N. B. Dahotre, *Mater. Char., 42 (1)* (1999) 31.

[7] A. Agarwal and N. B. Dahotre, *Surf. Coat & Tech.,106(2/3)* (1998) 242.

[8] A. Agarwal and N. B. Dahotre, *Int. J. Refractory Mater.& Hard Metals,17(4)* (1999) 283.

[9] A. Agarwal, N. B. Dahotre and L. F. Allard, *Pract. Metall., 36(5)* (1999) 250.

[10] R.A. Alfintseva, I.G. Bodrova and A.D. Verkhoturov, *J. Less Common Metals, 67* (1979) 443.

[11] A. I. Bushik and V. A. Shilov, *Elektronnaya Obrabotka Materialov, 1* (1991) 22.

[12] G. V. Samsonov, A.D. Verkhoturov, V. S. Sychev and A.I Bezykornov, *Fiziko-Khimicheskaya Mekhanika Materialov,7(5)* (1971) 3.

[13] R. N. Johnson, *Elevated Temperature Science and Technology I*, ed. N. B. Dahotre, J. M. Hampkian and J. J. Stiglich, The Minerals, Metal and Materials Society, (1995) 265.

[14] V.V. Kantsel, T.S. Kurakina, V.S. Potokin, V.I. Rakhovskii and L. G. Tkachev, *Soviet Physics-Technical Physics, 13(6)* (1968) 814.

[15] J. Mazumder, *Metallurgical and Ceramic Protective Coatings,* ed. Kurt H. Stern, Chapman and Hall, London, (1996) 74.

[16] K. Komvopoulos, *Materials Science Forum, 163-165,* (1994) 417.

[17] O. M. Akselsen, *J. Mater. Sci., 27,* (1992) 1989.

[18] W. A. Glaeser, *ASM Handbook: Friction, Lubrication and Wear Technology,* ASM International, OH, *18* (1998) 812.

[19] N. Axen, I. M. Hutchings and S. Jacobson, *Tribology Intl., 29 (6)* (1996) 467.

[20] C. Raghunath, M. S. Bhat and P.K. Rohatgi, *Scripta. Metall.,32 (4)* (1995), 577.

[21] P. K. Rohatgi, N. B. Dahotre, Y. Liu, M. Yin and T. L. Barr, *Proc. Intl. Syposium on Advances in Cast Reinforced Metal Composites,* ed. S.G. Fishman and A.K. Dhingra, ASM International, Ohio, 1988, 367.

Biographies

Arvind Agarwal earned his B.Tech. and M.Tech. degrees in Materials and Metallurgical Engineering from the Indian Institute of Technology, Kanpur, India. He is currently a Graduate Research Assistant and pursuing his Ph.D. degree in Materials Science and Engineering at the University of Tennessee Space Institute. He is a student member of TMS, ASM and American Ceramic Society.

Narendra B. Dahotre earned his M.S. and Ph.D. degrees in Materials Science and Engineering from the Michigan State University. He is currently a Professor of Materials Science and Engineering at the University of Tennessee Space Institute. He is a member of TMS, ASM and SME.

List of Figures

Figure 1. (a) SEM micrograph showing the top surface morphology of the TiB_2 coated surface using PES process and (b) the corresponding surface roughness profile for the coated surface.

Figure 2. (a) SEM micrograph showing the top surface morphology of the TiB_2 coated surface using LSE process and (b) the corresponding surface roughness profile for the coated surface.

Figure 3. SEM micrographs of the cross-sectional views of (a) PES sample and (b) LSE sample.

Figure 4. Cumulative weight losses over a 20-minute period during dry sliding wear block-on- disk test. Inset shows wear rates corresponding to various surfaces.

Figure 5. (a) SEM micrograph of the worn surface of TiB_2 coated PES sample and corresponding X-ray elemental map for (b) Ti and (c) Fe.

Figure 6. SEM micrograph showing the crack formation and propagation during the brittle fracture of TiB_2 coated PES sample.

Figure 7. Surface roughness profile of the wear surface for the PES sample.

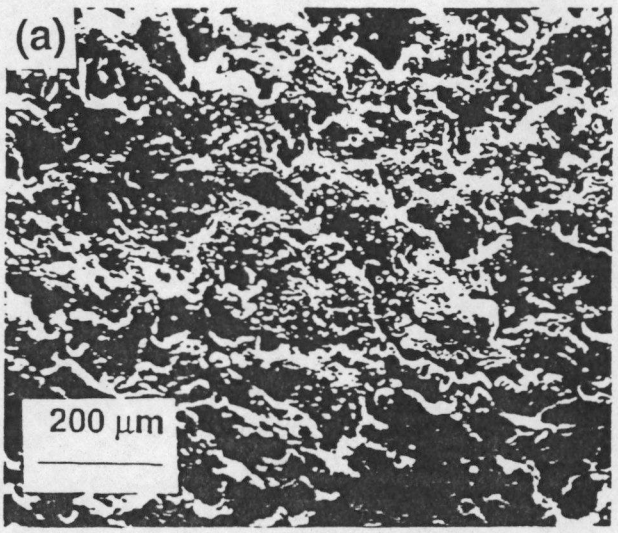
Figure 8. (a) SEM micrograph of the worn surface of TiB_2 coated LSE sample and corresponding X-ray elemental map for (b) Ti and (c) Fe.

Figure 9. Surface roughness profile of the wear surface for the LSE sample.

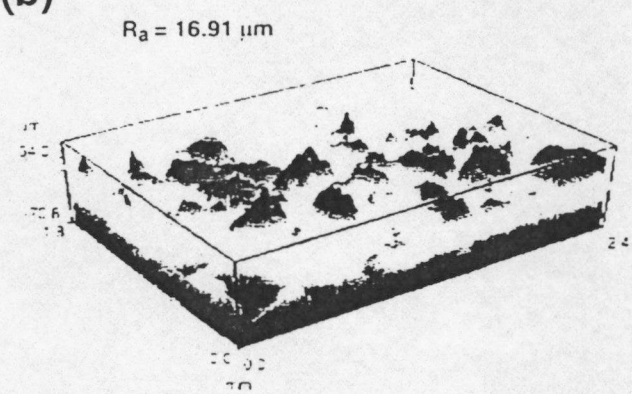
Figure 10. X-ray diffraction spectra before (B) and after (A) wear of TiB_2 deposited (a)PES and (b) LSE steel coupons.

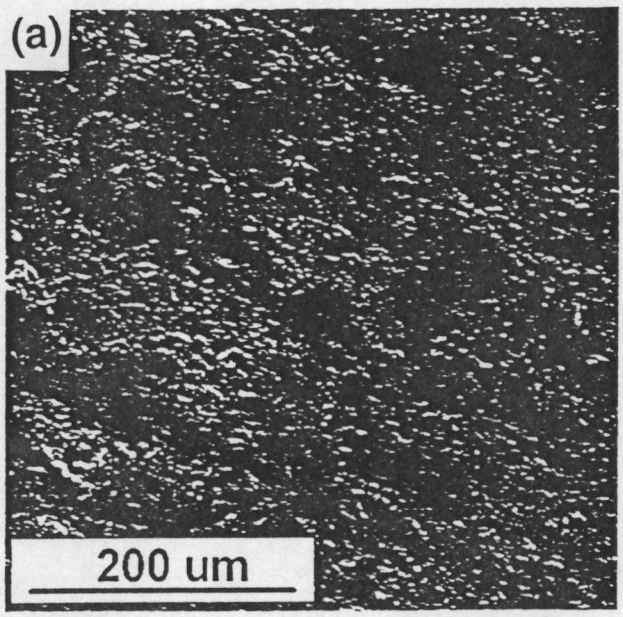
Figure 11. Variation in coefficient of friction with time during dry sliding test for PES sample.

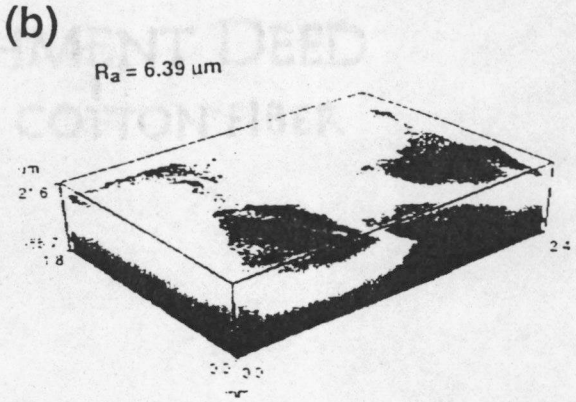
Figure 12. Variation in coefficient of friction with time during dry sliding test for LSE sample.

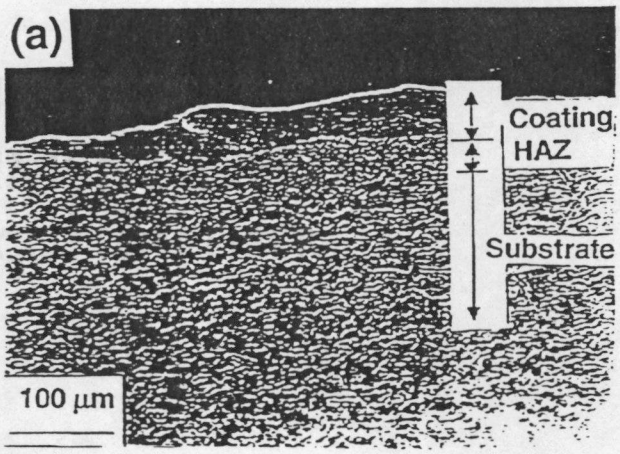


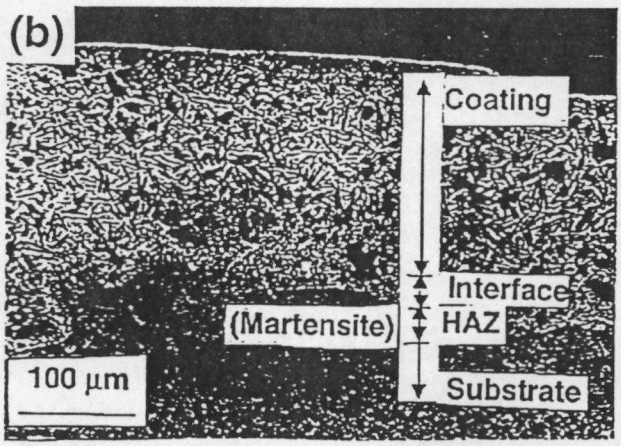
(b)

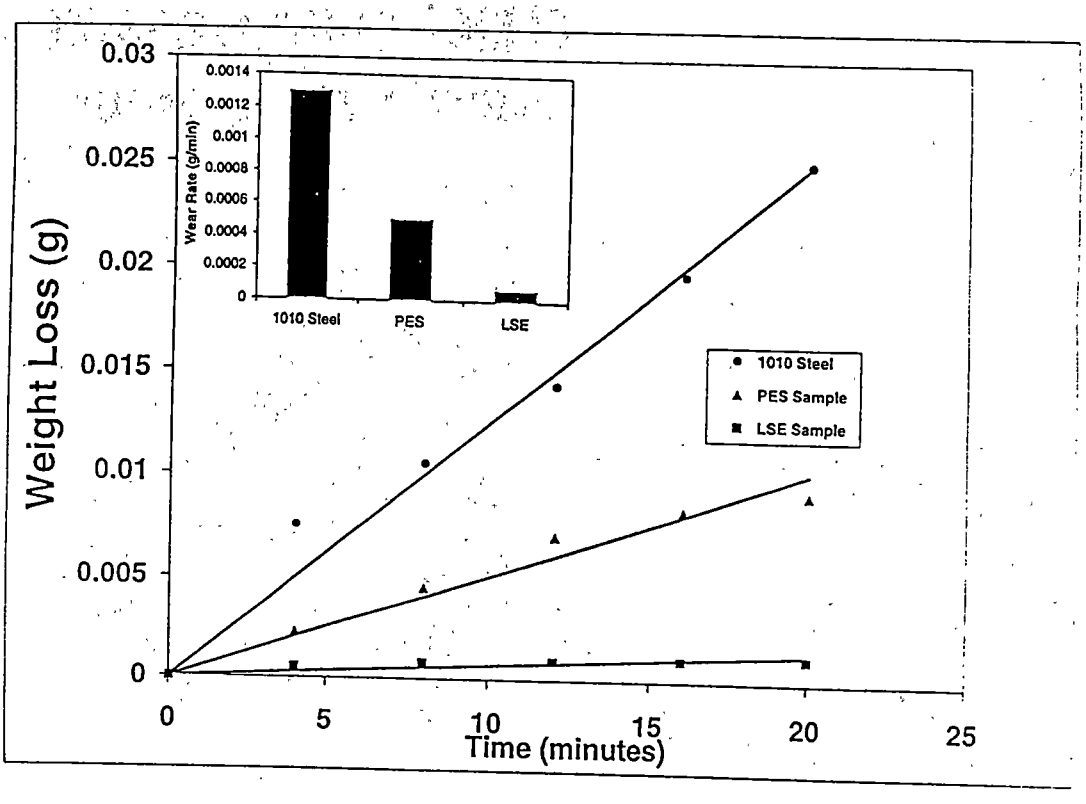


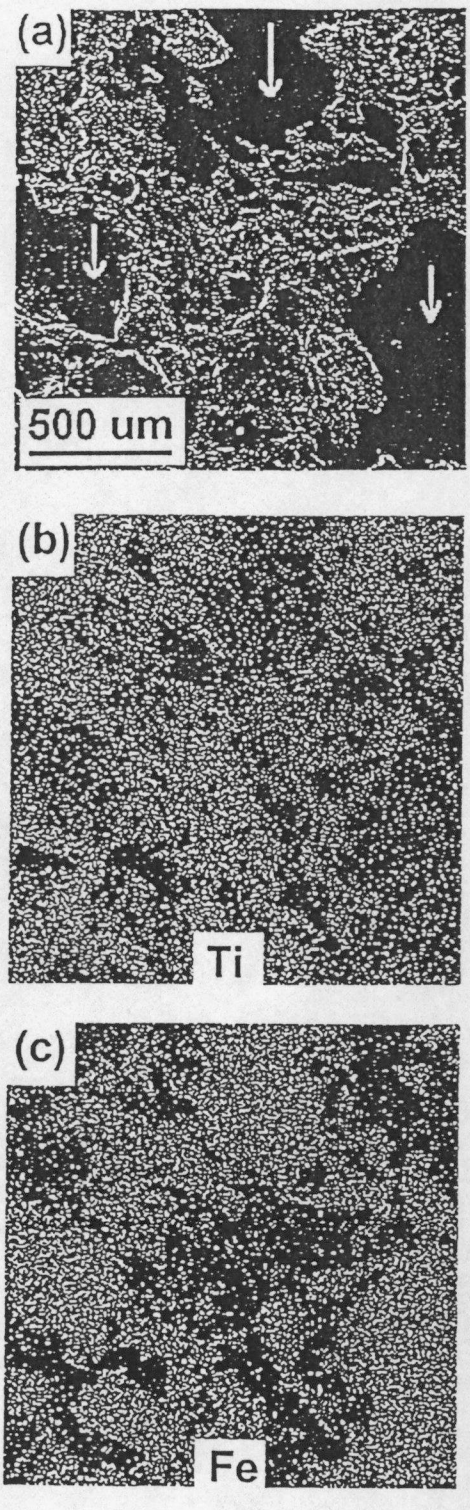

(a)
200 um

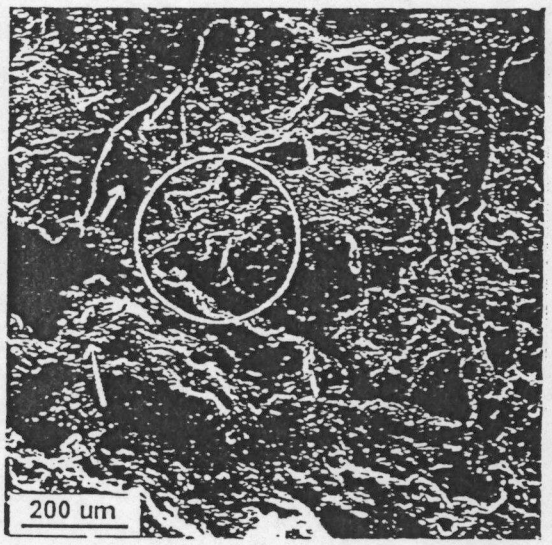

(b)
R_a = 6.39 um

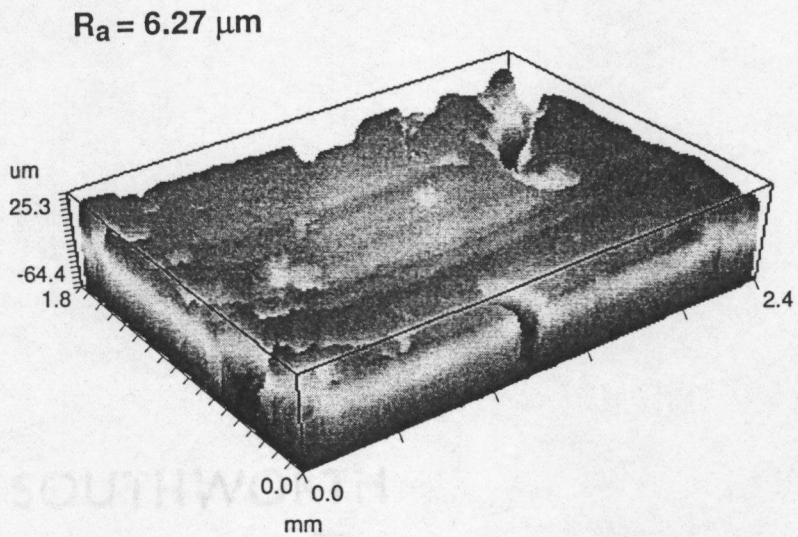

(a)
Coating
HAZ
Substrate
100 μm

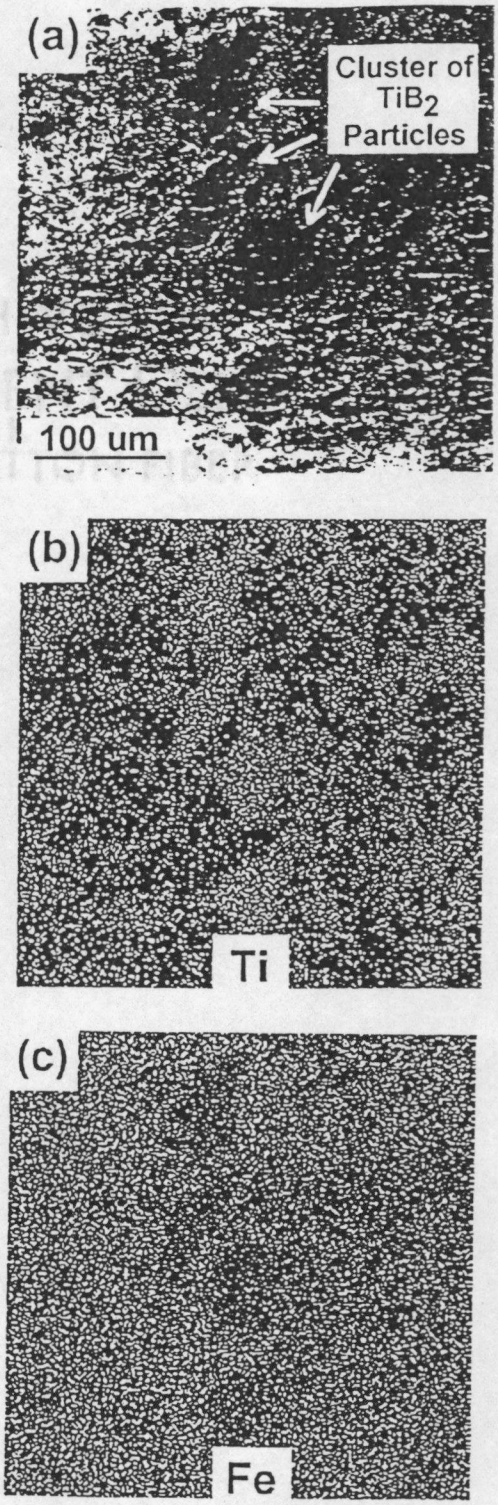

(b)
Coating
Interface
HAZ
(Martensite)
Substrate
100 μm

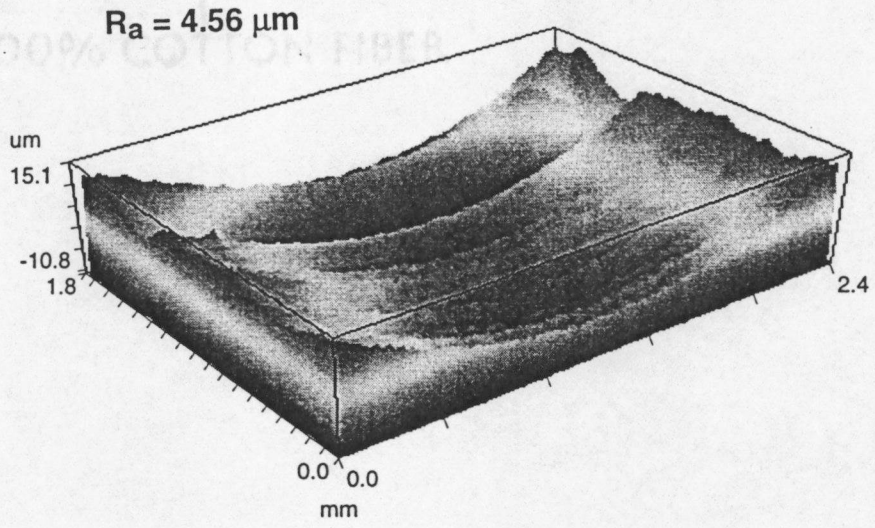

Weight Loss (g)
0.03
0.025
0.02
0.015
0.01
0.005
0
0
5
10
15
20
25
Time (minutes)
1010 Steel
PES Sample
LSE Sample
Wear Rate (g/min)
0.0014
0.0012
0.001
0.0008
0.0006
0.0004
0.0002
0
1010 Steel
PES
LSE

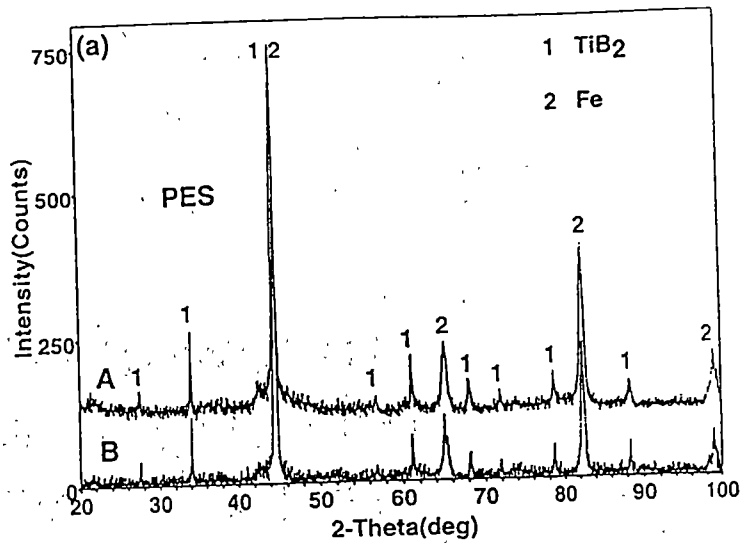

(a)
500 um
(b)
Ti
(c)
Fe


200 um

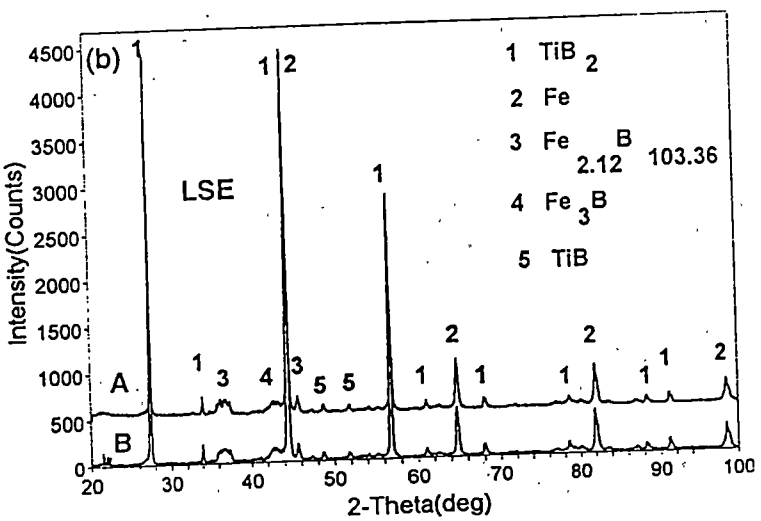

R_a = 6.27 μm
um
25.3
-64.4
1.8
2.4
0.0
0.0
mm

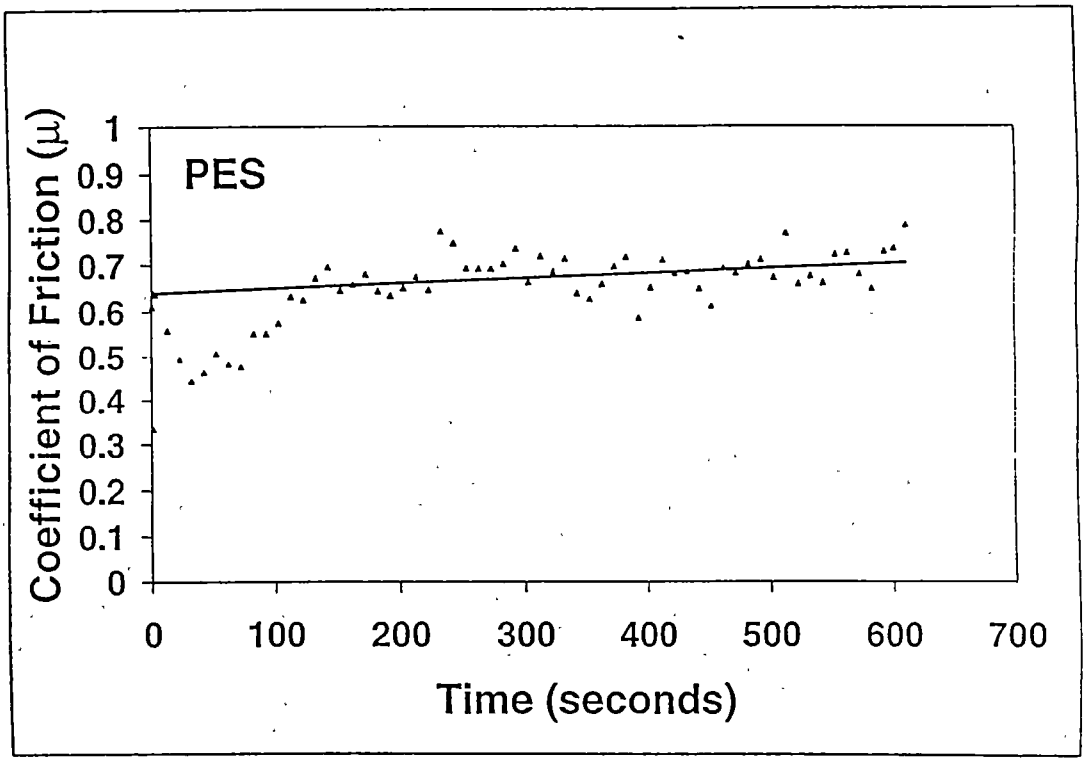

(a)
Cluster of TiB_2 Particles
100 um
(b)
Ti
(c)
Fe

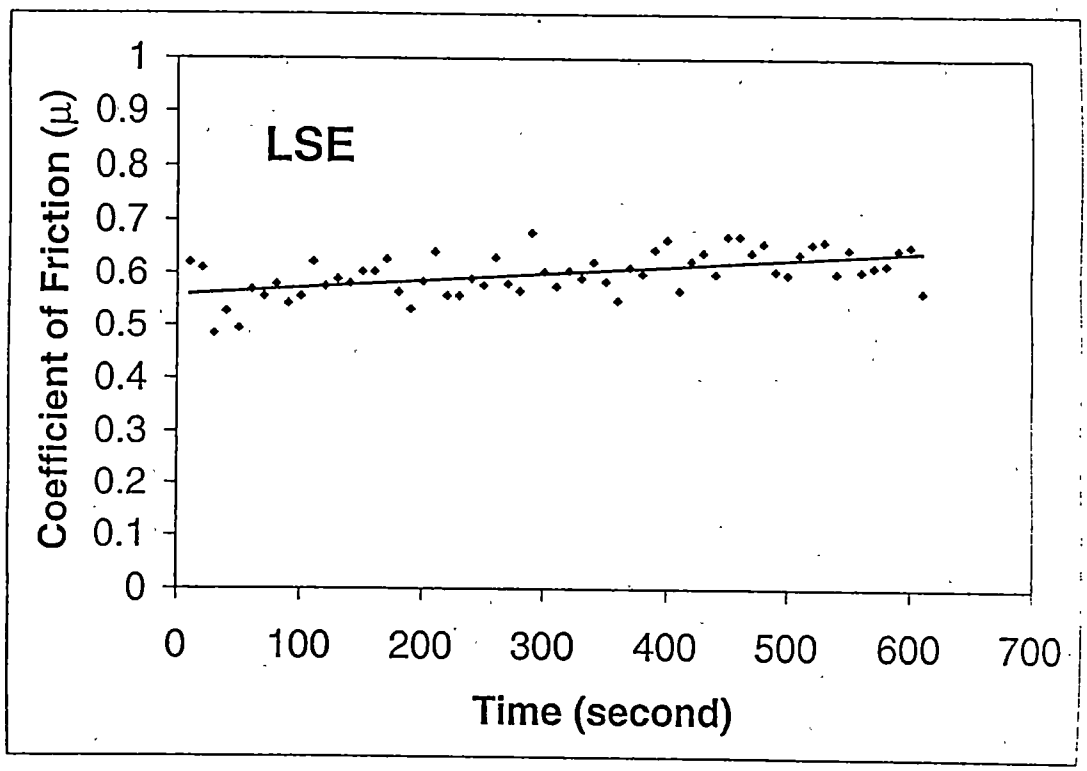

R_a = 4.56 μm
um
15.1
-10.8
1.8
2.4
0.0
0.0
mm



A - After Wear B - Before Wear




PES
Coefficient of Friction (μ)
1
0.9
0.8
0.7
0.6
0.5
0.4
0.3
0.2
0.1
0
0
100
200
300
400
500
600
700
Time (seconds)


LSE
Coefficient of Friction (μ)
1
0.9
0.8
0.7
0.6
0.5
0.4
0.3
0.2
0.1
0
0
100
200
300
400
500
600
700
Time (second)

APPENDIX VII

IN-SITU SYNTHESIS OF INTERMETALLIC AND CERAMIC COATING USING PULSE ELECTRODE SURFACING

(This paper has been accepted for publication in ***Scripta Materialia*** journal)

IN-SITU SYNTHESIS OF INTERMETALLIC AND CERAMIC COATING USING PULSE ELECTRODE SURFACING

Arvind Agarwal and Narendra B. Dahotre
Department of Materials Science and Engineering
Center for Laser Applications
University of Tennessee Space Institute
Tullahoma, TN 37388

Keywords: Pulse Electrode Surfacing (PES), Coating, Intermetallic, Ceramic, Thermodynamics

Introduction

Pulse Electrode Surfacing (PES) technique utilizes high current electrical pulses of short duration to modify the metal surface. A high current, short duration pulse via discharge capacitance and voltage circuit results in melting the electrode and depositing the material on the substrate (1-6). The primary requirement for the electrode material is that it should be electrically conductive and thus capable of melting in an electric arc. The main advantage of this process is its ability to apply metallurgically bonded coatings with low heat input to the substrate at ambient temperature. Since the process requires very little total heat input, it reduces heat affected zone (HAZ) and minimizes the chance of thermal distortion (4). Substrate material acts as huge heat sink leading to rapid solidification of the molten pool. This results in an extremely fine-grained coating of high density, hardness and strength. Coatings deposited using PES process are used for several applications such as nuclear, fossil and geothermal energy environment (4,6-7), high temperature turbine coatings (8), industrial cutting tools such as milling cutters and drills (9), wear resistant surfaces on large agricultural and textile equipment, high temperature sensors, systems used in petrochemical and pharmaceutical industry and for modern sport equipment(4). In the earlier studies based on PES process, ultrahard ceramic and intermetallic coatings have been deposited using an electrode of same material as that of coating (6-7,10-12). However, in the present study an attempt has been made to synthesize intermetallic and ceramic coating using reactive synthesis during PES process. Such an approach may eliminate the need of using electrodes of intermetallic and ceramic materials for coating, as often it is very difficult and expensive to produce electrodes from these materials without any impurities. Fe_3Al based intermetallic and AlN based ceramic coatings have been synthesized using PES process.

Iron aluminide (Fe_3Al) based intermetallics are well known for their excellent resistance to high-temperature sulfidizing and oxidizing environment (13). Moreover, they have high hardness with an excellent wear and erosion resistance (14). However, environmental effect such as hydrogen embrittlement [HE] causes brittle failure of the intermetallic and limits processing of this alloy into useful shapes and components (15). Though several have been made in Fe_3Al alloy development using alloying and thermomechanical treatments, it is still far from being used as commercially available structural material (15-17). It is envisaged that coating structural steel with Fe_3Al based intermetallic would allow the effective usage of its environmental and wear resistant properties. Fe_3Al based coating would also obviate the problems faced in fabrication of these alloys into useful shapes.

Aluminum Nitride (AlN) has been of prime importance to electronic industry due to its electrical insulating characteristic at high temperatures and high thermal conductivity (18). AlN also possess corrosion resistance properties against molten aluminum and can be used as an anti-corrosive coating for liquid aluminum handling tools and sensors (19). AlN has a considerable high oxidation resistance upto 700^{0}C and can be used as a coating on cutting tools and heating elements (19).

In the present study, Fe_3Al and AlN coatings have been synthesized using reaction synthesis during PES process in nitrogen and ammonia environment. Thermodynamic feasibility of such coating synthesis has been addressed. Characterization of these coatings has been performed using various tools such as x-ray diffractometer, microhardness tester and scanning electron microscope (SEM).

Experimental Procedures

Coating Process

Coupons of AISI 1018 steel of dimensions 25 mm x 10 mm were mechanically polished on emery paper of grit 240 and then rinsed with acetone. Aluminum electrode (99.99 % purity) was used to deposit coating on these steel coupons. Deposition was done using a hand held electrode gun in localized nitrogen (N_2) and ammonia (NH_3) environments provided around the region of deposition at room temperature. Pulsed electrode deposition was carried out at 100 volts and a spark time of 10 μs. The discharge capacitance used for the PES process was 300 μF with a current of 50 amperes.

Characterization

ISI Super III-A scanning electron microscope coupled with EDAX was employed for investigation of microstructural morphology and chemical characterization of the coating and interface. Structural characterization for phase(s) identification was carried out on a Philips Norelco x-ray diffractometer with CuK_α radiation operating at 40kV and 20 mA. Microhardness measurements were performed on Buehler Micromet II microhardness tester using a Knoop indenter with a load of 200 gm applied for 15 seconds.

Results and Discussion

Figure 1(a) shows x-ray diffraction spectrum of the coated surface in N_2 environment. Fe_3Al is the major phase present in the coating. However, few peaks of non-stoichiometric phase(s) such as Fe_xAl_y are also indicated. Figure 1(b) is x-ray diffraction spectrum of the coated surface in NH_3 environment. Though Fe_3Al is still the major phase in the coating, characteristic peaks of AlN are also observed between 30 and 40 degree values of two theta. AlN peaks are further resolved in a low speed x-ray scan shown in Figure 1(c). Fe_2N and Fe_3N peaks are also observed apart from AlN peaks. It is an interesting observation that both Fe_3Al and AlN peaks are observed in the coating synthesized in NH_3 environment whereas only Fe_3Al peaks are present in the coating synthesized in N_2 environment. Such behavior can be understood by the thermodynamic nature of reacting species. Equation 1 represents dissociation of NH_3 (20).

$$NH_3 = N + 3/2\ H_2\ ; \qquad \Delta G = 45.46 - 0.11T\ kJ/mol \qquad (1)$$

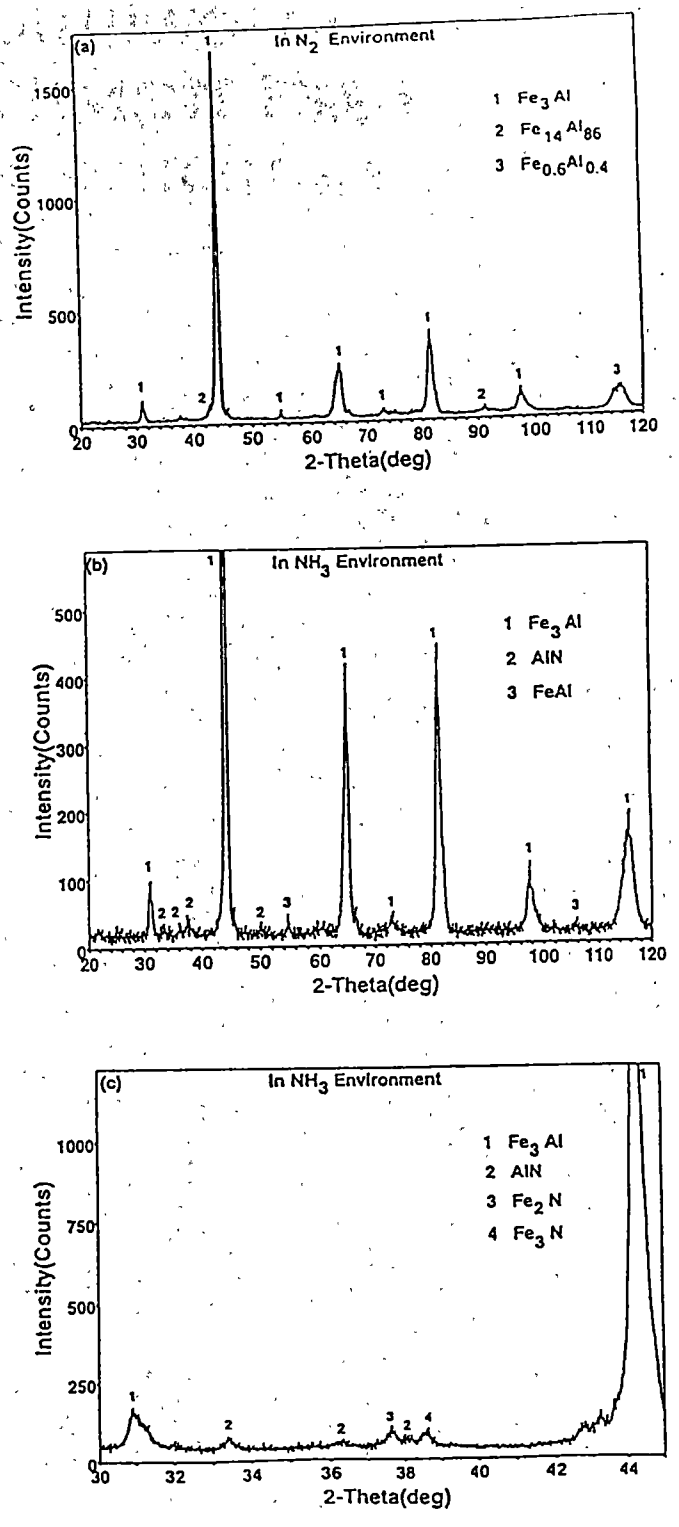


Figure 1. X-ray spectra of the PES coated surface in NH_3 and N_2 environment.

Pulse electrode surfacing is a high energy density process, which appears to provide sufficient energy input to cause dissociation of NH_3. Nascent N reacts with Al electrode to form AlN. Formation of AlN from its parent elements is represented by equation 2 (21).

$$Al + N = AlN; \quad \Delta G = -322.17 + 0.093T \ kJ/mol \qquad (2)$$

Adding equation (1) and (2) provides synthesis of AlN by PES process in NH_3 environment, which is represented by equation (3)

$$Al + NH_3 = AlN + 3/2\ H_2; \quad \Delta G = -276.71 + 0.104\ T \ kJ/mol \qquad (3)$$

Equation 3 is a thermodynamically feasible reaction and ceases AlN formation at 2387^{0}C ($\Delta G = 0$). During PES process, consumable Al electrode with a positive polarity is brought close to the substrate having a negative polarity, which results in arc formation of microsecond duration. Though temperature measurement during arc formation is a debatable issue, it has been successfully argued that material transfer from electrode tip to substrate occurs in liquid state (3). Hence, it is reasonable to assume that arc temperature is higher than melting point of Al. Liquid Al drop reacts with nascent N atom from dissociated NH_3 to form AlN as represented by equation 3.

On the contrary, N_2 is a very stable gas and does not dissociate significantly like NH_3 (22). The energy of dissociation of N_2 into N_{gas} varies between 412-455 kJ/mol for the temperature range of 298-1000 K (22). It further varies between 1783-1856 kJ/mol and 460-437 kJ/mol within the same temperature range for other electronic states viz. $N^+_{(gas)}$ and $N^-_{(gas)}$ (22).

$$N_2 = N_{gas} + N_{gas}; \quad \Delta G = +473.39 - 0.061\ T\ kJ/mol \quad (100\ K \leq T \leq 1300\ K)$$

Although PES is a high energy density process, due to its relatively inefficient mode of energy transfer, energy input is not high enough to cause dissociation of nitrogen (12). On the contrary, nitrogen dissociation has been observed during laser material processing which has very high energy input in comparison with PES process (12,23). Since nitrogen does not dissociate during PES process, liquid Al drop impinges on to 1018 steel substrate and forms Fe-Al based intermetallic. Fe_3Al is the most prominent phase formed represented by equation 4 (24-25).

$$3Fe + Al = Fe_3Al; \ \Delta H_f = 18.0 \ kJ/mol \qquad (4)$$

Formation of Fe_3Al is an exothermic reaction, which occurs after melting point of Al is achieved (24-25). The presence of Al rich liquid causes a rapid increase in the reaction rate resulting in heat evolution, which further increases reaction rate leading to synthesis of Fe_3Al within few seconds (25). A similar reaction mechanism occurs during PES process where liquid Al droplet reacts exothermically with steel substrate to form Fe_3Al based intermetallic coating. EDS analysis suggests 13 –16 wt % Al within the coating region. Such composition is further indicative of Fe_3Al formation within the coating (25).

Microhardness values within the coating, interface and substrate are elucidated in Figure 2. Coating synthesized in NH_3 environment has a higher hardness (774 Knoop) than coating formed in N_2 environment. This is attributed to the presence of AlN in addition to Fe_3Al intermetallic within the coating. AlN is a hard ceramic (1200 kg/mm^2) compared to Fe_3Al based intermetallic which has

hardness in the range of 380-620 kg/mm^2 (18,26). Presence of this hard phase causes an increased hardness in coating produced in NH_3 environment. On the contrary, coating produced in N_2 environment does not have AlN phase. Hardness (592 Knoop) of the coating produced in N_2 environment is mainly due to Fe_3Al.

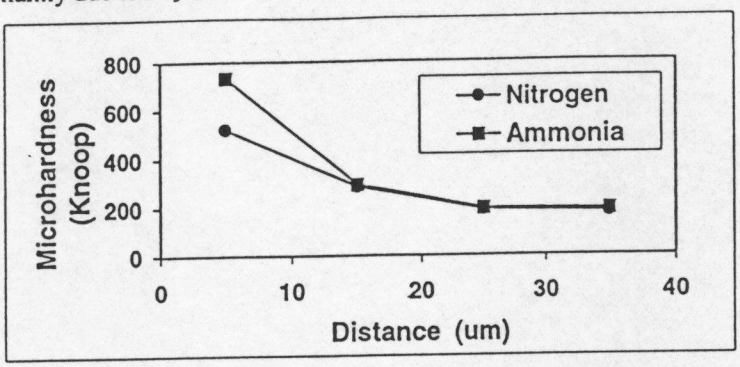


Figure 2. Microhardness variation within the coating, interface and substrate.

Figure 3 shows a SEM micrograph of the cross section of the coating produced by PES process in NH_3 environment. Coating is metallurgically bonded and adherent to the substrate. There are few vertical cracks within the coating, which could be due to differential thermal conductivity of Fe_3Al and AlN (18,26). Similar morphology was observed for the coating deposited in N_2 environment except with an absence of cracks.

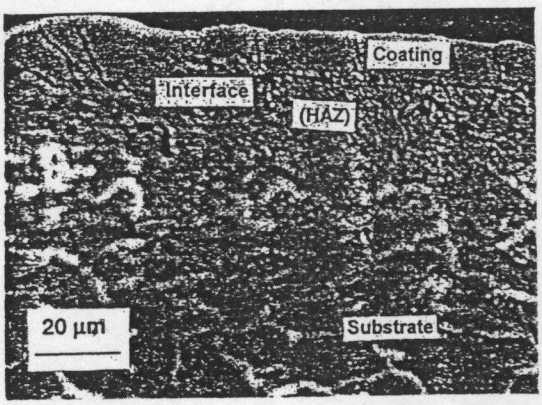


Figure 3. Cross-sectional view of the coating deposited in NH_3 environment.

Conclusions

Fe_3Al based intermetallic and AlN based ceramic coatings have been successfully synthesized using PES process in N_2 and NH_3 environment. AlN is synthesized only in NH_3 environment due to availability of N atoms from dissociated ammonia. Fe_3Al formation is exothermic in nature and occurs in both, N_2 and NH_3 environment. Hardness of coating synthesized in NH_3 environment is higher due to presence of AlN apart from Fe_3Al.

Acknowledgment

The authors wish to express their sincere appreciation to Dr. T. S Sudarshan at Materials Modifications Inc., Fairfax who provided the samples for the present work. The authors acknowledge the financial support from the US Air Force (Contract No. F40600-96-C-0004) for this work.

References

1. R. A. Alfintseva, I. G. Bodrova and A. D. Verkhoturov, J. Less Common Metals. 67, 443 (1979).
2. G. V. Samsonov, A. D. Verkhoturov, V. S. Sychev and A. I. Bezykornov, Fiziko-Khimicheskaya Mekhanika Materialov. 7(5), 3 (1971).
3. V. V. Kantsel, T. S. Kurakina, V. S. Potokin, V. I. Rakhovskii and L. G. Tkachev, Soviet Physics-Technical Phys. 13(6), 814 (1968).
4. R. N. Jhonson, Elevated Temperature Sci. and Techn. I. ed. N. B. Dahotre, J. M. Hampkian and J. J. Stiglich, The Minerals, Metal and Materials Society, Warrendale, PA, 265-277 (1995).
5. R. N. Johnson, Thin Solid Films. 118, 31-47 (1984).
6. R. N. Johnson, Surface Modification Technologies, ed. T. S. Sudershan and D. G. Bhat, The Metallurgical Society, Warrendale, PA, 189 (1988).
7. K. Natesan and R. N. Johnson, Surf. Coating Tech. 33, 341 (1987).
8. S. Raghunathan, J. J. Stiglich and T. S. Sudershan, Elevated Temperature Sci. & Tech. I. ed. N. B. Dahotre, J. M. Hampkian and J. J. Stiglich, The Minerals, Metals and Materials Society, Warrendale, PA 303 (1995).
9. E. A. Brown, G. L. Sheldon and A. E. Bayoumi, Wear. 138, 137 (1990).
10. A. Agarwal and N. B. Dahotre, Surf. Coating & Tech. 106, 242 (1998).
11. A. Agarwal and N. B. Dahotre, Surf. Engg. 15(1), 27 (1999).
12. A. Agarwal and N. B. Dahotre, Mater. Char. 42(1), 31 (1999).
13. C. G. McKamey, J. H. Devan, P. F. Tortorelli and V. K. Sikka, J. Mater. Res. 6, 1779 (1991).
14. M. Johnson, D. E. Mikkola, P. A. March and R. N. Wright, Wear. 140, 279 (1990).
15. C. T. Liu, E. H. Lee and C. G. McKamey, Scr. Metall. 23, 875 (1989).
16. A. Agarwal, R. Balasubramaniam and S. Bhargava, Metall. & Mater. Trans. 27A (10), 2985 (1996).
17. A. Agarwal, J. Akhtar and R. Balasubramaniam, J. Mater. Sci. 31(19), 5207 (1996).
18. B. Bhusan and B. K. Gupta, Handbook on Tribology: Materials, Coatings and Surface Treatments, McGraw Hill, New York, NY. 4.54 (1991).
19. Y. G. Roman and P. M. Adriaansen, Thin Solid Films. 169, 241 (1989).
20. CRC Handbook of Chemistry and Physics, eds. D. R. Lide and H. P. R. Frederikse, CRC Press, New York, 77, 5-81 (1996).
21. G. V. Samsonov and I. M. Vinitskii, Handbook of Refractory Compounds, IFI Plenum Data Company, New York, 77, 5-81 (1996).
22. M. W. Chase Jr., C. A. Davies, J. R. Downey Jr., D. J. Frurip, R. A. McDonald and A. N. Syverud, J. Phys. Chem. Ref. Data. 14(1), 1530 (1985).
23. I. Garcia and J. J. De Damborenea, Corr. Sci. 40(8), 1411 (1998).
24. J. K. Wright, R. N. Wright and G. A. Moore, Scripta Metall. 28, 501 (1993).
25. B. H. Rabin and R. N. Wright, Metall. Trans. 22A, 277 (1991).
26. Processing, Properties and Applicationa of Iron Aluminides, eds. J. H. Schneibel and M. A. Crimp, The Minerals, Metals and Materials Society, Warrendale, PA, 328 (1994).

APPENDIX -VIII

List of Publication from the Present Work

Refereed Journal Publications

- Arvind Agarwal and Narendra B. Dahotre, "Wear Behavior of Composite Boride Coating on Steel using High Energy Density Processes: A Comparative Study", ***Wear,*** (communicated September 1999).
- Arvind Agarwal and N. B. Dahotre, "Insitu Synthesis of Intermetallic and Ceramic Coatings using Pulsed Electrode Surfacing", ***Scripta Mater.*** (accepted September 1999).
- Lalitha R. Katipelli, Arvind Agarwal and Narendra B. Dahotre, "Laser Engineered TiC coating on 6061 Al Alloy: Microstructure and Wear", ***Appl. Surface Science,*** (in press) (1999).
- Arvind Agarwal and N. B. Dahotre, "Mechanical Properties of Laser Engineered Composite Boride Coating on Steel: A Nanoindentation Approach", ***Metallurgical and Materials Transactions A,*** (in press), (to be published in February 2000).
- Arvind Agarwal, L. R. Katipelli and N. B. Dahotre, "Elevated Temperature Oxidation of Laser Surface Engineered Composite Boride Coating on Steel", ***Metallurgical and Materials Transactions A,*** (in press), (to be published in February 2000).
- Anuradha Godavarty, Arvind Agarwal and Narendra B. Dahotre, " Neural Networks in Studies on Oxidation Behavior of Laser Surface Engineered Composite Boride Coating",***Applied Surface Science.*** (communicated November1999).
- Arvind Agarwal and N. B. Dahotre, "Laser Deposited Titanium Diboride Coating for Protection of Molten Aluminum Handling Tools and Molds", ***Lasers in Engg.,***Vol. 9(3), 1999.
- Arvind Agarwal, N.B. Dahotre and L.F. Allard, "Ceramic Metal Interface in Laser Deposited Hard Refractory Composite Coating: Electron Microscopic Study", ***Practical Metallography*** (Germany), Vol. 36 (3), 1999, pp. 250-263.
- Arvind Agarwal and N. B. Dahotre, "Pulsed Electrode Surfacing of Steel with TiC Coating: Microstructure and Wear Properties", ***J. Materials Engineering & Performance,*** Vol. 8(4), August 1999, pp. 479-486.
- Arvind Agarwal and N. B. Dahotre, "Synthesis of Boride Coating on High Energy Density Processes: Comparative Study of Evolution of Microstructure", ***Materials Characterization,*** Vol. 42(1), March 1999,pp. 31-44.
- Arvind Agarwal and N. B. Dahotre, "Laser Surface Engineering of Steel for Hard Refractory Ceramic Composite Coating", ***Intl. Jour. of Refractory Metals and Hard Mater.*** Vol. 17 (4), August 1999, pp. 283-293.
- Arvind Agarwal and N. B. Dahotre, "Pulse Electrode Deposition of Superhard Boride Coatings On Ferrous Alloy", ***Surface and Coatings Technology,*** Vol. 106/2-3, (1998), pp.242-250.
- Arvind Agarwal, N. B. Dahotre and T.S. Sudarshan, "Evolution of interface in pulsed electrode deposited titanium diboride on copper and steel", ***Surface Engineering,*** Vol. 15, No. 1, (1999), pp. 27-32.

- N. B. Dahotre and Arvind Agarwal, "Research Summary: Refractory Ceramic Composite Coating via Laser Surface Engineering", ***JOM***, Vol. 51, No. 4 (1999) pp 19-21.

Chapter in Book

- Surface Preparation and Properties for Coating Deposition: Arvind Agarwal and Narendra B. Dahotre in ***Intermetallic and Ceramic Coatings***, ed. Narendra B. Dahotre and T.S. Sudarshan, Marcel Dekker, New York, February 1999, pp.1-30.

Conference Proceedings

- Arvind Agarwal and N. B. Dahotre, "Characterization and Tribological Behavior of Composite Boride Coating Deposited on Steel using Laser Surface Engineering", ***Elevated Temperature Coatings –3***, Annual TMS Meeting, San Diego, 28th Feb-3 March, 1999
- Arvind Agarwal, N. B. Dahotre and T.S. Sudarshan, "Characterization of Titanium Diboride Coating Deposited on Metals using Pulse Electrode Surfacing (PES) Technique", ***Proc. of International Conf. on Surface Modification Technologies XI***, Paris, France, September 8-10, 1997.

VITA

Arvind Agarwal was born in Agra, India on 18th May, 1970. He did his most of the schooling in Agra and Allahabad. In August1989, he registered in B.Tech (Bachelor of Technology) program at the Department of Materials & Metallurgical Engineering at Indian Institute of Technology, Kanpur, India. After receiving his B.Tech degree in May 1993, he continued his graduate studies at the same department. He received his M.Tech (Master of Technology) degree in January 1995. His M.Tech. thesis was based on "Hydrogen Embrittlement of Iron Aluminides". He joined Tata Engineering and Locomotive Co. (TELCO) at Jamshedpur as a Senior Engineer. But his research interests drew him back to IIT Kanpur as a Research Associate in October 1995 where he continued his research on iron aluminide based intermetallics till July 1996. He moved to The University of Tennessee Space Institute in August 1996 to work on his Ph.D degree as a Graduate Research Assistant. He has more than 20 scientific publications to his credit in various refereed international journals.